

High Spatial Resolution Retrieval of LST and LSE for the Urban Environment

Thesis submitted for the degree of
Doctor of Philosophy
At the University of Leicester

By

Michael James Samuel Perry MPhys (Leicester)

Department of Physics and Astronomy
University of Leicester

September 2016

© Michael J. S. Perry, September 28, 2016

This thesis is copyright material and no quotation from it may be published without proper acknowledgement.

Declaration

I hereby declare that no part of this thesis has been previously submitted to this or any other University as part of the requirement for a higher degree. The work described herein was conducted by the undersigned except for contributions from colleagues as acknowledged in the text.

Michael J S. Perry

September, 2016

High Spatial Resolution Retrieval of LST and LSE for the Urban Environment

Michael James Samuel Perry

Abstract

Understanding the changing and complex urban thermal environment is key to addressing the health and sustainability of the cities in which more than half of the world's population live. The monitoring and assessment of the thermal environment requires spatial resolution that so far has precluded air temperatures from being a viable parameter in most cities. Land surface temperatures (LSTs) offer the ability through satellite remote sensing to investigate the urban environment in a robust and consistent manner. Additionally land surface emissivity (LSE) is required to enable accurate LST estimation and characterise broad-scale thermal infra-red properties of materials.

In this thesis, the first optimal estimation of simultaneous LST and LSE data optimised to be robust for urban areas with highly complex surfaces is presented. It uses the thermal channels of the ASTER instrument with a spatial resolution of 90 m. In simulations the algorithm retrieved LST to 1 K or better, and LSEs to within 0.01. The simulation uncertainties retrieved are better than 1 K in LST and 0.015-0.017 for LSE. This marks the first usage of an inverse method with ASTER data. Verification of the LSE for a non-urban scene (Algodones) was undertaken, through inter-comparison with the TES method. Results agreed well with both TES and the validation site in channel 12 and with very low retrieval radiance residuals.

The algorithm was also used in three urban case studies. In each, this scheme was able to address key scientific issues, including urban green space and rapid urban expansion, using a combination of the LST and the LSE. The high accuracy of the retrieved LSE was able to distinguish characteristic LSE spectra and identify surface changes.

These results show the retrieval of robust and scientifically meaningful LST and LSE data for the heterogeneous urban environment from ASTER, vital to urban studies.

Acknowledgements

There are many people who have helped guide and support me throughout this work and I would like to take a minute to offer my thanks. Firstly, John Remedios, you have helped and guided me through this entire journey. You have had the patience and vision to see me through this work, even when I didn't, thank you so much. Thank you for all the support you have shown me through the last four years and for the help you continue to give me. Thank you also, Nick Tate, our talks have really helped my writing, which I think you will agree is no mean feat!

Thanks go out to everyone in the EOS group who has helped me throughout this PhD. Thank you to those in the surface temperature group, especially Gary and Darren for offering advice and criticism when they were sorely needed. Special thanks to my office mates (past and present), Geddes, Eddy, Tim, Emma, Hannah and Sadie. Thank you for the distractions, and for keeping me sane, you did your best! In particular, I have to thank Alex and Peter, you two have been there for every procrastination, tea break and lunch! Alex, thank you working so hard to destroy my sanity!

Thanks go to Mel, you have put up with me for 8 years of friendship and have helped me at every stage, and I would not have made it this far without your help. Liam, Hannah, James, and Matt you guys know why you're here! I hope you'll join me Alex and Peter at a tavern soon for adventure! Additional thanks to Liam for taking on my musical education. Hannah thank you so much for helping me across the finishing line. James, still not sold on mushishi, but thank you for being the most amazing housemate and friend over the years!

Thanks to Ben for always being there knowing what to say and getting in the cider! Chan you make sure life is never boring. John and Amy, you guys have put up with me flaking out on plans and moaning over the phone more than I can say! To all of you, your support and friendship has been invaluable! Katie thank you for being as stupidly competitive as I am, bring on the next challenge!

I don't exactly know how to properly thank my family. Anthony and Theresa, you have been the most wonderful and supportive parents I could ever have asked for. Whatever and whenever I need help or support you have never paused for a moment before helping

me. Thank you for so much. Kate, thank you for being an incredible sister, for putting up with my countless annoyances and for reading my thesis, above and beyond the call of family!

Andrew, I cannot fully say how much you have helped me in this thesis. You have been there for each and every problem I have ever had. You have believed in me more than I believed in myself and you have carried me through this. Thanks so much.

Table of Contents

1	Introduction	1
1.1	Rationale for Urban Studies	1
1.2	The Urban Heat Island	1
1.3	The Urban Energy Balance	3
1.3.1	The Radiation Budget	4
1.3.2	The sensible heat flux	5
1.3.3	The latent heat flux	7
1.3.4	The ground heat flux	7
1.3.5	The Urban Energy Balance Equation	9
1.4	Rationale for Measuring LST and LSE.....	9
1.5	Requirements for LST and LSE.....	11
1.6	Summary	12
2	Instrumentation and Data Products	13
2.1	Introduction	13
2.2	ASTER	13
2.2.1	Instrument Specifications	14
2.2.2	Instrument Performance.....	20
2.3	MODIS	27
2.3.1	Infra-red window Instrument Specifications	28
2.3.2	Instrument Calibration	29
2.3.3	Instrument Performance.....	30
2.4	Data Products	31
2.4.1	ASTER L1b/L1T	32

2.4.2	MODIS MOD11_L2.....	32
2.5	Summary	33
3	Radiative Transfer and Retrieval Theory	34
3.1	Introduction	34
3.2	Radiative Transfer.....	34
3.3	Radiative transfer model	36
3.4	Simulated radiative transfer	38
3.4.1	RFM.....	38
3.4.2	RTTOV	38
3.5	Traditional LST Algorithms.....	40
3.6	The TES method	43
3.7	Optimal Estimation Theory.....	47
3.7.1	Bayesian Approach.....	48
3.7.2	Cost Function.....	50
3.7.3	Newton Hessian Methodology.....	50
3.7.4	Marquardt Levenberg Methodology.....	51
3.7.5	Averaging kernels and gain matrices.....	52
3.7.6	Error Analysis	53
3.8	Previous Optimal Estimation Algorithms for LST	55
3.9	Summary	56
4	Retrieval Development.....	58
4.1	Introduction	58
4.2	Algorithm formulation	58
4.3	Initial Processing.....	58
4.3.1	A priori parameter determination	59
4.3.2	A priori covariance determination	61
4.4	Convergence strategy	64

4.5	Simulated surface parameter retrieval.....	66
4.6	MODIS spectral library testing	66
4.6.1	Fixed LSE covariance	67
4.6.2	ASTER spectral library derived covariance	69
4.6.3	ASTER spectral library derived covariance including off-diagonal channel variance 70	
4.6.4	Summary of methodologies	72
4.7	SLUM Library test	76
4.8	Water Vapour retrieval.....	80
4.8.1	State vector inclusion of Water Vapour.....	81
4.9	Algodones TES inter comparison	87
4.9.1	Retrieval Comparison	88
4.9.2	Verification Assessment	97
4.9.3	Uncertainty and Radiance Residuals	100
4.10	Water LSE.....	103
4.11	Summary	104
5	Case Study I – Phoenix Arizona.....	106
5.1	Introduction	106
5.2	Phoenix Test Site.....	106
5.3	Data Pre-Processing	108
5.4	Land Classification.....	109
5.4.1	VNIR Classification.....	110
5.4.2	K-Means Cluster Analysis	111
5.5	Initial Scene.....	113
5.5.1	Retrieved LST and LSE.....	113
5.5.2	Retrieval Statistics	121
5.6	Variance analysis	125

5.6.1	LSE	126
5.6.2	LST	129
5.7	Scene Transects.....	132
5.7.1	Transect 1: Urban/Sand/Vegetation boundaries	133
5.7.2	Transect 2: LSE structures/Impervious surfaces	136
5.7.3	Transect 3: Urban Green Space	140
5.8	Summary	144
6	Case Studies II and III - Shanghai and New York	146
6.1	Introduction	146
6.2	Case Study II: Shanghai	146
6.2.1	Study area	147
6.2.2	Urban change detection	148
6.3	Case Study III: New York.....	169
6.3.1	Study area	169
6.3.2	Retrieval Performance	171
6.3.3	LST and LSE Spatial Structures	174
6.3.4	Transect Analysis.....	179
6.4	Summary	184
7	Conclusions and Future Work.....	186
7.1	Summary	186
7.2	Future work	189
7.2.1	Improvements to the retrieval	189
7.2.2	Future Instrumentation and datasets	193
7.2.3	Applications of data	196
7.3	Conclusions	198
8	Bibliography	199

List of Figures

Figure 1 – A diagram simply demonstrating the surface energy balance including the net radiative flux (NR), the sensible heat flux (H), the latent heat flux (LvE) and the ground heat flux (G).....	3
Figure 2 – A diagram simply demonstrating the surface radiation budget. Blue lines: (a) downward shortwave flux and (b) shortwave ground reflected flux. Red lines: (c) long wave thermal emission from surface and (d) long wave thermal emission from the atmosphere.	5
<i>Figure 3- An example showing the soil temperature amplitude attenuation with depth and the temporal phase shift of the peak. Plot based on that of Campbell and Norman, (2000).</i>	8
Figure 4 - Diagram of the VNIR subsystem in ASTER. Highlights: dark blue – The nadir telescope used with all three VNIR spectral bands. Red – The backwards telescope used with the third spectral channel only. Image taken from NASA (2004b).	15
Figure 5 – Diagram of the SWIR subsystem in ASTER. Highlights: Red – The telescope. Blue – The pointing mirror and mount. Green - The Stirling cooler. Image taken from (NASA, 2004a).....	16
Figure 6 – Diagram of the TIR subsystem in ASTER. The light enters at the top of the diagram, the dashed outline indicates the orientation of the pointing mirror when the instrument is in calibration mode.	18
Figure 7 – Radiometric flow diagram for the processes from the detection of incident photons through to the digitized signal for downlink.	19
Figure 8 - On-board Calibration of the ASTER Instrument, Sakuma Et.al. 2005. These plots show the trends of ten detectors present in TIR channel 12. The temperature changes shown are the differences from the first inflight calibration performed. The four selected DNs correspond to temperatures of 270, 300, 320 and 340 K.....	22
Figure 9 – The change in calibration coefficient over time in Band 12 of the TIR subsystem as a response to reduced detector responsivity, Sakuma et.al. 2005.	23
Figure 10 – The NEAT values for the TIR bands (Y-axis) calculated in-flight. Radiometric Performance Evaluation of ASTER VNIR, SWIR, and TIR, Arai and Tonooka, 2005.	24

Figure 11 – Diagram showing the scene rotation for the L1T dataset, the black arrow shows the orbit direction, (NASA, 2015). 26

Figure 12 – Diagram of the MODIS instrument showing the key components (Barnes et al., 1998). 28

Figure 13 – A simple layer model of radiative transfer. The atmosphere is described in three layers. The Blue lines show Emission, Red lines Transmission and Green Reflection. 36

Figure 14 – Laboratory derived empirical MMD-minimum emissivity relationship for 86 material types. Plot taken from Gillespie et al., (1999) 45

Figure 15 – Example of LSE spectra from the ASTER spectral library. The material is asphalt, the red dashed line is the LSE at the library resolution, and the blue squares denote the values calculated for the ASTER TIR bands using the instrument spectral response function..... 60

Figure 16 – Plot showing the variation in retrieved LST and LSE uncertainty (contours) with the input a priori parameters. (A) Shows the effect of the a priori LST and LSE on the retrieved LST uncertainty. (B-F) Shows the effect of the a priori LST and LSE on the retrieved LSE uncertainty in Channels 10-14 respectively. 62

Figure 17 – Flow chart diagram for the cost function strategy utilised in the retrieval. C represents the cost function in this diagram..... 65

Figure 18 - Sample retrievals for Goleta sands (bare soil), laurel trees (vegetation), red masonry (urban) and tan brickwork (urban) materials in the MODIS spectral library using the fixed a priori LSE approach..... 68

Figure 19 - Sample retrievals for Goleta sands (bare soil), laurel trees (vegetation), red masonry (urban) and tan brickwork (urban) materials in the MODIS spectral library using the a priori LSEs determined from the mean class values from the ASTER spectral library..... 69

Figure 20 - Sample retrievals for Goleta sands (bare soil), laurel trees (vegetation), red masonry (urban) and tan brickwork (urban) materials in the MODIS spectral library using the a priori LSEs determined from the mean class values from the ASTER spectral library with the inclusion of the off-diagonal LSE covariance. 71

Figure 21 - Correlation plot for LSE in each of the ASTER TIR channels (10-14) comparing the retrieved and true values for three different a priori set-ups..... 72

Figure 22 - Correlation plot for LSE in each of the ASTER TIR channels (10-14) comparing the retrieved and true values for the entirety of the SLUM spectral library.....	77
Figure 23 - Sample retrievals for asphalt and brick in the SLUM spectral library using the a priori LSEs determined from the mean class values from the ASTER spectral library with the inclusion of the off-diagonal LSE covariance.	78
Figure 24 - Sample retrievals for concrete and roofing tile in the SLUM spectral library using the a priori LSEs determined from the mean class values from the ASTER spectral library with the inclusion of the off-diagonal LSE covariance.	79
Figure 25 - Water vapour Jacobians calculated for each of the five ASTER TIR channels on a sample of 10,000 atmospheric profiles ranging from TCWV's of 0.5-10 mm. The darker blue points show the mean Jacobian values for each channel whilst the lighter blue region shows the area bounded by the standard deviation.....	81
Figure 26 - A histogram of the true TCWVs for the simulations. There is a clear bias towards TCWV values at 2mm which would be carried into the retrieved parameters.	84
Figure 27 - Histograms showing the Retrieved – True values for the (a) LST and the (b-f) LSEs for channel 10-14 respectively using the ABS-WV retrieval. The red bars show the raw data, and the blue bars show the filtered data where a priori LSE errors greater than 0.05 were omitted.	84
Figure 28 - Histograms showing the Retrieved – True values for the (a) LST and the (b-f) LSEs for channel 10-14 respectively using the INC-WV retrieval. The red bars show the raw data, and the blue bars show the filtered data where a priori LSE errors greater than 0.05 were omitted.	85
Figure 29 - (a) Histogram of the residuals for ABS-WV – INC-WV for LST. (b) The plot of the residual shown in (a) plotted against the true TCWV. The blue line represents the mean values for each TCWV bin and the green lines border the region encompassed by the mean \pm standard deviation.....	85
Figure 30 – Landsat image of the Algodones test site near the Salton Sea in New Mexico, USA. Image taken from Google Earth, 32.975 N, -115.048 E, image acquired 12/31/2014, accessed on 16/09/2016.	88

Figure 31 – LST Retrieved from the TES algorithm by JPL, for the Algodones site. Temperature in K.	89
Figure 32 – LST Retrieved using the Optimal Estimation algorithm, for the Algodones site. Temperature in K.	89
Figure 33 - Retrieved LSE TOP: OE, BOTTOM: TES. (a) Channel 10, (b) Channel 11 and (c) Channel 12.....	91
Figure 34 - Retrieved LSE TOP: OE, BOTTOM: TES. (d) Channel 13 and (e) Channel 14.....	92
Figure 35 – LEFT: OE, RIGHT: TES. (a,b) Retrieved LST, (c,d) Channel 10 LSE and (e,f) Channel 11 LSE	93
Figure 36 - LEFT: OE, RIGHT: TES. (g,h) Channel 12 LSE, (i,f) Channel 13 LSE and (k,l) Channel 14 LSE	94
Figure 37 - Correlation plots of the OE vs TES Retrieved results for LST and LSEs across all channels.....	96
Figure 38 – Retrievals tested against the validation data, for Algodones, USA. Green line shows the values for the validation data, purple the OE retrieval, and orange the TES values.	97
Figure 39 – The retrievals for both TES (orange) and OE (purple) for the vegetative region of the Algodones test case. The green shows the a priori data with the uncertainties.	99
Figure 40 - Histograms for the retrieved values of LST and LSE for Algodones, with the mean and standard deviation of each set.	102
Figure 41 – Histograms of the retrieved radiance residuals for the Algodones scene for each channel.	102
Figure 42 - Comparison of the a priori (green line) and retrieved (purple line) LSEs for water. The shaded purple region shows the retrieved uncertainty, and the green area the a priori covariance for water.	104
Figure 43 -False colour image of Phoenix, processed from Landsat 8's Channels 5, 4 and 3. The lime green represents the regions with increased vegetation whilst the darker green and turquoise sections show the impervious man-made materials	107
Figure 44 – A visible true colour image of the subset which was used in initial testing of the classification and the retrieval algorithm. Image taken from Google	

earth, 33.460 N, -112.060 E, image acquired 16/03/2015, image obtained 16/07/2016.....	110
Figure 45 – Land classification map over a spatial subset of Phoenix, Arizona. The classification is based off the ratio of the VNIR channel radiances.....	111
Figure 46 – K-means land classification map for the Phoenix scene subset. The four classifications returned here are: urban (black), soil/dust (red), vegetation (green) and mixed urban/vegetation (blue). Taken 20/05/2011.	112
Figure 47 – LEFT: A visible true colour image of the full scene, Image taken from Google earth, 33.460 N, -112.060 E, image acquired 04/03/2011, image obtained 16/07/2016. RIGHT: Retrieved LST (K) for the full study site on 20/05/2011	115
Figure 48 – LEFT: A visible true colour image of the full scene, Image taken from Google earth, 33.460 N, -112.060 E, image acquired 04/03/2011, image obtained 16/07/2016. RIGHT: Retrieved LSE in Channel 12 for the full study site on 20/05/2011	116
Figure 49 – LEFT: A visible true colour image of the full scene, Image taken from Google earth, 33.460 N, -112.060 E, image acquired 04/03/2011, image obtained 16/07/2016. RIGHT: Retrieved Water vapour for the full study site on 20/05/2011 (cm).....	117
Figure 50 – LEFT: A visible true colour image of the subset which was used in initial testing of the classification and the retrieval algorithm, Image taken from Google earth, 33.460 N, -112.060 E, image acquired 04/03/2011, image obtained 16/07/2016. RIGHT: Retrieved LST (K) for the spatial subset of Phoenix on 20/05/2011	118
Figure 51 – LEFT: A visible true colour image of the subset which was used in initial testing of the classification and the retrieval algorithm, Image taken from Google earth, 33.460 N, -112.060 E, image acquired 04/03/2011, image obtained 16/07/2016. RIGHT: Retrieved LSE in Channel 12 for the spatial subset of Phoenix on 20/05/2011	119
Figure 52 – LEFT: A visible true colour image of the subset which was used in initial testing of the classification and the retrieval algorithm, Image taken from Google earth, 33.460 N, -112.060 E, image acquired 04/03/2011, image obtained 16/07/2016. RIGHT: Retrieved Water Vapour for the spatial subset of Phoenix on 20/05/2011(cm).....	120

Figure 53 - Histograms for the retrieved values of LST and LSE for Phoenix, with the mean and standard deviation of each set..... 122

Figure 54 – Histograms for the retrieved uncertainties for LST and LSE for Phoenix. 122

Figure 55 – Histogram of the retrieved radiance residuals for Phoenix. 124

Figure 56 - The LSE standard deviations for all pixels in the subset. TOP: a map of the distribution of the standard deviation. BOTTOM: a histogram of all the pixels in the subset. LEFT to RIGHT: Channel 10, 11 and 13. White circles highlight water variation. 127

Figure 57 - The LSE standard deviations for all pixels in the subset. TOP: a map of the distribution of the standard deviation. BOTTOM: a histogram of all the pixels in the subset. LEFT to RIGHT: Channel 13 and 14. 128

Figure 58 - The standard deviation for the LST from a mean calculated from a composite of all the scenes studies. The LEFT, panel shows the spatial distribution of the LST standard deviations (K). The RIGHT panel shows the histogram of the standard deviations across the subset (K). 130

Figure 59 – Visible image from Google Earth for the site of Transect 1. Image taken from Google earth, 33.511 N, -111.860 E, image acquired 08/03/2014, image obtained 16/07/2016. The large red rectangle shows the area used in the LST and LSE maps. Each of the smaller boxes refers to a specific study site. 1: sand/soil, 2: cropland, 3: dry river basin and 4: urban. 133

Figure 60 - Latitudinal transect for 09/03/2014. The LEFT panel shows the retrieved LSE in channel 12 for the whole range of latitudes. The colours correspond the a priori classification given to the pixel: dark blue = urban, cyan = mixed vegetation and urban, gold = rock/bare soil and green = vegetation. The MID panel shows a map of the retrieved LSE in the area surrounding the transect with the transect path denoted by a black dashed line. The RIGHT panel shows a map of the retrieved LST in the area surrounding the transect, path denoted by a black dashed line. 134

Figure 61 – LSEs with associated uncertainties for the specific sites with in Transect 1, for all channels. 135

Figure 62 - Latitudinal transect for 09/03/2014. The LEFT panel shows the retrieved LSE in channel 12 for the whole range of latitudes. The colours correspond the a priori classification given to the pixel: dark blue = urban, cyan =

mixed vegetation and urban, gold = rock/bare soil and green = vegetation. The MID panel shows a visible image of the area with the transect denoted by a black dashed line. The RIGHT panel shows a map of the retrieved LSE in the area surround the transect with the transect path denoted by a black dashed line. Across all three panels are three bounding boxes. The red boxes highlight the latitudes associated with the airport runways, and the brown box with the dry river basin.

..... 137

Figure 63 - LSEs with associated uncertainties for the specific sites with in Transect 2, for all channels. 138

Figure 64 – Retrieved LST (K) for the area surrounding Transect 2. 139

Figure 65 – Park transect for 20/05/2011. (TOP) Panel showing transect overlaid on visible imagery, red dashed line denotes the transect path. Image taken from Google earth, 33.460 N, -112.060 E, image acquired 04/03/2011, image obtained 16/07/2016. (MID) A subset showing the LST for the area surrounding transect. The transect path denoted by black dashed line. (BOTTOM) LST of the right axis for the transect, NDVI on the left. The colours correspond the a priori classification given to the pixel: dark blue = urban, cyan = mixed vegetation and urban, gold = rock/bare soil and green = vegetation..... 140

Figure 66 – Channel 12 LSE for the area of the park and Transect 3 141

Figure 67 - LSEs with associated uncertainties for the specific sites with in Transect 2, for all channels. 141

Figure 68 – Transects for 22/03/2013 and 09/03/2014. Left axis is retrieved LST, right axis NDVI. The colours correspond the a priori classification given to the pixel: dark blue = urban, cyan = mixed vegetation and urban, gold =rock/bare soil and green = vegetation. The red shaded region highlights the area bounded by the park for inter-comparison.. Image taken from Google earth, 33.480 N, -112.040 E, image acquired 08/03/2014, image obtained 16/07/2016. 143

Figure 69 – RGB image from LANDSAT 8 data for Shanghai in 2014. 148

Figure 70 - K-means land classification map for the Shanghai observations. The five classifications returned here are: urban (blue), soil/dust (orange), vegetation (green), mixed urban/vegetation (cyan) and open water (red)..... 149

Figure 71 - Comparison of the a priori class changes to channel 12 LSE changes. LEFT: the change in class between observations, red indicates a change from urban in 2009 to non-urban in 2014, green indicates a change from non-urban in

2009 to urban in 2014. RIGHT: the change in channel 12 LSE between observations, red indicates an Increase in LSE from 2009 to 2014, green indicates a decrease in LSE from 2009 to 2014. In both cases black represent no significant change between the observations..... 151

Figure 72 – The Channel 12 LSE difference between observations (2014 – 2009). LEFT for the whole scene. RIGHT for a subset where there was a noticeable shift. 152

Figure 73 – Retrieved LSEs for change detected in region 1 with associated uncertainty. 152

Figure 74 –RGB imagery from LANDSATs 5 and 8 for Shanghai region 1. TOP: LANDSAT 5 RGB for 21/10/2009, BOTTOM: LANDSAT 8 RGB for 04/11/2014. 154

Figure 75 – The retrieved LST (K) for Region 1 in 2009 and 2014..... 155

Figure 76 – The Channel 12 LSE difference between observations (2014 – 2009). Region 2, highlighting a substantial increase in LSE in 2014..... 156

Figure 77 - RGB imagery from LANDSATs 5 and 8 for Shanghai region 2. TOP: LANDSAT 5 RGB for 21/10/2009, BOTTOM: LANDSAT 8 RGB for 04/11/2014. 157

Figure 78 - Retrieved LSEs for change detected in region 2 with associated uncertainty. 158

Figure 79 – Retrieved LST (K) for Region 2, for 2009 and 2014. 158

Figure 80 – The retrieved LSE for Region 3 in Shanghai in channel 12. LEFT: the retrieved LSE in 2009, RIGHT: the retrieved LSE in 2014. 160

Figure 81 - RGB imagery from LANDSATs 5 and 8 for Shanghai region 3. LEFT: LANDSAT 5 RGB for 21/10/2009, RIGHT: LANDSAT 8 RGB for 04/11/2014. 161

Figure 82 - The retrieved LST (K) for Region 3 in Shanghai. LEFT: the retrieved LST in 2009, RIGHT: the retrieved LST in 2014..... 162

Figure 83- Retrieved LSEs for change region identified as the car park in region 3 with associated uncertainty..... 163

Figure 84 –LEFT the a priori classifications. Class numbers correspond to a particular cover type: 0 - no data, 1 - urban, 2 - mix: urban/vegetation, 3 - vegetation, 4 - rock/soil, and 5 - water. RIGHT the retrieved LSE data for channel

12. TOP panels show the data for 2009, BOTTOM panels for the data for 2014.	165
Figure 85 - Visible imagery from DigitalGlobe and CNES ASTRIUM obtained from Google Earth for a subset of Region 4. LEFT shows data from 2009, RIGHT for 2014. The top panels show the Airport runways, the bottom panels show a close up view of a loading and taxi way for the aeroplanes.	166
Figure 86 – Retrieved LSEs for all channel for two locations: The eastern runway and the site which became the western runway. The LSEs are shown for both 2009 and 2014.....	166
Figure 87 - Visible imagery from DigitalGlobe and CNES ASTRIUM obtained from Google Earth for the Subset. LEFT shows data from 2009, RIGHT for 2014.	168
Figure 88 – Retrieved LST for Region 4, for 2009 and 2014.....	168
Figure 89 - Visible imagery of the selected New York City test site. Image taken from Google earth, 40.718 N, -74.012 E, image acquired 28/08/2016, image obtained 16/07/2016.	170
Figure 90 - Histograms of the Retrieved LST and LSEs for all TIR channels for the New York case study site. Means and standard deviations for each retrieved parameter are displayed below the main panel.	172
Figure 91 - Histogram of the retrieved LST and LSE uncertainty for all the TIR channels. Mean and standard deviation values for each retrieved parameter are displayed below the relevant panel.	172
Figure 92 - Histogram of the Radiance residuals for the OE retrieval for all the TIR Channels.	173
Figure 93 – LST map for the Manhattan study area for 01/07/2012.	174
Figure 94 – LSE retrievals for the New York case study site in TIR channel 12.	175
Figure 95 Visible imagery for the subset identifying the locations of the three urban subsets analysed. Image taken from Google earth, 40.738 N, -73.934 E, image acquired 28/08/2016, image obtained 16/07/2016.....	177
Figure 96 – Air temperature readings taken during a nocturnal traverse through central park in July 2006, temperature in Celsius. Taken from Gaffin et al., (2008) .The two lines represent the boundaries of the park on either side of the transect.	179

Figure 97 – TOP The LST for the region surrounding the park transect, the red dashed line denote the transect path. BOTTOM the transect LST and NDVI. The colours correspond the LST for different a priori classifications given to the pixel: dark blue = urban, cyan = mixed vegetation and urban, gold = rock/bare soil and green = vegetation. The solid line shows the NDVI..... 180

Figure 98 – TOP The LST for the region surrounding the extended transect, the red dashed line denote the transect path. BOTTOM the extended transect LST and NDVI. The colours correspond the a priori classification given to the pixel: dark blue = urban, cyan = mixed vegetation and urban, gold = rock/bare soil and green = vegetation..... 181

Figure 99 - The extended transect LSE and NDVI. The colours correspond the a priori classification given to the pixel: dark blue = urban, cyan = mixed vegetation and urban, gold = rock/bare soil and green = vegetation..... 182

Figure 100 – Retrieved LSE in all channels for four samples from Transect 2. The four samples are for industrial, parkland, water and urban background areas. 182

Figure 101 - LST transects for all observations. The colours correspond the a priori classification given to the pixel: dark blue = urban, cyan = mixed vegetation and urban, gold = rock/bare soil and green = vegetation..... 183

Figure 102 - Radiance differences between the gases used in the RFM and RTTOV simulations. Gases include N₂O, NHO₃, CO₂, and a collection of CFCs. 191

Figure 103 – Backtracked materials identified within the Phoenix subset for the 26/05/2011. The labels correspond to sub groups of materials from within the MODIS and SLUM spectral libraries. 192

Figure 104 LEFT: the retrieved LST offset from truth values for the 3 band retrieval RIGHT: the 5 band retrieval..... 194

Figure 105 – LEFT: the retrieved LST uncertainty values for the 3 band retrieval RIGHT: and the 5 band retrieval 194

Figure 106 - Analysis of the effect of the location of the band centroid on the water vapour and surface temperate Jacobians, the y and x axes respectively. The TOP panel shows the location of potential bands with a band width of 50 cm⁻¹ (the grey triangles). The black triangles correspond to those areas within the ozone absorption spectrum. And the coloured markers correspond to the locations the ASTER bands: channel 10 – red, channel 11 – gold, channel 12 –green, channel

13 – blue and channel 14 – purple. The BOTTOM panels show the same but for new proposed channels, where the coloured markers denote the new channels.
..... 196

List of Tables

Table 1 – Variations in zero plane displacement height and momentum / heat roughness lengths for the land cover type present in Fuzhou China taken from Zhang, Balzter, and Wu (2013).	6
Table 2 – Ratio between the heat fluxes and the net radiation. Adapted from the study by Zhang et al., (2013)	9
Table 3 – VNIR subsystem spectral ranges for all channels, including the design requirements for radiometric resolution and absolute accuracy (Yamaguchi et al., 1998).	15
Table 4 - SWIR subsystem Spectral ranges for all channels, including the design requirements for radiometric resolution and absolute accuracy (Yamaguchi et al., 1998).	17
Table 5 - TIR subsystem Spectral ranges for all channels, including the design requirements for radiometric resolution and absolute accuracy (Yamaguchi et al., 1998).	18
Table 6 – The radiometric sensitivity requirements and lab measured for the ASTER TIR subsystem, adapted from Fujisada et.al. 1998.	20
Table 7 – The MTF results both pre and post launch for the ASTER TIR subsystem, adapted from Arai and Tonooka, 2005). AT: Along track, CT: cross track.	25
Table 8 – MODIS spectral channels for the thermal bands used in the LST products (Barnes et al., 1998).	29
Table 9 – MODIS NEAT and MTF performance pre-launch adapted from (Barnes et al., 1998).	30
Table 10 – The a priori LSE values for LSE in four classes. Values determined from the mean of all materials in each class drawn from the ASTER spectral library. These classification based LSEs are applied in all of the retrieval methodologies used in this thesis.....	60
Table 11 – The a priori covariance values for LSE in four classes. Values determined from the standard deviation of all materials in each class drawn from the ASTER spectral library. This covariance is applied in the “ASTER Spectral	

library” method and the “ASTER spectral library with off-diagonal covariance method”.....	63
Table 12 – Summary statistics for the uncertainty contributions to each of the methods tested.....	73
Table 13 – Summary of the reduction in the retrieved uncertainty from the a priori estimates.....	74
Table 14 – Averaging Kernels for each of the methodologies. Broken down by material type.	75
Table 15 – The sub classifications of the materials within the SLUM database and the number of different samples of those sub classes (Kotthaus et al., 2014)...	76
Table 16 - Mean radiance residual values for all data points in each channel for both methodologies.....	86
Table 17 – The mean and standard deviations for the retrieved LSEs from the Algodones inter-comparison for both the OE and TES datasets.	95
Table 18 – RMSE from the validation site for TES and OE algorithms, for all surrounding pixels.....	98
Table 19 – Mean and standard deviations for the radiance residuals for all channels in the retrieval.	125
Table 20 – Mean and Standard deviations for the LSE in all channels for the centre of the park between observations.....	129
Table 21 – The mean and standard deviation for all pixels with in the subset for all observations in (K). The data is divided into the a priori classifications used in the retrieval. For each class relevant percentage of the scene it covers is given in the right most column.	132
Table 22 - The mean and standard deviation for all pixels with in the subset for the observations in (K). The data is divided into the a priori classifications used in the retrieval. For each class relevant percentage of the scene it covers is given in the right most column.	150
Table 23 – The mean and standard deviations from the MODIS LST data for the observations. Also the station data from Hongqiao Airport, in Shanghai.	150
Table 24 – The mean and standard deviations for the radiance residuals for both retrievals.....	151
Table 25 - The mean and standard deviation for all pixels with in the subset for all observations in (K). The data is divided into the a priori classifications used in	

the retrieval. For each class relevant percentage of the scene it covers is given in the right most column. 176

Table 26 - The mean and standard deviation for all pixels with in the subset for all observations the LST in (K). The data is divided into the urban sub-classes. 178

List of Acronyms

AATSR	Advanced Along Track Scanning Radiometer
ATSR	Along Track Scanning Radiometer
ASTER	Advanced Spaceborne Thermal Emission and Reflection Radiometer
AVHRR	Advanced Very-High-Resolution Radiometer
BOA	Bottom of Atmosphere
BT	Brightness Temperature
CAP-LTER	Central Arizona Phoenix – Long Term Ecological Research
CCD	Charged Coupled Detector
DN	Digital Number
ECMWF	European Centre for Medium-Range Weather Forecasts
ENVISAT	Environmental Satellite
ESA	European Space Agency
HIRS	High-resolution Infrared Radiation Sounder
HyTES	Hyperspectral Thermal Emission Spectrometer
JAXA	Japanese Space Agency
JPL	Jet Propulsion Laboratory
LCLU	Land-Class Land-Use
LSE	Land Surface Emissivity
LST	Land Surface Temperature
MASTER	MODIS/ASTER airborne simulator
MIPAS	Michelson Interferometer for Passive Atmospheric Sounding
MODIS	Moderate Resolution Imaging Spectroradiometer
MODTRAN	MODerate resolution atmospheric TRANsmission
MMD	Max-Min Difference
MTF	Modular Transfer Frequency
NASA	National Aeronautics and Space Administration
NDVI	Normalised Differential Vegetation Index

NEM	Normalised Emissivity Module
NEdT	Noise Equivalent delta Temperature
OE	Optimal Estimation
PRT	Platinum Resistance Thermometer
RFM	Reference Forward Model
RMSE	Root-Mean-Squared Error
RTTOV	Radiative Transfer for TOVS
SEVIRI	Spinning Enhanced Visible Infra-Red Imager
SLUM	Spectral Library for Urban Materials
SST	Sea Surface Temperature
SWIR	Short-Wave InfraRed
TCWV	Total Column Water Vapour
TES	Temperature Emissivity Separation
TIMS	Tropospheric Infrared Mapping Spectrometers
TIR	Thermal InfraRed
TM	Thematic Mapper
TOA	Top of Atmosphere
UCI	Urban Cool Island
UHI	Urban Heat Island
VNIR	Visible Near InfraRed
WV	Water Vapour

1 Introduction

1.1 Rationale for Urban Studies

The world's population exceeded 7.3 billion in 2015, showing an increase of nearly one billion people over 12 years of growth, (United Nations, 2015). A huge proportion of this population is focused within urban zones, with approximately 50% of people, some three billion, living within urban areas. Current trends show that the vast majority of future population growth to be centred in the urban environment,(Cohen, 2006; Grimm et al., 2008).

Such a high proportion of people living in the urban environment emphasises the health issues unique to these areas. Rapid urbanisation has highlighted issues of pollution, poor air quality, water pollution, heat risks and increased energy costs, (Akbari & Konopacki, 2005; Gong et al., 2012; Petkova et al., 2016; Stone, Hess, & Frumkin, 2010; Tomlinson, Chapman, Thornes, & Baker, 2011). Understanding these issues requires knowledge of the main physical processes associated with the urban environment. Of these issues, heat is extremely important, and thermal stresses have been linked to higher mortality rates (Gabriel & Endlicher, 2011). Air pollution has also been linked to the urban heat island effect, showing increased particulate matter correlating to high urban heating, (Xu, Yin, & Xie, 2014). Due to the extreme responses of cities to heat events, research into the locations and populations most vulnerable to risks have been identified as crucial to informing and mitigating health risks (Harlan & Ruddell, 2011).

1.2 The Urban Heat Island

Understanding the spatial distribution of heat within an urban area and how this influences the urban energy balance is of significant importance for human health and comfort (Tan

et al., 2010; Tomlinson et al., 2011). This also has implications for future urban development as a consequence of climate change (Corburn, 2009; Stone et al., 2010).

The urban heat island (UHI) is an area of industrial or urban cover which, due to anthropological activity experiences generally higher temperatures than seen in nearby rural regions (Badarinath, Chand, Madhaviatha, & Raghavaswamy, 2005). The main drivers of the UHI can be divided into three parts; the surface albedo, the evapotranspiration of vegetation, the anthropogenic heating within the urban environment (Taha, 1997) and the effect of the urban structures on sensible heat fluxes.

The urban surface albedo is primarily altered from the rural background through the introduction of artificial materials such as asphalt and concrete which have significantly different properties when compared to vegetation or bare soil. Additionally these materials not only have an impact on the albedo and emissivity of a surface but also the ground heat flux as they typically possess higher thermal conductivities than natural materials found in the same localities (Anandakumar, 1999). In investigating this change knowledge of high spatial resolution emissivity is required over the entire urban region, in order to be able to accurately account for the changing properties of the surfaces throughout the urban region.

Evapotranspiration enabled by vegetation has a significant cooling effect on the land surface temperature (Weng, Lu, & Schubring, 2004). The urban environment, with the exemption of parks and urban green-space, is markedly deficient in vegetation in comparison with its rural surroundings. The loss of the majority of this cooling effect is a contributing factor to the UHI effect (Bäckström, 2005).

Anthropogenic heating is a broad term which can apply to nearly any exothermic process in which humans can be said to have played a part. For clarification the following definition from (Fan & Sailor, 2005) will be used;

“Anthropogenic heating is the combination of waste heat released from vehicle fuel combustion, building and industrial energy consumption, and human metabolism”

Given this definition the abundance of anthropogenic heating in the urban environment is obvious. However to truly encompass all the urban effects at play the definition should perhaps be broadened to include the physical effects on the urban structures themselves, as now described.

Urban structures can create street canyons which while small in scale can feedback into and alter, the boundary layer (Harman, 2003) while also creating shadowing and obscuration which can impact the observed LST (Masson, 2000). The canyon effect can also impact the magnitude of the sensible heat flux and the spread of pollutants to a degree that can be observed in mesoscale models (Martilli, Clappier, & Rotach, 2002).

The UHI effect is not the only possible outcome of anthropological influences in the urban environment. A study by Clinton & Gong, (2013) analysed urban locations across the globe and found not only UHI regions but also urban cold island (UCI), where the urban environment was actually cooler than its surroundings.

1.3 The Urban Energy Balance

Urban energy balance impacts the mesoscale weather and indirectly may influence the hydrology, ecology and is a vital component of any model attempting to simulate dynamic/thermodynamic patterns above the surface (Piringer et al., 2002).

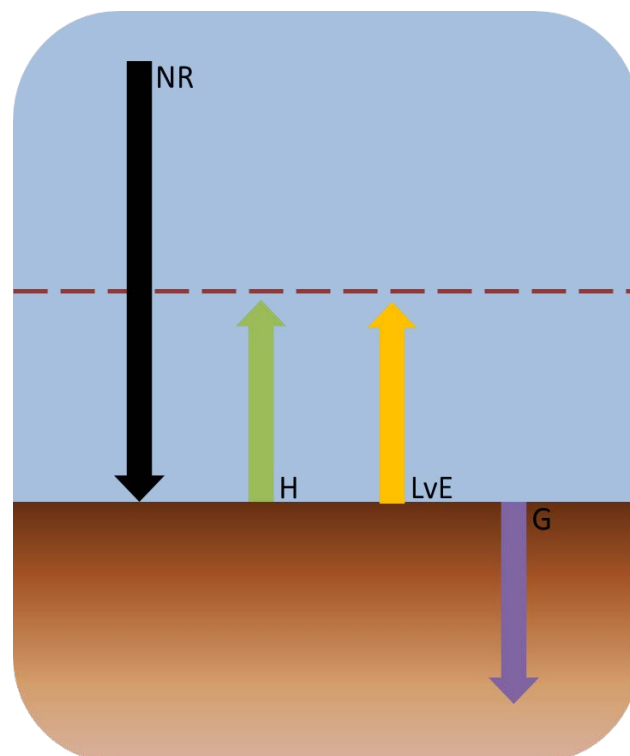


Figure 1 – A diagram simply demonstrating the surface energy balance including the net radiative flux (NR), the sensible heat flux (H), the latent heat flux (LvE) and the ground heat flux (G).

Understanding surface energy balance grants insight into many of these processes and additionally into the level of anthropogenic heat flux, which is of particular interest in the urban environment (Bäckström, 2005).

Surface energy balance describes conservation of energy at the surface-air boundary, although in the urban context the definition of the surface becomes increasingly complex due to the mixture of ground, build facet and rooftops, (Oke, 1988). It encompasses all the energy fluxes at this boundary; sensible, latent, ground and radiative. The full energy system can be represented in terms of four principal components (Liang, Wood, & Lettenmaier, 1999); the net radiation (NR) as discussed in the radiation budget section, the sensible heat flux (H), the latent heat flux (LvE) and the soil heat flux (G).

1.3.1 The Radiation Budget

The radiation budget at the surface can be divided into two categories: the short wave fluxes and the long wave fluxes. The short wave flux has two principal components that affect the surface energy balance; (a) the downward component of the solar radiation incident upon the surface and (b) the portion of that downward flux which is reflected by the surface back into the atmosphere. The proportion of the downward short wave flux that is reflected back is determined by the albedo of the surface, which in turn is a function of wavelength.

The long wave flux also can be considered as two principal components at the surface; (c) the thermal emission of the surface and (d) the downward component of the atmospheric thermal emission. The thermal emission is given through an approximation of the surface to that of a blackbody. A blackbody is a perfect absorber and emitter of radiation. As no real surface will possess this property the radiance must be corrected through the application of an emissivity factor associated with the surface at a particular wavelength.

The radiation budget can be simplified for use within a full energy budget by calculating the net radiative flux at the surface, see Equation 1.1 (Zhang, Balzter, & Wu, 2013).

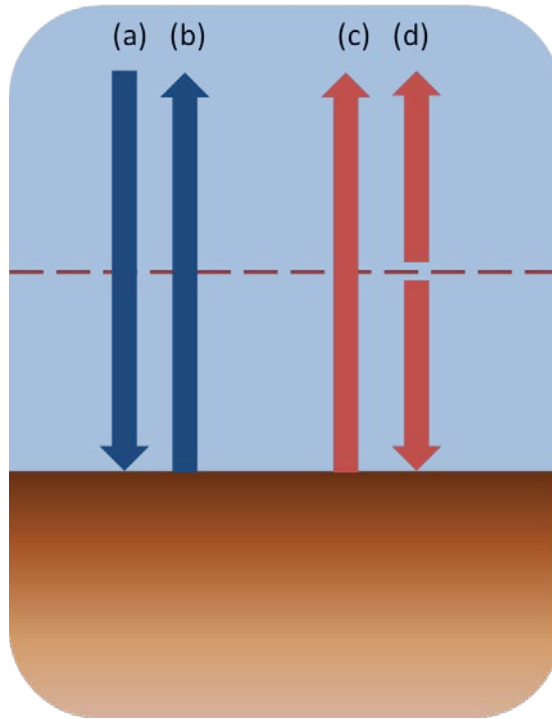


Figure 2 – A diagram simply demonstrating the surface radiation budget. Blue lines: (a) downward shortwave flux and (b) shortwave ground reflected flux. Red lines: (c) long wave thermal emission from surface and (d) long wave thermal emission from the atmosphere.

$$NR = (1 - a_\lambda)R_{swd} + \varepsilon_{a,\lambda}R_{lwd} - \varepsilon_{s,\lambda}\sigma T_s^4 \quad \text{Equation 1.1}$$

where a_λ is the wavelength-dependent surface albedo, R_{swd} is the downward component of the short wave radiative flux, R_{lwd} is the downward component of the long-wave thermal emission of the atmosphere with $\varepsilon_{a,\lambda}$ as the wavelength dependent atmospheric emissivity, $\varepsilon_{s,\lambda}$ is the wavelength-dependent surface emissivity, σ is the Stephan-Boltzmann constant and T_s is the LST.

1.3.2 The sensible heat flux

The sensible heat flux describes the process whereby heat and momentum are transferred from the Earth's surface into the Earth's atmosphere by conduction and convection. The sensible heat flux was defined by (Bastiaanssen, 2000) as:

$$H = \frac{\rho_a c_p \delta T}{r_{ah}} \quad \text{Equation 1.2}$$

where ρ_a is the atmospheric density c_p the specific heat of air, δT the difference between surface and near-surface air temperatures and r_{ah} the aerodynamic resistance to heat transport. It is this last factor, the aerodynamic resistance to heat transport, which contains the principal variables that affect the sensible heat flux over different environments. It has been expressed by Choudhury, Reginato, & Idso, (1986) as:

$$r_{ah} = \frac{\left\{ \ln \left[\frac{(z-d)}{z_{om}-\varphi} \right] \ln \left[\frac{(z-d)}{z_{oh}-\varphi} \right] \right\}}{(k^2 u_z)} \quad \text{Equation 1.3}$$

where φ is the stability correction function, d is the zero plane displacement height, z, z_{om}, z_{oh} are the measurement height, momentum roughness length and heat roughness length respectively, k is von Karmen's constant and u_z the wind speed at measurement height. The d, z_{om}, z_{oh} terms vary dependant on the properties of the surface an example of which is shown in Table 1.

Land cover	d (m)	Z _{om} (m)	Z _{oh} (m)
Water	0	0.001	0.0001
Bare soil	0	0.01	0.001
Field	0.02	0.004	0.0004
Grass	0.133	0.026	0.0026
Forest	4	0.78	0.078
Urban	7.5	1.5	0.15
Suburban	2.5	0.5	0.05

Table 1 – Variations in zero plane displacement height and momentum / heat roughness lengths for the land cover type present in Fuzhou China taken from Zhang, Balzter, and Wu (2013).

Traditionally, sensible heat is calculated as a comparison of turbulent fluxes in the boundary layer through eddy covariance (Allen, Tasumi, Morse, & Trezza, 2005). However if certain atmospheric properties such as the zero plane displacement height and momentum / heat roughness lengths as shown in Table 1 are known then the sensible heat flux can be estimated through knowledge of the surface and atmospheric temperatures (Zhang et al., 2013).

1.3.3 The latent heat flux

The latent heat flux is associated with the evaporation of water from the Earth's surface and its subsequent condensation in the troposphere. It includes all the energy used in the transport of water vapour from the surface layer into the atmosphere whether by straightforward evaporation or through vegetative means such as evapotranspiration and can be stated in the form of Equation 1.4, Monteith & Unsworth, (2013):

$$L_v E = \frac{\rho_a C_p (e_s - e_a)}{\gamma (r_a + r_s)} \quad \text{Equation 1.4}$$

where e_s is the saturation water vapour pressure at surface, e_a is the atmospheric water vapour pressure, γ is the psychrometric constant which relates the partial pressure of water vapour in air to the air temperature and r_a, r_s are the resistances of the atmosphere and surface/vegetation respectively to vapour flow. The value of this flux is highly dependent upon the surface properties, particularly that of vegetation cover, with much higher latent heat fluxes observed in highly vegetated environments and far lower values recorded in urbanised areas (Grimmond & Oke, 2002).

1.3.4 The ground heat flux

The ground heat flux describes the transferal of heat energy by conduction from the surface layer down into the substrate. The transfer of heat is dependent on the physical properties of the substrate and often creates a reduced amplitude and time lag in temperature changes at greater depth (Wang & Bras, 1999).

As a surface is warmed by the input of the radiative fluxes, a temperature imbalance is created between the air-surface boundary layer. As the surface layer is connected to the deeper substrate directly, heat will be drawn down to the cooler layers by conduction. Therefore the flux of energy into the ground will be determined simplistically by the thermal conductivity of the substrate and the temperature gradient (Campbell & Norman, 1998).

$$G = k \frac{\partial T}{\partial z} \quad \text{Equation 1.5}$$

Whilst measurements of the thermal conductivity on any given surface are relatively easy to find as many databases for such properties exist, such as SRD 81 NIST (Zarr, Chavez, Lee, Dalton, & Young, 2015), accurately measuring the temperature gradient with depth can be more problematic. In an idealised homogenous substrate of known thermal conductivity the temperature at a given depth z_d may be expressed as (Campbell & Norman, 1998).

$$T(z_d, t) = T_{ave} + A(0) \exp\left(-\frac{z_d}{D}\right) \sin\left[\omega(t - 8) - \frac{z_d}{D}\right] \quad \text{Equation 1.6}$$

where T_{ave} is the daily mean temperature over the surface, $A(0)$ is the amplitude of the temperature fluctuations at the surface, D is the soil dampening depth which determines temperature amplitude attenuation and temporal phase and is dependent on the diurnal period and thermal conductivity. ω is the diurnal period, and t is the hour at which the observation is being made. A temporal phase shift and decrease in temperature amplitude with depth due to the thermal resistances in the substrate can be seen in Figure 3.

This method requires remotely sensed LST and detailed ground data assessing the thermal properties of the material and its fluctuation over time, i.e. LSE.

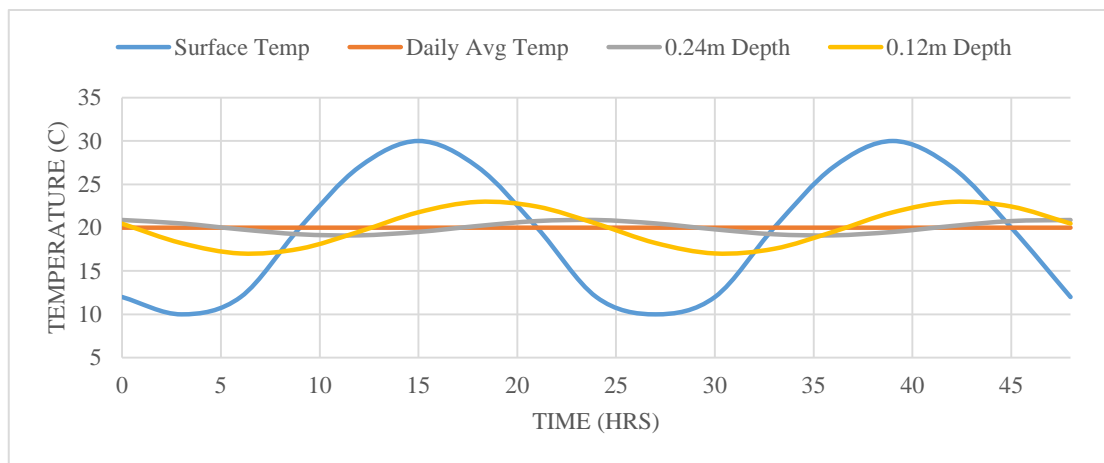


Figure 3- An example showing the soil temperature amplitude attenuation with depth and the temporal phase shift of the peak. Plot based on that of Campbell and Norman, (2000).

Alternative ground flux determination can be coefficient based, using a series of modelled coefficients linking thermal gradients to land classification and season (Anandakumar, 1999). However extensive modelling and ground validation is required to generate these coefficients.

Geothermal heat fluxes show this process also describes the flow of heat upward from warmer pockets beneath the ground towards the surface, (Beltrami, 2001).

1.3.5 The Urban Energy Balance Equation

The components described in sections 1.3.1 to 1.3.4 can be combined to yield the full urban energy balance equation:

$$NR + A_F = G + H + L_v E \quad \text{Equation 1.7}$$

where the NR, G, H and $L_v E$ are as previously defined and A_F is the contribution of the anthropogenic heat flux. This equation shows that for the system at equilibrium, the net radiation and anthropogenic fluxes will be balanced by the ground, latent and sensible heat fluxes. Example values for these fluxes in an urban setting are shown in Table 2.

Land use	Observation period	H/R _n	L _v E/R _n	G/R _n
Urban	04/03/2001	0.53	0.04	0.57
Urban	15/06/1989	0.49	0.06	0.56
Suburban	04/03/2001	0.37	0.04	0.57
Suburban	15/06/1989	0.36	0.07	0.58

Table 2 – Ratio between the heat fluxes and the net radiation. Adapted from the study by Zhang et al., (2013)

The urban environment is dominated by the Sensible and ground heat fluxes, with little contribution from the latent heat flux, primarily due to the reduction in vegetation.

1.4 Rationale for Measuring LST and LSE

Assessing the observational needs for the analysis of the UHI and the urban energy balance, it is clear that high spatial resolution data for the air temperature in the urban environment would provide the greatest advancement. However there is currently no

robust manner in which to remotely observe the air surface temperature, and certainly not at high spatial resolution over a whole city. This leads to a large gap in the required data that has to be filled. LST is not as directly linked to thermal comfort, heat risk and pollution as the air temperature. However it is still an important factor and provides a robust way to determine thermal information about the urban environment, with spatial and temporal consistency.

Additionally LST has been highlighted as a key parameter for integration into surface energy balance studies in its own right, (Friedl, 2002; Voogt & Oke, 2003). As the surface energy balance describes the balance of energy fluxes through the surface air boundary, one of most important components of the energy balance is the temperature of the surface itself. The LST describes the temperature at the surface-air boundary and has a reciprocal relationship with many of the energy fluxes previously described, both causing alteration in the values of those fluxes and itself being altered by the surface inputs of the fluxes. It is a vital parameter in all surface processes including but not limited to being a driver of; climatology, hydrology and ecology. It has been used as a parameter in Numerical Weather Prediction (NWP) models for case studies in Spain and in the Netherlands (van den Hurk, Jia, & Menenti, 2002).

Satellite remote sensing provides a means to retrieve surface LST and LSE at high spatial and spectral resolution on a global scale. Satellites can provide global and regular coverage consistently; and as such present an incredible tool for both active monitoring and long term analysis of parameters such as LST (Ward, Phinn, & Murray, 2000).

When considering the LST with regard to remote sensing it is important to note that the surface is whatever the satellite observes; this does not necessarily mean ground level. For example, a nadir observing satellite would view a road and a building rooftop as the surface regardless of the height difference.

It is also important to understand that while the LST is considered to be the temperature of the skin layer, the reality is that of a complex and heterogeneous surface comprised of many materials and morphologies (Qin & Karnieli, 1999). The fact that even at the sub-pixel level there is much inhomogeneity, which complicates the estimation of LST.

LST retrieval typically requires prior estimates as to the land surface emissivity (LSE) of the observed surface and is often obtained at coarse spatial resolutions (1 km). Due to the inextricable link between LST and LSE the retrieval of LSE has direct benefits for the

applications already described for the LST. However, it also has additional usage as a parameter in its own right in energy balance assessments (Zhang et al., 2013). The complexity of the surfaces within an urban area varies with both LSE and heterogeneous spatial distribution presents a clear challenge for accurate emissivity estimation.

In particular knowledge of the LSE presents the opportunity to increase the knowledge of the surface land class/land use change (LCLU). Typically these studies centre around object detection at visible wavelengths (Chen, Hay, Carvalho, & Wulder, 2012; Hussain, Chen, Cheng, Wei, & Stanley, 2013; Ridd & Liu, 1998). However, these methods give information on the LCLU which, for energy balance studies and assessments of the thermal properties of the surface, must be matched to an emissivity. The direct retrieval of LSE allows not only change detection but also a direct measure of the pixel scale emissivities (if they have changed) which can be assimilated in energy balance studies. Assessments of change detection have been made using LSE with the Advanced Spaceborne Thermal Emission and Reflection Radiometer (ASTER), Temperature and Emissivity Separation (TES) product, but not for urban areas where the heterogeneity is much higher (French et al., 2008).

1.5 Requirements for LST and LSE

Due to the wide range of potential applications for both LST and LSE there are a number of differing requirements for the observation and retrieval of these parameters.

In assessing the spatial resolution requirement there is naturally a large divide between the idealised, desired resolution and the currently feasible objectives. Within the scientific community studying land classification in the visible wavelengths there is a requirement of less than 5 m spatial resolution (Herold, Gardner, & Roberts, 2003). Whilst this is possible with aerial and satellite observations in the visible, with the exception of the Hyperspectral Thermal Emission Spectrometer (HyTES) (Hook, Johnson, & Abrams, 2013) this data is not available in the thermal infra-red (TIR). For the purposes of urban studies, the highest resolution thermal data currently available is that of the LANDSAT satellites, with a spatial resolution of 60-120 m and ASTER with a 90 m resolution. These resolutions are a distinct improvement on the moderate resolution retrievals such as Moderate Resolution Imaging Spectroradiometer (MODIS) or Advanced Along-Track Scanning Radiometer (AATSR) where inaccuracies due to the sub-pixel variation is high.

However, even at these fine scales there will be the effect of class mixing within pixels, (Feng, Foody, Aplin, & Gosling, 2015). Studies have found that a resolution of 100 m or less is required for urban studies to prevent excessive mixing of pixels and loss of structural details, (Roth, Oke, & Emery, 1989; Voogt & Oke, 2003).

In the context of retrieving LST, the effect of an LSE uncertainty of 0.01 has been to induce an uncertainty of 0.5 K in the LST, dependant on the retrieval algorithm used (Jiménez-Muñoz & Sobrino, 2003). Chen, Yang, Su, & Wang, (2016) specifically explored the effect of LSE variation with in the urban environment and concluded that whilst the previous figure of 0.5 K variation in LST for a 0.01 change in LSE is true for homogeneous areas, that the complex urban environment makes achieving this extremely difficult, and that targets in this environment must be somewhat relaxed to meet the reality of the situation.

1.6 Summary

Investigations into the thermal structure of the urban environment and the urban energy balance requires high resolution temperature data. At the present it is not feasible to acquire air temperature data at the spatial resolution or coverage needed to be give a detailed view of the entire urban environment. Studies in this area would benefit from LST retrieved to a resolution of 100 m or less from a consistent observation system, which is something that can only be provided by remote sensing from satellite instrumentation.

In the urban environment, retrieval of the LST in isolation is not sufficient to fully assess the complex heterogeneous surface observed. LSE is required to achieve both accurate LSTs and also to provide surface information on LULC with in the observations. Again there is not a current system for in situ measurement of the LSE at the spatial or temporal scale or resolution required, remote sensing provides a solution. The simultaneous retrieval of LST and LSE offers the best solution as the LST and LSE will be temporally and spatial coincident. In line with previous studies and methodologies, the LST should aim to retrieve to 1.5 K or better, with mean LSE uncertainty across the channels to 0.015, (Hulley, Hughes, & Hook, 2012).

2 Instrumentation and Data Products

2.1 Introduction

The retrieval developed in this thesis utilises data from two satellite instruments. The primary instrument is ASTER. ASTER data from two of its subsystems provided the key thermal and visible data on which the retrieval and the classification inputs to the retrieval are based. The secondary instrument is MODIS. MODIS provides the medium resolution a priori LST data for the retrieval. Before investigating the retrieval itself it is important to understand the capabilities and limitations of these instruments. This chapter will assess the ASTER and MODIS instruments and provide the key information on the relevant data sets used from each of them.

2.2 ASTER

The Advanced Spaceborne Thermal Emission and Reflection Radiometer (ASTER) is a joint USA-Japanese instrument launched aboard TERRA in 1999. It operates over a large wavelength range with channels in the visible near-infra-red (VNIR), the short wave infra-red (SWIR) and the thermal infra-red (TIR). The instrument is described in Abrams, (2000).

ASTER had a broad scientific mandate across a wide variety of geo-spheric, hydro-spheric and cryo-spheric processes. The scientific aims behind the rationale for ASTER were broken down into 8 key areas of scientific investigation by Yamaguchi, Kahle, Tsu, Kawakami, & Pniel, (1998):

1. Geology and soil

2. Volcano monitoring
3. Carbon cycling and marine ecosystems
4. Aerosols and clouds
5. Evapotranspiration
6. Hydrology
7. Vegetation and Ecosystem dynamics
8. Land surface climatology

In these research areas ASTER aimed to advance knowledge through the acquisition of higher thermal and Short-Wave Infra-Red (SWIR) spatial resolution imagery than was obtainable at the time Fujisada, Sakuma, Ono, & Kudoh, (1998).

The ASTER instrument is mounted on the Terra satellite along with several other scientific instruments involved in the NASA Earth observing system (EOS). TERRA is a near-polar orbiting satellite with an equatorial crossing time of 10:30 am local time. It is on a cycle with a revisit time of 16 days.

2.2.1 Instrument Specifications

ASTER is a high spatial resolution imager. As a radiometer with multiple channels, it operates 14 bands ranging from the visible to thermal spectrum. The bands are divided between three spatial subsystems for which all observations are spatially and temporally coincident and so observe the same geospatial region. It achieves a spatial resolution from 15 m in the visible to 90 m in the thermal, observing with a swath width of 60 km.

2.2.1.1 VNIR

The Visible Near Infra-Red (VNIR) subsystem as seen in Figure 4 consists of two telescopes to provide a three band nadir view (bands 1 ,2 and 3N) and a backward facing view for one band (band 3B), operating a push-broom scanning pattern. Both telescopes used silicon Charged-Coupled Devices (CCDs). However the backward facing telescope only uses a single line array detector, whereas the nadir views use two-dimensional arrays of detectors.

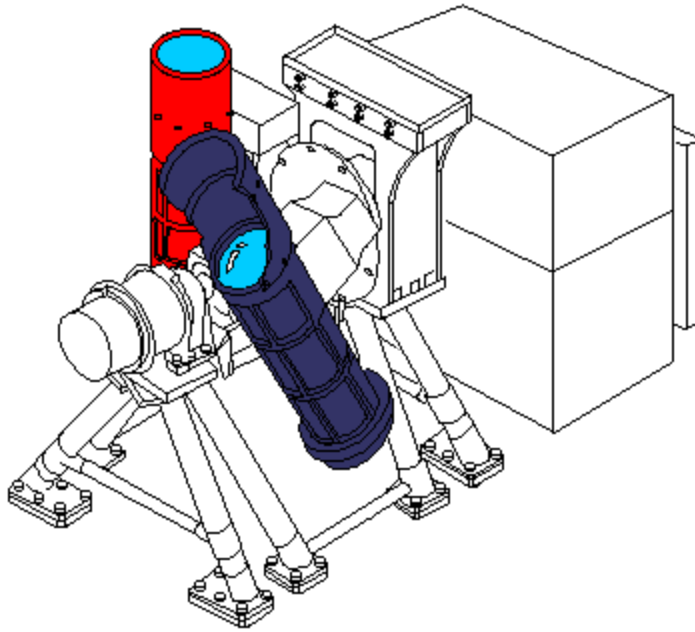


Figure 4 - Diagram of the VNIR subsystem in ASTER. Highlights: dark blue – The nadir telescope used with all three VNIR spectral bands. Red – The backwards telescope used with the third spectral channel only. Image taken from NASA (2004b).

Subsystem	Channel No.	Spectral Range (μm)	Radiometric Resolution	Absolute Accuracy (σ)	Spatial Resolution
VNIR	1	0.52 - 0.60	$\text{NE}\Delta\rho \leq 0.5\%$	$\leq \pm 4\%$	15 m
	2	0.63 - 0.69			
	3N	0.78 - 0.86			
	3B	0.78 - 0.86			

Table 3 – VNIR subsystem spectral ranges for all channels, including the design requirements for radiometric resolution and absolute accuracy (Yamaguchi et al., 1998).

All the telescopes include spectral bandpasses which follow closely the bandpasses used in the LANDSAT Thematic Mapper instrument, making use of the scientific heritage of the LANDSAT missions and extending them. The telescopes are on rotating mounts allowing both telescopes a rotation of $\pm 24^\circ$, enabling cross track pointing. The detectors have on-board calibration using a halogen lamp as the source in conjunction with photo-diodes. The VNIR instrument is capable of a spatial resolution of 15 m.

The inclusion of two NIR views (3N and 3B) was to facilitate the topographical capabilities of ASTER through stereo imaging. The topographical maps produced as a result of the analysis of these channels are available from the ASTER Global Digital Elevation Map (GDEM) archive, (Tachikawa, Hato, Kaku, & Iwasaki, 2011).

The channels, as described in Table 3, have been specifically selected for use with existing VNIR scientific analysis techniques utilised for vegetation analysis and land use classification. A key parameter used in a number of land classification techniques is the Normalised Differential Vegetation Index (NDVI) which makes use of the red visible channel (channel 2) and the NIR channel (3N and 3B) (Stefanov & Netzband, 2005). The inclusion of the channels makes possible the generation of spatially and temporally collocated land classification to be utilised to construct a priori emissivity data to be used in the LST/LSE retrievals, of this thesis.

2.2.1.2 SWIR

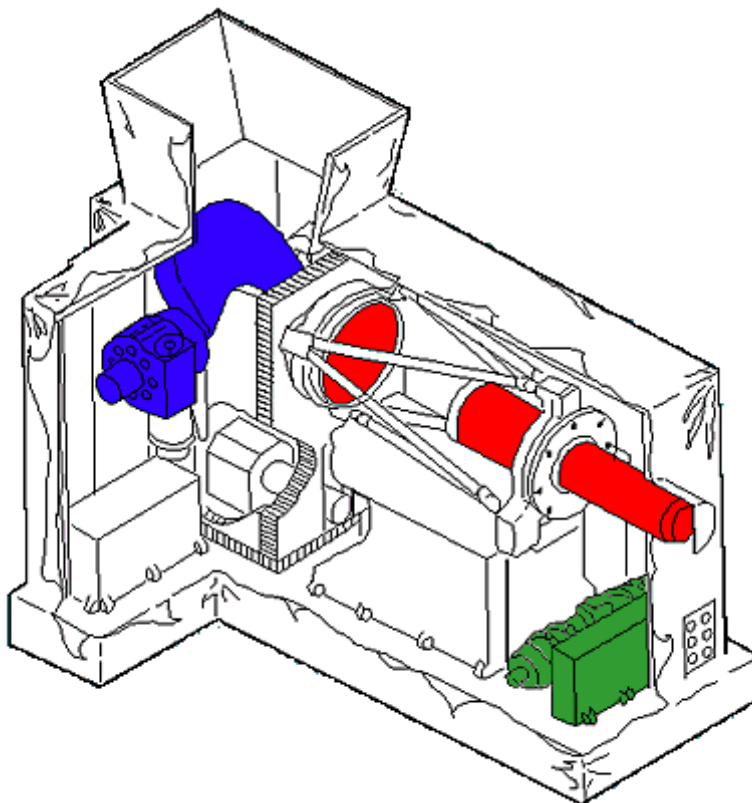


Figure 5 – Diagram of the SWIR subsystem in ASTER. Highlights: Red – The telescope. Blue – The pointing mirror and mount. Green - The Stirling cooler. Image taken from (NASA, 2004a)

Subsystem	Channel No.	Spectral Range (μm)	Radiometric Resolution	Absolute Accuracy (σ)	Spatial Resolution
SWIR	4	1.600 - 1.700	$\text{NE}\Delta\rho \leq 0.5\%$	$\leq \pm 4\%$	30 m
	5	2.145 - 2.185	$\text{NE}\Delta\rho \leq 1.3\%$		
	6	2.185 - 2.225	$\text{NE}\Delta\rho \leq 1.3\%$		
	7	2.235 - 2.285	$\text{NE}\Delta\rho \leq 1.3\%$		
	8	2.295 - 2.365	$\text{NE}\Delta\rho \leq 1.0\%$		
	9	2.360 - 2.430	$\text{NE}\Delta\rho \leq 1.3\%$		

Table 4 - SWIR subsystem Spectral ranges for all channels, including the design requirements for radiometric resolution and absolute accuracy (Yamaguchi et al., 1998).

The SWIR subsystem as seen in Figure 5 uses a single telescope mounted to allow movement for cross track pointing, and employing a push-broom scanning pattern. A push broom scanning pattern utilises a line of detectors, which are arranged perpendicular to the flight direction. Each detector looks at one region at a time sequentially in the flight direction. The detector is a Scholttky barrier linear array cooled down to a temperature of 80 K. The detector is calibrated with a single halogen radiation source and photo-diode setup. A primary mechanical feature of the system is the split Stirling cryocooler which is used to keep the detector at the required 80 K. This system operated with a spatial resolution of 30 m.

As seen in Table 4 the SWIR subsystem uses six channels; these channels were specifically selected for the study of soils and minerals. The channel centres are aligned with the absorption features associated with several key material such as clay minerals, sulphate minerals, carbonite minerals, iron oxides and silica, (van der Meer et al., 2012).

In February 2008 a notice was released detailing an increase in the SWIR detector temperature that could be adversely affecting the scenes obtained ('SWIR - ASTER User Advisory', 2016). By late April it was found that scenes were heavily saturated and showing signs of striping. Several attempts were made to correct for this issue until in January 2009 a final advisory alert was issued notifying that all SWIR data since April 2008 was considered unusable and that no further work to rectify this was envisioned. A summary is printed in the 2016 user advisory note, ('SWIR - ASTER User Advisory', 2016.).

2.2.1.3 TIR

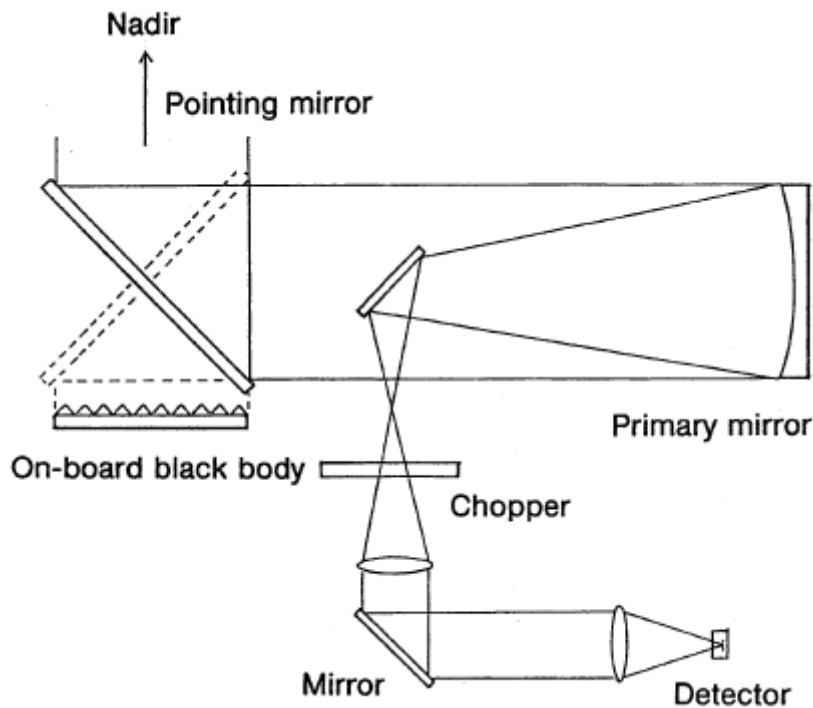


Figure 6 – Diagram of the TIR subsystem in ASTER. The light enters at the top of the diagram, the dashed outline indicates the orientation of the pointing mirror when the instrument is in calibration mode.

Subsystem	Channel No.	Spectral Range (μm)	Radiometric Resolution	Absolute Accuracy (σ)	Spatial Resolution
	10	8.125 - 8.475		$\leq \pm 3$ K (200 -240 K)	
	11	8.475 - 8.825		$\leq \pm 2$ K (240 -270 K)	
TIR	12	8.925 - 9.275	$\text{NE}\Delta\rho \leq 3$ K	$\leq \pm 1$ K (270 -340 K)	90 m
	13	10.25 - 10.95			
	14	10.95 - 11.65		$\leq \pm 2$ K (340 -370 K)	

Table 5 - TIR subsystem Spectral ranges for all channels, including the design requirements for radiometric resolution and absolute accuracy (Yamaguchi et al., 1998).

The TIR subsystem, see Figure 6, uses a fixed Newtonian cata-dioptric telescope system in conjunction with a staggered array of Mercury-Cadmium-Telluride detectors, and a whisk-broom scanning pattern. A whisk broom sensor or across track scanner uses a movable mirror to reflect the incoming radiance into the detector. The mirror oscillates allowing a series of detectors to be scanned across track, aligned in the cross track direction. The pointing mechanisms allow a tilt of $\pm 18.55^\circ$ from image tasking. Each

spectral band uses ten of these detectors in a staggered configuration along the cross-track direction. All of the detectors are cooled to 80 K using the Stirling cryocoolers.

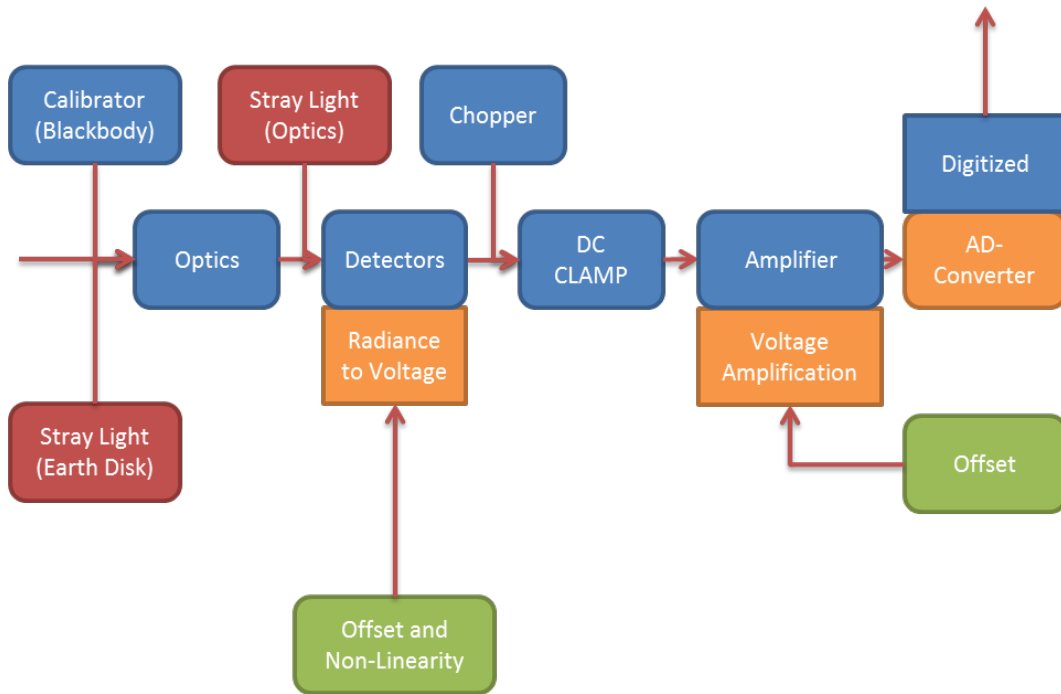


Figure 7 – Radiometric flow diagram for the processes from the detection of incident photons through to the digitized signal for downlink.

The radiance entering the TIR subsystem passes through the optics seen in Figure 6 and is registered at the detector as an induced charge in the CCD. The detected signal is then amplified and calibrated. On-board calibration coefficients for the temperature offset and non-linearity based upon the calibration coefficients are applied to the voltage before the signal is amplified and digitized to 12 bits for downlink as a digital number (DN) relating to a temperature, see the full system flow chart in Figure 7. The system attempts to minimise stray thermal emissions interfering with the detectors but there still several sources of stray light including the thermal emission of the instrument and satellite, which the on-board calibrations must account for.

2.2.2 Instrument Performance

The operational performance of the TIR instrument is extremely important to the scientific analysis of the data produced. Assessing and assigning the performance of the instrumentation enables the science users to properly understand and constrain the limitations and uncertainties of the data being analysed. The most important considerations are:

- Pre-flight calibration
- In-flight calibration
- Verification of in-flight performance
- ASTER geometric calibration

2.2.2.1 Pre-Flight Calibration

The ASTER instrument was tested extensively prior to its launch on the TERRA satellite in 1999, (Barnes, Pagano, & Salomonson, 1998; Fujisada et al., 1998; Justice et al., 1998; Sakuma & Ono, 1993; Yamaguchi et al., 1998). In particular testing was conducted to assess the ability of the instrument to match its required Noise Equivalent Temperature (NEAT).

Subsystem	Band No.	NEAT at High Radiance Values		NEAT at Low Radiance Values	
		Specified	Measured	Specified	Measured
TIR	10	< 0.3 K	0.17 – 0.07 K	< 2.5 K	1.34 – 0.68 K
	11	< 0.3 K	0.14 – 0.09 K	< 2.5 K	1.27 – 0.63 K
	12	< 0.3 K	0.13 – 0.07 K	< 2.5 K	1.05 – 0.42 K
	13	< 0.3 K	0.09 – 0.05 K	< 1.5 K	0.49 – 0.26 K
	14	< 0.3 K	0.13 – 0.09 K	< 1.5 K	0.65 – 0.33 K

Table 6 – The radiometric sensitivity requirements and lab measured for the ASTER TIR subsystem, adapted from Fujisada et.al. 1998.

The results in Table 6, show the measured performance of the TIR subsystem to be significantly improved with respect to the specified requirement at high radiance values

of 0.3 K and the respective low radiance requirements of 1.5-2.5 K. In fact, in most of the channels the measured NE Δ T is less than half of the required value. The ASTER TIR instrument was evaluated pre-flight and found to have an absolute accuracy of better than 1 K in the temperature range of 270 to 340 K (Fujisada et al., 1998). Based on this ASTER is expected to have an excellent radiometric performance.

2.2.2.2 In-Flight Calibration

Over time it is expected that the instruments responsivity will change due to sensor degradation. In order to assess and account for this the instrumentation must be calibrated against a radiantly stable source. For the VIS and SWIR a Halogen lamp as a stable light source is used. In the case of the TIR subsystem an on-board heated blackbody is used. The TIR subsystem is defined here as it is more relevant to this thesis.

On-board calibration for TIR uses a flat plate honeycomb black body with an emissivity of greater than 0.99. The black body is monitored by platinum resistance thermometers (PRTs) as the temperature of the blackbody must be known. Once every sixteen days the blackbody is heated to 340 K. The blackbody is monitored by the PRTs and signals recorded continuously by the TIR detectors during the entirety of the heating and cooling, a process which takes 4 hours.

The plots in Figure 8 show the detector / PRT temperature offset over time. The four digital numbers correspond to the average DN calculated in the first in-flight calibration at the temperatures of 270, 300, 320 and 340 K. Each subsequent calibration, the temperature of the blackbody was continuously ramped and the detector readings recorded that the same DNs. The temperature the DN represented in the first calibration is then compared to the PRT temperature and the difference shows the degradation or drift seen in Figure 8. The results in Figure 8 are for the TIR channel 12 which is the channel which showed the largest degradation over time. Over a five year period, the channels developed a bias ranging from -6 K at the lower temperature to +12 K at the upper temperature.

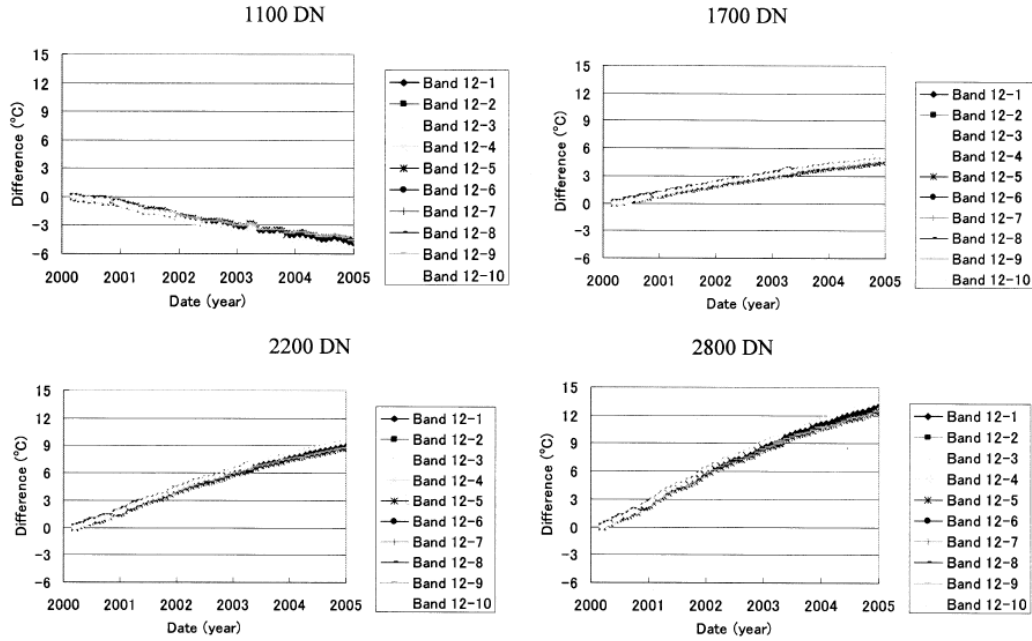


Figure 8 - On-board Calibration of the ASTER Instrument, Sakuma Et.al. 2005. These plots show the trends of ten detectors present in TIR channel 12. The temperature changes shown are the differences from the first inflight calibration performed. The four selected DNs correspond to temperatures of 270, 300, 320 and 340 K.

In order to account for this the coefficients used in the calculation of the Top Of Atmosphere (TOA) radiances had to be updated. The equation used in the operational product of ASTER TIR is:

$$L = c_0 + c_1 DN + c_2 DN^2 \quad \text{Equation 2.1}$$

where L is the radiance, DN is the digital number produced from the on-board systems and c_0 , c_1 and c_2 are the calibration coefficients. c_0 and c_2 were calculated once during the first in-flight calibration and have remained unaltered since. c_1 is the coefficient which is updated based upon the detected calibration offset see in Figure 9.

The calibration is used to monitor the temperature change in the detector responsivity. When the change passes a threshold value, it is treated as a radiometric offset and c_1 is updated to account for the difference. The largest difference seen was in band 12, in which a reduction in detector response of 24% was observed from 2001 to 2004. The loss in responsivity is thought to be due to contamination in the optics, (Sakuma et al., 2005).

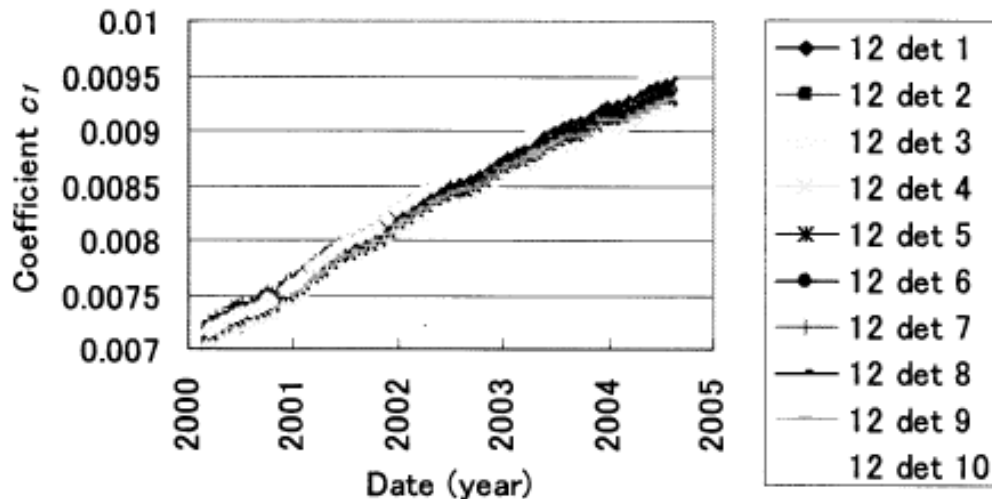


Figure 9 – The change in calibration coefficient over time in Band 12 of the TIR subsystem as a response to reduced detector responsivity, Sakuma et.al. 2005.

2.2.2.3 Verification of In-Flight Performance

In flight ASTER TIR's performance was assessed vicariously through the analysis of scenes which had ground truth data available.

2.2.2.3.1 Scene NEAT

In the Japan Aerospace Exploration Agency (JAXA) study by Arai & Tonooka, (2005), all three subsystems were analysed over the sea. The thermal infra-red results are described here. The sea surface makes for a more suitable ground truth than highly heterogeneous land surfaces as the sea surface temperatures (SST) do not change particularly quickly. Also the surface is well-known, with essentially constant emissivity values. In total 32 scenes were selected from March 2000 to March 2004. For each scene 30x30 pixels were extracted and the mean and standard deviations calculated for both cross and along the image track, see Figure 10.

For all of the five TIR bands, Figure 10, shows standard deviations ranging between 0.1 and 0.2 K. The detectors are aligned in the along track direction so the fact that the along track noise is slightly higher was expected and indicates detector to detector variations as well as noise. The NEATs are consistent with the pre-flight evaluations.

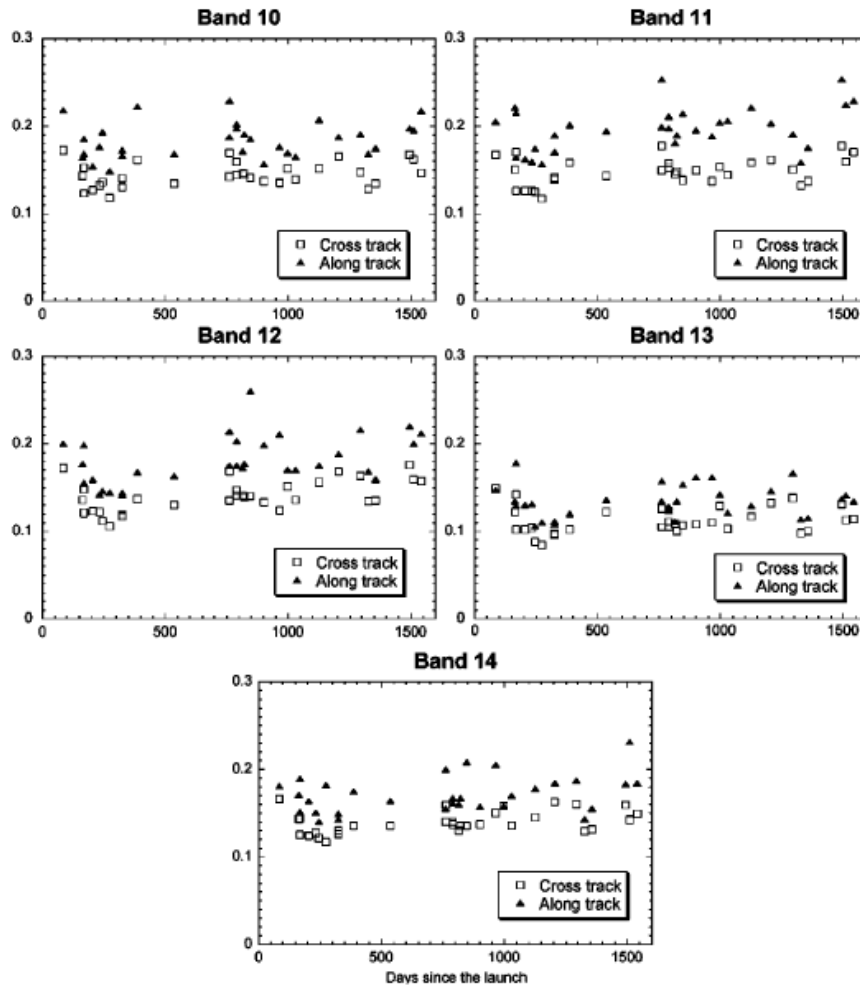


Figure 10 – The NEAT values for the TIR bands (Y-axis) calculated in-flight. Radiometric Performance Evaluation of ASTER VNIR, SWIR, and TIR, Arai and Tonooka, 2005.

2.2.2.3.2 Modular Transfer Function

The modular transfer function (MTF) is the quantification of an imaging system's response to different sinusoidal frequencies, and presents a measure of the optic's ability to define details at the scale being observed (Boreman, 2001). In addition to the performance in terms of the NEAT, the vicarious studies also assessed the performance in terms of the MTF. The sites needed to study the MTF were markedly different to those used in the NEAT study. The MTF analysis requires scenes with features of sharp spectral contrast, such as coastlines or desert borders. In these scenes a point of inflection is located and the edge response calculated. Using the normalised edge response for all the pixel in the column at the point of inflection the line spread function was calculated.

Frequency	When	Dir.	Band 10	Band 11	Band 12	Band 13	Band 14
½ Nyquist	Pre - Launch	AT	0.79 – 0.83	0.78 – 0.81	0.78 – 0.81	0.74 – 0.78	0.69 – 0.76
Nyquist			0.36 – 0.41	0.37 – 0.42	0.37 – 0.39	0.34 – 0.37	0.31 – 0.37
½ Nyquist		CT	0.79 – 0.83	0.77 – 0.81	0.79 – 0.82	0.79 – 0.83	0.78 – 0.83
Nyquist			0.34 – 0.38	0.34 – 0.36	0.34 – 0.37	0.35 – 0.37	0.34 – 0.39
½ Nyquist	Post - Launch	AT	0.716	0.707	0.720	0.702	0.689
Nyquist			0.261	0.249	0.268	0.241	0.224
½ Nyquist		CT	0.712	0.711	0.710	0.721	0.709
Nyquist			0.256	0.254	0.253	0.269	0.252

Table 7 – The MTF results both pre and post launch for the ASTER TIR subsystem, adapted from Arai and Tonooka, 2005). AT: Along track, CT: cross track.

The results of this analysis as seen in Table 7 show good performance at the half Nyquist frequency at which ASTER TIR is designed to operate. The high values of the MTF point towards a high degree of spectral and spatial sensitivity to the variations in the observed scenes.

2.2.2.4 ASTER Geometric Calibration

The images obtained from ASTER of level 1 or higher are all geometrically corrected for the rotational and line of sight vectors between the light registered at the detector and the corresponding location in a geo-coordinate system.

The first calibrations are the prelaunch calculated parameters for the geometric line of sight and satellite pointing information based upon the orbital path and the spacecraft orientation. These parameters were pre-calculated and applied to all ASTER data, (Abrams, Hook, & Ramachandran, 2014).

In post-launch operation the geometric calibration is updated through the use of ground control points which assess the satellite pointing and update a series of three coordinate transformations. Firstly from the spacecraft centered coordinate system into the satellites orbital coordinates. Secondly from the orbital coordinates to an inertial geo-centric coordinate system, and finally from this system to Greenwich coordinates.

In addition to these processes the three subsystems are assessed at ground control points to ensure the band to band registration is correct using image matching techniques. Based upon these calibrations the ASTER L1 data subsystem pixel registration between the TIR

and VNIR subsystems is <0.2 pixels. The relative and absolute pixel geolocation registrations are <15 m and <50 m respectively, (Abrams, Hook, and Ramachandran 2014).

2.2.2.4.1 ASTER L1T Geometry

The ASTER L1T dataset is the current operational at sensor registered radiance dataset. As such it is the dataset primarily used in this thesis. The L1T dataset applies a northern rectification to ensure that all ASTER scenes are re-projected so the top of the scene is facing due north. As shown in Figure 11, in the L1a scenes the top of the scene would be the first line of scanned pixels in the direction of the orbit swath. However the L1T scene is now rotated such the top of the scene is the most northerly latitude creating a new larger scene with the original swath inside.

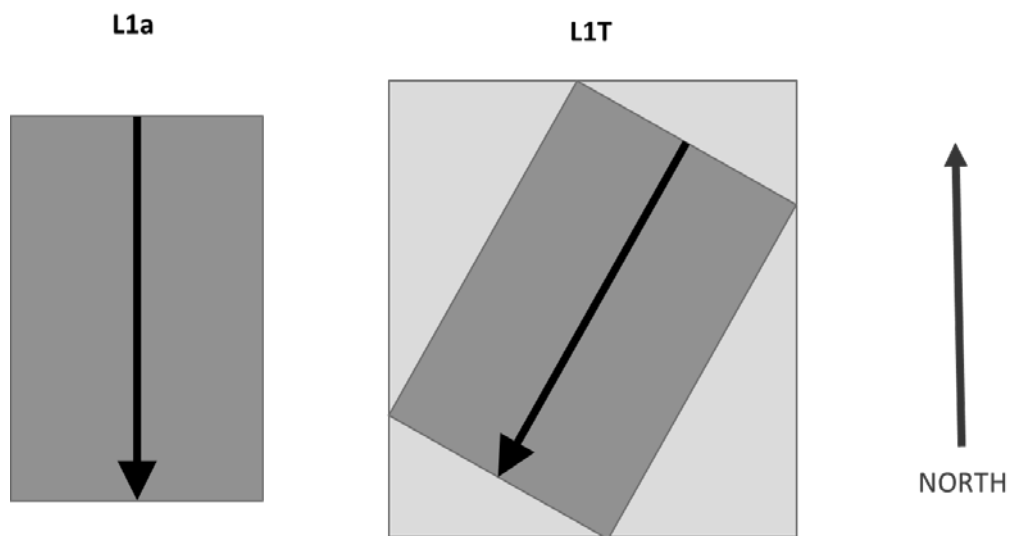


Figure 11 – Diagram showing the scene rotation for the L1T dataset, the black arrow shows the orbit direction, (NASA, 2015).

2.2.2.5 Performance Summary

The VNIR, TIR and SWIR (until the cession of data due to channel saturation) subsystems all perform within or better than their mission requirements. The in-flight calibration studies show degradation in the sensitivity of the detector responses that was expected.

The on-board calibration by means of empirically derived coefficients has been updated to account for the changes in the detector responses.

The vicarious calibrations studies for the TIR subsystem have shown low NE Δ T values for ocean scenes, with values typically with 0.1 – 0.2 K. Additionally the MTF shows high values at the half Nyquist frequency used with all bands except band 14 reporting MTFs of 0.7 or higher in both along and cross track.

The pixel geolocation of the subsystems has been regularly assessed with relative pixel registrations of 15 m per pixel, and absolute pixel registrations of 50 m. The VNIR/TIR inter pixel registration of <0.2 pixels. This level of inter subsystem registration enables to usage of the VNIR land classification data to be used as prior data for the retrieval outlined in this thesis.

2.3 MODIS

The Moderate Resolution Imaging Spectroradiometer (MODIS) is the name of two current instruments mounted on the NASA satellites TERRA and AQUA, launched in 1999 and 2002, respectively. The two satellites are on orbits that allow different temporal insight in the observations. For example, over the UK the MODIS on TERRA will record an image in the morning and the early night, whereas AQUA will observe at midday and midnight (Neteler, 2004). The local equatorial crossing times are 10.30 am and 1.30 pm for TERRA and AQUA respectively.

MODIS was designed to improve knowledge globally in the areas of land, ocean and lower atmospheric processes. Additionally MODIS aimed to continue and enrich the data record associated with heritage missions including the Advanced very-high-resolution radiometer (AVHRR), High resolution Infrared Radiation Sounder (HIRS) and LANDSAT TM (Xiong, Chiang, Esposito, Guenther, & Barnes, 2003). Using both Aqua and Terra MODIS is able to monitor and analyse short term climate and environmental phenomena.

MODIS has 36 spectral bands ranging from the visible through the NIR to the TIR, each focussed on a variety of different scientific objectives and with spatial resolutions varying

from 250 m to 1 km. The TIR system and performance of the relevant channels is described here.

2.3.1 Infra-red window Instrument Specifications

MODIS has a swath of 2330 x 10 km, utilising double sided beryllium cross-track scanning mirror allowing views which are $\pm 55^\circ$ off nadir. The detectors used in bands 31 and 32 are photovoltaic HgCdTe detectors. These are the bands used in the retrieval of the MODIS LST used in this thesis and therefore will be the bands focussed upon in this section. Each of the bands has ten of the HgCdTe detectors, capable of viewing the full aperture on-board blackbody.

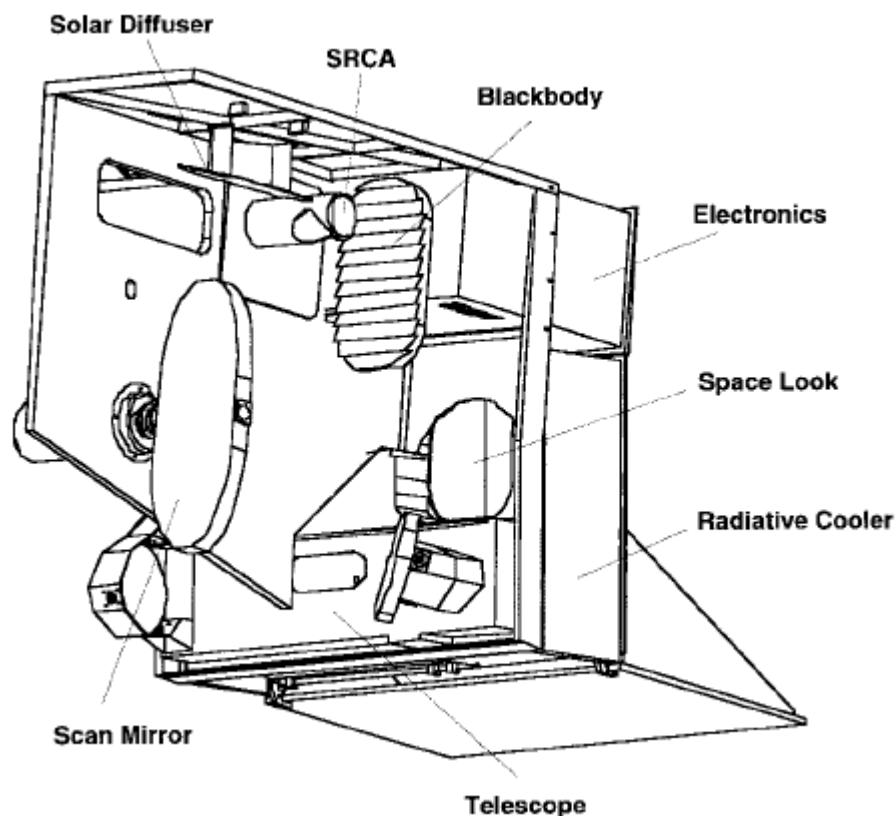


Figure 12 – Diagram of the MODIS instrument showing the key components (Barnes et al., 1998).

Band	Spectral range (μm)	Radiometric Resolution (K)	Spatial Resolution
31	10.780-11.280	0.05	1 km
32	11.770-12.270	0.05	1 km

Table 8 – MODIS spectral channels for the thermal bands used in the LST products (Barnes et al., 1998).

The spectral characteristics of bands 31 and 32 can be seen in Table 8. Both the spectral range and radiometric resolution were selected based upon the science requirements for the investigation of surface and cloud temperature outlined by the ad hoc science team.

2.3.2 Instrument Calibration

The initial calibration was conducted simultaneously with the pre-flight performance testing done by Rautheon Santa Barbara Remote Sensing using a thermal vacuum environment and the large aperture blackbodies at set temperatures (Xiong & Barnes, 2006).

Upon launch the calibration is conducted using a quadratic formula which links the at-aperture radiance of the sensor to the background corrected digital number recorded. Similar to the calibration of the ASTER TIR subsystem there are three coefficients: a_0 , a_2 , and b_1 . b_1 is the blackbody coefficient calculated from the detector response when observing the blackbody.

$$L = a_0 + b_1 DN + a_2 DN^2 \quad \text{Equation 2.2}$$

The coefficients a_0 and a_2 are the offset and the non-linearity of the system pre-calculated before launch and updated during the first in-flight calibration. After the first post launch calibration only b_1 will be updated.

This thesis relies on MODIS-Terra LST and so its calibration is important to discuss. In-flight, MODIS is calibrated by both blackbody observation and space views. This is especially important to the thermal channels for which the ground calibration data sets were considered to be insufficient to calculate a valid Response Versus Scan-Angle (RVS) calibration, (Xiong et al., 2004).

On MODIS-Terra, but not on MODIS-Aqua, there is a small optical leak which leads to cross-talk between channels 31 and 32 (Xiong et al., 2007). The effects are relatively stable so that an effective calibration correction can be applied (Xiong et al., 2007). Hook, Vaughan, Tonooka, & Schladow, (2007), show that at least for SST values channels 31 and 32 show biases in brightness temperatures of less than 0.05 K and close to 0.1 K respectively. Standard deviations are less than 0.4 K.

Absolute calibration uncertainties are likely less than 0.3 K according to further in-flight studies. MODIS-Aqua and MODIS-Terra differ in comparisons to SST analyses by this value, a difference which persists in Collection 5 and Collection 6 and is unexplained (XingMing Liang & Ignatov, 2013).

2.3.3 Instrument Performance

The radiometric performance of MODIS in the thermal channels was assessed based upon the NE Δ T. Initially this was conducted by the instrument supplier; Rautheon Santa Barbara Remote Sensing. This testing was conducted under three instrument thermal phases: The hot phase (283 K), the nominal phase (273 K), and the cold phase (256 K). In the hot phase the bands 31 and 32 reported NE Δ Ts of under the specification of 0.05 K, as shown in Table 9.

Band	Required NEΔT (K)	Measured NEΔT (K)	MTF (SCAN)	MTF (TRACK)
31	0.05	0.024	0.34	0.54
32	0.05	0.040	0.37	0.55

Table 9 – MODIS NE Δ T and MTF performance pre-launch adapted from (Barnes et al., 1998).

Since its launch the thermal bands on MODIS have been performance analysed in several key areas. To assess this performance this section will focus on the studies published by Xiong et al., (2003).

The four key areas of performance which have been analysed in these studies are the on-board blackbody performance, the detector noise characterisation, the short term stability and the long term changes.

The on-board blackbody is usually kept at a fixed temperature of 290 K and is monitored by 12 platinum resistance thermistors. The output of the thermistors was monitored over time and the variations between each scan assessed. Overall the blackbody was found to have a scan to scan variation of less than 30 mK and a drift of 2 mK per year.

The NE Δ T is tracked for each detector every day through assessing the detector response to the blackbody at a fixed temperature. All of the detectors within each band showed similar performance. All of the thermal bands meet the design requirements except band 36 which had known issues pre-launch.

The short term stability is based on the temperature variation of the instrument components including the scan mirror and blackbody as compared to the detectors. Analysis shows that over the course of one orbit the scan mirror is the most susceptible to changes in solar heating, but that this effect is not significantly carried to the detector temperature with orbital variations of less than 0.1%.

The long term assessment looked at data over 7 years of operation and found that apart from changes in operational mode, which were expected to produce detector response changes, that the mean change in the detector response per year is less than 0.2% of the measured radiance.

In-flight calibrations conducted using data taken over Lake Tahoe by Hook, Vaughan, Tonooka, & Schladow, (2007) show the differences between the on-board calibrations and the vicarious calibration brightness temperatures to be less than 1%, usually less than 0.5% for the time period 2000 to 2005, with absolute difference of less than 0.16 K. Overall channels 31 and 32 presented biases of 0.024 and 0.098 K with standard deviations of 0.332 and 0.375 K, (Hook et al., 2007)

2.4 Data Products

The primary data products used in this thesis are level 1b and level 2 products from MODIS and ASTER. These products are well established and have a long history of detailed scientific usage in Earth observation. As such the development and historical usage of these products is beyond the scope of this thesis but a top level view is important to understanding the quality and applicability of the data.

2.4.1 ASTER L1b/L1T

The ASTER L1b/L1T registered radiance at the sensor is the primary ASTER product used within this thesis. This product is the radiometrically calibrated and geo-registered scaled radiances. The L1b product also co-registers the SWIR and TIR bands to the higher resolution VNIR data, this is not done in L1T. However, because this is a scaled radiance from the DNs and must be converted to true at-sensor radiance, using Equation 2.3.

$$L_{rad,\lambda} = UCC_{\lambda} * (DN_{\lambda} - 1) \quad \text{Equation 2.3}$$

where $L_{rad,\lambda}$ is the TOA spectral radiance, UCC_{λ} is the band Unit conversion coefficient for conversion to brightness temperatures.

The data is supplied with a 11x11 geo-location array per subsystem and the product meta-data contains the four scene corners, scene centre longitudes and latitudes, used from geo-referencing.

2.4.2 MODIS MOD11_L2

The MOD11 L2 product is the moderate resolution LST product used in this thesis. The product is the result of the split-window technique developed by Wan, (2006), based on the theory outlined in Chapter 3. The aim was to retrieve LST to 1 K or better.

The split-window algorithm enable the removal of the atmospheric effect on the retrieval but still requires emissivity knowledge of the surface. The MOD11 product uses land classification with associated emissivities to fill this knowledge gap. The split window methodology used pre-generated coefficients derived from the linear regression of simulated radiances generated using the MODTRAN forward model.

The MOD11 product has been validated (Wan, 2008; Wan & Li, 2008; Wan, Zhang, Zhang, & Li, 2004; Wan, Zhang, Zhang, & Li, 2002) through stage 1: small independent validation sites and stage 2: extended and widespread validation looking into spatial and temporal variation validation, the product has been consistently found to retrieve to 1 K or better in most cases.

2.5 Summary

MODIS and ASTER have both been the subject of extensive calibration and performance analysis pre and post launch. The calibrations and performance of both these instruments have significant impacts on the work presented in this thesis. The calibration of the ASTER TIR subsystem has been reviewed and the thermal drift is accounted for in the updating of the calibration coefficients. Given that the channels developed biases ranging from -6 to + 12 K over the course of five years the thermal drift is likely to continue requiring a continual update in the calibration coefficients. Whilst in theory this update should account for the change in detector sensitivity, the updates are applied periodically and therefore there will be transition periods where the data maybe marginally compromised pending an update. This is not currently known to be a significant issue as these offsets would be extremely small.

ASTER TIR subsystem has been found to perform to a NE Δ T of 0.1 to 0.2 K in vicarious calibration over ocean scenes and consistently performs to better than the requirement of 0.3 K. This is a key parameter in the algorithm developed in this thesis as the retrieval cost function, see Equation 3.40, and has a dependence on the instrument noise, as does the retrieved uncertainty. The VNIR and TIR pixels have been shown to have a coincident pixel registration of 0.2 pixels or better with an absolute registration of 50 m, an essential correlation given the reliance on the VNIR to provide a priori information to the retrieval using the TIR in this thesis.

MODIS is very well calibrated and its performance has been evaluated rigorously. The LST product in particular has been found to have an accuracy of 1 K or better in the majority of cases. As the MOD11 LST is the dataset used for the a priori LST in this retrieval the accuracy of this product is an important parameter in ensuring optimal performance of the retrieval algorithm in this thesis

3 Radiative Transfer and Retrieval Theory

3.1 Introduction

The algorithm developed in this thesis uses the satellite instrumentation outlined in Chapter 2 to retrieve LST and LSE for uses in the urban environment described in Chapter 1. LST/LSE retrievals necessitate a full understanding of the processes undergone by surface-leaving-radiance as it propagates through the atmosphere. Furthermore, knowledge of the underlying statistical and physical theories used in the retrieval of LST and LSE from TOA radiances is required to formulate a robust and accurate methodology.

3.2 Radiative Transfer

In order to understand the retrieved LST, it is necessary to review the physics acting upon the observed photons. The radiances observed by the satellite instrument at the top of the atmosphere are the result of a large and complex series of processes based upon complex physical interactions of the photons with the medium through which they are travelling, essentially emission, scattering and absorption. The mathematical description of the relationship between the radiances from the surface and atmospheric sources and the observed radiance is commonly referred to as the Radiative transfer equation:

$$L^{TOA} = L^{surf} + L^{atm} + L^{reflected\ atm} \quad \text{Equation 3.1}$$

where L^{TOA} is the radiance observed at the Top of Atmosphere (TOA) and L^{surf} , L^{atm} and $L^{reflected\ atm}$ are the radiance contributions from the ground, the atmospheric upwelling and the reflected atmospheric downwelling respectively.

All of the radiances described in the radiative transfer equation are wavelength dependent. Both the surface emissivity, atmosphere emission and transmittance will interact with photons differently according to their wavelength (λ). Each of the terms on the right-hand side of Equation 3.1 can be expanded to express these effects. They can then be expressed in terms of the observations of a radiometer (Dash, Göttsche, Olesen, & Fischer, 2002; Noyes, 2005):

$$L_i^{surf} = \int_{\lambda_1}^{\lambda_2} f_i(\lambda) \varepsilon(\lambda) B(\lambda, T_s) \tau(\lambda) d\lambda \quad \text{Equation 3.2}$$

$$L_i^{atm} = \int_{\lambda_1}^{\lambda_2} \int_{p=0}^{psurf} f_i(\lambda) B(\lambda, T_p) \frac{d\tau}{dp} d\lambda dp \quad \text{Equation 3.3}$$

$$L_i^{reflected\ atm} = \int_{\lambda_1}^{\lambda_2} \int_{\theta=0}^{\frac{\pi}{2}} \int_{\phi=0}^{2\pi} f_i(\lambda) (1 - \varepsilon(\lambda)) L^{Downwelling}(\lambda, \theta, \phi) \tau(\lambda) \sin 2\theta d\lambda d\theta d\phi \quad \text{Equation 3.4}$$

where i is the radiometer channel, f_i is the channel spectral response function, θ and ϕ are the zenith and azimuth angles, p is the atmospheric pressure, $psurf$ is the surface pressure, T_p is the temperature at a given pressure p , T_s is the surface temperature, $\tau(\lambda)$ and $\varepsilon(\lambda)$ are the atmospheric transmissivity and the surface emissivity for a given wavelength and $L^{Downwelling}$ is the downwelling atmospheric radiance. B is the Planck function for the surface and atmospheric temperatures at a wavelength.

Retrieval of the LST using the equations outlined in this section require the emissivity and the atmospheric transmissivity to be known. With these parameters known, the TOA radiance can be used to calculate the surface leaving radiances, which in turn can be used to calculate the LST using Planck's function. In practice this process is calculated numerically, rather than in explicit equations in forward models.

3.3 Radiative transfer model

A forward model is a simulation that given the initial state of a system can apply the relevant physical processes and dynamics of that system and correctly calculate the system state at a different point in time. In this case the system is the signal detected by a satellite instrument, and comprises the surface and atmosphere over which the signal is observed. Therefore in this thesis the forward model will refer to the processes which are modelled to simulate the radiances observed by the satellite instrumentation.

The objective of the forward model is to describe the TOA radiance in terms of the surface and atmospheric thermal emissions and simulate the TOA radiances based upon the real physical system. The physical system at work in this case has many components, starting with the surface; a simple, conceptual diagram of this can be seen in Figure 13 for a three-layer atmosphere.

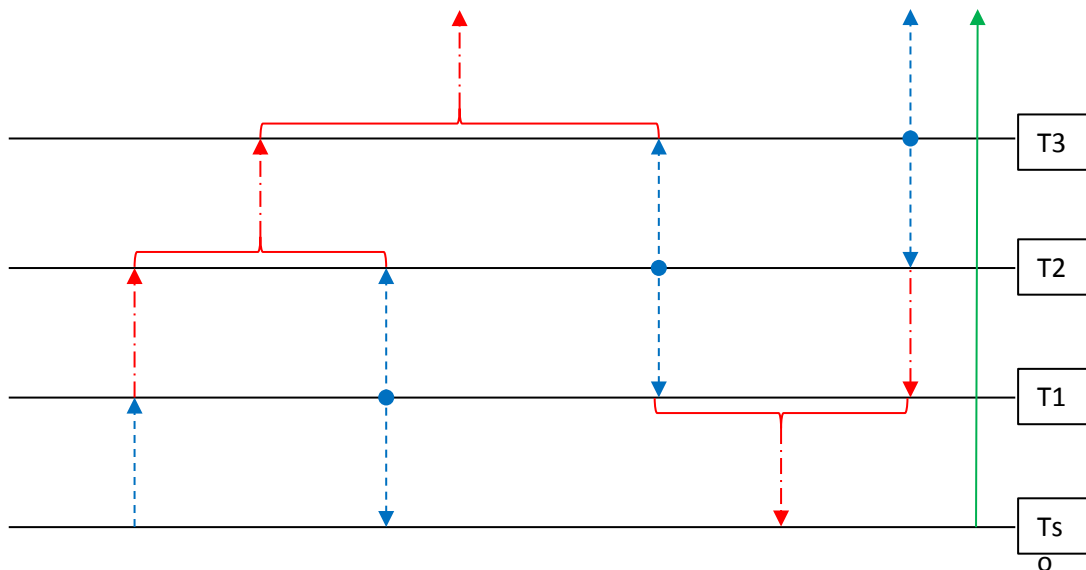


Figure 13 – A simple layer model of radiative transfer. The atmosphere is described in three layers. The Blue lines show Emission, Red lines Transmission and Green Reflection.

The thermal energy of the surface is emitted as photons at a wavelength λ , as described by the Planck function for surface temperature (T_s) multiplied by the surface emissivity ($\epsilon_s(\lambda)$). The surface radiance then travels through the atmospheric layers T1-3, at each layer reducing in intensity due to absorption by gases in the atmosphere such as water vapour and ozone. The proportion of the surface radiance

which arrives at the TOA is given by the transmittance of the total atmosphere through which it travels, as shown by the red lines in Figure 13.

The TOA radiance does not exclusively consist of transmitted surface radiance; there is an additional component from the atmosphere. The atmosphere possesses a thermal energy which emits radiance based on its temperature and emissivity. It emits spherically and a proportion of this radiance will match the direction of the surface radiance and be observed by the satellite instrument. Figure 13 shows these emissions as the blue circular points at each level boundary. The atmospheric emissivity ($\epsilon(\lambda)$) at a wavelength λ is equal the absorption ($\alpha(\lambda)$) of the atmosphere at λ . The transmittance ($\tau(\lambda)$) of the atmosphere may be calculated from the atmospheric absorption as the transmission of light at λ will be given by:

$$\tau(\lambda) = (1 - \alpha(\lambda)) \quad \text{Equation 3.5}$$

There is also a third source of TOA radiance in the thermal infra-red; a portion of the atmospheric emissions will reach the surface and be reflected, this reflected component will then undergo the same processes as the surface radiance as it travels through the atmosphere adding to the observed signal, denoted by the green line in Figure 13. Since emissivity is high in the infra-red and the atmosphere is cold, this reflected component is usually small compared to the surface emissivity term.

In this forward model the observed radiances at TOA are the measured parameters of the system and the surface parameters are the unknown variables. The relation between the measured parameter \mathbf{y} and a given set of variables \mathbf{x} can be expressed as a simple equation:

$$\mathbf{y} = \mathbf{F}_{True}(\mathbf{x}) + \epsilon \quad \text{Equation 3.6}$$

where \mathbf{F}_{True} represents the entire forward model causing \mathbf{y} to result from \mathbf{x} and ϵ is the combination of the measurement and forward model errors. Equation 3.6 assumes a complete physical model, which is not a capability practically available, and definitely not in a computationally efficient scheme. In order to find a balance between computational efficiency and physical accuracy approximations are made

allowing the model to simulate only those processes deemed physically relevant to the desired simulated parameters.

3.4 Simulated radiative transfer

To treat the physical model in a computationally manageable fashion the atmosphere is divided into layers, such as the simplified arrangement shown in Figure 13. In a realistic calculation, the system would be expanded to include many more layers, in order to achieve a good accuracy in the final TOA radiance. In each of these layers the transmittance and the thermal emission are dependent upon the atmospheric temperature and absorption coefficients of the gases included in the forward model.

3.4.1 RFM

The Reference Forward Model (RFM) is a line-by-line radiative transfer model developed for the Michelson Interferometer for Passive Atmospheric Sounding (MIPAS) instrument on the Environmental Satellite (ENVISAT) but expanded to nadir calculations. It can incorporate into its simulations the effects of 184 gases at high spectral resolution (Dudhia, 2014); however only a small number of these gases are required for the thermal infra-red windows. Line-by-line models calculate the TOA radiance through the application of radiative transfer functions dependent upon the atmospheric properties relevant to each wavenumber being simulated, and can be computationally expensive.

3.4.2 RTTOV

Radiative Transfer for TOVS (RTTOV) is a fast radiative transfer model developed by the UK Meteorological (MET) Office. It conceptualises spectral windows as independent channels. RTTOV gas transmittances within the atmosphere are incorporated as a function of predictors associated with the profile. Through the

parameterisation of the various transmittances the computational speed of the model is increased significantly compared to the line-by-line methodology (Matricardi, 2009).

However this increase in computational speed does mean a reduction in the accuracy and spectral resolution of the simulated radiances. In comparison to RFM, RTTOV has coarser effective spectral resolution as the forward model uses channel coefficients which rather than a spectral range (Hocking et al., 2014).

3.4.2.1 *Jacobians*

Using knowledge of the atmospheric and surface states, Equation 3.6 can be rewritten in terms of a weighting function which links the measured and retrieved parameters in terms of their sensitivity to changes in the various atmospheric states. This can be achieved through the use of a Taylor expansion

$$\mathbf{y} \approx \mathbf{K}(\mathbf{x} - \mathbf{x}_L) + y_L \quad \text{Equation 3.7}$$

$$\mathbf{K}_{i,j} = \frac{d\mathbf{F}(\mathbf{x}_i)}{d\mathbf{x}_j} \quad \text{Equation 3.8}$$

where $\mathbf{K}_{i,j}$ is the Jacobian matrix or differential weighting function in band i for parameter j . It shows the change in the result of the forward model run due to a change in the parameter \mathbf{x}_j and $\mathbf{F}(\mathbf{x}_i)$ is the simulation made by the forward model for channel, i , for all retrieved and a priori parameters \mathbf{x}_i . \mathbf{x}_L is the point about which the linear approximation is made. y_L is non-linearity of the observation. Equation 3.7 and Equation 3.8 allow the forward model to estimate a TOA radiance given surface parameters and selected atmospheric variables. For the surface parameter, the Jacobian is a matrix with terms for the forward model sensitivity to surface temperature and emissivity. As ASTER has five thermal channels, if the state has six desirable parameters then the Jacobian has dimensions of 5x6, see Equation 3.9.

$$\mathbf{K} = \begin{bmatrix} \left(\frac{dF}{dT}\right)_{c10} & \left(\frac{dF}{d\epsilon}\right)_{c10} & 0 & 0 & 0 & 0 \\ \left(\frac{dF}{dT}\right)_{c11} & 0 & \left(\frac{dF}{d\epsilon}\right)_{c11} & 0 & 0 & 0 \\ \left(\frac{dF}{dT}\right)_{c12} & 0 & 0 & \left(\frac{dF}{d\epsilon}\right)_{c12} & 0 & 0 \\ \left(\frac{dF}{dT}\right)_{c13} & 0 & 0 & 0 & \left(\frac{dF}{d\epsilon}\right)_{c13} & 0 \\ \left(\frac{dF}{dT}\right)_{c14} & 0 & 0 & 0 & 0 & \left(\frac{dF}{d\epsilon}\right)_{c14} \end{bmatrix} \quad \text{Equation 3.9}$$

Equation 3.9 shows the sensitivity in five channels (c10, c11, c12, c13 and c14). The surface temperature Jacobians are in the same column as they correspond to one surface temperature output, whereas the emissivity channels are kept separate as they are considered independently in the retrieval. However, later, the correlations between emissivities are discussed. Within the full retrieval there are also Jacobians for atmospheric parameters, including temperature, water vapour content and ozone content.

3.5 Traditional LST Algorithms

Historically, LST has been derived using single or split-window algorithms (two channels). Of these, the split window algorithm is more accurate due to the intrinsic atmospheric correction. These algorithms have been applied to instruments such as ATSR and MODIS (Prata, 2002; Zhengming Wan, 2006 respectively).

A multi-channel approach such as that used within AATSR enables the calculation of LST without precise specification of the mean atmospheric temperature (T_a), to the first order. This is facilitated by the assumption that T_a is approximately equal for the two channels and thereby through combination the T_a can be removed from the calculation (McMillin, 1941). The following expression of the mathematics of this method is adapted from Noyes, (2005). It should also be noted that this retrieval derivation is for the idealised case of unity emissivity.

The typical choice for two window channels in the infra-red is to have a channel at 11 μm and one at 12 μm . The TOA brightness temperatures can be described by:

$$B_{11}(T_{11}) = B_{11}(T_s)\tau_{11} + (1 - \tau_{11})B_{11}(T_a) \quad \text{Equation 3.10}$$

$$B_{12}(T_{12}) = B_{12}(T_s)\tau_{12} + (1 - \tau_{12})B_{12}(T_a) \quad \text{Equation 3.11}$$

where $B_{11}(T_{11})$ and $B_{12}(T_{12})$ are the observed TOA brightness temperatures for the 11 and 12 micron channels, $B_{11}(T_s)$ is the surface emitted radiance from a surface at T_s , observed by the 11 micron channel, and likewise for the 12 micron channel. $B_{11}(T_a)$ is the atmospheric radiance and τ_{12} is the atmospheric transmittance; similarly for the 12 micron channel.

Equation 3.10 and Equation 3.11 are both dependent on T_a . However, for small departures of T_a from assumed knowledge, then T_a can be approximated through Taylor expansion using:

$$f(x) = f(b) + \frac{f'(b)}{1!}(x - b) + \dots \quad \text{Equation 3.12}$$

where b is the assumed knowledge. If $B_{12}(T_a)$ is taken as the mean atmospheric radiance then the expansion can be performed in two cases, once for T_{12} and once for T_s . These cases result in,

$$B_{11}(T_{12}) = B_{11}(T_a) + \frac{\partial B_{11}}{\partial B_{12}}(B_{12}T_{12} - B_{12}T_a) \quad \text{Equation 3.13}$$

and
$$B_{11}(T_s) = B_{11}(T_a) + \frac{\partial B_{11}}{\partial B_{12}}(B_{12}T_s - B_{12}T_a) \quad \text{Equation 3.14}$$

The differentials represent the wavelength dependent responses of the radiances to changes in T_a . Therefore by substitution of Equation 3.13 and Equation 3.14 into Equation 3.11 the $B_i(T_a)$ term can be isolated purely in terms of the channel radiances and surface radiance.

$$B_{11}(T_a) = \frac{B_{11}(T_{12}) - \tau_{12}B_{11}(T_s)}{1 - \tau_{12}} \quad \text{Equation 3.15}$$

This can then be substituted into Equation 3.11 allowing the surface radiance to be found solely in terms of the two channel radiances with no dependence upon T_a .

$$B_{11}(T_s) = B_{11}(T_{11}) + [B_{11}(T_{11}) - B_{11}(T_{12})] \left(\frac{1 - \tau_{11}}{\tau_{11} - \tau_{12}} \right) \quad \text{Equation 3.16}$$

Such a form gives the surface radiance based upon the TOA channel radiances requiring only knowledge of the atmospheric transmittance at each wavelength. Therefore by an inversion of the Planck function the LST can be found from the brightness temperature.

$$T_s = T_{11} + (T_{11} - T_{12}) \left[\frac{1 - \tau_{11}}{\tau_{11} - \tau_{12}} \right] \quad \text{Equation 3.17}$$

For LST retrieval the algorithm must be expanded to include the effects of emissivity on the radiative transfer. Firstly, Equation 3.17 can be re-written in the generalised split window form:

$$T_s = a_1 T_{11} + a_2 T_{12} \quad \text{Equation 3.18}$$

where

$$a_1 = 1 + \left[\frac{1 - \tau_{11}}{\tau_{11} - \tau_{22}} \right] \quad \text{Equation 3.19}$$

and

$$a_2 = - \left[\frac{1 - \tau_{11}}{\tau_{11} - \tau_{12}} \right] \quad \text{Equation 3.20}$$

Introducing a dependence on the surface emissivity yields a new generalised split window form, expansion adapted from Comyn-Platt, (2013):

$$T_s = a_0 + b_0 T_{11} + c_0 T_{12} \quad \text{Equation 3.21}$$

$$a_0 = \alpha \left(\frac{\partial B_{11}}{\partial T} \right)^{-1} + [1 - (b_0 - c_0)] \left[T_a + B_{11}(T_a) \left(\frac{\partial B_{11}}{\partial T} \right)^{-1} \right] \quad \text{Equation 3.22}$$

and

$$b_0 = \frac{(1 - \tau_{12})}{\eta} \quad \text{Equation 3.23}$$

$$c_0 = \frac{(1 - \tau_{11})}{\eta} \quad \text{Equation 3.24}$$

$$\alpha = \frac{1}{\eta} [(1 - \tau_{11})\tau_{12}(1 - \varepsilon_{12})L_{12}^{Downwelling} - (1 - \tau_{12})\tau_{11}(1 - \varepsilon_{11})L_{11}^{Downwelling}] \quad \text{Equation 3.25}$$

$$\eta = \varepsilon_{12}\tau_{12}(1 - \tau_{11}) - \varepsilon_{11}\tau_{11}(1 - \tau_{12}) \quad \text{Equation 3.26}$$

In reality the coefficients a_0 , b_0 and c_0 are not calculated iteratively during a retrieval. Rather they are calculated using a regression analysis over a large number of input atmospheric and surface parameters. Linking these coefficients to parameters such as biome allow the coefficients to be applied to the retrieval based upon the individual locations and conditions of the observation. The coefficients are banded by biome and an estimate of the Total Column Water Vapour (TCWV), and are used to calculate the uncertainty dependant on the biome and TCWV band.

3.6 The TES method

TES is a major step forward in deriving LST and LSE. The TES methodology retrieves simultaneous surface temperature and emissivity from the ASTER TIR channels using a hybridisation of two pre-existing algorithms: Normalised Emissivity Module (NEM) and the RATIO algorithm (RAT). The emissivities are processed with the empirically derived max-min difference (MMD) spectral contrast, to find the minimum emissivity to improve the accuracy of the retrieved emissivity (Gillespie, Rokugawa, Hook, Matsunaga, & Kahle, 1999).

The TES algorithm utilised the atmospherically corrected surface leaving radiance product and the down-welling sky irradiance. The process chain begins with the estimation of the maximum emissivity for each band ε_{max} . The observed surface leaving radiance is then taken to be equal to the surface emission plus the reflected down-welling irradiance, see Equation 3.27.

$$L^{surf} = L^{TOA} - (1 - \varepsilon_{max})L^{Downwelling} \quad \text{Equation 3.27}$$

This surface leaving radiance is then used with the maximum emissivity to calculate the minimum LST, within the NEM module.

$$T = \frac{c_2}{\lambda} \left[\ln \left(\frac{c_1 \epsilon_{max}}{\pi L^{surf} \lambda^5} + 1 \right) \right]^{-1} \quad \text{Equation 3.28}$$

where T is the estimated LST and c_2 and c_1 are constants from Planck's law. This is done for all five TIR channels separately and the highest LST value is selected as the value to use moving forward. The emissivities are then recalculated using this relationship:

$$\epsilon_{max}' = \frac{L^{surf}}{B(T)} \quad \text{Equation 3.29}$$

The processes in Equation 3.28 and Equation 3.29 are repeated iteratively until the change in the L^{surf} between iterations is less than a pre-determined threshold value, where the number of steps is greater than a pre-defined value, e.g. 12 (Gillespie et al., 1999). The resulting LST and emissivity values are passed forward to the RAT module.

The RAT module calculates the relative values of the emissivities ϵ_{ratio} with respect to the five TIR channels by dividing each channel emissivity by the average emissivity across the five channels. This ratio does not represent the actual values of the emissivity and requires rescaling. To do this MMD is used.

The MMD is the difference between the minimum and maximum emissivities across the channels.

$$MMD = \max(\epsilon_{ratio}) - \min(\epsilon_{ratio}) \quad \text{Equation 3.30}$$

This value is then applied in the Equation 3.31 to determine the minimum emissivity ϵ_{min} using empirically derived constants.

$$\epsilon_{min} = 0.994 - 0.687 * MMD^{0.737} \quad \text{Equation 3.31}$$

The MMD constants have been determined from substantial empirical laboratory testing of 86 spectrally different material types. The resulting relationship is plotted in Figure 14.

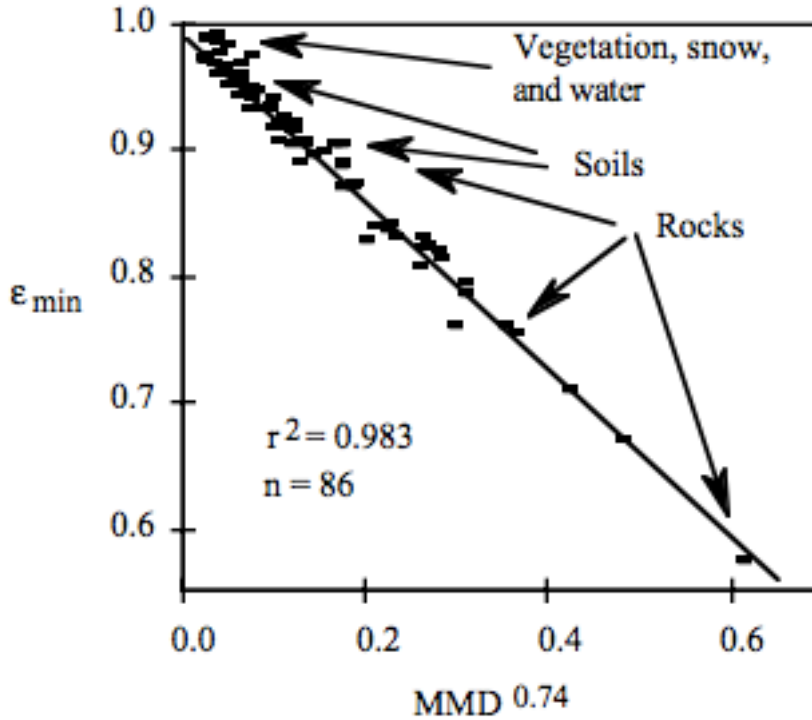


Figure 14 – Laboratory derived empirical MMD-minimum emissivity relationship for 86 material types. Plot taken from Gillespie et al., (1999)

The scaled emissivities based on the empirical data are calculated for the bands using Equation 3.32, for the emissivity in each channel.

$$\varepsilon_{final} = \varepsilon_{ratio} \left(\frac{\varepsilon_{min}}{\min(\varepsilon_{ratio})} \right) \quad \text{Equation 3.32}$$

This is the final emissivity output of the TES methodology. The final step of the process is to recalculate the LST with the new emissivities using Equation 3.28. Importantly if the MMD is less than the empirically derived threshold value of 0.032 then the MMD is not used and the ε_{min} is set to a default value of 0.983, selected to represent grey bodies. If this is not a true representation of the pixel this could lead to errors in the retrieved quantity.

In the retrieval the data is then quality flagged based on the detected cloud in the pixel, the success or failure of NEM and the number of iterations need in NEM (Gillespie et al., 1999). Additional flags are included representing the retrieved ε_{max}

and $L^{Downwelling}$, these flags classify the type of surface and atmosphere represented by these components as well as returning an error flag for unrealistic values.

The performance of the TES algorithm has been evaluated through extensive numerical simulation. In simulations, the TES algorithm was able to retrieve LST to an accuracy of 1.5 K for 95% of the spectral library materials using a surface at 300 K. The emissivity errors were found co-dependently with the LST, and in monte-carlo simulations; for a surface at 300 K, a 1 K LST over estimate was found to correspond to a emissivity underestimate of around 0.017 (Gillespie et al., 1999). Overall the numerical simulations showed a performance across the majority of tests comparable to the design specifications of ± 1.5 K and ± 0.015 emissivity, which are often the values quoted when looking at the uncertainty of the TES product.

In the initial simulated scene testing the Thermal Infrared Multispectral Scanner (TIMS) and the MODIS/ASTER airborne simulator (MASTER) data were used to create proxy ASTER data. Three scenes were tested using the TIMS data: Castic Lake, Lake Tahoe and the Hawaiian south coast. The Lake Tahoe test showed the TES algorithm performing well; with both LST and emissivity retrieved to within the design specifications. The Hawaiian and Castic scenes had poorer performances; the Castic and Hawaiian emissivities were consistently too low by around 0.05. Due to the poorer performance in the scenes than in the simulated materials, the errors were attributed to issues in the atmospheric correction applied to create the surface radiance used in the TES algorithm rather than an error in TES itself.

TES is primarily sensitive to errors induced due to problems with spectral contrast in the channels as this informs the MMD module, which can substantially alter the retrieved parameters. TES is inherently dependant on the materials used in the laboratory empirical tests; therefore it could be subject to error if the material observed is not represented in the laboratory tests.

TES has been continuously re-evaluated and improved. Atmospheric water vapour was highlighted as the primary driver of poor performance in numerous tests. In order to address the uncertainties included in TES retrievals as a result of high or variable atmospheric water vapour, a new module was developed: the water vapour scaling (WVS) method.

As discussed previously, TES utilises an atmospherically corrected ground leaving radiance as its observational input. Therefore, the WVS methodology is applied to the instrument observed radiance before its usage in TES. The WVS methodology aims to enhance the output from the MODTRAN radiative transfer model, used in the atmospheric correction. The wavelength / band dependant surface upwelling radiance, atmospheric downwelling radiance and the atmospheric transmittance are defined in terms of Water Vapour Scaling factor that varies per pixel (Grigsby et al., 2015). This method requires the calculation of the apparent surface brightness temperature using the Enhanced MultiChannel Water Vapour Dependant Split-Window algorithm. These factors are applied to the radiances given to TES to account for the water vapour effects with improvements seen in the retrieved uncertainty of ~ 0.3 K (Hulley et al., 2012).

However in the case of the urban environment TES has been found to have issues. TES was found to overestimate the urban LSEs by 0.017 and under estimate the LST of 0.9 K in the Dual-use European Security IR Experiment (DISIREX) campaign, which consisted of 30 independent scenes over the large city of Madrid. The MMD relationship was analysed for the urban materials and found that excluding the metal surfaces which were poorly modelled, the man-made material LSE could be retrieved with a RMSE of 0.025, higher than the normally stated error, and the LST between 0.8 and 1.8 K. (Oltra-Carrio, Cubero-Castan, Briottet, & Sobrino, 2014).

3.7 Optimal Estimation Theory

The previous forms of LST retrieval use approximations to the radiative transfer to define LST in terms of brightness temperature. However, the forward model can provide a simulated direct brightness temperature for a physical system, but only if provided with the true surface parameters. Optimal estimation can use the a priori knowledge of the surface and atmospheric parameters to create a simulated brightness temperature for the observed radiance, which can then be mathematically compared to the actual observed brightness temperatures. The offset between the simulated and observed brightness temperatures can then be used to provide an improved estimate of the true parameters. The retrieved parameters in this investigation are the surface parameters of LST and LSE, and the atmospheric parameter of total column water vapour.

The a priori surface parameters are input to a forward model which simulates the radiance seen by the satellite. The algorithm takes the resulting simulated TOA radiances and input surface parameters and computes the differences between the real and simulated radiances and the a priori and estimated surface parameters. Optimal estimation aims to reduce the radiance residual, whilst statistically constrained to the a priori surface parameters. If the constraints are physically representative and the uncertainties are well specified, then the resulting surface estimate achieved should be optimal through minimisation of the cost function.

3.7.1 Bayesian Approach

In order to correctly identify a solution which reduces the radiance residual while being constrained to the true physical system the probabilities of the retrieved results need to be considered. The optimal solution should be the result with the highest probability of a true representation of the surface given an input measured radiance (Rogers, 2000).

The relationship between the measured and retrieved parameters can be described using probability density functions (pdf). If the prior pdf of the measured variable \mathbf{y} is $P(\mathbf{y})$ and the prior pdf of the desired variable \mathbf{x} is $P(\mathbf{x})$ then the probability that \mathbf{x} will lie within a given range for a particular measurement of \mathbf{y} is given by $P(\mathbf{x}|\mathbf{y})$. Conversely $P(\mathbf{y}|\mathbf{x})$ is the probability that \mathbf{y} will lie within a given range for a particular value of \mathbf{x} . Using Bayes' theorem:

$$P(\mathbf{x}|\mathbf{y}) = \frac{P(\mathbf{y}|\mathbf{x})P(\mathbf{x})}{P(\mathbf{y})} \quad \text{Equation 3.33}$$

Before the retrieval the prior information about the measurement and surface state can be characterised by pdfs ($P(\mathbf{x})$, $P(\mathbf{y})$), a forward model is utilised to relate the surface state to measurement space ($P(\mathbf{y}|\mathbf{x})$). The prior pdf is then re-evaluated and improved with the measurement pdf to provide a posterior pdf ($P(\mathbf{x}|\mathbf{y})$). (Rogers, 2000)

Each element of Equation 3.33 can be assumed to follow a Gaussian distribution where the pdf is given by:

$$P(\mathbf{x}) = \frac{1}{(2\pi)^{\frac{n}{2}} |\mathbf{S}|^{\frac{1}{2}}} \exp \left[-\frac{1}{2} (\mathbf{x} - \mathbf{x}_a)^T \mathbf{S}^{-1} (\mathbf{x} - \mathbf{x}_a) \right] \quad \text{Equation 3.34}$$

This equation can then be re-arranged for the particular retrieval required; it is most common to write the equations in the natural logarithm form:

$$-2 \ln P(\mathbf{x}) = (\mathbf{x} - \mathbf{x}_a)^T \mathbf{S}_a^{-1} (\mathbf{x} - \mathbf{x}_a) + c_1 \quad \text{Equation 3.35}$$

$$-2 \ln P(\mathbf{y}|\mathbf{x}) = (\mathbf{y} - \mathbf{F}(\mathbf{x}))^T \mathbf{S}_y^{-1} (\mathbf{y} - \mathbf{F}(\mathbf{x})) + c_2 \quad \text{Equation 3.36}$$

where \mathbf{x}_a is the a priori mean state of \mathbf{x} , \mathbf{S}_a^{-1} is the inversion of the a priori covariance matrix and \mathbf{S}_y^{-1} is the inversion of the covariance matrix for the observational errors associated with \mathbf{y} . c_1 and c_2 are constants that are independent of the both the measured and retrieved variables.

$$\begin{aligned} -2 \ln P(\mathbf{x}|\mathbf{y}) &= (\mathbf{x} - \mathbf{x}_a)^T \mathbf{S}_a^{-1} (\mathbf{x} - \mathbf{x}_a) \\ &+ (\mathbf{y} - \mathbf{F}(\mathbf{x}))^T \mathbf{S}_y^{-1} (\mathbf{y} - \mathbf{F}(\mathbf{x})) + c_3 \end{aligned} \quad \text{Equation 3.37}$$

where c_3 now incorporates c_1 , c_2 and $P(\mathbf{y})$. The state of $\hat{\mathbf{x}}$ with the maximum probability is found by setting the derivative of Equation 3.37 to zero.

$$(\mathbf{S}_a^{-1} + \mathbf{K}^T \mathbf{S}_y^{-1} \mathbf{K}) \hat{\mathbf{x}} = \mathbf{S}_a^{-1} \mathbf{x}_a + \mathbf{K}^T \mathbf{S}_y \mathbf{y} \quad \text{Equation 3.38}$$

Rearranging for $\hat{\mathbf{x}}$

$$\hat{\mathbf{x}} = (\mathbf{S}_a^{-1} + \mathbf{K}^T \mathbf{S}_y^{-1} \mathbf{K})^{-1} (\mathbf{S}_a^{-1} \mathbf{x}_a + \mathbf{K}^T \mathbf{S}_y^{-1} \mathbf{y}) \quad \text{Equation 3.39}$$

This equation is the basic form on which the algorithm in this thesis is constructed.

3.7.2 Cost Function

The Bayesian approach allows the algorithm to improve upon the initial first guess surface parameters. However, the result of this simulation is unlikely to be the optimal estimation of the true parameters, due to the presence of non-linearity in the system. In order to improve the retrieved results multiple iterations are performed building upon the previous runs to reduce the residuals between the observed and simulated radiances with the a priori parameters considered. In this retrieval the cost function is a measure of the agreement between the retrieved parameters and the a priori parameters, and residual of the simulated and real radiances, and can be written:

$$C = (\mathbf{x} - \mathbf{x}_a)^T \mathbf{S}_a^{-1} (\mathbf{x} - \mathbf{x}_a) + (\mathbf{y} - \mathbf{F}(\mathbf{x}))^T \mathbf{S}_y^{-1} (\mathbf{y} - \mathbf{F}(\mathbf{x})) \quad \text{Equation 3.40}$$

The cost function as shown in Equation 3.40 returns one scalar value per iteration. For each iteration the current value of the cost function is compared to that of the previous iteration. The increase or decrease of the cost function is then evaluated on a basis unique to each retrieval so to assess whether any improvement has been made in this iteration step. The exact manner in which this value is calculated to determine the optimal estimate varies between different methodologies.

3.7.3 Newton Hessian Methodology

A common methodology for non-linear retrievals is the Newton Hessian. This methodology relies on the calculation of the Hessian ($\nabla \mathbf{g}$), the term from which the method derives its name.

$$\mathbf{x}_{i+1} = \mathbf{x}_i + \nabla \mathbf{g} \quad \text{Equation 3.41}$$

$$\nabla \mathbf{g} = \frac{dC}{dx} \quad \text{Equation 3.42}$$

The Hessian describes the change in cost function with regard to the change in the retrieved parameter. One run is performed and the cost function calculated, this value is then compared to the cost function of the next iteration. As long as the cost function

is being reduced, then the retrieved surface parameters of this iteration maybe used as the new input surface parameters for the forward model simulation. The forward model can then be run again, and assuming that the problem is not highly nonlinear this process can be repeated to find a minimum value of the cost function. The iteration can be written in the inverse Hessian form through the substitution of the cost function in Equation 3.39 into Equation 3.41:

$$\mathbf{x}_{i+1} = \mathbf{x}_i + (\mathbf{K}_i^T \mathbf{S}_y^{-1} \mathbf{K}_i + \mathbf{S}_a^{-1})^{-1} [\mathbf{K}_i^T \mathbf{S}_y^{-1} (\mathbf{y} - \mathbf{F}(\mathbf{x}_i)) - \mathbf{S}_a^{-1} (\mathbf{x}_i - \mathbf{x}_a)] \quad \text{Equation 3.43}$$

Here the new parameters are entirely dependent on the previous parameters modified by the current simulated Jacobians and radiance residuals.

3.7.4 Marquardt Levenberg Methodology

The Newton Hessian method aims to minimise the cost function to a value of zero, and because of this applies well to cases which are moderately non-linear, with a clear local minimum. However in cases where the situation may be distinctly non-linear, such as where there are more than one minima in the cost function this method may not reach the best result. An increase in the cost function may not always be detrimental to the retrieval as the movement away from the current minima may lead the retrieval to find a lower minima further from the starting point of the retrieval. Instead, in order to facilitate better identification of the true minima the Marquadt Levenberg methodology aims at finding the steepest descent in the cost function gradient.

$$\hat{\mathbf{x}} = \mathbf{x}_i + (\mathbf{S}_a^{-1} + \mathbf{K}_i^T \mathbf{S}_y^{-1} \mathbf{K}_i + \gamma \mathbf{D})^{-1} [\mathbf{K}_i^T \mathbf{S}_y^{-1} (\mathbf{y} - \mathbf{F}(\mathbf{x}_i)) - \mathbf{S}_a^{-1} (\mathbf{x}_i - \mathbf{x}_a)] \quad \text{Equation 3.44}$$

where γ is a scaling factor of arbitrary size, and \mathbf{D} is a scaling matrix to allow γ to be of the same dimension as \mathbf{S}_a^{-1} . In this case it is simplest to set \mathbf{D} equal to \mathbf{S}_a^{-1} .

$$\hat{\mathbf{x}} = \mathbf{x}_i + (\mathbf{K}_i^T \mathbf{S}_y^{-1} \mathbf{K}_i + \mathbf{S}_a^{-1} (1 + \gamma))^{-1} [\mathbf{K}_i^T \mathbf{S}_y^{-1} (\mathbf{y} - \mathbf{F}(\mathbf{x}_i)) - \mathbf{S}_a^{-1} (\mathbf{x}_i - \mathbf{x}_a)] \quad \text{Equation 3.45}$$

The premise of this methodology is that γ is selected for each iteration with the goal of minimising the cost function and thereby driving the retrieval towards the optimal solution. Therefore if an increase in the cost function is found, the run can be repeated with a larger gamma factor allowing greater movement in the system. Theoretically this methodology enables the retrieval to settle on a result other than the local minimum with a lower cost function.

3.7.5 Averaging kernels and gain matrices

In order to properly characterise the retrieval, two key quantities provide information on retrieval performance and influence error calculations: Averaging kernels and gain matrices.

Averaging kernels represent the sensitivity of the retrieval to the true state and can be written:

$$\mathbf{A} = \mathbf{G}_y \mathbf{K} = (\mathbf{S}_a^{-1} + \mathbf{K}^T \mathbf{S}_y^{-1} \mathbf{K})^{-1} \mathbf{K}^T \mathbf{S}_a^{-1} = \frac{d\hat{\mathbf{x}}}{d\mathbf{x}} \quad \text{Equation 3.46}$$

where \mathbf{G}_y the gain matrix.

The gain matrix for the retrieval is also known as the contribution function matrix and represents the effect on the retrieved parameters of the input, in this case the TOA radiance. For this algorithm the gain matrix can be represented as:

$$\mathbf{G}_y = (\mathbf{S}_a^{-1} + \mathbf{K}^T \mathbf{S}_y^{-1} \mathbf{K})^{-1} \mathbf{K}^T \mathbf{S}_y^{-1} = \frac{d\hat{\mathbf{x}}}{d\mathbf{y}} \quad \text{Equation 3.47}$$

3.7.6 Error Analysis

Errors in optimal estimation retrievals can be classified into four principal sources: The smoothing error, model parameter error, forward model error and the retrieval noise error. In order to properly quantify these errors there are several key parameters to define.

3.7.6.1 The smoothing error

The smoothing error refers to the error induced through the loss of high resolution structure in the retrievals due to the limitations of the observations relative to the a priori. As the true values of the retrieved states are not known, aside from validation studies, the smoothing error arises from the practice of likening the retrieved state estimation to the true state value rather than the reality, which is that the retrieved state is being compared to a smoothed true state value:

$$\mathbf{S}_s = (\mathbf{A} - \mathbf{I}_n)\mathbf{S}_a(\mathbf{A} - \mathbf{I}_n)^T \quad \text{Equation 3.48}$$

where \mathbf{I}_n is an identity matrix of the same dimensions as the covariance matrix. This is the contribution of instrument sensitivity plus a priori smoothing in the a priori covariance matrix.

3.7.6.2 The retrieval noise error

The retrieval noise error is a conceptually straight forward error encapsulating the random errors associated with the retrieval. It generally possesses no correlation between the various channels and does not typically encompass intrinsic bias.

$$\mathbf{S}_m = \mathbf{G}_y\mathbf{S}_y\mathbf{G}_y^T \quad \text{Equation 3.49}$$

3.7.6.3 The model parameter error

The model parameter error describes the error associated with differences between the non-retrieved model parameters and the ideal input estimates which would perfectly describe the system. For example; a model parameter could be atmospheric

water vapour: the difference between the estimated water vapour profile inputted into the model and the true profile associated with the retrieved state will be represented in the model parameter error.

$$\mathbf{S}_f = \mathbf{G}_y \mathbf{K}_b \mathbf{S}_b \mathbf{K}_b^T \mathbf{G}_y^T \quad \text{Equation 3.50}$$

This quantity can be calculated through the calculation of the Jacobians of each atmospheric factor included in the simulation.

3.7.6.4 The forward model error

The forward model error commonly refers to a systematic error associated with the model's ability to accurately describe the physics of the system being simulated. Any error in the simulation made by the model's inevitable physical approximations and simplifications from the true physical system will be represented in this term.

$$\mathbf{G}_y \Delta \mathbf{F}_{True} = \mathbf{G}_y [\mathbf{F}_{True}(\mathbf{x}, \mathbf{b}, \mathbf{b}') - \mathbf{F}(\mathbf{x}, \mathbf{b})] \quad \text{Equation 3.51}$$

where \mathbf{F}_{True} are the brightness temperatures produced using the a forward model which perfectly represents the true physic of the system, and \mathbf{b} are the model parameters not included in the state vector, such as methane of carbon dioxide gases. The forward model error can be assessed in the RTTOV radiative transfer model can be assessed through comparison with the RFM line-by-line model.

3.7.6.5 Retrieved covariance matrix

The retrieved estimate itself requires some metric of the quality of the result. The matrix for covariance of the retrieved state represents the sum total of our knowledge about accuracy of the retrieved values. Substituting Equation 3.46 into Equation 3.48 gives

$$\mathbf{S}_s = (\mathbf{S}_a^{-1} + \mathbf{K}^T \mathbf{S}_y^{-1} \mathbf{K})^{-1} \mathbf{S}_a^{-1} (\mathbf{S}_a^{-1} + \mathbf{K}^T \mathbf{S}_y^{-1} \mathbf{K})^{-1} \quad \text{Equation 3.52}$$

which when added to Equation 3.47 gives the total error from these two sources:

$$\hat{\mathbf{S}} = (\mathbf{S}_a^{-1} + \mathbf{K}^T \mathbf{S}_y^{-1} \mathbf{K})^{-1} \quad \text{Equation 3.53}$$

This term is the covariance matrix of the retrieved result and is the same as the pdf ($P(\mathbf{x}|\mathbf{y})$). The retrieval uncertainty is commonly taken to be the diagonal elements of this matrix. However, care must be taken not to ignore the off-diagonal elements as they may contain correlations showing a level of inter-dependence in the retrieved uncertainty.

3.8 Previous Optimal Estimation Algorithms for LST

There have been several studies to use optimal estimation in the retrieval of surface temperature using optimal estimation, including Sea Surface Temperatures (SST) (MacCallum & Merchant, 2012), and LST (Liang, Goward, Ranson, Dubayah, & Kalluri, 1995). A study by Comyn-Platt, (2014), devised an optimal estimation scheme which was used with AATSR and Spinning Enhanced Visible and Infrared Imager (SEVIRI) data to retrieve LST. This method was given a full diagnostic evaluation and found that under the condition of a known emissivity surface this method compared favourably with existing split window methods.

There have been simulated studies looking into the development of an LSE and LST retrieval using optimal estimation. A study by Matsumoto-Moriyama and Arai, (1994), investigated the use of optimal estimation on a simulated ASTER band before the launch of ASTER in 1999. Their study found that the theory was highly promising and could even potentially be useful in accounting for the atmospheric influences by retrieving water vapour. However, they found that the retrieved LST, at the expected NEAT of 0.3 K, resulted in high LST errors with an RMSE of 2.23. The study also used broad LSE covariance allowing potentially any value of LSE between 0 and 1. This study did not move beyond simulation; and to the best knowledge of the author did not move beyond a limited simulated study.

Liang (2001), investigated an algorithm that was suitable for multi spectral radiometers that could be utilised with an instrument such as MODIS or ASTER, but

was designed to be generally applicable. The study assessed a wide variety of LSE types and was successful in retrieving LSE in simulation with various atmospheres, using an empirical method to fit the a priori LSE based on the channel radiances. This method shares a common assumption with TES; it assimilated surface leaving radiances as its observations, assuming an accurate atmospheric correction had already been successfully applied. Based on these assumptions, simulation were able to retrieve LST to 1 K in the majority of cases with outliers within ± 4 K.

The algorithm developed within this thesis aims to expand upon the knowledge in the field of LST and LSE retrievals. This thesis represents the first concerted effort to retrieve these parameters for real ASTER data in an optimal estimation scheme. Further to this the algorithm designed here aims to work not with the surface leaving radiances but with the TOA radiance and to correct for the atmospheric effect within the retrieval. Additionally this algorithm uses the a priori knowledge of the surfaces to create variable LSE covariance to allow the retrieved result flexibility, whilst maintaining a high precision in the returned uncertainty.

3.9 Summary

In this Chapter the underlying physics of the radiative transfer has been outlined as well as the theory behind the retrieval of LST from forward models. RTTOV will be used moving forward in this thesis given the demands of computational time and the relative insignificance of many of the trace gases included in a line-by-line method, due to the lack of sensitivity in the ASTER bands.

The split-window methodology was explored as the traditional method by which LST is retrieved in a number of data products. One of which, from MODIS, will be described in Chapter 3 as it will provide a key component of the a priori input the retrieval developed in thesis.

The existing ASTER TES algorithm was described and the uncertainties addressed, finding an average LSE uncertainty of 0.015 but with poorer performance over the urban materials showing a bias towards higher LSE and an RMSE of 0.025.

In particular the theoretical basis of optimal estimation and the Bayesian methodology has been described. This OE scheme is based upon the methodology of Rodgers, (2000). This OE scheme will form the basis of the algorithm developed in Chapter 4 of this thesis and will be used in all subsequent results. Successful use of the OE methodology to simultaneously retrieve LST and LSE from ASTER data would provide a key step forward in providing robust and high spatial resolution data to use in investigation of the urban environment.

4 Retrieval Development

4.1 Introduction

In order to fulfil the requirements for studies of heat within the urban environment outlined in Chapter 1, data for both LST and LSE is needed. To do this effectively from remote sensing observations a retrieval is required that can simultaneously obtain the LST and the LSE over whole scene. In this Chapter an OE retrieval is developed based on this requirement, and tested for a full range of materials to demonstrate suitability for urban applications.

4.2 Algorithm formulation

The algorithm developed in this thesis utilises the five thermal channels of the ASTER instrument on the Terra satellite operating at 90 m resolution, as described in Chapter 2. The retrieval algorithm is based upon the optimal estimation methodology of Rodgers, (2000) see Chapter 3, with the intention of testing whether this method can obtain more robust and representative LST and LSE data for urban areas, where complex and variable structures exist. In this context it is important that the products of the retrieval are well characterised, which optimal estimation achieves.

4.3 Initial Processing

The a priori parameters of the retrieval represent the best understanding of the physical variables that are available prior to the retrieval. These parameters are often, but not always, utilised as the first guess used in the first iteration of the optimal estimation run. For the purposes of the algorithm described in this chapter the a priori parameters will be the same as the retrieval first guess.

4.3.1 A priori parameter determination

In the initial concept for the retrieval algorithm six parameters were selected to be retrieved based upon the channels available from ASTER TIR. The six parameters are; the LST which, is spectrally consistent across the five ASTER TIR channels, and five LSE values, one for each of the TIR channels. The LST a priori values for this methodology are drawn from the MODIS MOD11 L2 LST dataset described in Chapter 2. This product is spatially and temporally coincident with the ASTER TIR data, but is at 1 km spatial resolution and therefore each ASTER pixel must be matched to the appropriate MODIS pixel at the same geographical location.

The a priori LSE values are more complicated to determine. The MODIS MOD11 L2 data is provided with accompanying LSE data, but this is a pre-determined biome dependent dataset and is not actively retrieved. Due to this and the heterogeneous nature of the urban environment, for which a 1 km pixel at one wavelength may not be representative, a classification approach was adopted instead. Given scene analysis and classification a pre-calculated set of LSEs linked to that classification could be used as the a priori input.

The pre-calculated LSE values were derived by applying ASTER channel spectral responses to the relevant reference data in the ASTER spectral library, such as the example shown in Figure 15. All the materials present in the library were grouped into three categories: urban, rock/soil and vegetation. These materials were then analysed and their mean and standard deviations calculated. Subsequently a fourth and fifth category were added: urban-vegetation mix and rock/soil-vegetation mix. The additional categories were designed to create more flexible classes which could be applied to regions in which the blend of urban and vegetation or rock/soil and vegetation is such that a discrete distinction is a poor descriptor, such as large suburbs and the fringes of the urban environment.

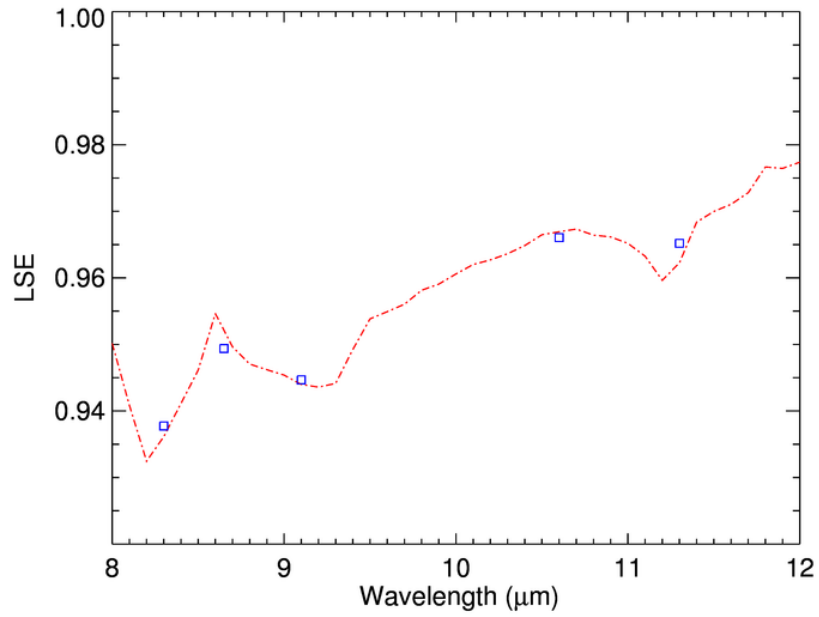


Figure 15 – Example of LSE spectra from the ASTER spectral library. The material is asphalt, the red dashed line is the LSE at the library resolution, and the blue squares denote the values calculated for the ASTER TIR bands using the instrument spectral response function.

Classification	A priori LSE				
	Channel	Channel	Channel	Channel	Channel
	10	11	12	13	14
Urban	0.925	0.923	0.902	0.952	0.956
Rock/Soil	0.912	0.924	0.917	0.964	0.967
Vegetation	0.981	0.981	0.977	0.965	0.965

Table 10 – The a priori LSE values for LSE in four classes. Values determined from the mean of all materials in each class drawn from the ASTER spectral library. These classification based LSEs are applied in all of the retrieval methodologies used in this thesis.

The LSE values shown in Table 9 are for the three basic classes. For the two additional classes for the mixed pixels, a blended a priori LSE was calculated, using the Normalised Differential Vegetation Index (NDVI). Firstly the NDVI was calculated using the TOA reflectance's in the ASTER VNIR bands, see Equation 4.1.

$$NDVI = \frac{VNIR\ Band\ 3 - VNIR\ Band\ 2}{VNIR\ Band\ 3 + VNIR\ Band\ 2} \quad \text{Equation 4.1}$$

The NDVI uses the ratio between the spectral response of chlorophyll in the visible and the spectral response of the structure of the plant in the near-infrared to infer the level of vegetation in the pixel. The NDVI index provides a mean by which to weight the amount of vegetation to rock/soil or urban in the pixel and hence derive an a priori LSE. The resulting means for the LSE in each ASTER TIR channel for each classification were utilised as the a priori LSE data for the retrieval.

4.3.2 A priori covariance determination

The a priori LST and LSE parameters all require covariance to determine the constraints applied to the retrieval. There are multiple approaches to isolating the optimal a priori covariance, three of which were explored in the development of this algorithm.

The first method and simplest investigated was to use only two values; a covariance for LST and one covariance for all LSEs. A number of simulations were conducted varying the a priori covariance for LST and LSE which was then analysed to find the optimal configuration, see Figure 16.

As Figure 16 shows, the LST a priori covariance could vary significantly without an increase in retrieved uncertainty at low LSE covariance. The LST a priori covariance was found to allow a range of values from 2-5 K with no significant decrease in performance, as the sensitivity to the true surface is high for the LST. Therefore a value of 5 K was selected for LST covariance to give the retrieval the most flexibility to adapt to situations where the prior data poorly represents the truth, whilst maintaining the expected LST precision.

Small changes to the LSE priors had significantly greater impact on the retrieved uncertainties. The retrieval aimed to match the LST uncertainty of the medium resolution sensors at ± 1 K so therefore the LSE a priori covariance was selected to be ± 0.05 to maintain this. This approach is called the “fixed LSE method”.

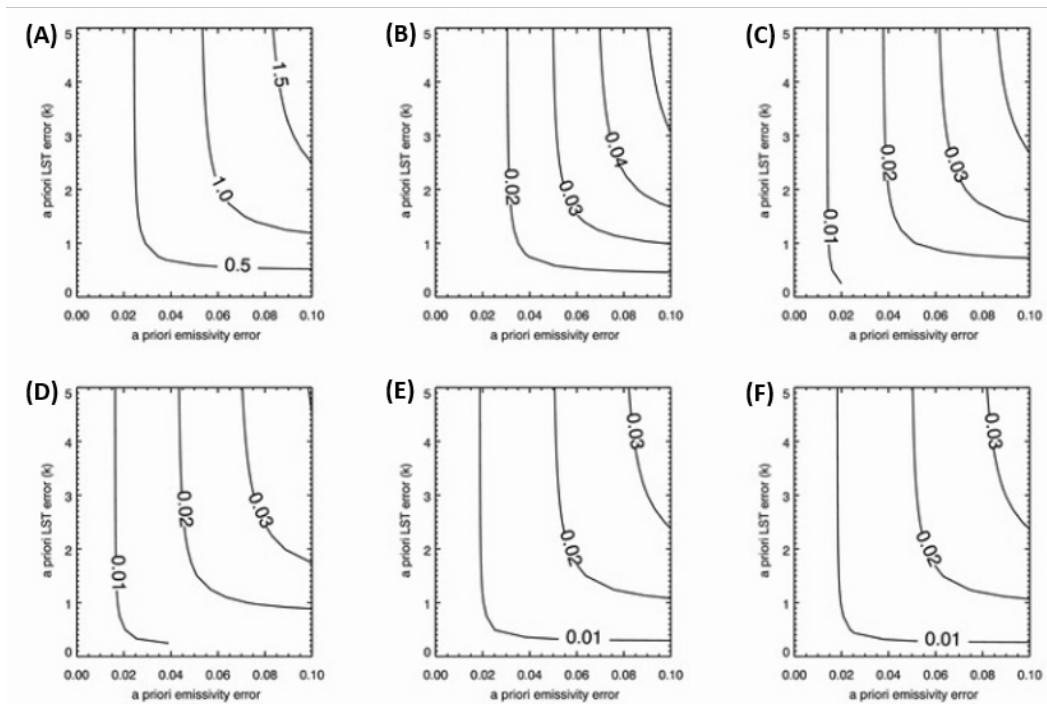


Figure 16 – Plot showing the variation in retrieved LST and LSE uncertainty (contours) with the input a priori parameters. (A) Shows the effect of the a priori LST and LSE on the retrieved LST uncertainty. (B-F) Shows the effect of the a priori LST and LSE on the retrieved LSE uncertainty in Channels 10-14 respectively.

After analysis of the spectral variance of the LSE for materials in the ASTER spectral library, a second approach was attempted. Analysis of the ASTER spectral library showed that five channels did not experience the same degree of variability in LSE across a wide range of materials. To account for this each retrieval was assigned a covariance based upon the land classification categories listed in Table 10. The covariance was set to the standard deviation of each material classification, as shown in Table 11.

Classification	A priori LSE covariance				
	Channel	Channel	Channel	Channel	Channel
	10	11	12	13	14
Urban	0.058	0.052	0.059	0.016	0.012
Rock/Soil	0.041	0.048	0.064	0.021	0.016
Vegetation	0.013	0.007	0.010	0.034	0.037

Table 11 – The a priori covariance values for LSE in four classes. Values determined from the standard deviation of all materials in each class drawn from the ASTER spectral library. This covariance is applied in the “ASTER Spectral library” method and the “ASTER spectral library with off-diagonal covariance method”.

The mixed pixels had covariance assigned by the same methodology used to calculate the a priori values utilising the weighting from the NDVI. This approach was called the “ASTER spectral library method”.

In producing the spectrally variable LSE covariance for each channel, degrees of covariance between the LSEs in each channel were observed. Particularly notable is the covariance between the channels based upon their grouping spectrally. As shown in Chapter 3 the TIR channels are grouped with Channels 10, 11 and 12 overlapping and bands 13 and 14 overlapping. This grouping structure was observed in the analysis of the materials from the ASTER spectral library. Therefore a third approach was constructed adding off diagonal covariance to the a priori covariance matrix.

$$S_a = \begin{bmatrix} T & 0 & 0 & 0 & 0 & 0 \\ 0 & \epsilon_{10} & *_{11}^{10} & 0 & *_{13}^{10} & *_{14}^{10} \\ 0 & *_{11}^{10} & \epsilon_{11} & 0 & *_{13}^{11} & *_{14}^{11} \\ 0 & 0 & 0 & \epsilon_{12} & 0 & 0 \\ 0 & *_{13}^{10} & *_{13}^{11} & 0 & \epsilon_{13} & *_{14}^{13} \\ 0 & *_{14}^{10} & *_{14}^{11} & 0 & *_{14}^{13} & \epsilon_{14} \end{bmatrix} \quad \text{Equation 4.2}$$

Equation 4.2 shows the location of the off-diagonal elements within the a priori covariance matrix as the red asterisk, the two numbers list the channels linked by this covariance. The size of these values varies with $*_{14}^{13}$ and $*_{11}^{10}$ showing very high correlation 0.94 and 0.86 respectively. Channel 12 is the only channel not to include any off-diagonal covariance as the emissivity of this channel as there were no correlations found between the urban, mix and rock/soil classifications tested. This approach was called the “ASTER spectral library with off-diagonal covariance method”.

4.4 Convergence strategy

As described in Chapter 2 a Marquardt-Levenberg scheme finds a more robust convergence routine for non-linear systems than the Newton-Hessian LST/LSE retrieval. Tests showed a high failure rate for the retrieval using the Newton-Hessian method. The introduction of the gamma factor allowed the algorithm the flexibility to move towards solutions of true rather than local minima. However the Marquardt-Levenberg methodology requires a manual fine-tuning of both the value of gamma used and the thresholds for updating the cost function. The basic strategy for the iterations as given by Press et.al (1995) states two principal rules:

- If cost function increases as a result of the iteration, increase the value of γ and do not accept the new values for x
- If the cost function decrease,s decrease the value of γ and accept the new values for x

This strategy is effective at reducing the cost function and driving the retrieval towards convergence. However it has no definite end criteria. The iteration will be repeated as long as there is a change in value of the cost function, which, could result in excessively long processing time with little or no improvement in the dataset produced.

In order to allow convergence within a sensible number of iterations without removing any cost function reductions of numerical significance the strategy was adapted through extensive testing to include a further restriction.

- If the cost function increases, increase γ and don't accept the new value for x
- If the cost function decreases and change in the cost function is greater than 3% of the value of the cost function, decrease γ and accept the new value for x
- If the cost function decreases and change in the cost function is less than 3% of the value of the cost function, accept the value for x and end the iterations

This functionality will always allow significant reductions in the cost function driving the retrieval to a minima; however it will not continue to iterate once the

reductions in the cost function are providing negligible gain. The value of 3% stated here was determined experimentally through simulations of identical algorithm runs with varying cut off thresholds. It was the lowest value found to reliably limit the number of iterations without significantly (more than 0.0001 K) effecting change on the retrieved result.

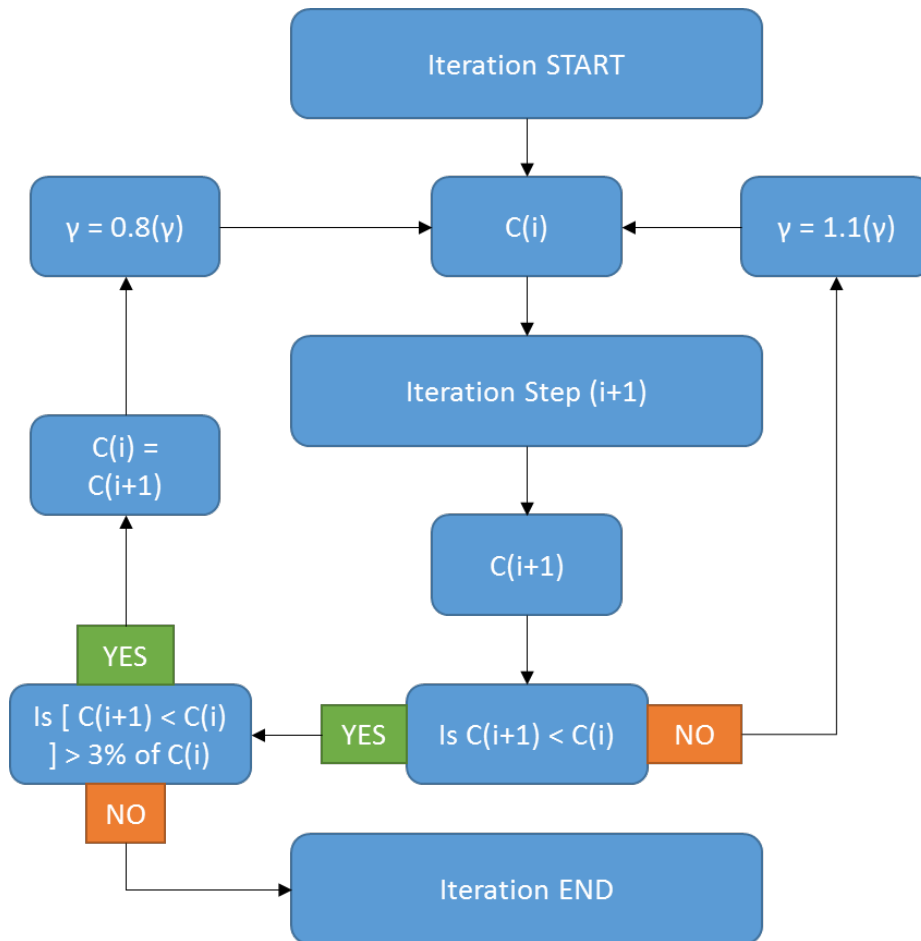


Figure 17 – Flow chart diagram for the cost function strategy utilised in the retrieval. C represents the cost function in this diagram.

The value of gamma used was also established through iterative simulation. The optimal initial value of gamma estimated was 10. This value enabled the first step of the iterative process to be close to, but still slightly relaxed from, the Newton-Hessian methodology. In the event that the retrieval results in an increase in the cost function, gamma will be increased by 10 leading to a method of steepest descent optimal estimation. The iterative cost function strategy is shown in Figure 17. Upon arriving

at a reduction in the cost function the value of gamma will reduce by 0.2 returning the system to a closer approximation of the Newton-Hessian methodology. The variation in step size when increasing gamma was selected to minimise the number of iterations for which gamma would need to be increased before finding a new minima, whilst the smaller reduction ensures that the minima is less likely to be overshoot in the iteration.

4.5 Simulated surface parameter retrieval

Simulations were conducted implementing the three different a priori LSE covariance approaches to the same data set. In every case the atmospheric parameters were the same and the a priori atmospheric information was set to be the truth in order to purely test the algorithms ability to retrieve the surface parameters.

4.6 MODIS spectral library testing

Testing the ability of the retrieval to adapt and retrieve surface parameters from a wide variety of material types required a large data set independent of the one used to construct the retrievals prior estimates. The MODIS spectral library has over 116 materials across a broad range of structures and compositions including a significant number which fall within the classifications set up in Table 10. Each material was used to generate simulated ASTER TIR TOA radiances with an LST of 295 K and the same mid-latitude atmospheric parameters from the ECMWF ERA-Interim reanalysis for the Algodones and Phoenix Arizona (Dee et al., 2011). These radiances would then be used as the instrument observations and their generating parameters as the truth data set. In these cases the atmosphere is fixed and perfect knowledge of the atmosphere is assumed, atmospheric influences are considered later in this chapter.

4.6.1 Fixed LSE covariance

The “fixed LSE method” showed generally poor retrieved values across the majority of samples. The poor trueness and accuracy is apparent when analysing the materials individually. Figure 18 shows four materials used in the simulated retrievals: one bare soil, one vegetation and two different urban materials. In each case the a priori covariance is the same (the light green region) and the truth is displayed as the orange line. The retrieved values are displayed as the dark purple line with the corresponding uncertainty from the covariance matrix represented by the lighter purple region around it. For all sample the a priori and true LST values were 295 K, and the retrieved LST is displayed at the top of each material panel.

The first sample is sand from Goleta beach California. This sample was selected for further analysis as it shows significant deviation from the mean LSE values in the bare soil/rock classification and should test the retrieval’s ability to adapt to situations where the priori information is a poor descriptor of the truth.

The second sample is Laurel. This is a deciduous green leaved plant commonly found around Mediterranean regions but possessing foliage common to many plants round the world making it a good generic marker for the retrieval performance for high LSE vegetation.

The final two samples are two urban materials, red masonry and tan brick work representing a test of the algorithm’s suitability for urban areas. These two are in the same classification but have different spectral LSEs and allow insight of the retrieval’s flexibility within the same a priori classification.

The Goleta sand sample shows significant issues immediately. The retrieved LSE values in channels 10, 11 and 12 are over 0.15 higher than the truth and the retrieved LST is over 4.2 K offset from the truth.

Even the LSEs in channels 13 and 14, which are far closer to the truth, are offset to higher values. This is indicative of the retrieval settling in a false minima, where the lack of appropriate a priori constraint has allowed the retrieval to converge to a mathematically valid but physically incorrect set of parameters.

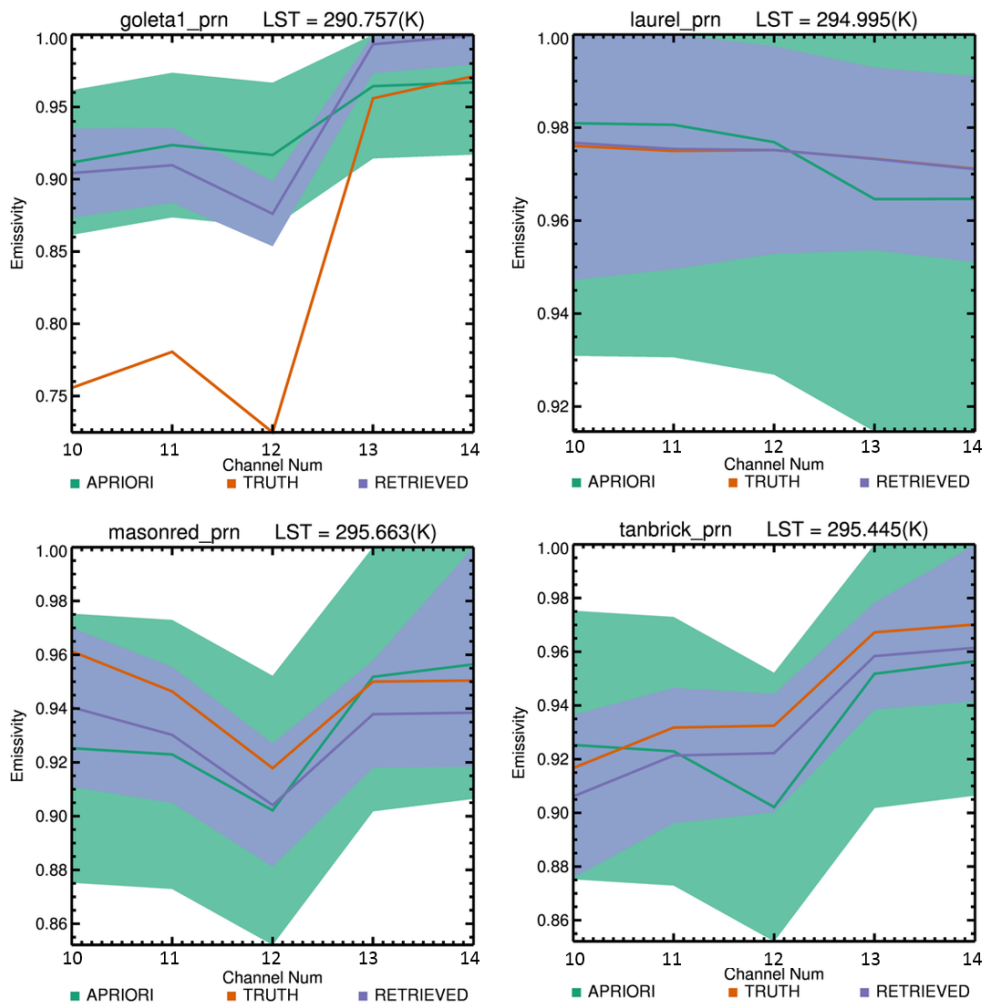


Figure 18 - Sample retrievals for Goleta sands (bare soil), laurel trees (vegetation), red masonry (urban) and tan brickwork (urban) materials in the MODIS spectral library using the fixed a priori LSE approach.

The laurel sample shows very different behaviour. The retrieved result is an extremely good match to the truth in both the LSE and the LST. However the large a priori covariance has a consequence in that the retrieved uncertainty is also very large, despite the good trueness of the result.

The urban materials show the retrieval has the desired ability to adapt to different LSE spectral shapes from the same a priori starting point. There is however, a small but systematic underestimation of the LSE in all channels and a corresponding over estimate of the LST. The tan brick sample shows substantially different LSE spectral shape to that to the a priori data. The average LSE values used to construct the a priori data describe the urban sample as having a lower LSE value in channel 12; however, in this sample the spectral shape is notably different. The retrieval is shown

here to not only scale the component of the a priori data to the truth as is the case in the red masonry sample, but to entirely change the relative strengths of the retrieved LSEs away from the a priori values toward the truth.

4.6.2 ASTER spectral library derived covariance

The results of the ASTER spectral library methodology, utilising a priori covariance data calculated from the ASTER spectral library, can be seen in Figure 19.

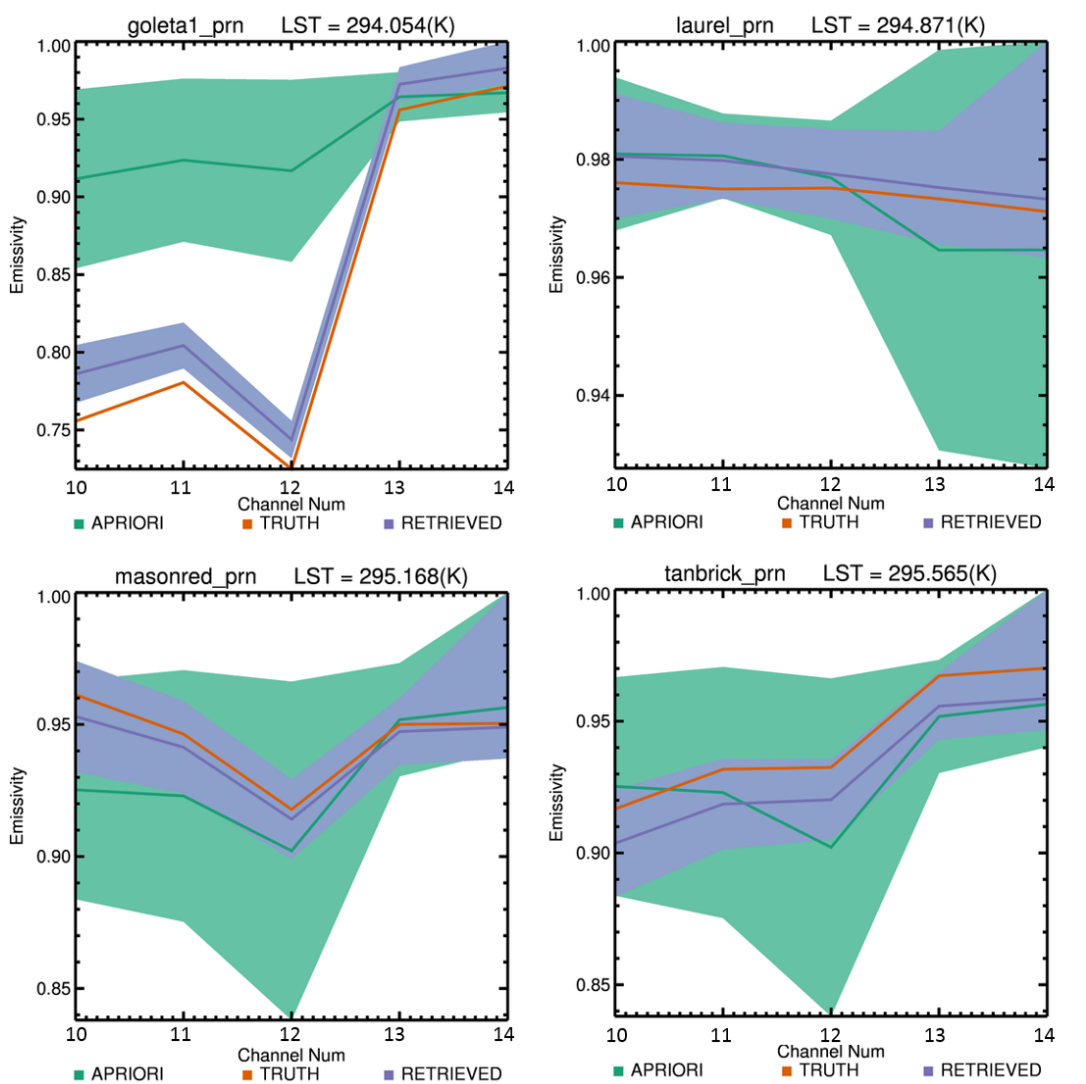


Figure 19 - Sample retrievals for Goleta sands (bare soil), laurel trees (vegetation), red masonry (urban) and tan brickwork (urban) materials in the MODIS spectral library using the a priori LSEs determined from the mean class values from the ASTER spectral library.

The Goleta sand sample shows a dramatic reduction in the offset between the retrieved LSEs and the truth. Where previously the retrieved data had only a small degree of movement from the a priori state and was substantially offset from the true values in Figure 18, the retrieval now has been able to deviate significantly away from the priori, converging on LSEs which better represent the true state. Additionally the retrieved LST is now close to the true value showing an improvement on the fixed a priori covariance method of nearly 4 K. The uncertainties in the LSE are also reduced now.

The laurel sample in Figure 19 shows a marked departure from the a priori LSEs, particularly in channels 13 and 14, however the offset between the retrieved and true values is larger than those shown in Figure 18 for the fixed covariance approach. While the trueness of the retrieved result is poorer the reduced uncertainty allows the retrieved result to be used with far greater confidence than the previous approach when dealing with situations in with the true value is not already known.

The urban materials also have a reduction in the associated uncertainty for the retrieved LSEs. The retrieved LSEs themselves are relatively unchanged in the tan brick sample and marginally improved in the red masonry sample.

Overall the samples highlighted in Figure 19 combined with the improvement in the correlations seen in Figure 21 point to the ASTER spectral library derived covariance being an improvement in the majority of cases, with a substantial improvement in the retrieved results for materials with large LSE spectral contrast between the various channels such as the Goleta sands sample. However, there still exists a noticeable offset (approximately 0.03) between the retrieved and true values in channels 10, 11 and 12 in samples with low LSEs such as the Goleta sands.

4.6.3 ASTER spectral library derived covariance including off-diagonal channel variance

The ASTER spectral library with off-diagonal covariance method shows further improvement in the retrieved results from the simulations, see Figure 20. The

retrieved results have the greatest precision with a reduced uncertainty for both LST and LSE across all the channels.

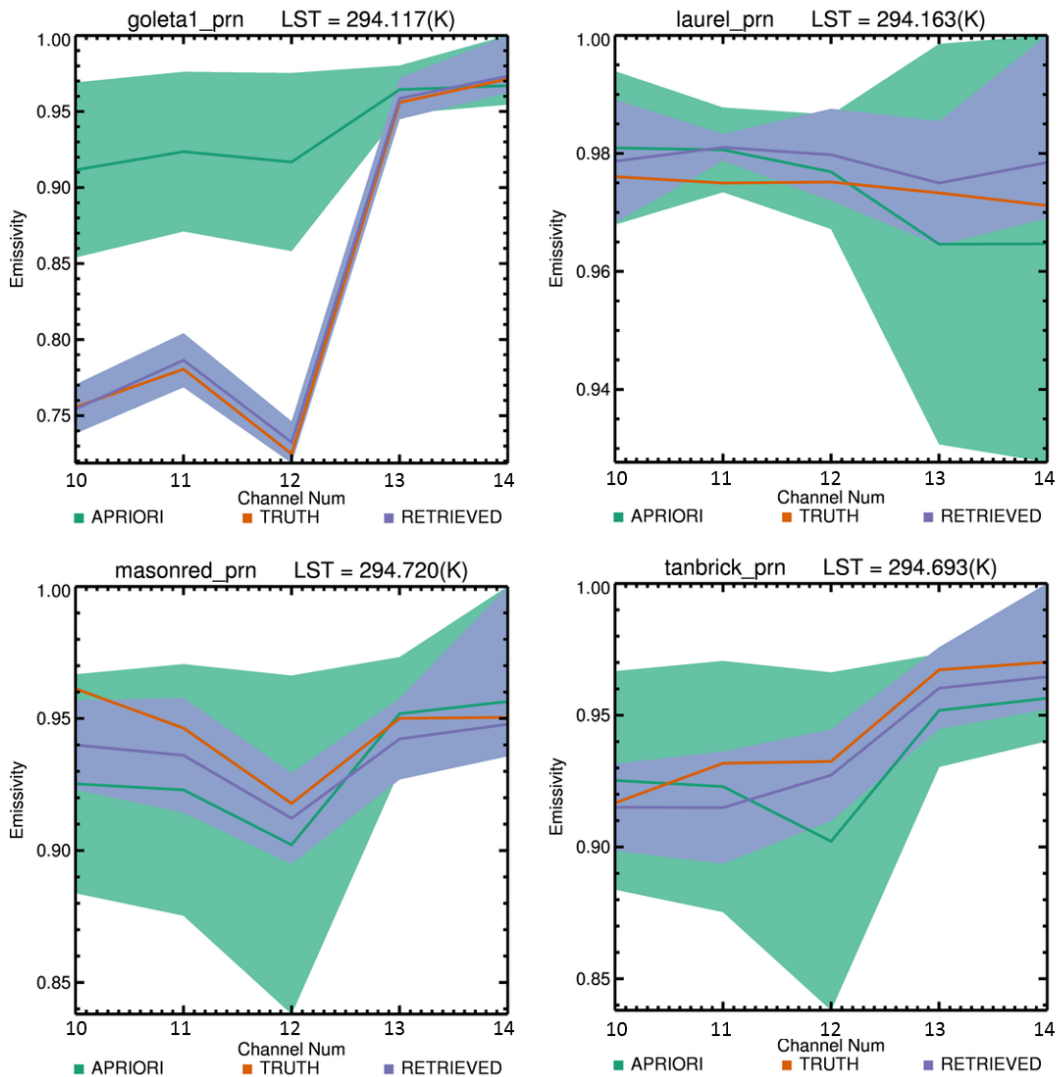


Figure 20 - Sample retrievals for Goleta sands (bare soil), laurel trees (vegetation), red masonry (urban) and tan brickwork (urban) materials in the MODIS spectral library using the a priori LSEs determined from the mean class values from the ASTER spectral library with the inclusion of the off-diagonal LSE covariance.

Furthermore the Goleta sands sample shown in Figure 20 displays a large reduction in the offset between the retrieved and true LSE values, whilst maintaining a well constrained uncertainty.

The laurel sample conversely shows a reasonable trueness in channels 12 and 14 with a maximum difference of 0.008, and an overly constrained uncertainty in channel 11, showing little information gain. The urban materials show only a small net change across the channels with small increases in the trueness in channels 12, 13 and 14

and small decreases in channels 10 and 11. The overall ability to move from the a priori toward the true values remains consistent.

4.6.4 Summary of methodologies

The correlation between the retrieved and true LSE values improves significantly from method 1 to method 3. In channels 13 and 14, the improvement is limited by the small variation in the emissivities found for the materials at these wavelengths, see Figure 21.

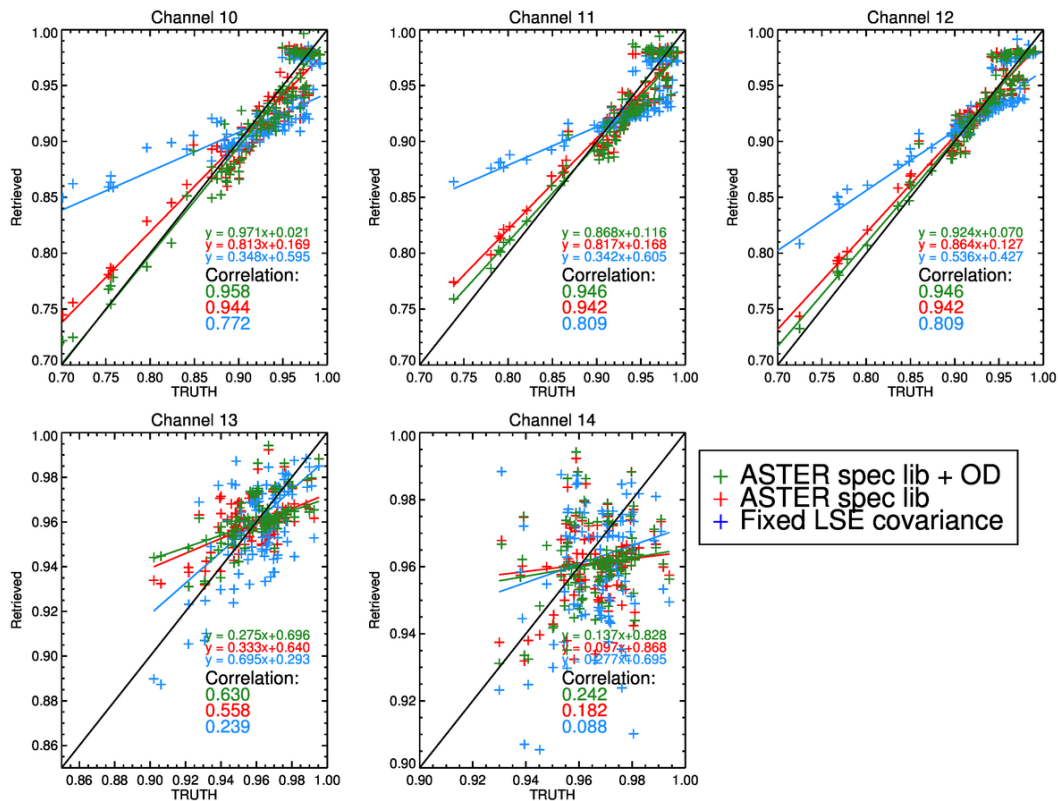


Figure 21 - Correlation plot for LSE in each of the ASTER TIR channels (10-14) comparing the retrieved and true values for three different a priori set-ups.

The “fixed prior LSE method”, as shown by the blue data in Figure 21, has the worst performance observed in the simulations. In this approach the correlation between the true and retrieved parameters for each channel across all materials is the lowest of the applied methods. The correlations are particularly poor in channels 13 and 14 where the a priori covariance of 0.05 is significantly greater than the ASTER spectral library derived values as shown in Table 11. Channels 13 and 14 have not only low

accuracy but also very poor precision, with a large spread in the agreement of the results in these channels suggesting a lack of robustness in the retrieval process.

The “ASTER spectral library method” shows greatly improved performance. These results have significantly higher correlations between the true and retrieved LSE values, especially in channels 10 and 13. This increase in correlation is also immediately visible in the samples seen in Figure 19.

The “ASTER spectral library with off-diagonal covariance method”, as shown by the green points in Figure 21, has the best correlation between the retrieved and true values, in channels 13 and 14 in particular. Notably not only is the trueness of the results good but the precision of the results is far higher than that of the other two methods, with a far smaller spread seen in the data.

		LST Uncertainty (K)		
		Smooth	Noise	Total
ASTER Spectral Library with Off-diagonal covariance	Urban	0.373	0.826	0.906
	Bare Soil	0.542	0.915	1.064
	Vegetation	0.593	0.650	0.880
ASTER Spectral Library	Urban	0.174	0.691	0.713
	Bare Soil	0.195	0.575	0.607
	Vegetation	0.198	0.256	0.323
Fixed prior uncertainty	Urban	0.153	1.140	1.150
	Bare Soil	0.153	1.140	1.150
	Vegetation	0.153	1.140	1.150

Table 12 – Summary statistics for the uncertainty contributions to each of the methods tested.

Table 12 shows the uncertainty breakdown for the different methodologies explored in this chapter. Both the ASTER spectral library methods perform well with uncertainties of around 1 K or lower for this idealised situation. The fixed priori uncertainty is consistently the poorest performer with uncertainties above 1 K.

		Reduction in uncertainty from a priori (Ret/Prior)					
		LST (K)	E 1	E2	E3	E4	E5
ASTER Spectral Library with Off-diagonal covariance	Urban	0.181	0.509	0.443	0.284	0.714	0.780
	Bare Soil	0.213	0.458	0.449	0.363	1.084	1.171
	Veg	0.176	1.160	3.739	1.327	0.383	0.401
ASTER Spectral Library	Urban	0.143	0.428	0.339	0.231	0.564	0.678
	Bare Soil	0.121	0.278	0.272	0.223	0.648	0.740
	Veg	0.065	0.676	0.849	0.701	0.215	0.187
Fixed prior uncertainty	Urban	0.230	0.652	0.514	0.351	0.900	1.116
	Bare Soil	0.230	0.469	0.467	0.384	1.219	1.453
	Veg	0.230	2.079	3.420	2.322	0.569	0.489

Table 13 – Summary of the reduction in the retrieved uncertainty from the a priori estimates (Ret/Prior).

Likewise the fixed methodology shows the smallest decrease in uncertainty between the a priori and the retrieved, see Table 13. This parameter is used as an indication of the skill of the retrieval, and therefore shows little skill in the fixed methodology. Here it is apparent that on average the ASTER spectral library with off-diagonal covariance has both a lower skill and a slightly larger uncertainty than the ASTER spectral library method.

The retrieval averaging kernels, shown in Table 14, show a high sensitivity to the true LST in all methods, with the fixed priori uncertainty again showing the least sensitivity. Interestingly the LSE sensitivity is high for channels 10, 11 and 12 for urban surfaces, and high in 13 and 14 for vegetation surfaces. This pattern matches the variability of the spectral emissivity for these material types.

Based on the trace of the averaging kernels the degrees of freedom (DOF) for the method can be found.

		Averaging Kernel					
		LST	E1	E2	E3	E4	E5
ASTER Spectral Library with Off-diagonal covariance	Urban	0.97	0.52	1.33	0.92	0.61	-0.34
	Bare Soil	1.02	1.31	1.42	1.05	-0.92	-0.02
	Veg	1.00	0.52	-1.86	0.84	1.29	0.74
ASTER Spectral Library	Urban	0.98	0.82	0.89	0.95	0.68	0.54
	Bare Soil	0.99	0.92	0.93	0.95	0.58	0.45
	Veg	1.00	0.54	0.28	0.50	0.95	0.97
Fixed prior uncertainty	Urban	0.95	0.71	0.76	0.80	0.85	0.87
	Bare Soil	0.95	0.71	0.76	0.80	0.85	0.87
	Veg	0.95	0.71	0.76	0.80	0.85	0.87

Table 14 – Averaging Kernels for each of the methodologies. Broken down by material type.

ASTER Spectral Library with Off-diagonal covariance has a DOF of 3.5, the ASTER Spectral Library has 4.6 and the fixed methodology has 4.9. As a measure of the number of pieces of information that can be extracted in a retrieval, the lower DOF in the off-diagonal case is due to the introduction of strong correlations between the retrieved parameters. The DOF of ~1 for LST is however misleading as the LSE and LST are highly coupled with correlations consistently above 0.8.

Overall the ASTER spectral library a priori covariance has the highest correlation between the retrieved and true parameters across the full range of LSEs. There are instances where the fixed covariance approach yields a truer retrieved value but at the cost of a much larger uncertainty in the retrieved result, LSE values are typically offset from the truth by 0.01 in most simulations. The overwhelming majority of the retrievals utilising the off-diagonal covariance to obtain LSTs with both errors and uncertainties of less than 1 K which meets the initial criteria for performance with the medium resolution LST retrievals, outlined in chapter 1. Channel 14 has the least sensitivity and Channel 12 shows the greatest sensitivity to the LSE and the highest consistent performance across the simulations.

The ASTER spectral library without the off-diagonal covariance does have lower uncertainty and a greater reduction in the uncertainty from the a priori, however the ability to of the last approach to converge to the true LSEs in cases where the true LSE is very low or significantly offset from the a priori lends a generic applicability

which marks it as the most practical retrieval to move forward with in development and deployment.

Based upon these results, the ASTER spectral library with off-diagonal covariance will be to the methodology used moving forward in this thesis.

4.7 SLUM Library test

The Spectral Library for Urban Materials (SLUM) has over 70 high quality lab spectra for different urban materials broken down into ten classes, see Table 15 (Kotthaus, Smith, Wooster, & Grimmond, 2014). The materials have a very large range of LSEs but in theory would all be classified into one a priori LSE group with in the current classification methodology. The data are used here to test the retrieved algorithm in more detail for its applicability to urban studies.

The material database was treated similarly to the MODIS spectral library and simulated ASTER TIR TOA BTs were generated for fixed atmospheres and surface temperatures.

Material Sub classification	Number of Samples
Quartzite	3
Stone	5
Granite	4
Asphalt	10
Cement/Concrete	8
Brick	14
Roofing shingle	4
Roofing tile	13
Metal	8
PVC	6

Table 15 – The sub classifications of the materials within the SLUM database and the number of different samples of those sub classes (Kotthaus et al., 2014).

Using these BTs as the observations and the parameters used to generate them as the truth, the retrieval was tested on all the materials in the library. The resulting correlation plots can be seen in Figure 22.

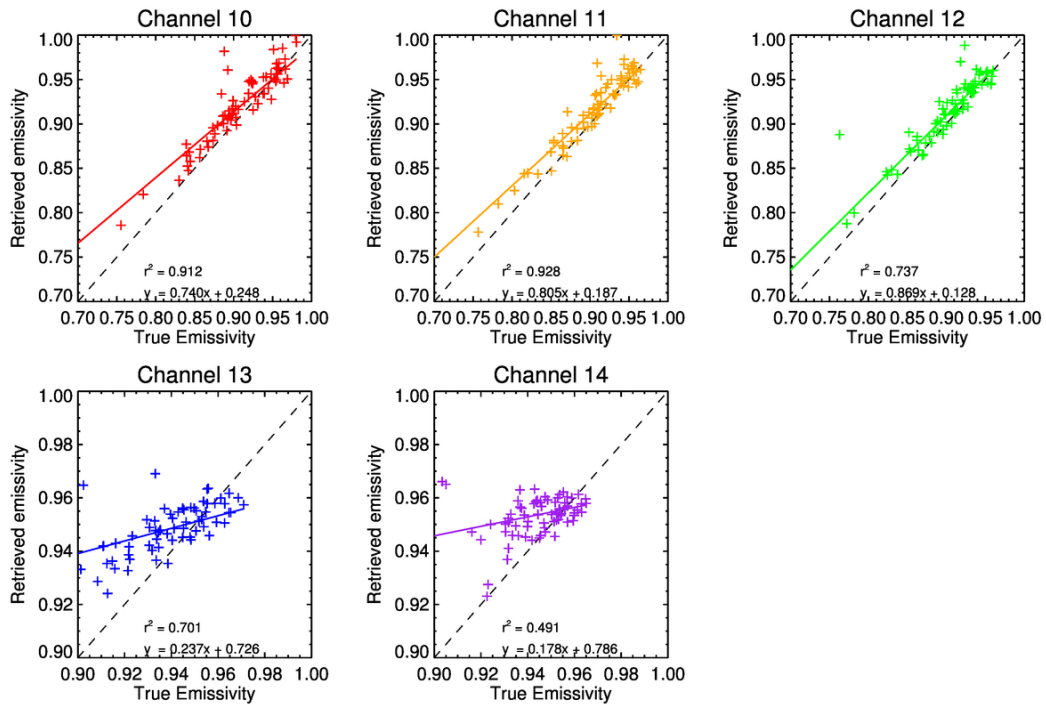


Figure 22 - Correlation plot for LSE in each of the ASTER TIR channels (10-14) comparing the retrieved and true values for the entirety of the SLUM spectral library.

The correlations seen here are relatively high when compared to the MODIS spectral library tests. The quality of the data is high with very few anomalous points. The performance in channels 13 and 14 in particular is the highest seen in the simulated testing.

The high correlation in the results shown in Figure 22 is encouraging toward the applicability of the retrieval to the urban area, as the materials found with in SLUM are far more representative of the types of surface that are likely to be found in the heterogeneous urban environment.

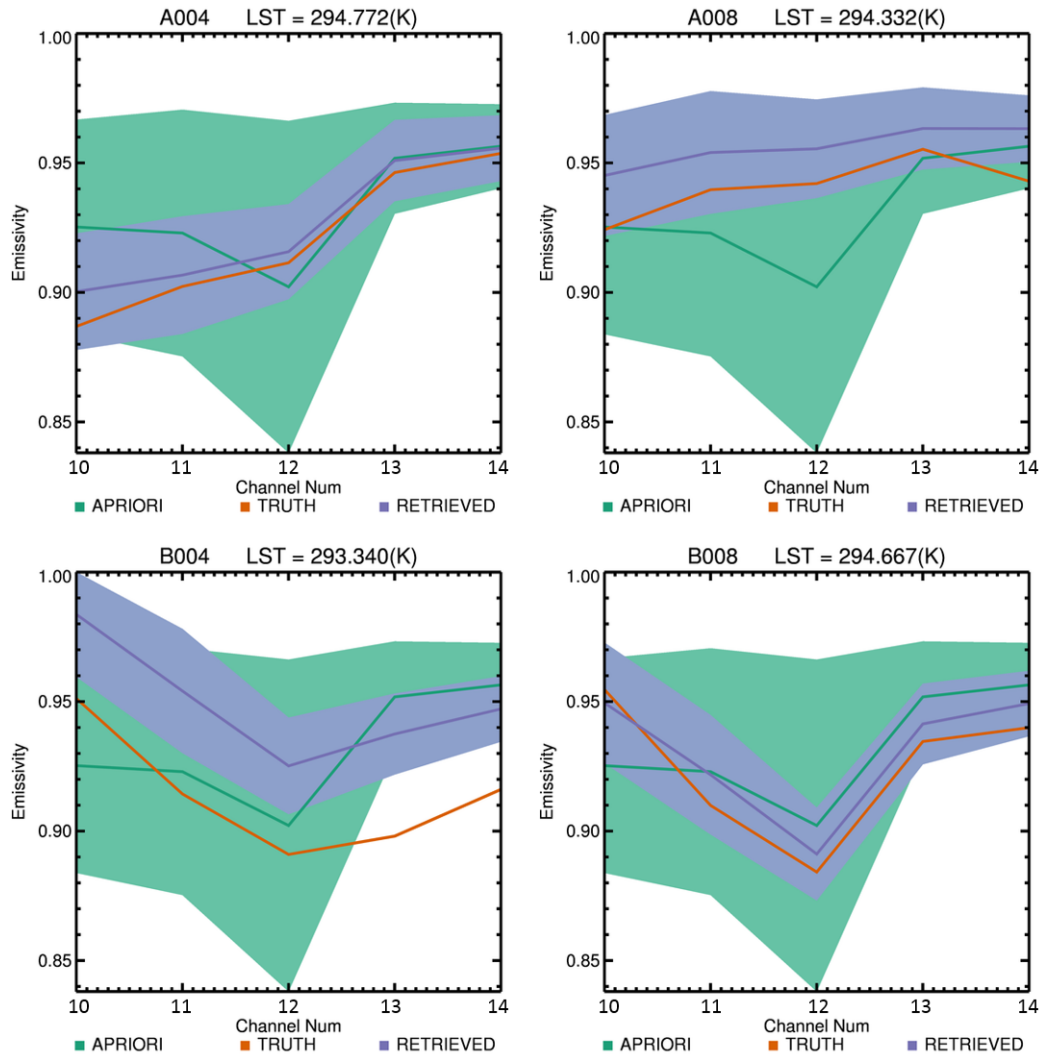


Figure 23 - Sample retrievals for asphalt and brick in the SLUM spectral library using the a priori LSEs determined from the mean class values from the ASTER spectral library with the inclusion of the off-diagonal LSE covariance.

Figure 23 and Figure 24 show two samples from each of the most populated classes in the SLUM dataset. The four classes are: asphalt (samples: A004 and A008), brick (samples: B004 and B008), concrete (samples: C004 and C008) and roofing tile (samples: R004 and R008). As can be seen in the asphalt samples even for the same material sub type there can be significant spectral variability in the LSE. A004 has lower values of LSE in channels 10, 11 and 12 than A008, yet both retrievals are given exactly the same a priori information.

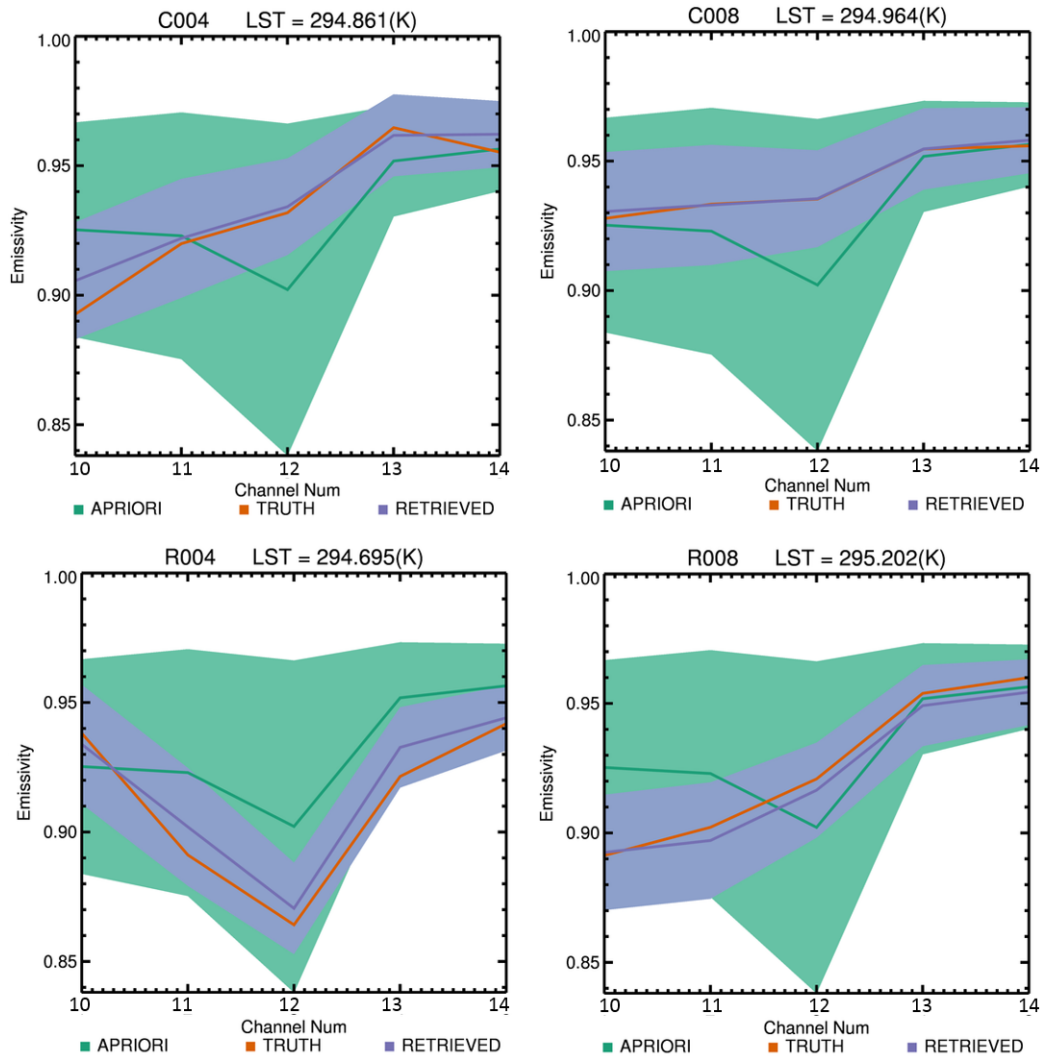


Figure 24 - Sample retrievals for concrete and roofing tile in the SLUM spectral library using the a priori LSEs determined from the mean class values from the ASTER spectral library with the inclusion of the off-diagonal LSE covariance.

The retrieved LST performs well in both samples with errors and uncertainty of less than 1 K except in B004. The LSE also manages a high degree of trueness in the majority of channels with mean offsets of less than 0.01 a value which is well within the uncertainty for the retrieval. The asphalt samples show a high degree of trueness with only channel 14 in sample A008 with an offset outside the range of the uncertainty, and the uncertainty itself is highly constrained across all of the channels.

The brick samples have markedly different spectral shaping for LSE. B004 displays a true shape which is extremely different to that of a priori. Whereas the a priori has channels 10, 11 and 12 with lower LSE values than channels 13 and 14, this ratio is reversed in the true LSE. Due to this the retrieved results have to move substantially

more from the a priori to converge to the truth. B008 shows far greater trueness in all channels and the LST offset is less than 0.5 K which is well within the retrieved uncertainty.

The concrete samples and the roofing tile samples, in Figure 24, all show very good trueness between the true and retrieved data. The small offset between truth and retrieved LSEs is even maintained where the retrieval has moved significantly from the a priori, such as in R004 where the a priori LSE for channel 12 is nearly 0.04 higher than the truth. The retrieved LSE in this case had an offset of 0.006, a substantial reduction.

Overall the testing on the SLUM data set allowed the retrieval to be tested on a large and diverse dataset covering some of the most likely materials to be found in the real world application of the retrieval. In these tests the retrieval performed above initial expectations, adapting to a number of complex and varying LSEs often deviating considerably from the priors.

However several issues were highlighted. Perhaps most significantly the issue of the spectral shape of the priori LSE data. The retrieval was shown in multiple cases to be capable of significant movement away from the prior LSE values to converge on the truth as seen in R004 and R008. The retrieval is even capable of adapting to situations where the spectral shape can alter by a large fraction, A008. However, differences between the a priori and true LSE spectral shapes can cause the retrieval perform poorly, as in B004.

4.8 Water Vapour retrieval

Water vapour is a key parameter when calculating the transmittance of the atmosphere in the TIR window channels. In the case of LANDSAT's 5 and 7, large water vapour variations were shown to induce errors as high as 4 K in the LST due their impact on the atmospheric transmittance (Qin, Karnieli, and Berliner 2001). For systems such as AATSR this effect is reduced due split-windows ability to mitigate the effect of the atmospheric water vapour on the retrieved LST resulting in in reduce errors. For a mid-latitude profile a perturbation of 10% in the water vapour can lead

to LST error of up to 0.57 K and for a tropical profile errors of up to 1.366 K, (Noyes, 2005).

The TIR channels used by ASTER have a low but notable sensitivity to the presence of atmospheric water vapour (Roberts, Selby, & Biberman, 1976) particularly in Channel 10 but also with notable contributions in Channels 12 and 14, as shown in the Jacobians in Figure 25.

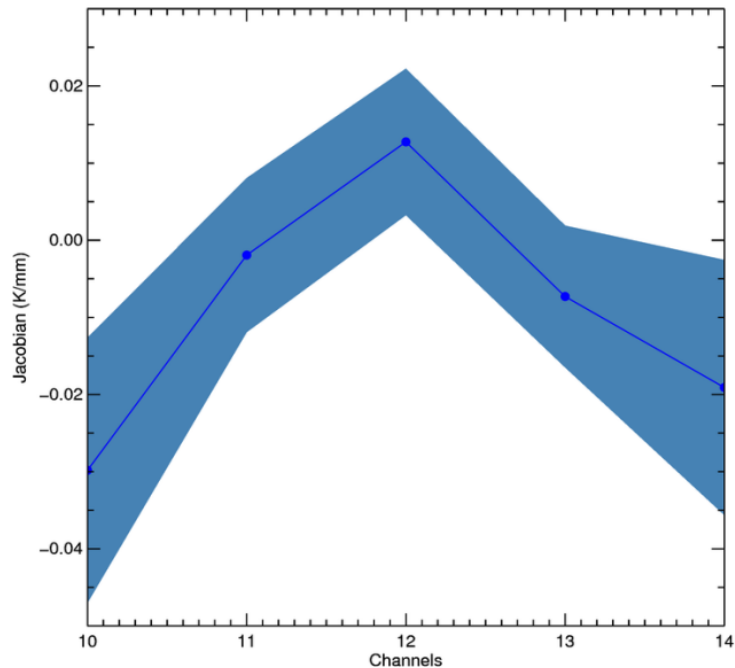


Figure 25 - Water vapour Jacobians calculated for each of the five ASTER TIR channels on a sample of 10,000 atmospheric profiles ranging from TCWV's of 0.5-10 mm. The darker blue points show the mean Jacobian values for each channel whilst the lighter blue region shows the area bounded by the standard deviation.

Whilst the potential LST deviations shown in Figure 25 are small in comparison to the errors associated with the LSE, they are not negligible. As such the potential to incorporate a term for the water vapour into the state vector and in doing so allow the retrieval to correct for incorrect or poorly known a priori water vapour is explored.

4.8.1 State vector inclusion of Water Vapour

The initial retrieval efforts utilised fixed atmospheric conditions drawn from ECMWF ERA-Interim reanalysis for the Algodones and Phoenix Arizona (Dee et

al., 2011). These results will be referred to as ABS-WV or absent water vapour retrieval. However these profiles cannot exactly match the conditions for every pixel spatially and temporally; the resolution of the ECMWF profiles is at best a 0.125 x 0.125 degree grid and is output four times a day at fixed time intervals. It is therefore desirable to retrieve total column water vapour simultaneously with LST and LSE; these results will be referred to as INC-WV or including water vapour.

To account for the potential impact of an inaccurate a priori atmospheric profile, the retrieval was modified to include water vapour in the state vector. The ASTER TIR channels lack the spectral information to constrain a water vapour profile to a full range of altitude levels; therefore, total column water vapour (TCWV) was included into the state vector to account for the water vapour contributions. The simulated data was constructed using full profiles from ECMWF ERA Interim over the selected scene for a month of data. For each of these profiles simulated radiances for ASTER were created using the ASTER spectral response functions, with each profile being tested over the full range of 115 materials from the MODIS spectral library. The resulting dataset of several thousand, five channel radiance sets were then utilised in testing the impact of variable water vapour on the retrieval.

When used within the retrieval the profiles were converted into TCWV values:

$$TCWV = \frac{1}{g} \int_{\min(p)}^{\max(p)} q dp \quad \text{Equation 4.3}$$

Where g is gravity, p is pressure in hecto-Pascal and q in the profile level value of water vapour in kg/kg.

This TCWV could then be included as 7th element of the state vector:

$$x_{a \text{ priori}} = [LST, \varepsilon_{10}, \varepsilon_{11}, \varepsilon_{12}, \varepsilon_{13}, \varepsilon_{14}, TCWV] \quad \text{Equation 4.4}$$

The covariance for the TCWV was set to 2 mm. This was obtained through the comparison of large numbers of simulations initialised with the all of the same inputs except the TCWV covariance and is of the same order as the standard deviation of

the TCWV parameter in these tests. The covariance is therefore representative of the majority of variance found in the water vapour between iterations allowing the retrieval a significant degree of flexibility.

As the retrieval itself utilises full water vapour profiles rather than TCWVs any update to the state vector required by the iteration process was transformed into an update to the whole profile through the following equation:

$$q_{n+1} = q_n + \left(\frac{q_n p}{\sum(q_n p)} \right) \sum (q_n \delta_{TCWV}) \quad \text{Equation 4.5}$$

where q_n is the current water vapour profile, q_{n+1} is the updated water vapour full profile, p is the pressure profile and δ_{TCWV} is the update to the TCWV as a fraction. This process thereby updates the profile by the fractional change in TCWV but also weights the distribution of the update to match the pressure weighting of the profile.

Due to the lack of spectral sensitivity to water vapour in the ASTER TIR channels the TCWV in the state vector is better described as a proxy for TCWV included to account for the impact of water vapour on the retrieval rather than as a retrieval of the true water vapour itself.

Simulations were performed using a test set of ECMWF ERA Interim data for January 2014 over the Algodones scene. As such the distribution of TCWV values was not homogeneous, see Figure 26.

As Figure 26 shows there are significantly more profiles in the range of 2-3 mm. In order to account for this imbalance in the analysis the data was re-binned at 0.1 mm intervals for each material type. Furthermore a filter was applied to the data to correct for misclassification in the a priori LSE as this introduced significant offsets which were unrelated to the TCWV being tested, see Figure 27.

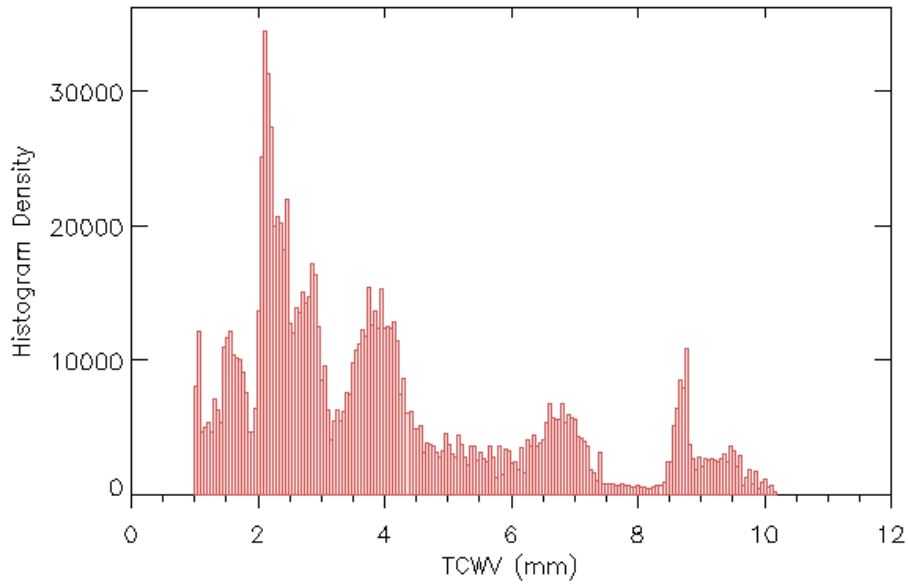


Figure 26 - A histogram of the true TCWVs for the simulations. There is a clear bias towards TCWV values at 2mm which would be carried into the retrieved parameters.

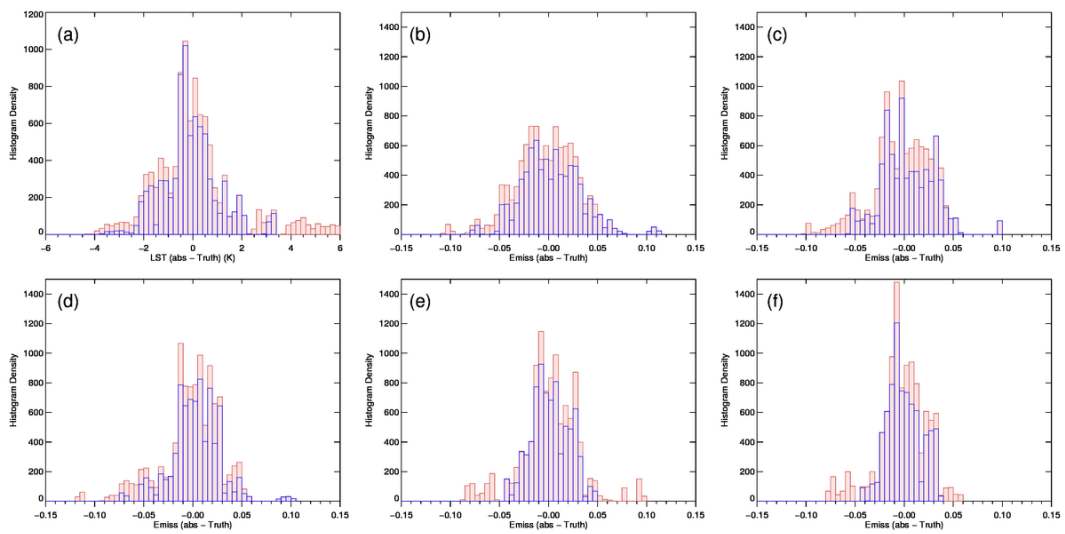


Figure 27 - Histograms showing the Retrieved - True values for the (a) LST and the (b-f) LSEs for channel 10-14 respectively using the ABS-WV retrieval. The red bars show the raw data, and the blue bars show the filtered data where a priori LSE errors greater than 0.05 were omitted.

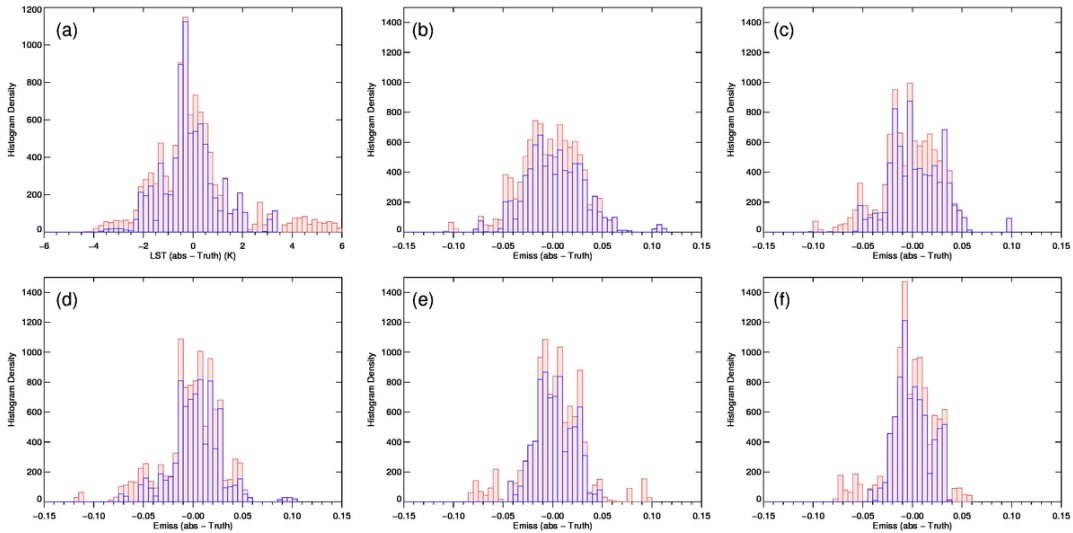


Figure 28 - Histograms showing the Retrieved – True values for the (a) LST and the (b-f) LSEs for channel 10-14 respectively using the INC-WV retrieval. The red bars show the raw data, and the blue bars show the filtered data where a priori LSE errors greater than 0.05 were omitted.

The filtered results in Figure 27 show that the classification errors account for the largest errors in the data especially in the channels 13 and 14 (plots (e) and (f)). Using the same filter the results including the INC-WV results were tested against the true data set, see Figure 28.

The INC-WV retrieval shown in Figure 28 has small quantitative differences when compared to the ABS-WV retrieval seen in Figure 27, the differences are subtle and do not strongly impact the larger scale features. A closer analysis of the LSTs retrieved by the two schemes is shown in Figure 29.

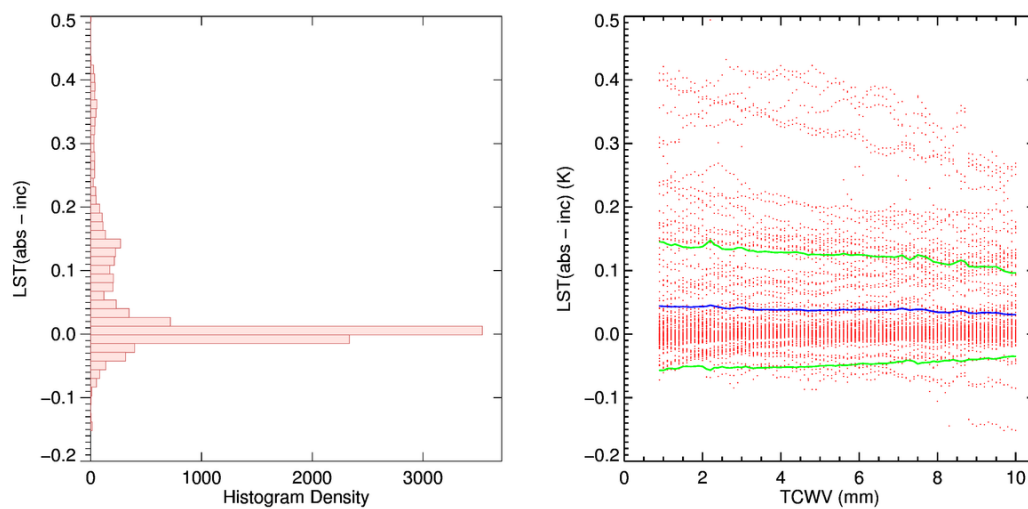


Figure 29 - (a) Histogram of the residuals for ABS-WV – INC-WV for LST. (b) The plot of the residual shown in (a) plotted against the true TCWV. The blue line represents the mean values for each TCWV bin and the green lines border the region encompassed by the mean \pm standard deviation.

Figure 29 (a) clearly shows that the majority of the offsets introduced through the addition of TCWV into the retrieval are very small, less than 0.1 K. The peak offset is shown at under 0.5 K which is considerably smaller than both the LST offset from the truth and the uncertainty associated with the retrieved LST (± 1 K). Panel (b) shows the full plot of the data against the true TCWV and shows very little overall trend for the majority of the data. The mean for each TCWV bin (blue line) is stable throughout the range of TCWV values with a small positive bias throughout. The area bounded by the mean (between the green lines) does show some small variation as it narrows toward the higher TCWV values slightly, showing fractionally improved stability at higher water vapour levels. In comparison with the results shown in Figure 27 and Figure 28 there is a strong indication that the system is dominated by the LSE effects. However the potential to improve the retrieval by 0.5 K in certain cases is still significant as is the impact this has on the residuals.

The radiance residual as an indication of how well the forward model matches the observations is very important. Analysis of the differences between the radiance residuals of the two methods shows a reduction in the INC-WV retrieval residual radiances.

All of the channels except channel 12 show a reduced radiance residual value, as seen in Table 16.

Radiance residual (K)	Channel 10	Channel 11	Channel 12	Channel 13	Channel 14
	<i>ABS-WV</i>	0.057	0.016	0.006	-0.129
<i>INC-WV</i>	0.050	0.015	0.009	-0.124	0.049

Table 16 - Mean radiance residual values for all data points in each channel for both methodologies.

The overall improvement in the radiance residuals demonstrates a better representation of the true surface in the forward model simulation. The additional of

a further parameter has allowed the retrieval reduce the dependency on ancillary data without inducing large additional errors.

Adapting to the variability of the water vapour is an important issue in successfully retrieving LST and LSE at high spatial resolution. The INC_WVs was able to reduce the radiance residuals. The inclusion of water vapour within the state vector, whilst increasing the retrieval uncertainty, eliminates the water vapour from the model parameter error which reduced the overall uncertainty. Due to this, the INC_WV was included in the main methodology and all further retrievals conducted within this thesis are made using the INC_WV algorithm.

4.9 Algodones TES inter comparison

To assess the performance of the new algorithm an inter-comparison and limited verification was conducted with the existing TES algorithm for ASTER by collaboration with JPL. Data were supplied by JPL. (Hulley, personal correspondence 2015) for both LST and LSE along with the corresponding ASTER L1b scene. The inter-comparison was conducted over Algodones, USA. This site has been used extensively in testing with both MODIS and ASTER (Hulley & Hook, 2011). The site, shown in Figure 30, is a mixture of sand and impervious rock, with a large agricultural development toward the south west of the scene. Within the sand covered area there is a high degree of homogeneity allowing the single point validation site within this region to be representative of a large proportion of the scene.

The test scene was processed using the full INC-WV optimal estimation algorithm which includes the water vapour retrieval. The scene was also processed with a land classification scheme derived from ASTER VNIR, which is discussed in detail in Chapter 5 section 4. The retrieved results were then compared to the TES retrieved values and the validation point within the site.



Figure 30 – Landsat image of the Algodones test site near the Salton Sea in New Mexico, USA. Image taken from Google Earth, 32.975 N, -115.048 E, image acquired 12/31/2014, accessed on 16/09/2016.

4.9.1 Retrieval Comparison

The retrieved TES LST as seen in Figure 31 shows a temperature range of between 290 and 330 K. The agricultural region in the south-west is clearly visible, and very distinct from the rest of the scene. The validation site is located at 32.9678N, 115.1355W, at the bottom right of the scene, as was selected to be representative of the materials present in this sand dominated region.

Figure 32 shows the same scene retrieved using the optimal estimation method. The features in both scenes match spatially with very similar temperature patterns appearing at the Terrain boundaries and within the differing Terrain types themselves. Overall the OE retrieval shows a strong consistency with the TES LSTs.

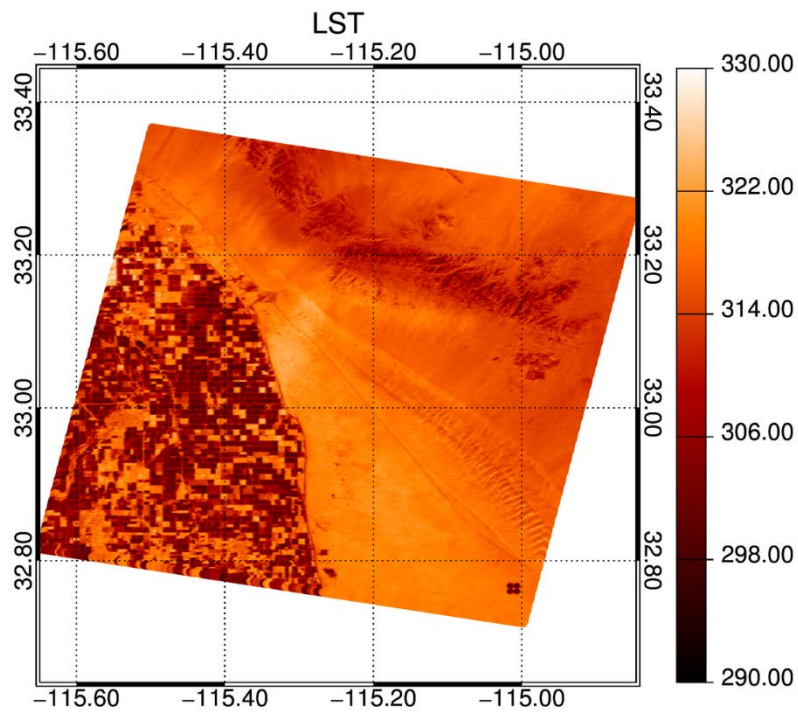


Figure 31 – LST Retrieved from the TES algorithm by JPL, for the Algodones site. Temperature in K.

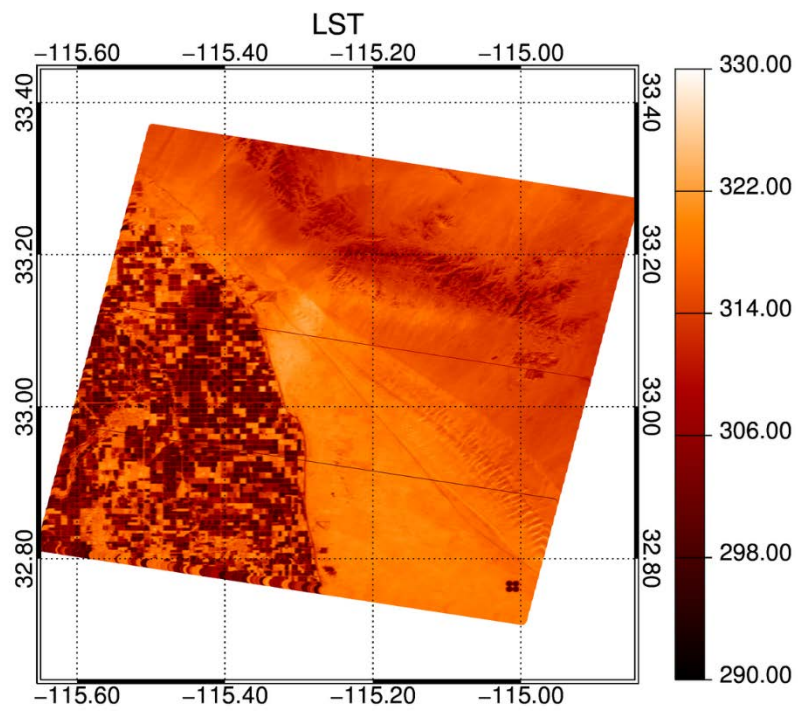


Figure 32 – LST Retrieved using the Optimal Estimation algorithm, for the Algodones site. Temperature in K.

The LSEs across all the ASTER TIR channels show consistent spatial structures, between the different surface material types. In all cases the vegetation present in the agricultural region presents with significantly higher LSE values as would be expected. However, the LSEs derived in the OE retrieval are systematically lower than those seen in the TES data, see Figure 33 and Figure 34, except in the vegetated areas where the LSEs retrieved by the OE retrieval in channels 13 and 14 are higher than those of the TES algorithm. Additionally the spatial distribution of the high vegetative LSEs is different between the two algorithms. As seen Figure 34 and channels 13 and 14 show distinctly different structures. The TES retrieval shows higher LSEs across the majority of the scene ranging between 0.96 and 0.98. The OE retrieval however has significantly lower emissivities over the rock/soil ground cover types but has sharply higher and contrasting LSEs in the vegetative areas, the range here is from 0.91 and 0.99.

A possible explanation for this lies in the fact that TES relies upon spectral contrast in its calculation of the LSE, see Chapter 2. The sand and impervious surfaces offer this contrast and as such are usually considered the materials over which TES performs the best. The vegetative LSEs however, as seen in the results in 4.3, have a far less distinct spectral contrast and are therefore more likely to result in a poorer retrieval performance.

The OE retrieval is also dependent upon the a priori information pertaining to the surface composition but does not rely on the spectral contrast. In the case of the OE the a priori information is drawn from the VNIR land classification and therefore can distinguish between land types which lack thermal contrast.

The statistics shown in Figure 35 and Figure 36 further emphasise the observations of the spatial maps. The mean TES LST and the OE retrieval have an extremely similar distribution. There are slight temperature offsets, but both the magnitude and distribution of retrieved temperatures are comparable.

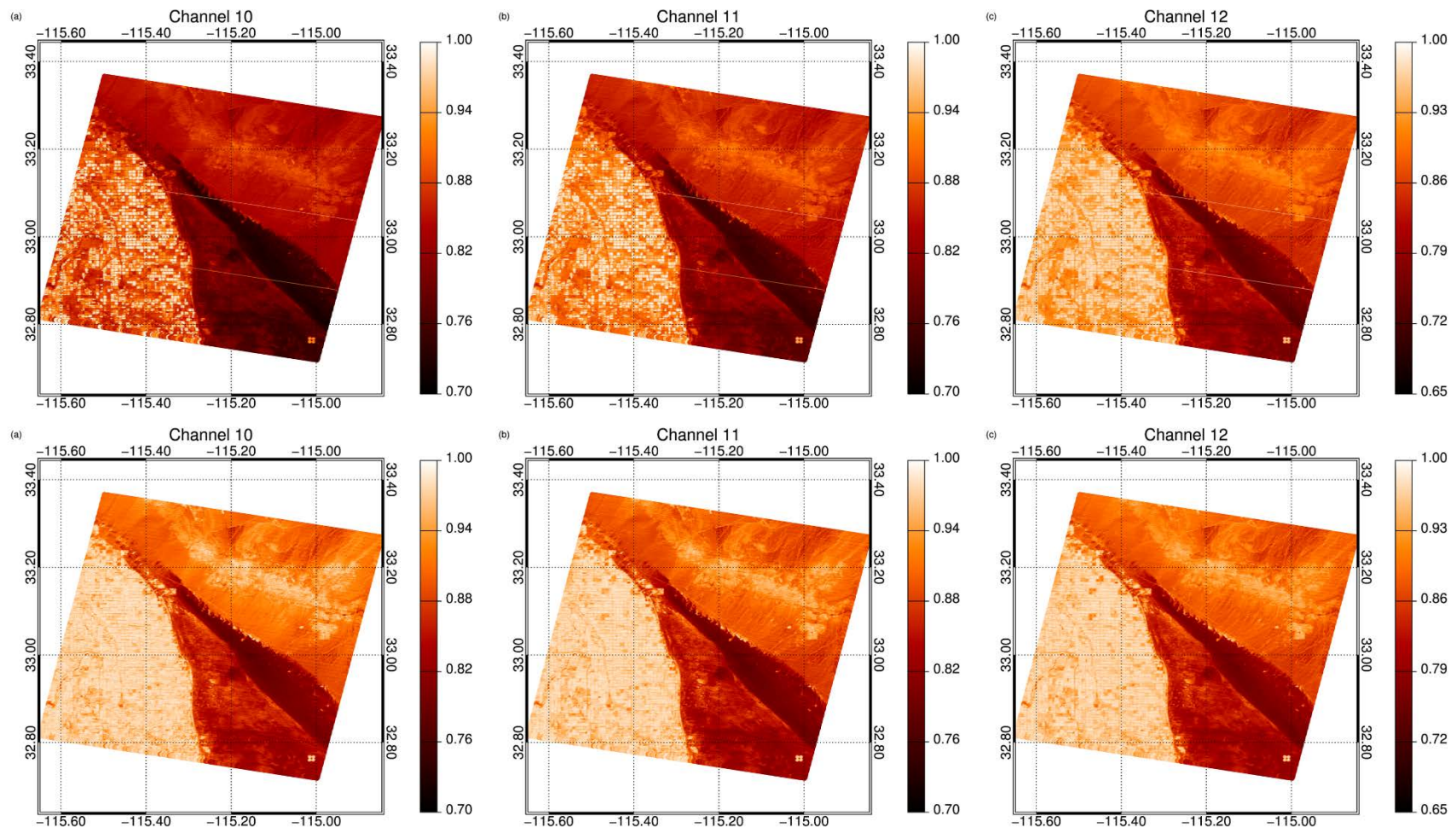


Figure 33 - Retrieved LSE TOP: OE, BOTTOM: TES. (a) Channel 10, (b) Channel 11 and (c) Channel 12

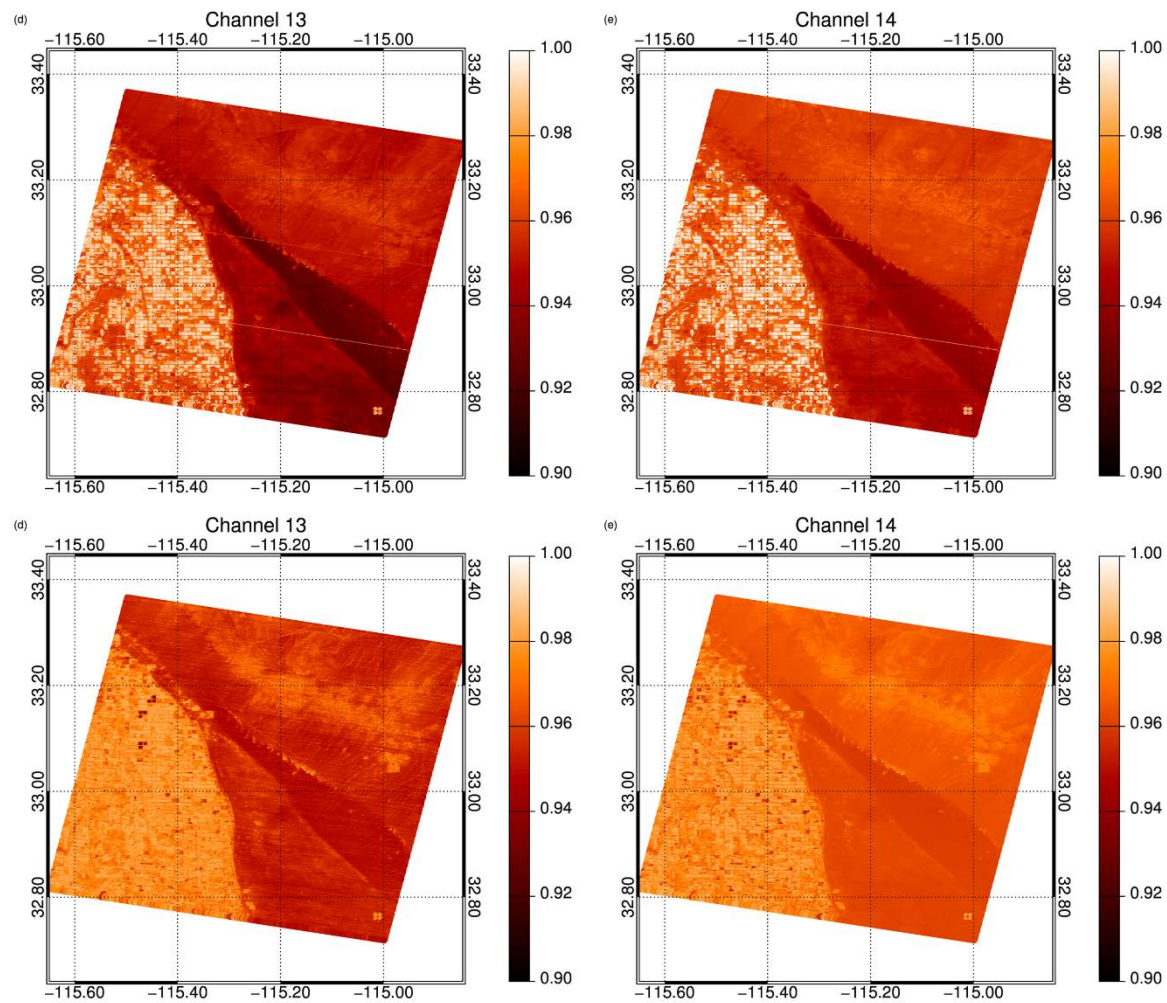


Figure 34 - Retrieved LSE TOP: OE, BOTTOM: TES. (d) Channel 13 and (e) Channel 14

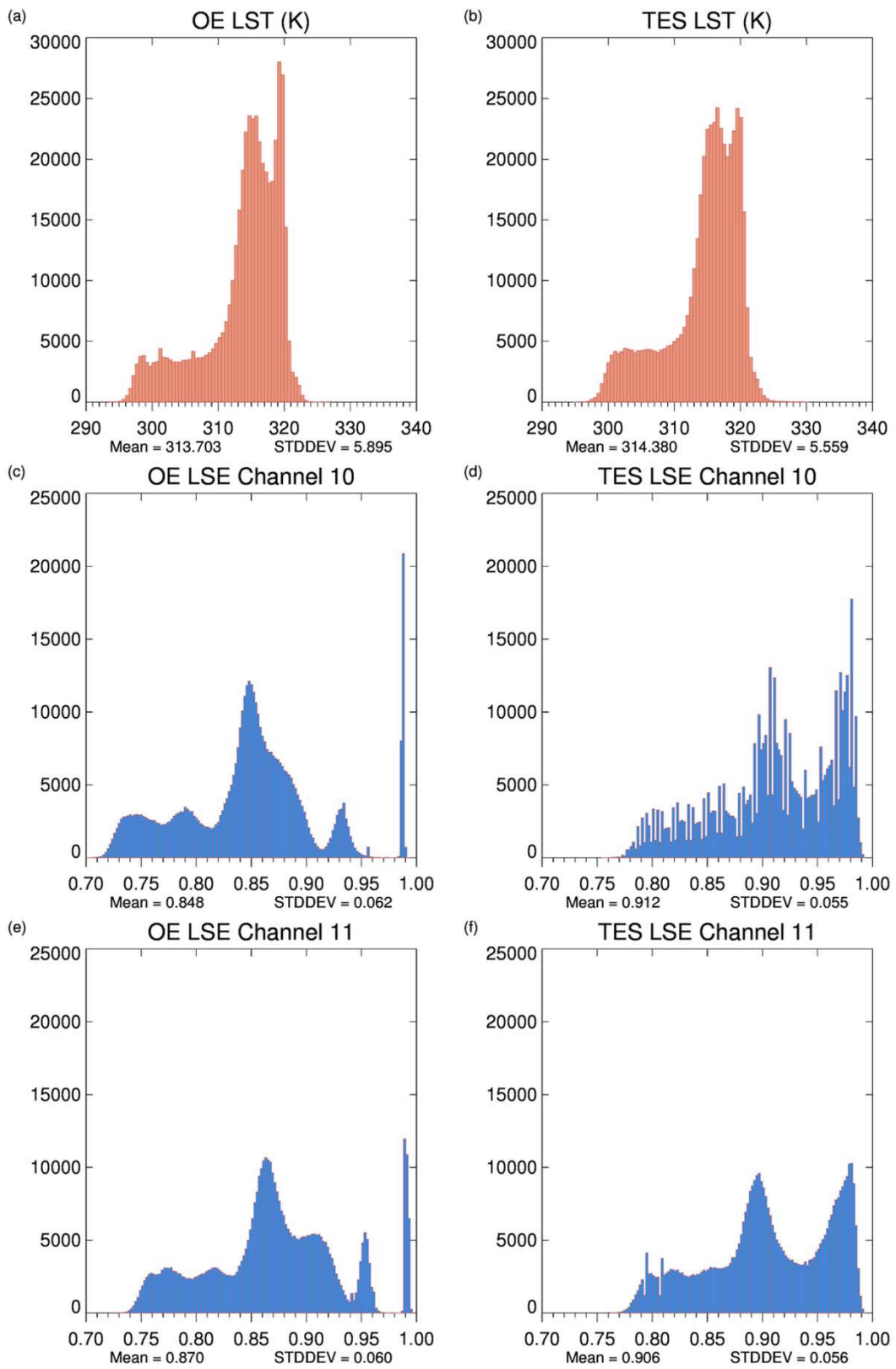


Figure 35 – LEFT: OE, RIGHT: TES. (a,b) Retrieved LST, (c,d) Channel 10 LSE and (e,f) Channel 11 LSE

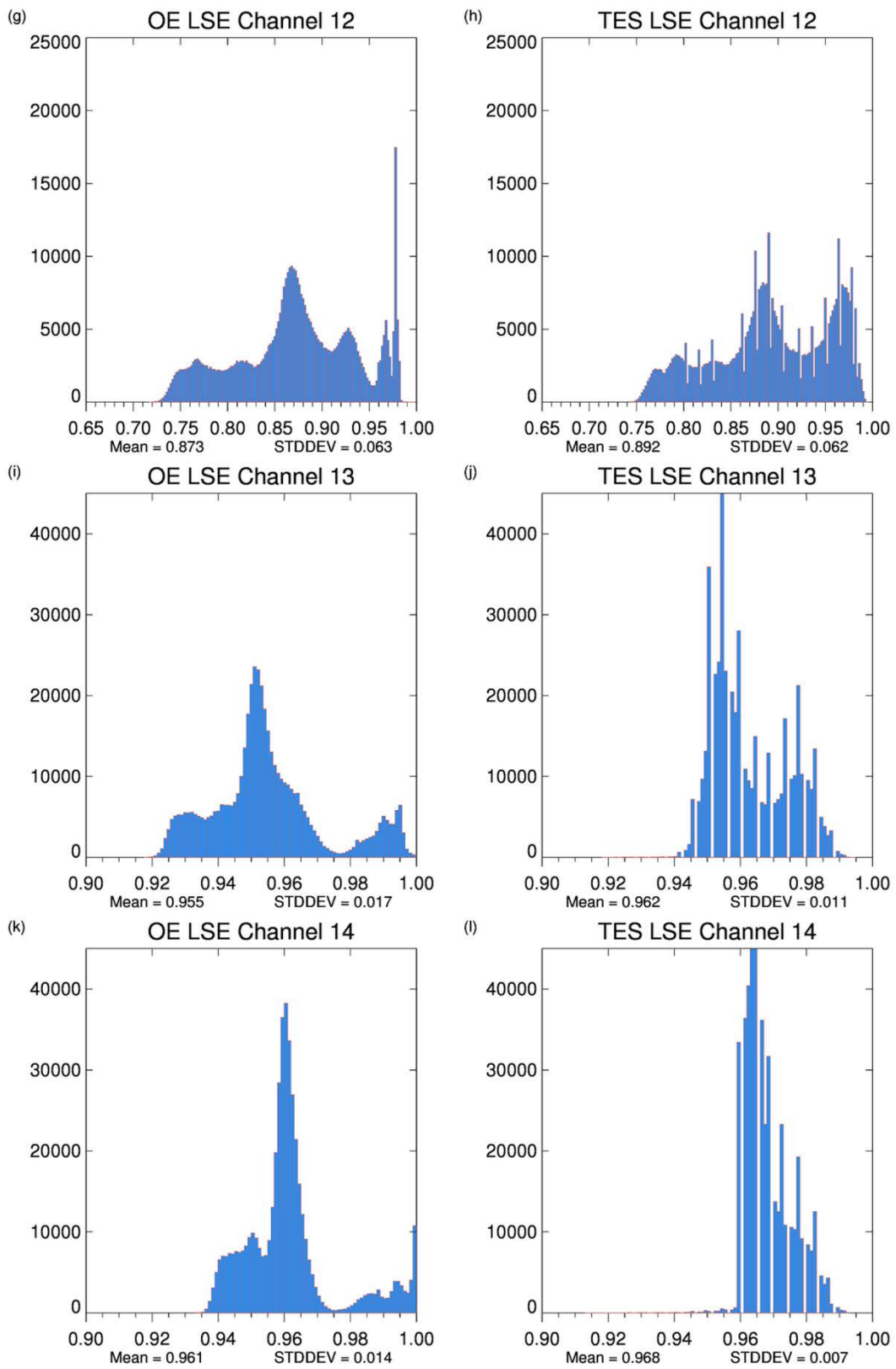


Figure 36 - LEFT: OE, RIGHT: TES. (g,h) Channel 12 LSE, (i,f) Channel 13 LSE and (k,l) Channel 14 LSE

The LSE values vary considerably more between the two retrievals. In channel 10 the mean TES LSE values are over 0.06 higher, see Table 5, a trend which carries across all the channels. The offset narrows marginally in channels 13 and 14, but this is due to the presence of small fractions of very high LSE values in the OE data over vegetation rather than a systematic reduction in the offset between the two retrievals. Additionally the TES data has a significant quantity of regular spiking in the data values that stand out from the overall trend of the distribution. Without knowing the full processing which has been applied to the TES algorithm it is difficult to assess the exact cause of these structures but given the consistency of the surface and the absence of these structures in the channel 12 LSE data it is unlikely they are representative of a real physical distribution.

Retrieval	LSE	C10	C11	C12	C13	C14
TES	Mean	0.912	0.906	0.892	0.962	0.968
	Std Dev	0.055	0.056	0.062	0.011	0.007
OE	Mean	0.848	0.87	0.873	0.955	0.961
	Std Dev	0.062	0.06	0.063	0.017	0.014
TES - OE	ΔLSE	0.064	0.036	0.019	0.007	0.007

Table 17 – The mean and standard deviations for the retrieved LSEs from the Algodones inter-comparison for both the OE and TES datasets.

The data spikes aside the distributions generally match to a high degree in the shape of the distribution in the first three channels, however there is an offset whereby the LSEs in the OE are shifted down in value is consistent across all the channels.

The distributions in channels 13 and 14 are markedly different. Whilst the dominant peaks of the distribution lie in the same locations between the two retrievals the distribution around these is substantial different. The OE has a broader spread of values and has a far greater concentration of LSEs at higher values ~0.99 or above. This shows a significant difference in the way that the methods deal with the high LSE materials types, such as vegetation.

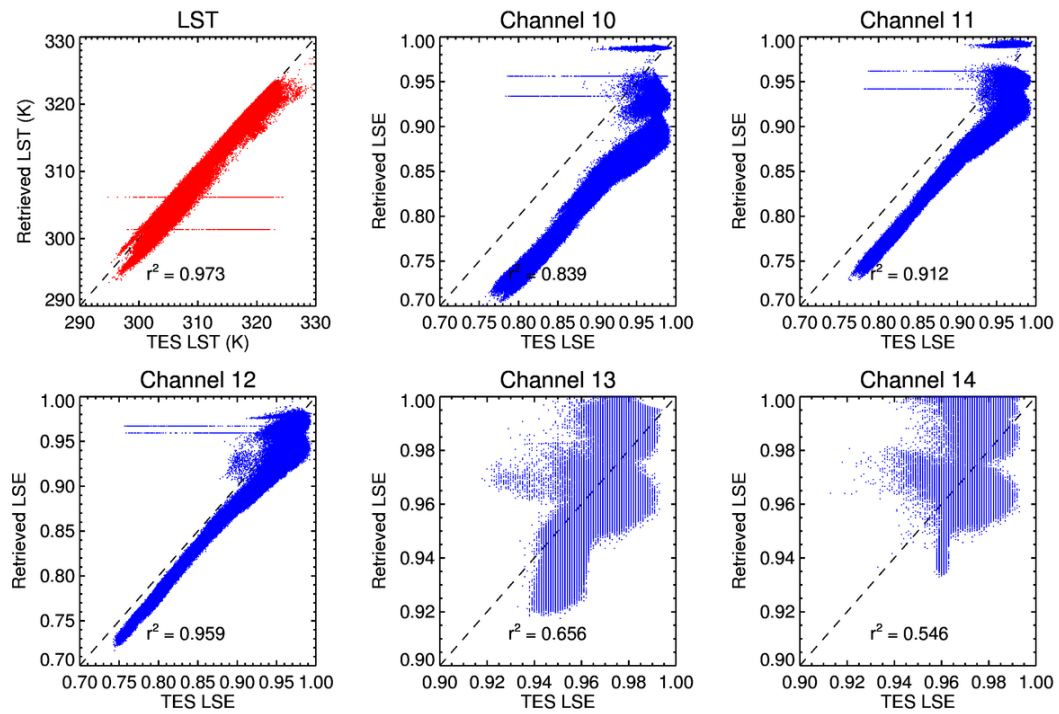


Figure 37 - Correlation plots of the OE vs TES Retrieved results for LST and LSEs across all channels.

Figure 37 highlights the variation between the two algorithms, showing the correlation between the OE retrieval and the TES retrieval. Overall the LST shows a high degree of correlation with an R^2 of 0.973. Interestingly the LST shows a fractionally higher bias at higher temperatures, where TES is more consistently lower. The fact that TES shows both higher LST and LSE demonstrates that there is a clear difference in the atmospheric treatment. TES is showing a smaller reduction in the effect of the atmosphere in absorbing the outgoing radiance.

LSEs for channels 10 and 11 correlate strongly but have a distinct bias at low to mid values of LSE, the TES values are seen to be higher across a large range of LSEs. Here there is a decrease in the offset at higher LSE values. Channel 12 maintains a high R^2 value and shows the least offset between the LSEs retrieved of any of the channels, however the LSE offset is still apparent, especially at lower LSE values matches Table 17. The Channel 13 and 14 LSE correlations are the lowest in the comparisons and show clear structure. For a significant proportion of the retrieved pixels at high LSE the OE retrieval is higher than the TES. However TES shows a region of pixels with an LSE of 0.95 and 0.96 in channels 13 and 14 respectively which correspond to a large and varying range of LSE in the OE retrieval. This is

most often due to the difference in classification. The OE method allows a continuous range of a priori values in the mixed classes based upon the NDVI, a continuous range of priors allows the retrieval the flexibility to adapt to and retrieved a greater range of LSEs dependant on the observed radiance, but the limited range of LSE variation also contributes.

4.9.2 Verification Assessment

To assess the nature of the offset and its implications for the physical accuracy of the retrievals, a validation point representative of the homogeneous sands was analysed to give an independent assessment of the performance of both methods using ground based data.

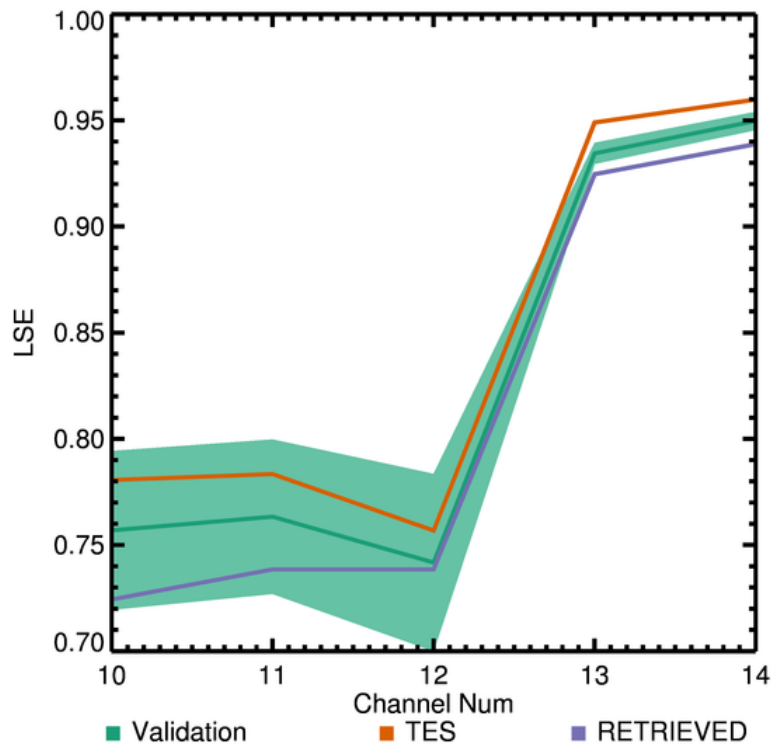


Figure 38 – Retrievals tested against the validation data, for Algodones, USA. Green line shows the values for the validation data, purple the OE retrieval, and orange the TES values.

The validation site is shown by the green data line in Figure 38. The lighter green region shows the standard deviation of the validation data. The orange line shows the

TES data at the validation point. The TES retrieved LSEs are well within the standard deviation of the validation site in channels 10, 11 and 12, the LSEs in channel 13 and 14 are outside the validation site uncertainty but are consistent allowing for the stated uncertainty of the TES LSEs of ± 0.019 . Importantly the TES LSEs all have a positive bias. On the other hand the OE LSEs, shown by the purple line are also with in the validation standard deviation in channel 10, 11 and 12 and also slightly outside that range in channels 13 and 14. Similarly, the values are consistent when factoring the retrieved uncertainty averaging ± 0.015 . However, these values show a negative bias compared to the validation results.

Retrieval	RMSE: Retrieved LSE – Validation site LSE				
	C10 Δ LSE	C11 Δ LSE	C12 Δ LSE	C13 Δ LSE	C14 Δ LSE
TES	0.024	0.020	0.015	0.015	0.010
OE	0.033	0.025	0.003	0.010	0.011

Table 18 – RMSE from the validation site for TES and OE algorithms, for all surrounding pixels.

As stated previously, the Algodones validation site is not representative of the whole scene but it does represent a significant proportion, the dunes are 72 km long with a width of up to 10 km as such is reasonable to expect that the validation site should be indicative of a large fraction of the rock/ bare soil.

Overall the OE algorithm performs marginally better than the TES algorithm at the validation site with a lower total difference from the validation LSE, see Table 18. However, with it is important that whilst the overall performance is better, the performance in Channel 10 is substantially worse in the OE method. The cause of this is the influence of the atmosphere on the retrieval. The TES does not correct for the atmosphere, this is done separately before the application of the TES algorithm, due to this if the additional atmospheric correction is of a high standard the effect of the atmosphere is minimised. OE however does do atmospheric correction, whilst in theory this make the algorithm more adaptable and less dependent on ancillary data sets and products, it does mean that the retrieval will face issues in Channel 10 where the atmospheric sensitivity is highest.

Additional analysis was conducted to look into the vegetated area at the south east of the scene. This area is a large patchwork of agricultural vegetation with many different types of crops being grown within it. The TES and OE retrievals from this region are plotted along with the vegetation a priori for the OE in Figure 39.

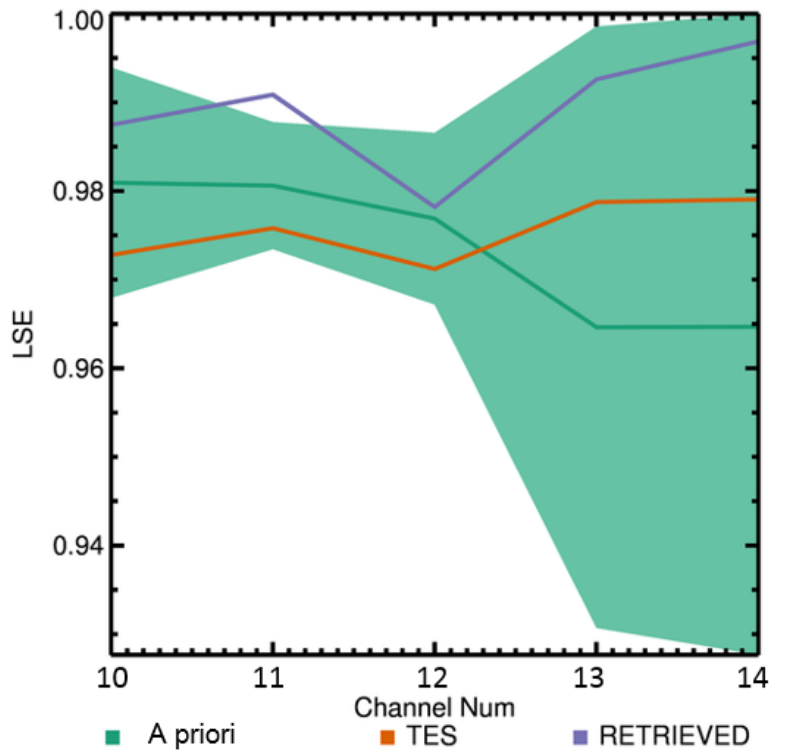


Figure 39 – The retrievals for both TES (orange) and OE (purple) for the vegetative region of the Algodones test case. The green shows the a priori data with the uncertainties.

It is immediately apparent that both the TES and OE LSEs show significantly different spectral shape to the a priori used. The vegetation a priori was drawn from the ASTER spectral library and as such does not include a large crop database. The vegetation used in the construction for the a priori data was mainly for leaves and dry grasses, therefore there is a bias away from the spectral shape of crops which in general have higher LSEs in channels 13 and 14 than those used in the vegetation a priori (Pandya et al., 2013). Despite this the OE LSE has been able to adapt to the new spectral shape. However there are a higher number of unphysical retrievals flagged in this region, where the retrieval was not able to adapt and attempted to

consistently move toward values of >1 . These should be removable with the inclusion of a more detailed vegetation training set that includes multiple crop types.

4.9.3 Uncertainty and Radiance Residuals

The OE methodology produces a full a posteriori uncertainty matrix. This uncertainty breaks down the uncertainty into the various retrieved parameters giving a uncertainty for each individually.

The retrieved uncertainty in OE retrieval over Algodones has LST retrieved to better than 1.5 K which is the stated performance of the ASTER TES algorithm, see Figure 32. The distribution follows one main cluster in Gaussian around 1.35 K and two clusters at 0.45 and 0.9 K respectively. The cluster at 0.45 K matches the points where the emissivity tends to non-physical values of extremely close to 1 or higher and should not be taken as realistic retrieval uncertainties. The data at 0.9 K however is a reasonable retrieved uncertainty for LST in simulations and in other retrieved scenes.

The LSE uncertainty varies from channel to channel. As would be expected give the increased atmospheric sensitivity and poorer performance, channel 10 has the highest associated uncertainty for LSE at a mean of 0.21. This and the uncertainty in channel 11 are higher than the TES stated LSE uncertainty of 0.19. However in the case of channel 11 there is a wide range of retrieved uncertainties making any comparison pixel dependant. Channels 12, 13 and 14 perform better with retrieved LSE uncertainty of equal or better performance than TES.

The radiance residuals seen in Figure 41 show strong a Gaussian relationship across the majority of the retrieved data. The radiances residuals in channels 10, 11 and 12 are low, with a majority of the distribution under 0.1 K. Channel 12 in fact has a distribution tending to be under 0.05 K due to the nature of the retrieval and the tendency to fixate upon the channel 12 LSE.

Channels 13 and 14 have a broader spread of radiance residuals but still with the majority under 0.2 K. Channels 12 and 14 are highly centralised with the Gaussian centred on 0. The other channels all have biases. Channels 10 and 11 have a negative

bias with generally higher observed radiances compared to those simulated, potentially due to an over compensation for the atmospheric effects in channel 10.

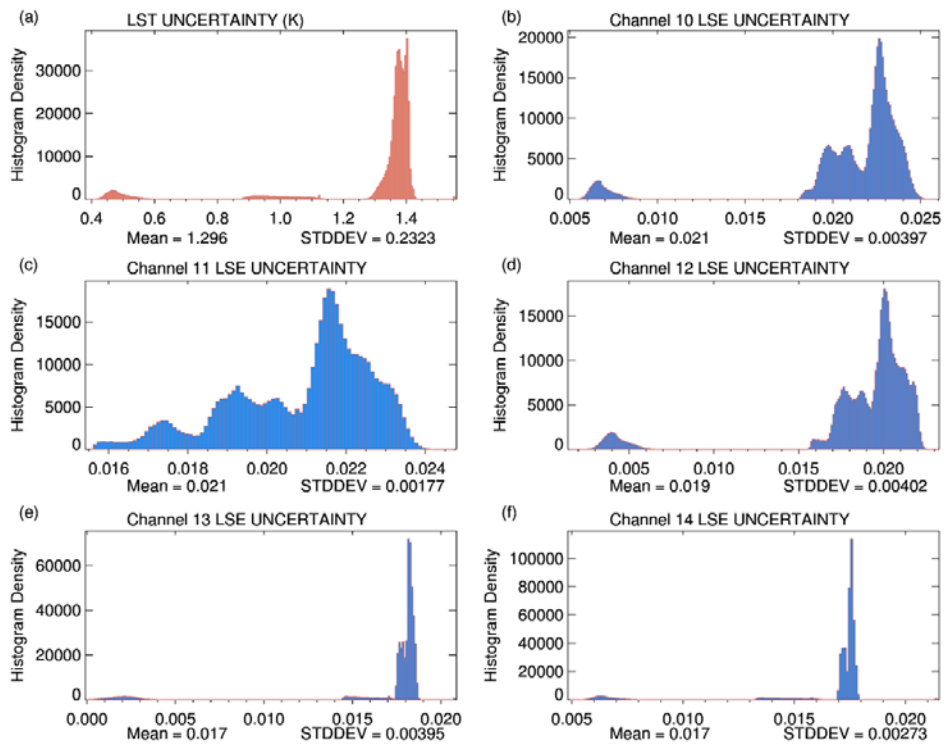


Figure 40 - Histograms for the retrieved values of LST and LSE for Algodones, with the mean and standard deviation of each set.

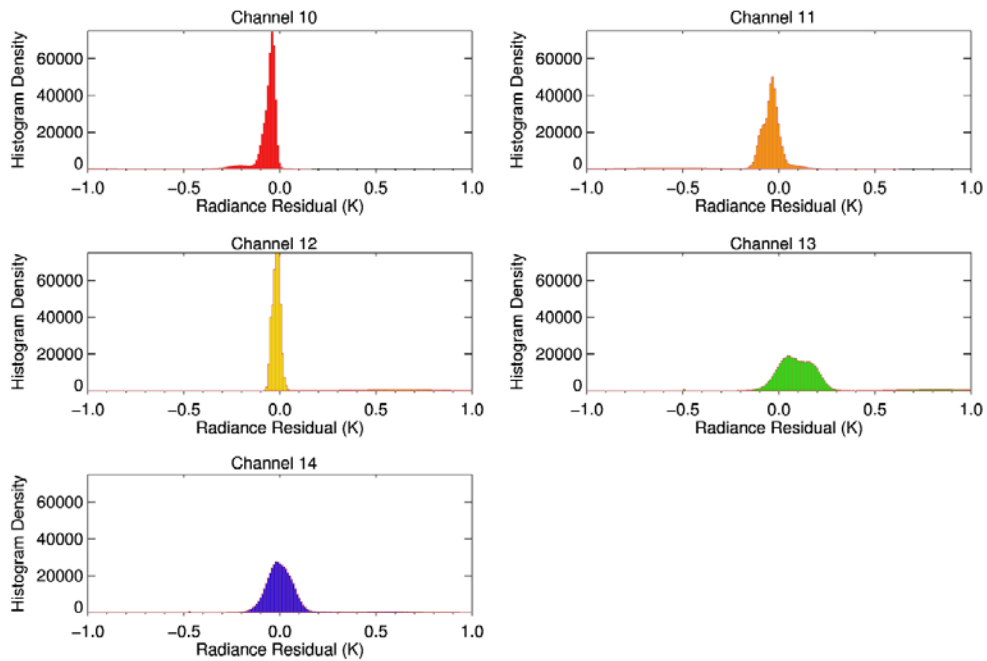


Figure 41 – Histograms of the retrieved radiance residuals for the Algodones scene for each channel.

Channel 13 has a positive bias showing an over estimation of the brightness temperatures in the forward model. These biases when analysed as a whole give substantial insight into the behaviour of the retrieval. Within the ASTER spectral library testing it was found that there were three groups in the channels where the emissivity varied co-dependently depending upon the dominate surface type, see Table 2 in 4.2.2. The groups were group 1: Channels 10 and 11, group 2: Channel 12, and group 3: Channels 13 and 14. Due to this as a proportion of the variance within in the LSE retrieved channel 12 has a greater impact on successfully retrieving the correct LSE. Mathematically this means the most cost effective way to minimise the cost function is found by reducing the radiance residual in channel 12, as it will have the strongest bearing on the retrieved LST and LSE.

4.10 Water LSE

A test was conducted over water for data off the coast of New York. The retrievals over the water pixels were not given any special distinction with in the retrieval algorithm. Typically in SST retrieval using the split window methodology the LSE of the water is taken to be fixed. In this retrieval the LSE was not fixed and was still allowing variation from the a priori. This was done as a sanity check of the retrievals operation. Whilst mathematically the retrieval can vary substantially in LSE for these pixels, the physical reality would make these variations unrepresentative of the surface. Figure 42 shows the a priori LSE in green and the retrieved in purple.

The retrieved LSE varied within the covariance bounds and in the majority of cases does not deviate far from the a priori LSE. This is the expected result and shows the retrievals ability to identify a spectrally invariant surface in terms of LSE and react accordingly. The variation seen in the standard deviation shows the influence of random error and the potential miss-classification of pixels near the land-sea boundary, where pixels may contain both types.

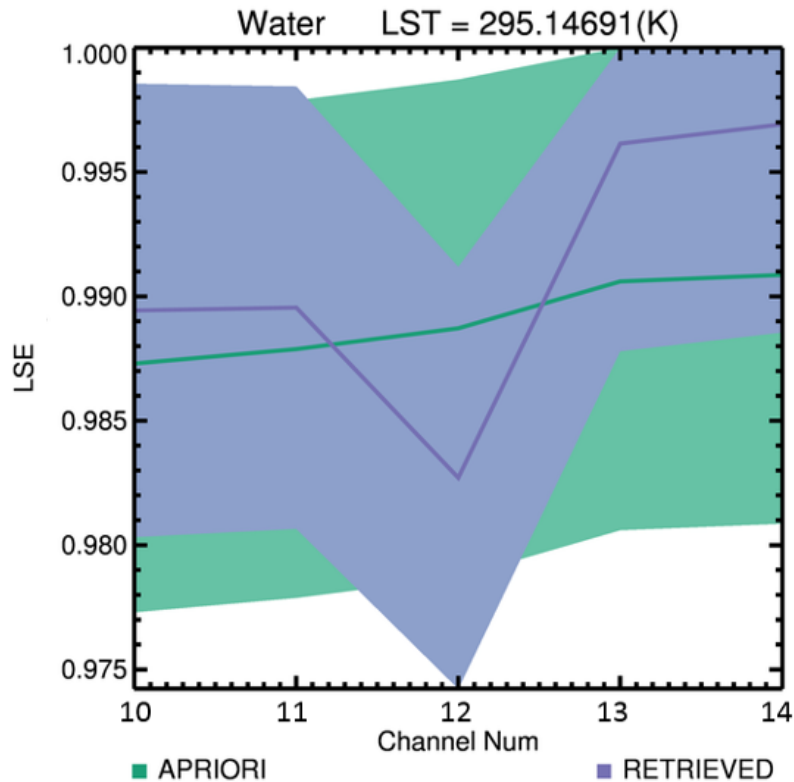


Figure 42 - Comparison of the a priori (green line) and retrieved (purple line) LSEs for water. The shaded purple region shows the retrieved uncertainty, and the green area the a priori covariance for water.

This result is encouraging and lends confidence to the retrievals ability to recreate the physical characteristic of the surface whilst maintaining the mathematical functionality to reduce the difference between the observed and simulated radiances.

4.11 Summary

The retrieval as outlined in this chapter operates an optimal estimation scheme to retrieve LST and LSE from the ASTER TIR channels with the additional use of the ASTER VNIR channels for land classification. The retrieval was evaluated over a large range of materials from several different datasets including the SLUM dataset which is specifically tailored to the urban environment.

Utilising a method that accounted for both the spectrally varying values of LSE from the ASTER spectral library, and also the inter-channel covariance, gave the retrieval the ability to converge to the true LSE even in cases where the true LSE is very low / significantly offset from the a priori. This method lends a generic applicability

which marks it as the most practical retrieval to move forward with in development and deployment.

The retrieval was adapted and re-tooled to retrieve a proxy for water vapour in order to account for the effect that the water vapour could have on the retrieval, most notably in channel 10. The retrieval was able to successfully incorporate this additional parameter without significant detriment to the retrieved values or uncertainties. The addition of water vapour correction improves the ability of the retrieval to adapt to situations where the atmospheric profile may be poorly or incorrectly known, as could often be the case at high spatial resolution.

An analysis of the OE retrieval's performance was conducted on real ASTER data, for a desert site in Algodones USA. The analysis tested the OE algorithm against the existing TES methodology and a validation point. The OE algorithm performed comparably LST to TES across the scene but exhibited LSE difference, with lower LSE in rock/ bare soil areas and higher LSE in vegetative areas, creating a bias in channels 10 and 11. Comparing this to the validation site the OE method was seen to perform marginally better than the TES algorithm and showed a more consistent match with the expected LSE values. The retrieved radiance residuals were very good, especially in channel 12, showing the retrieval as a good representation of the observations.

5 Case Study I – Phoenix Arizona

5.1 Introduction

The retrieval algorithm developed in Chapter 4 was extensively tested in simulated environments to examine its accuracy and uncertainty. However, in order to assess the algorithm's practical applicability, it requires analysis when used with real data, for an urban environment. To this end, an initial case study was conducted. Firstly, the algorithm should be tested over an urban subset where there are clear features observed in the visible wavelengths. The analysis of the algorithm's performance over these features as well as its consistency temporally allows quantification of its performance with real data.

A secondary consideration during initial site selection was the availability of the data from the ASTER archive. Scenes were to be gathered from the existing historical archive rather than being explicitly tasked. At the time of first algorithm tests, the majority of the ASTER archive was not freely available. Due to this, the decision to use a city within the USA was made as this data was made freely available as part of the JAXA-NASA collaboration.

The preliminary requirements for a test scene were relatively broad. A city was required, preferably in a region with statistically low cloud fraction to ensure a maximum number of cloud free scenes and a low water vapour fraction to reduce the atmospheric effect on the retrieval.

5.2 Phoenix Test Site

The site selected for the investigation in this case study was Phoenix, Arizona. The city is large and heterogeneous, containing distinct surface types including desert, vegetation, residential roofing and large impervious surfaces associated with industrial land use. This diversity provides a representative range of sample materials

found within the urban environment. The presence of an extensive desert surrounding the city also provides a baseline for a more homogeneous surface type to assess the spatial variation in the retrieval, see Figure 43.

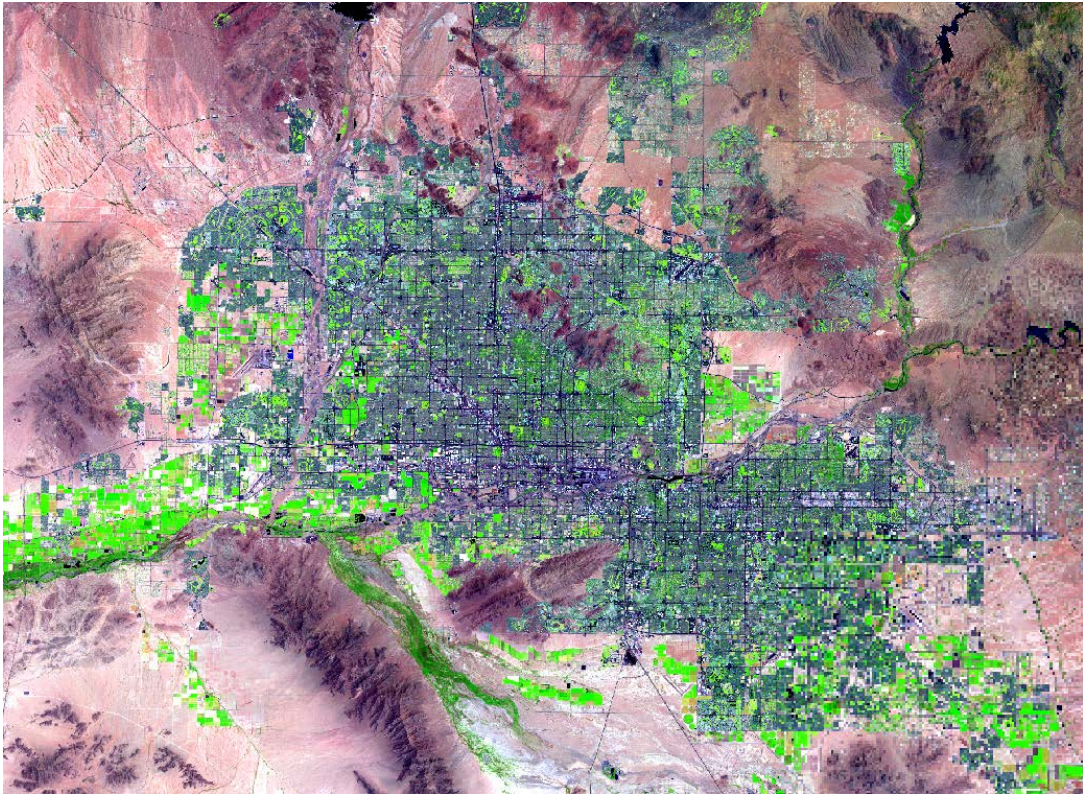


Figure 43 -False colour image of Phoenix, processed from Landsat 8's Channels 5, 4 and 3. The lime green represents the regions with increased vegetation whilst the darker green and turquoise sections show the impervious man-made materials

The city of Phoenix has an extensive heritage in studies of the urban environment and the UHI specifically, (Balling Jr & Brazel, 1987; Brazel et al., 2007; Fast, Torcolini, & Redman, 2005; Hawkins, Brazel, Stefanov, Bigler, & Saffell, 2004). Research across the scope of urban studies has intensified due to the formation of Central Arizona Phoenix—Long Term Ecological Research (CAP-LTER), for which Phoenix is a study site (Grimm & Redman, 2004). In particular, temperature studies have started to investigate the finer scale spatial structure associated with the UHI and the land class/land use implications in the UHIs evolution and effects (Jenerette et al. 2016; Wang et al. 2016). The application of high spatial resolution satellite data that can assess land class, through a combination of LST and LSE, and traditional UHI studies could greatly enhance understanding of urban heat in Phoenix (Connors et al., 2013). As the IR LSE data can be directly input to energy balance models without the need for class loop up tables.

Phoenix is particularly invested in study of vegetation in the UHI as Phoenix is a desert city and therefore vegetation growth is the product of artificial irrigation and watering. Vegetation has been identified as a key parameter in understanding urban heating, (Zhang, Zhong, Feng, & Wang, 2009), but the influence of vegetation can be more complex in this arid environment, where the energy cost associated with watering and irrigation can be high, requiring further study (Gober et al., 2009; Guhathakurta & Gober, 2007; Halper, Scott, & Yool, 2012).

Given this, a key focus of this study was not only to evaluate the performance of the algorithm in terms of consistency and uncertainty, but also to assess its potential applicability to investigate specific questions relating to the urban environment of Phoenix; most prominently the effect of vegetation on the LST and the ability to identify differing land types through the LSE.

5.3 Data Pre-Processing

In order to facilitate efficient and high quality retrievals, several stages of pre-processing are required.

Firstly, the atmospheric water vapour section of the retrieval outlined in section 4.4 utilises a large number of water vapour profiles to construct valid retrieval Jacobians and to generate well defined a priori profiles. To this end, several thousand ECMWF ERA interim profiles were obtained representative of the atmosphere for Phoenix and used to generate simulated ASTER TOA at the various a priori LSEs.

Secondly, a classification is required for the method to derive a priori LSE. The classification is best achieved with optical channels in the VNIR. Hence daytime scenes are studied here. The VNIR and TIR datasets are at different resolutions, (L1T data additionally has an irregular number of pixels in each L1T scene see section 3.2.2.4.1), and therefore it is necessary to re-grid the data so that both datasets are given on the same geo-spatial grid at the same scale, for both L1b and L1T. To do this, both the VNIR and the TIR are independently geo-registered and the VNIR pixels within each TIR pixel then averaged to produce a VNIR dataset at the same resolution as the TIR data.

At this point a basic cloud screening is conducted. Many of the scenes dealt with in this thesis are arid or semi-arid and therefore clouds have not been a significant issue, nevertheless the scenes were selected initially based upon the native cloud flag provided with the ASTER L1b/L1T data. If the scene was not listed as having a high cloud content a second screening was made using the VNIR data to identify visible clouds missed by the flag. Finally a check of the TIR BTs was made to identify anomalously lower temperatures indicative of clouds. The resulting filtered dataset is used in subsequent analysis.

Finally the MODIS LST data must be matched to the same geo-spatial grid as the finer scale TIR data. For each ASTER TIR pixel the MODIS pixel that it lies within is found and that LST information is attached to the ASTER TIR pixel.

5.4 Land Classification

The a priori LSE for each channel is drawn from the ASTER spectral library as discussed in 4.2. The a priori LSEs used in the simulated cases were drawn from 3 classifications: vegetation, soil/dust and urban. However, these classifications need to be assigned to each pixel in the scene before the retrieval can be started. In order to do this, a prior land classification capable of identifying these three classes must be used. Two methods were investigated to achieve this prior classification and they were tested using a subset of the Phoenix image centred on the city airport, see Figure 44.

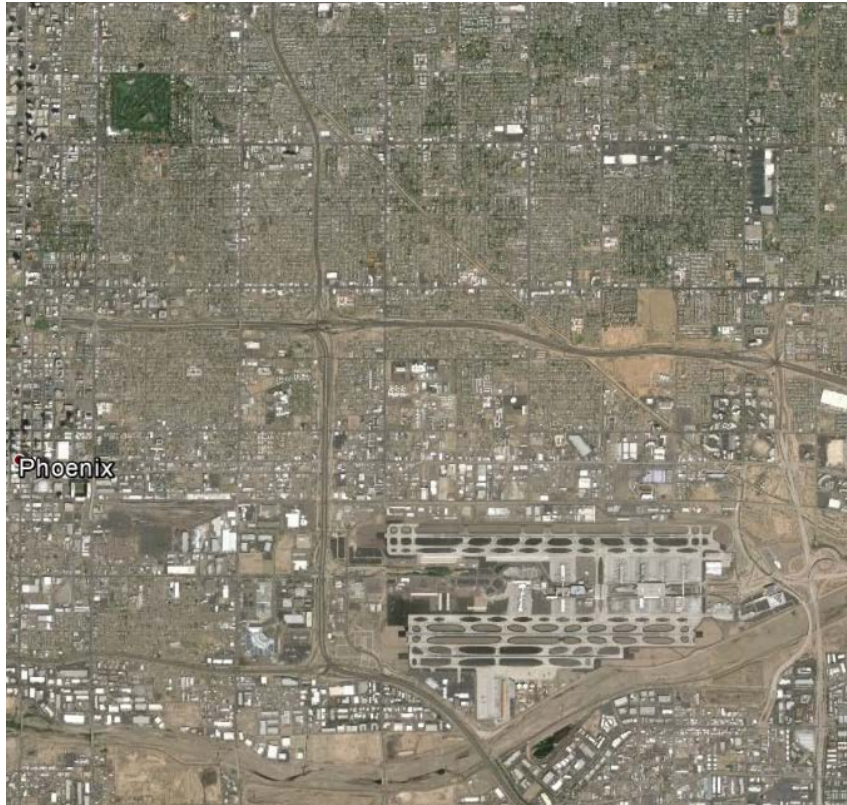


Figure 44 – A visible true colour image of the subset which was used in initial testing of the classification and the retrieval algorithm. Image taken from Google earth, 33.460 N, -112.060 E, image acquired 16/03/2015, image obtained 16/07/2016.

5.4.1 VNIR Classification

The first and simplest method used was a direct radiance based classification using the ASTER VNIR bands. In this method, the ratios of the radiances seen in each band were assessed and estimated thresholds applied to these radiances, attempting to group the different spectral responses of the different material types, see Figure 45. This method requires manual identification or Regions Of Interest (ROIs) and assigning each ROI to a spectral characteristic seen in the ration of the VNIR channels.

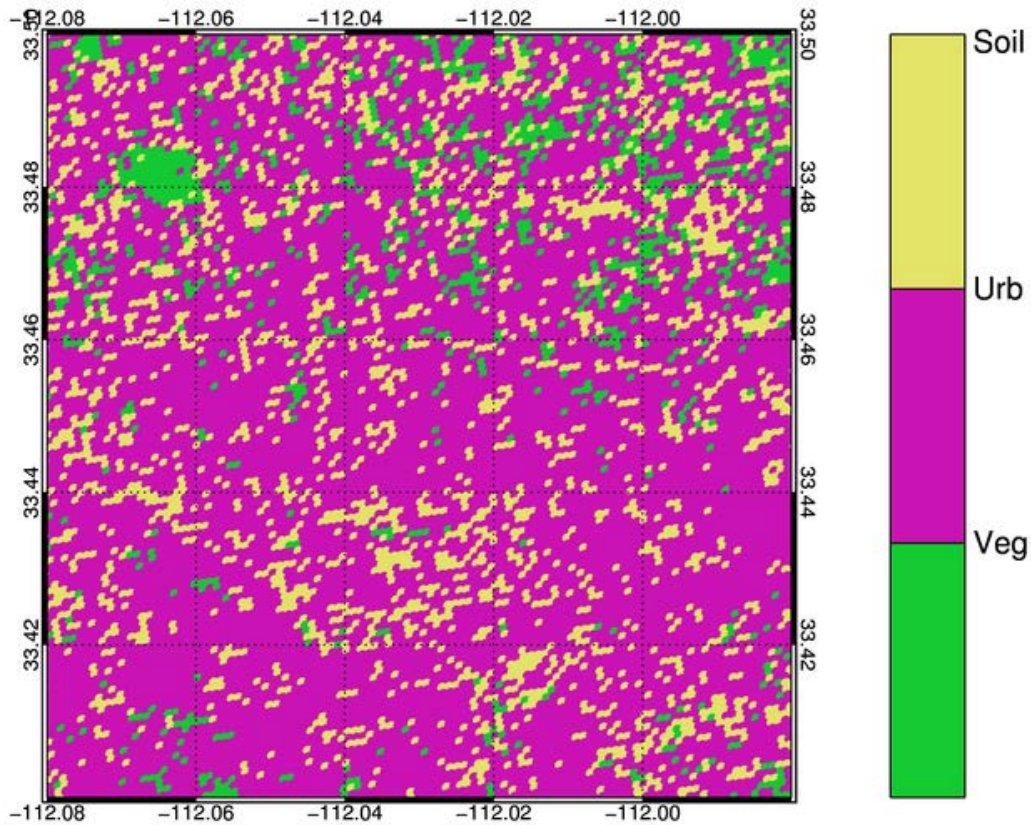


Figure 45 – Land classification map over a spatial subset of Phoenix, Arizona. The classification is based off the ratio of the VNIR channel radiances.

As seen in Figure 45, there is a significant amount of soil and vegetation in addition to the urban class. The large block of vegetation seen in the top left of the scene was mapped to a park/recreation ground in the subset; the park is clearly visible in Figure 44 and Figure 45. However, much of the vegetation seen in the rest of the scene was not seen to correspond to fully vegetated areas; rather, it was found to be highlighting sub-urban housing where the land class was a mixture of garden, buildings and road. Subsequent analysis was unable to further refine the radiance ratio thresholds to a point where it was robustly identifying these sub-urban regions separately from the larger vegetative regions, indicating either a spectral similarity at these wavelengths or a lack of spectral sensitivity in the VNIR channels to the differences.

5.4.2 K-Means Cluster Analysis

A second method investigated was that of k-means cluster analysis in an unsupervised classification. K-means clustering is a computational grouping scheme

allowing information to be clustered based only upon the information of a point and its relationship to the other points around it (Burrough, van Gaans, & MacMillan, 2000). In the case of the ASTER VNIR land classification the k-means assesses the division of data into clusters based upon the radiances similar to the previous method, but it takes into account spectral contrast and spatial separation. The algorithm takes into account the spatial separation of the points it is comparing as well as the similarity to the all of the points already assigned to the cluster. The analysis starts with a number of randomly selected points equal to the number of clusters requested as an output, in this case 8 starting clusters to be manually refined latter. The algorithm begins iteratively assessing each point to the clusters, weighting the radiant similarity by the pixels spatial location. Having completed the first iteration, the properties of the clusters are recalculated based upon its new member composition.

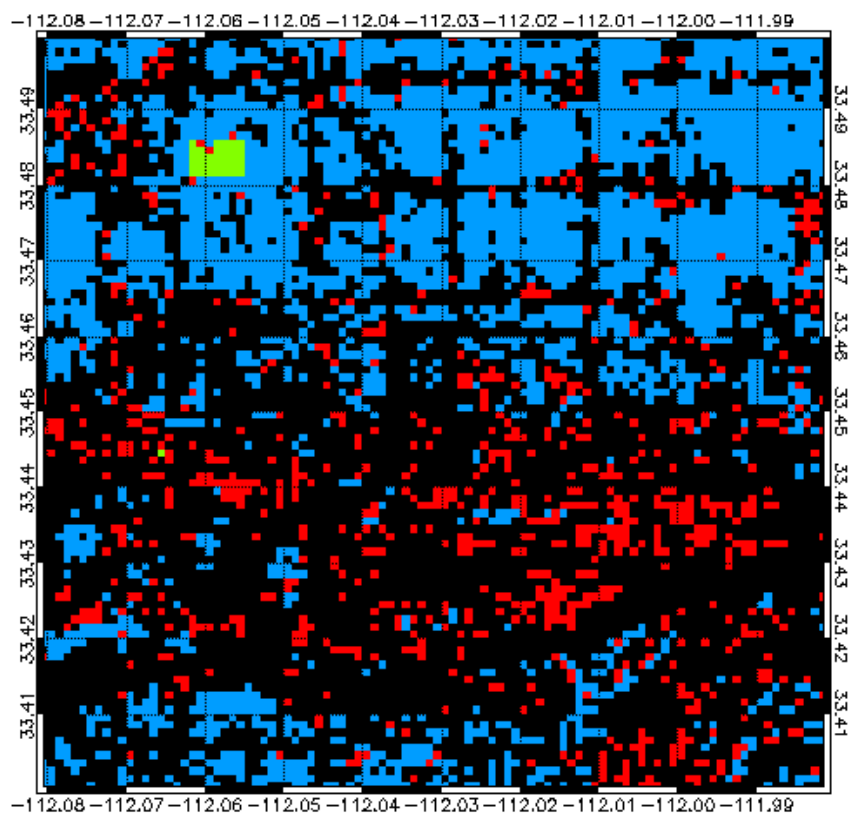


Figure 46 – K-means land classification map for the Phoenix scene subset. The four classifications returned here are: urban (black), soil/dust (red), vegetation (green) and mixed urban/vegetation (blue). Taken 20/05/2011.

This approach enables the classification to a finer degree of distinction than the previous method allowing the introduction of a fourth classification type: mixed urban and vegetation.

Comparing Figure 46 to Figure 44, it is immediately apparent that the visually identified vegetation areas are now better represented in this classification scheme. Additionally the blue mixed areas are a strong match to the regions in which the suburban sprawl dominates. Furthermore, the bare soil/sand category no longer follows the major road network as it did in Figure 45, indicating that the algorithm is better able to correctly classify the distinction between natural and manmade impervious materials.

The mixed class was designed to be a flexible representation of a variable ratio of urban and vegetative materials. To that end, the class itself is not fixed from the ASTER spectral library as the other classes are: In this case, the mixed LSE is calculated as a proportionately weighted mean of the urban a priori case and the vegetation a priori class. The weight of each class to be used in the calculation of the mixed a priori is determined using the Normalised Differential Vegetation Index (NDVI) calculated from the VNIR bands TOA radiances.

5.5 Initial Scene

The retrieval was applied to the first of the Phoenix scenes using the k-means derived land classification scheme and the water vapour methodology outlined in 4.6. The processing focussed on the subsection dealt with in the previous section, a scene that is 100x100 pixels in size.

5.5.1 Retrieved LST and LSE

Figure 47 shows the full scene retrieval for LST, for a daytime retrieval on 20th May 2011. Temperatures range from around 290-325 K. The spatial structure that emerges immediately raises several areas of interest. The vegetative region seen in the false colour imagery in Figure 43 is clearly visible in both the LST and the LSE in Figure 47 and Figure 48 respectively as a region of LST depression and heightened LSE (Lat 33.485, Lon -112.06). The depressed LST is large ~ 10 K, as would be expected, due to the combination of the albedo change and the heat loss associated with evapotranspiration associated with the plant matter. The LSE is consistent with the spectrum of vegetation.

Additionally, low LSE and high LST structures are seen surrounding the vegetative region at 33.5 N -111.85 W and towards the north west of the scene. Both of these locations correspond to impervious surfaces associated with exposed rock and sand, as can be observed from the false colour image in Figure 43.

The spatial subset used in the assessment of the land classification schemes in 5.4 is highlighted in Figure 50 and Figure 51. Many of the key features identified in the k-means cluster classification are visible in the subset. The park/golf course in the north west of the subset identified in the classification as vegetation is also present in both the LST and LSE with the expected characteristic for vegetation.

However, there are several features emerge that were not apparent in the a priori data. The LST and the LSE shown in Figure 50 and Figure 51 show the airport distinctly and have markedly different structures. There is a region of low LSE, as seen in Figure 51 beneath the main airport structure. This pattern can be seen in Figure 44 to match a dry river basin south of the airport itself. These regions have similar LST to the surrounding urban pixels but sharply lower LSE due to the high proportion exposed rock/sand showing a change in LSE but little anthropogenic heating.

On the other hand, the main airport building is, in term of LSE, quite similar to the urban background. The LSE seen in Figure 51 shows consistent levels between the airport structure and feature seen throughout the scene. The LST in Figure 48 is in sharp contrast. The main airport structure in fact denotes the warmest section of the retrieved scene, with temperatures up to 5 K above the scene mean. The disparity between the seemingly normal LSE ranges corroborated by the visual imagery and the retrieved LST shows signs pointing towards the effect of anthropogenic heating. The structure is a heavily used industrial complex, which leads to a significant increase in the net heat produced; this provides the most probable source of the increase in the emitted radiation observed by the satellite.

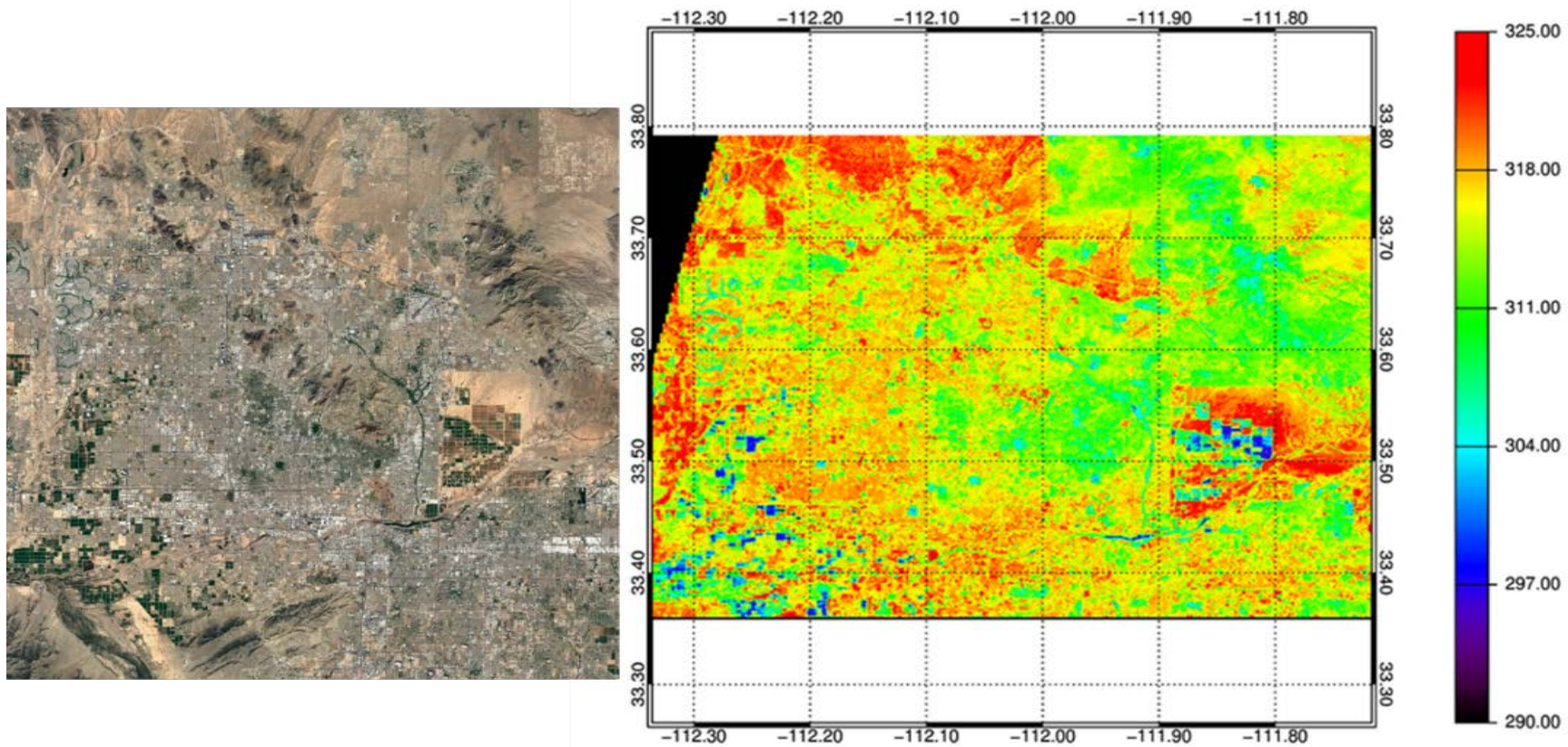


Figure 47 – LEFT: A visible true colour image of the full scene, Image taken from Google earth, 33.460 N, -112.060 E, image acquired 04/03/2011, image obtained 16/07/2016. RIGHT: Retrieved LST (K) for the full study site on 20/05/2011

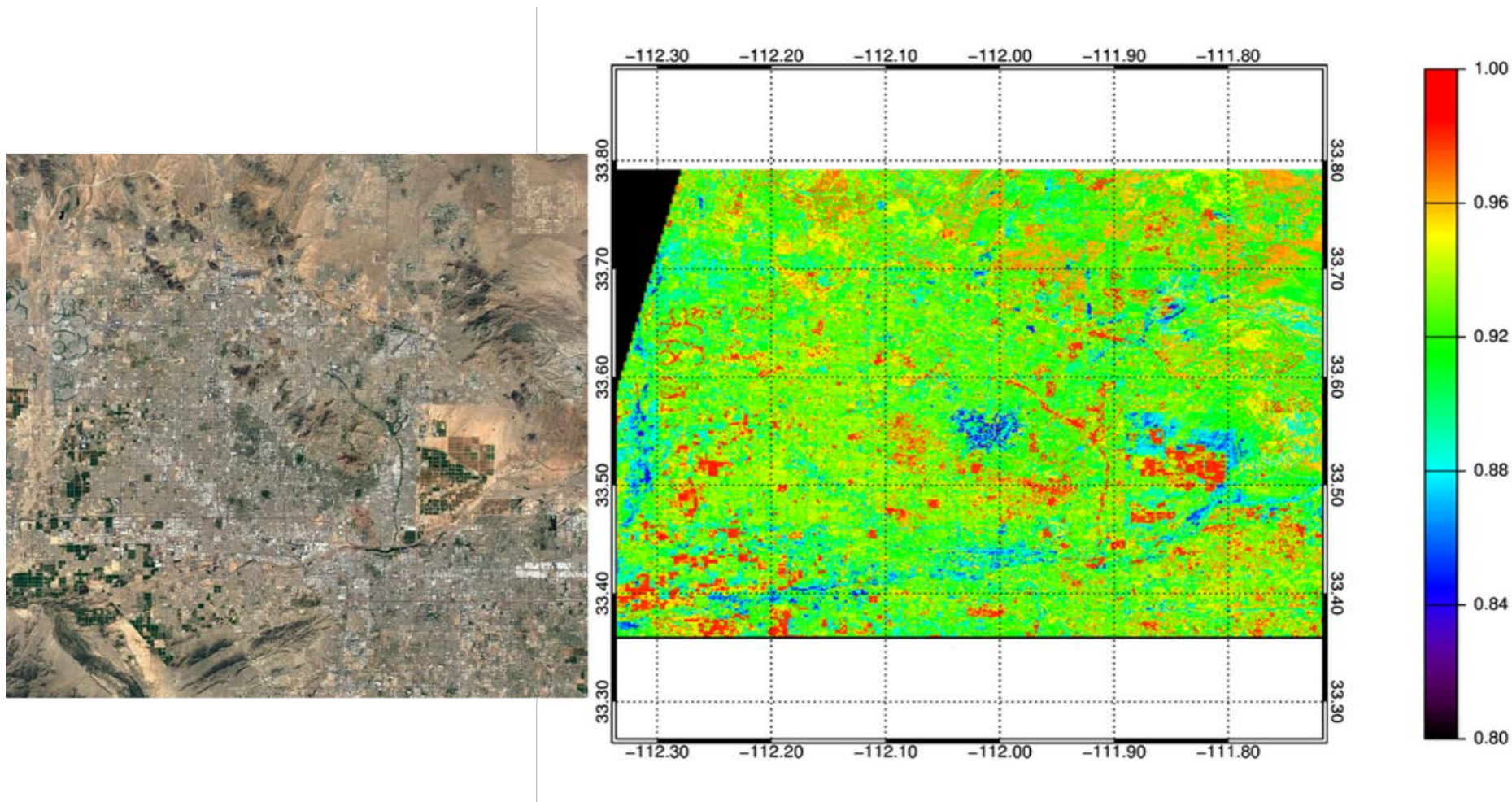


Figure 48 – LEFT: A visible true colour image of the full scene, Image taken from Google earth, 33.460 N, -112.060 E, image acquired 04/03/2011, image obtained 16/07/2016. RIGHT: Retrieved LSE in Channel 12 for the full study site on 20/05/2011

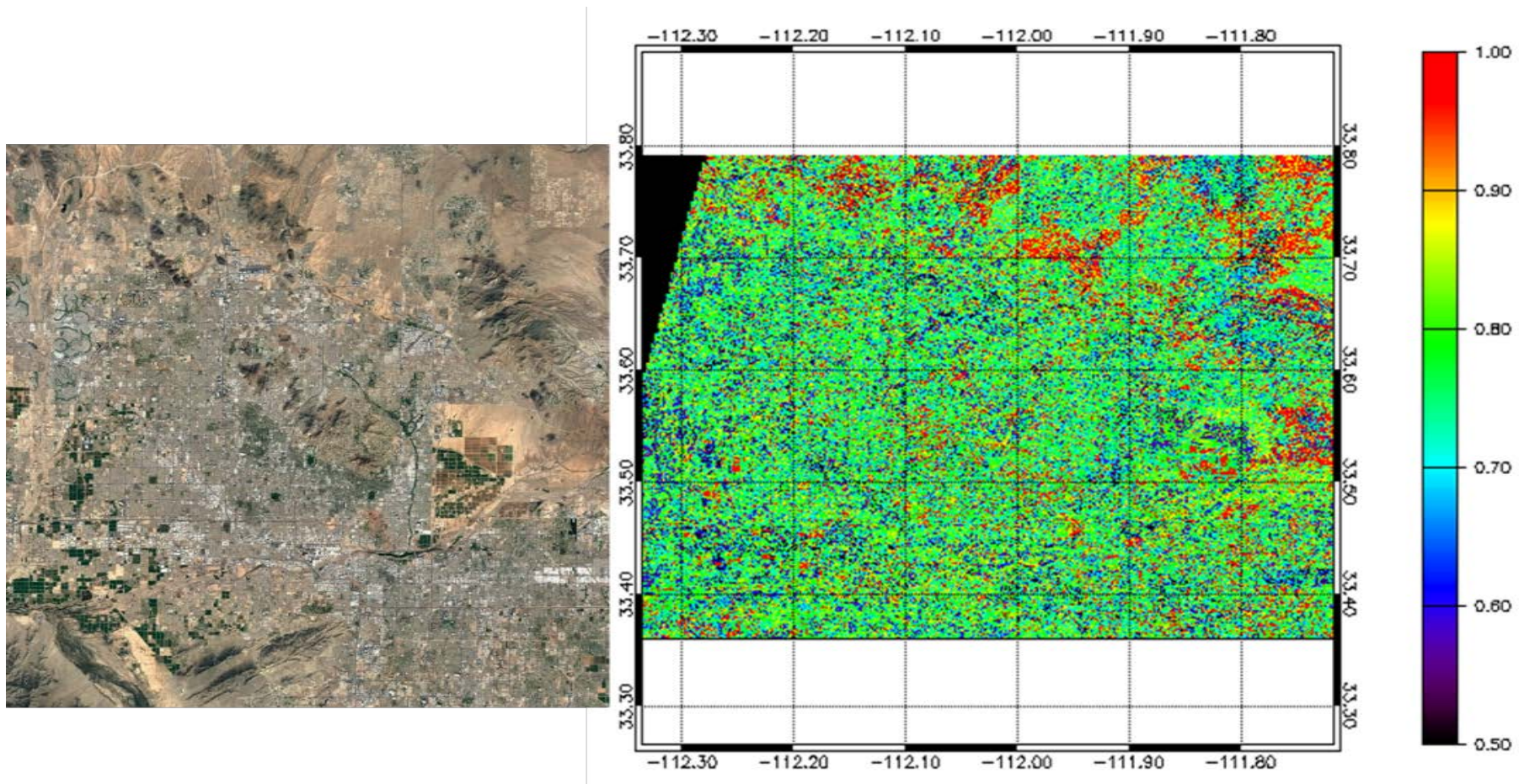


Figure 49 – LEFT: A visible true colour image of the full scene, Image taken from Google earth, 33.460 N, -112.060 E, image acquired 04/03/2011, image obtained 16/07/2016. RIGHT: Retrieved Water vapour for the full study site on 20/05/2011 (cm)

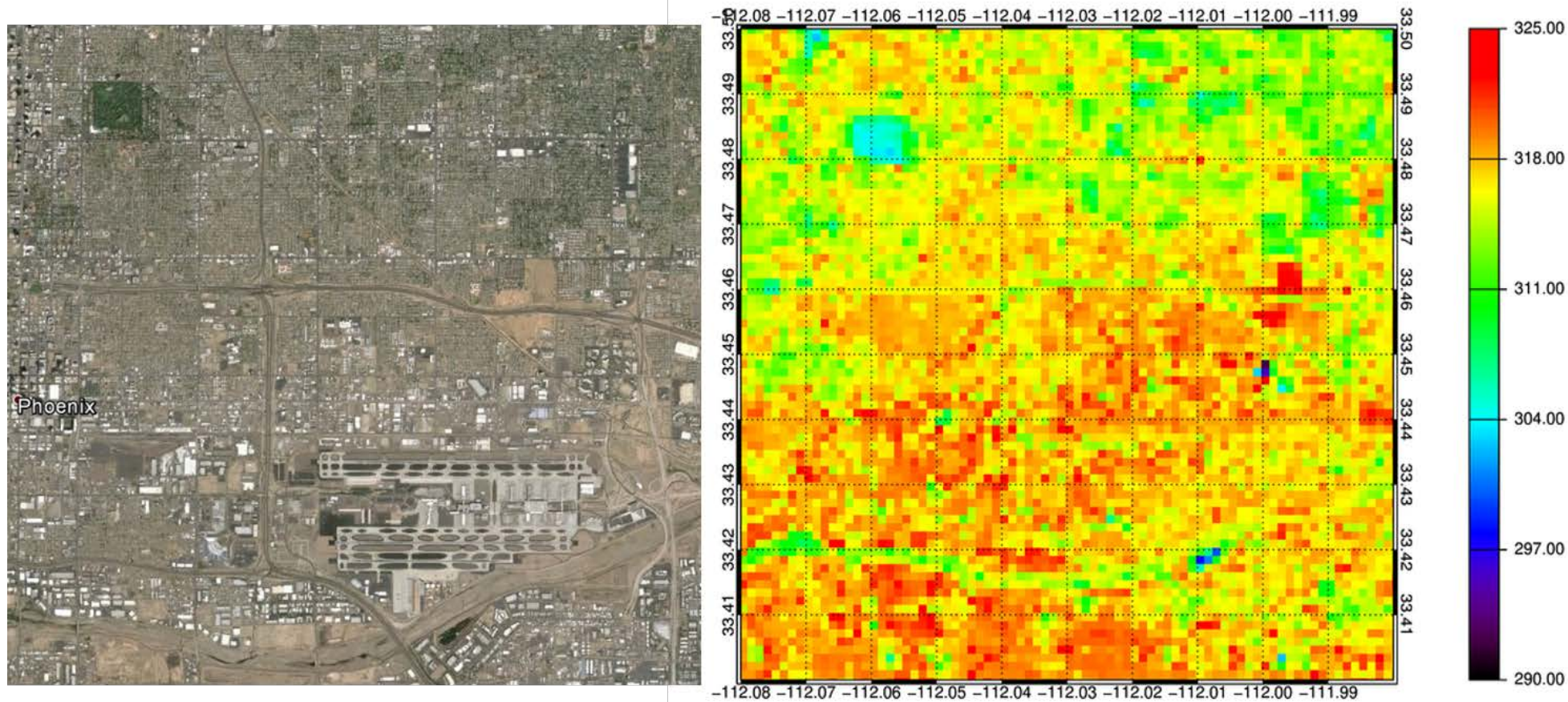


Figure 50 – LEFT: A visible true colour image of the subset which was used in initial testing of the classification and the retrieval algorithm, Image taken from Google earth, 33.460 N, -112.060 E, image acquired 04/03/2011, image obtained 16/07/2016. RIGHT: Retrieved LST (K) for the spatial subset of Phoenix on 20/05/2011

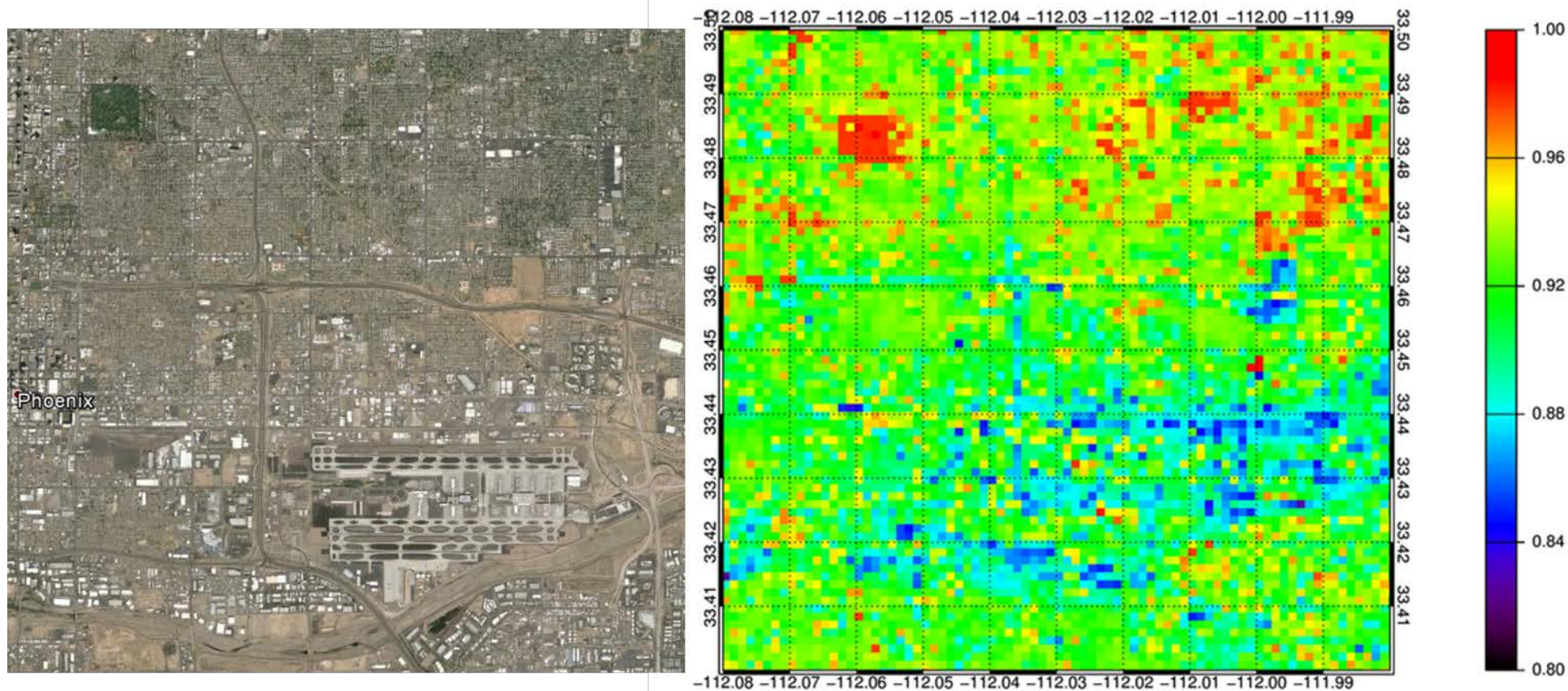


Figure 51 – LEFT: A visible true colour image of the subset which was used in initial testing of the classification and the retrieval algorithm, Image taken from Google earth, 33.460 N, -112.060 E, image acquired 04/03/2011, image obtained 16/07/2016. RIGHT: Retrieved LSE in Channel 12 for the spatial subset of Phoenix on 20/05/2011

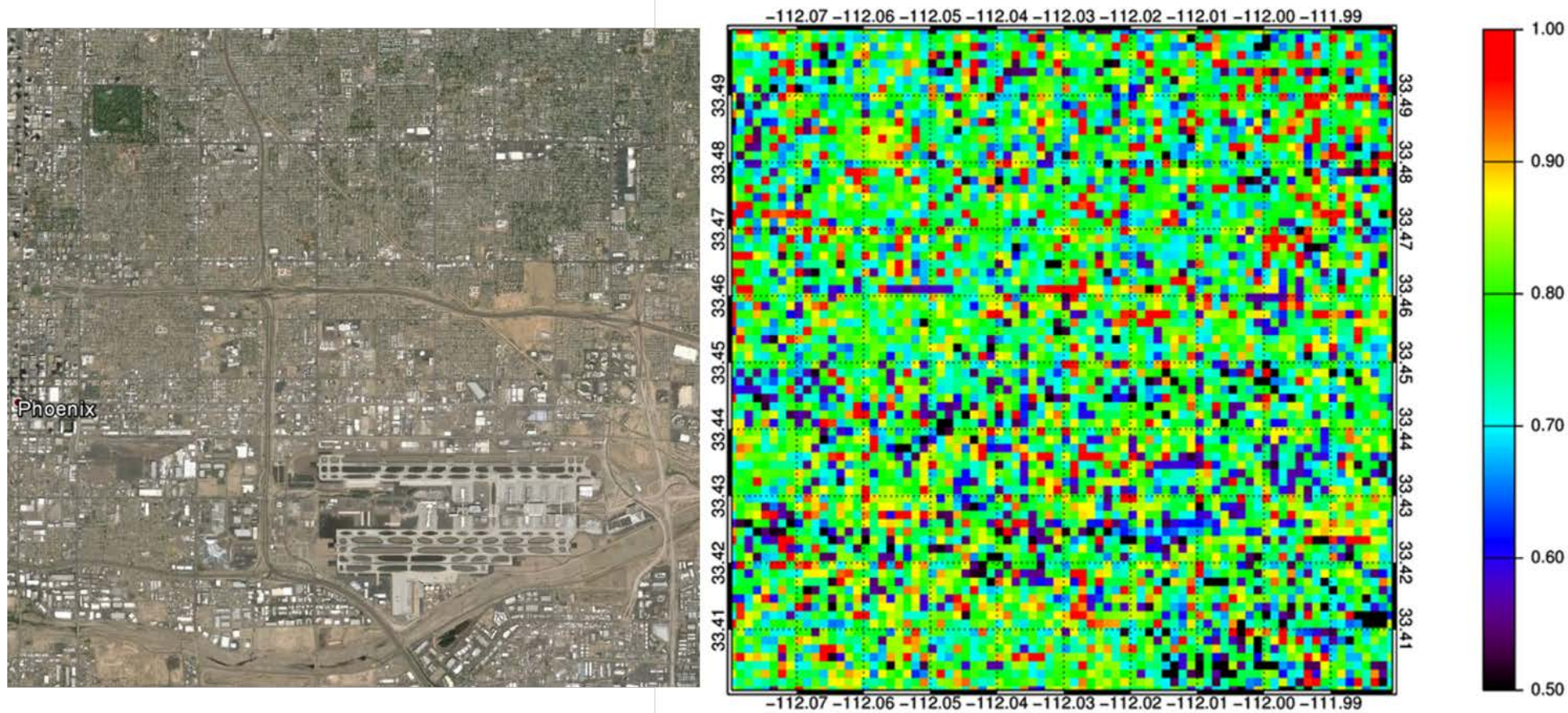


Figure 52 – LEFT: A visible true colour image of the subset which was used in initial testing of the classification and the retrieval algorithm, Image taken from Google earth, 33.460 N, -112.060 E, image acquired 04/03/2011, image obtained 16/07/2016. RIGHT: Retrieved Water Vapour for the spatial subset of Phoenix on 20/05/2011(cm)

The regions specified in the land classification scheme as mixed urban/vegetation have a notable impact on the retrieved LST and LSE. These areas present an example of urban green space being used as a cooling force through the process of evapotranspiration, similarly to the park highlighted previously. However these are also the regions with the largest potential error in classification as the criteria for the distinction between this class and the urban or vegetative classes relies upon the use on an NDVI constructed from non-atmospherically corrected radiances.

This means that due to atmospheric influences, the boundaries between this class and the vegetation and urban could move, independent of the physical surface cover.

The mixture of the housing and gardens in these regions leads to a retrieved LSE that is far less distinct than the pure vegetative areas. The cooling effect even with this incomplete vegetation cover shows the importance of urban green space even at the sub-pixel level. Demonstrating a mitigation of anthropogenic heating of approximately 10 K from the mean difference between the park and the surrounding urban region.

The retrieved proxy for water vapour as shown in Figure 49 and Figure 52 shows some spatial structure, most likely due to surface influences. The full scene water vapour appears to have noisy distribution with features scene in the north-east of the scene over regions of high elevation. However this variation is all within 0.5 to 1 cm TCWV showing little absolute variation, as would be expected for a semi-arid region. The subset shows some signs of surface influences, with some roads and the dry river basin regions visible in the retrieved proxy. However the majority of the subset has the same noisy distribution across all land classifications, showing no clear bias.

5.5.2 Retrieval Statistics

The statistics of the retrieved results from the whole scene allows the behaviour of the retrieval to be investigated. The histograms seen in Figure 53 show the distribution of the retrieved LST and the LSEs across the five channels. The distribution of the LST is a skewed Gaussian about a mean of 315.4 K with a standard deviation of 3.982 K. The distribution trails off more gradually towards the lower LSTs, the lower values correspond to the LSTs associated with the vegetative areas.

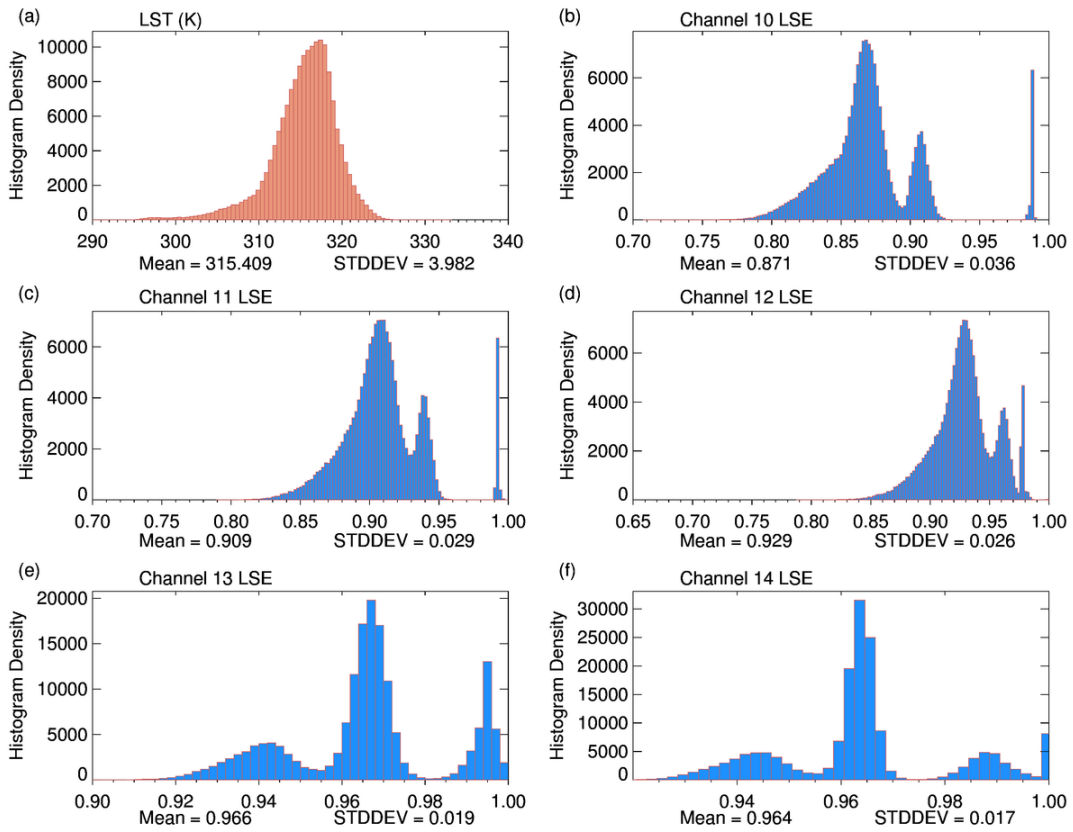


Figure 53 - Histograms for the retrieved values of LST and LSE for Phoenix, with the mean and standard deviation of each set.

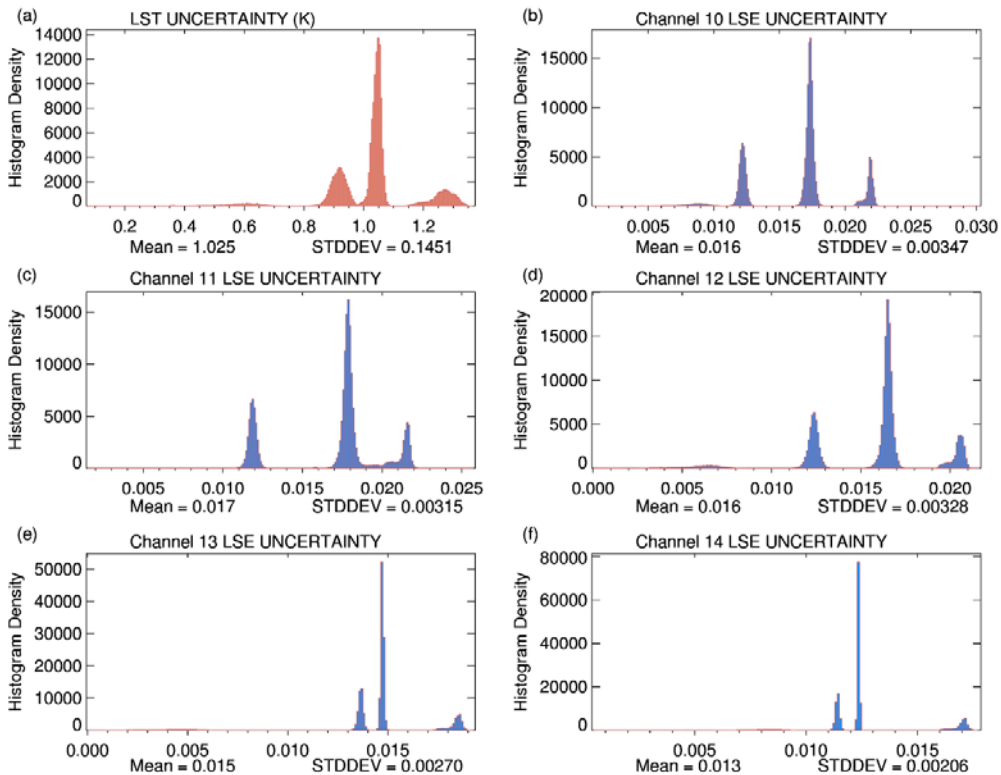


Figure 54 - Histograms for the retrieved uncertainties for LST and LSE for Phoenix.

All of the retrieved LSEs lie within a range of 0.78 to 0.99 which is within the range for materials expected within the scene. The LSE results show two distinct distributions. In channels 10, 11 and 12 there is a main Gaussian distribution with a double peak, and a separate peak in a second distribution. The peak close to one corresponds to the pixels over pure vegetation such as crop land and parks, or the areas in the suburban regions with a high proportion of vegetation. The secondary peak on the main distribution matches the pixels identified as being a mixture of urban and vegetative materials. The main peak is for the urban materials which dominate the scene land cover.

Channels 13 and 14 have LSEs over a far smaller range and also show a different three peaks in the distribution. The pixels with the highest LSEs are once again those associated with vegetation, but peaks at around 0.97 now include the urban vegetation mix and the majority of the urban pixels. The third peak at lower LSE includes the impervious surfaces with low LSEs including both manmade and natural surfaces such as sandy soil and asphalt. The spectral similarities of these materials makes it difficult to make a clear separation between these low LSE materials.

Channel 14 in Figure 53 has a small number of pixels with values extremely close to 1, approximately 0.999. These values are thought to be non-physical as materials with such LSEs are not naturally occurring, especially not at such scale. Instead these pixels result from the balancing of the mathematical process of the iteration with the physical limitations of the system.

The retrieved uncertainties in both the LST and the LSE show very distinct groups, see Figure 54. These groupings relate to the a priori LSEs given to the retrieval which follow three main classifications: urban, soil/sand and vegetation. The LST uncertainties range between 0.5 and 1.35 K with a majority of LST retrievals having an uncertainty of 1.025 K which approaches the desired requirements the LST at medium spatial resolution and is better than the requirement of 1.5 K from Chapter 1. The retrieved results are statically statistically on a par or better than the stated uncertainties for the TES algorithm.

The largest LSE uncertainties are seen in the first three channels in the 8-9 micron window. Channels 10, 11 and 12 are all under ± 0.025 , and the LSE in channels 13

and 14 retrieved with an uncertainty of less than 0.019 and with mean LSE uncertainties of 0.016-0.013 across the channels.

The radiance residuals seen in Figure 55 are also close to Gaussian in distribution. However there are some tails on the Gaussians. Channel 12 stands out as the channel with the lowest radiance residuals for all the retrievals. These residuals are extremely small and peak at a value of 0.001 K. It is possible that the retrieval finds it easiest to minimise the residual in this channel. The majority are with the instrument noise of 0.3 K.

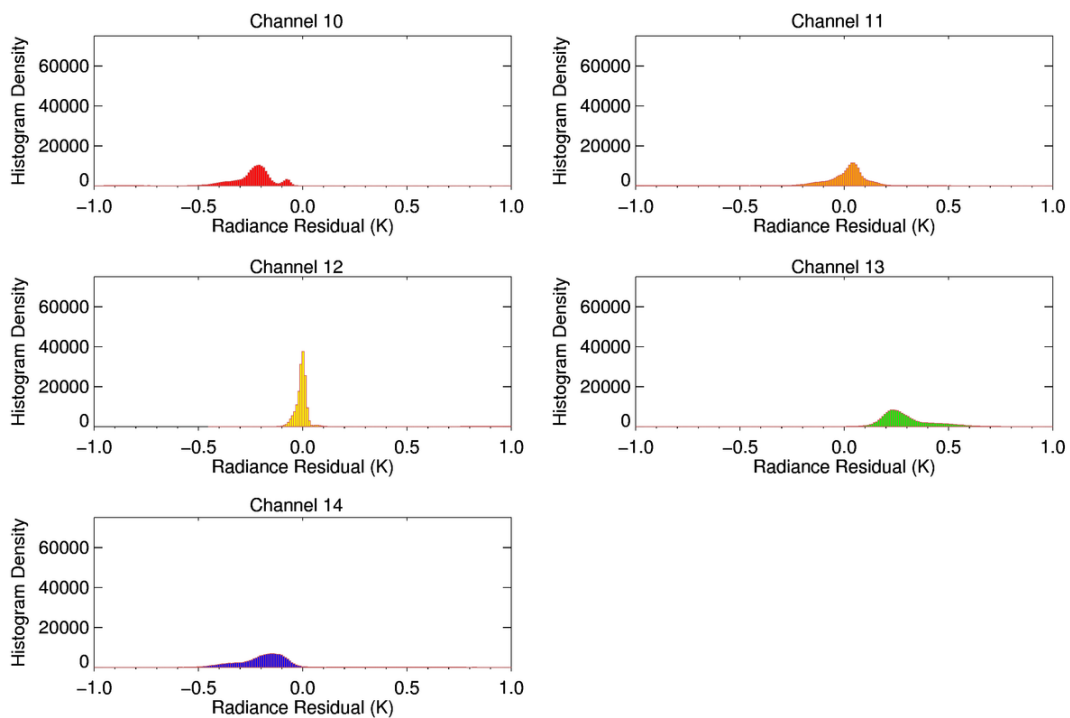


Figure 55 – Histogram of the retrieved radiance residuals for Phoenix.

In testing these scenes and in the simulated cases in Chapter 4, channel 12 was found to have a greater significance for the success or failure of the iteration procedure. Tests on the ASTER spectral library found that there were three groups in the channels where the LSE varied co-dependently depending upon the dominant surface type, see Table 2 in 4.1.2.

Date		Radiance Residual				
		C10	C11	C12	C13	C14
20/05/2011	Mean	-0.346	-0.013	0.037	0.344	-0.167
	Std Dev	0.491	0.194	0.216	0.264	0.201

Table 19 – Mean and standard deviations for the radiance residuals for all channels in the retrieval.

The values of the radiance residuals are small and show a good agreement between the observed and simulated radiances, see Table 19. Channel 10 is the channel most susceptible to atmospheric influences and is typically expected to have the worst performance of the channels given an imperfect atmosphere, and has the largest mean radiance residual and standard deviation. All are under 0.5 K showing that the retrieval has a good representation of the observations.

5.6 Variance analysis

In order to assess the consistency of the retrieval's performance, the same Phoenix Arizona test scene was analysed for images recorded at different dates. In total five scenes overlooking the same spatial region and with comparable cloud and atmospheric conditions were assessed.

The subset selected in the classification study was used to assess the LSE stability between scenes. Each pixel in the scene was averaged and the standard deviation calculated, see Figure 56 and Figure 57. The retrieved LSEs were not expected to match perfectly as there will inherently be variation associated with small surface changes such as water, dust and particularly for Phoenix, moving sand and changing the pixel scale LSE. There will also vegetation changes within the urban environment based upon season in addition to actual urban land use change over the same time scale.

5.6.1 LSE

Channel 10 shows the greatest LSE variation between the scenes, while much of this may be due to this channel due to the sensitivity to atmospheric influence. It is also in channels 10, 11 and 12 that the LSE of material types analysed in Chapter 4 show the greatest variation. However the LSE differences between observations seen in channel 10 are greater than those seen in channel 11 and 12.

In the Channel 10 image, there is a cluster of points with extremely high LSE variation in the south eastern corner of the subset, denoted in Figure 56 by the white circles. This large standard deviation is likely due to the presence of water. The pixels lie within a dried out river bed, however sections of the river basin still periodically fill with water. Therefore from scene to scene there is a large LSE difference between water and the underlying sandy soil providing a large variation, the detection of this points towards the possibility of change detection with this methodology.

By far the most stable region of the scene, as evidenced by the LSE, is the park/golf course in the north west of the subset. The LSE across all of the five TIR channels has very low standard deviations, see Table 20, across all the temporal snapshots, this shows a high precision in the LSE retrieved and reflects well on our prior knowledge of the vegetation here. Also the absolute LSE values are in line with those expected for vegetation in all channels.

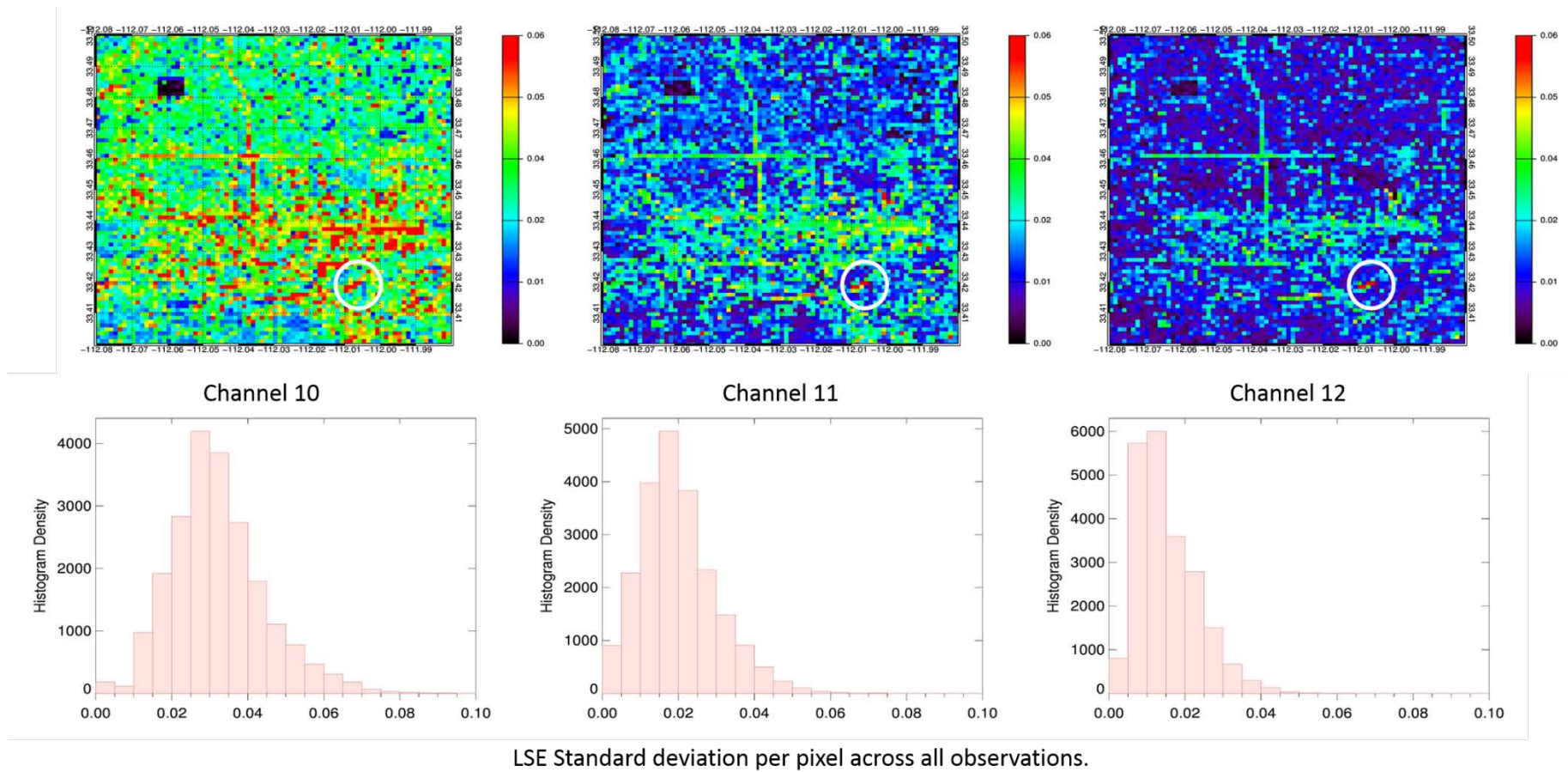


Figure 56 - The LSE standard deviations for all pixels in the subset. TOP: a map of the distribution of the standard deviation. BOTTOM: a histogram of all the pixels in the subset. LEFT to RIGHT: Channel 10, 11 and 13. White circles highlight water variation.

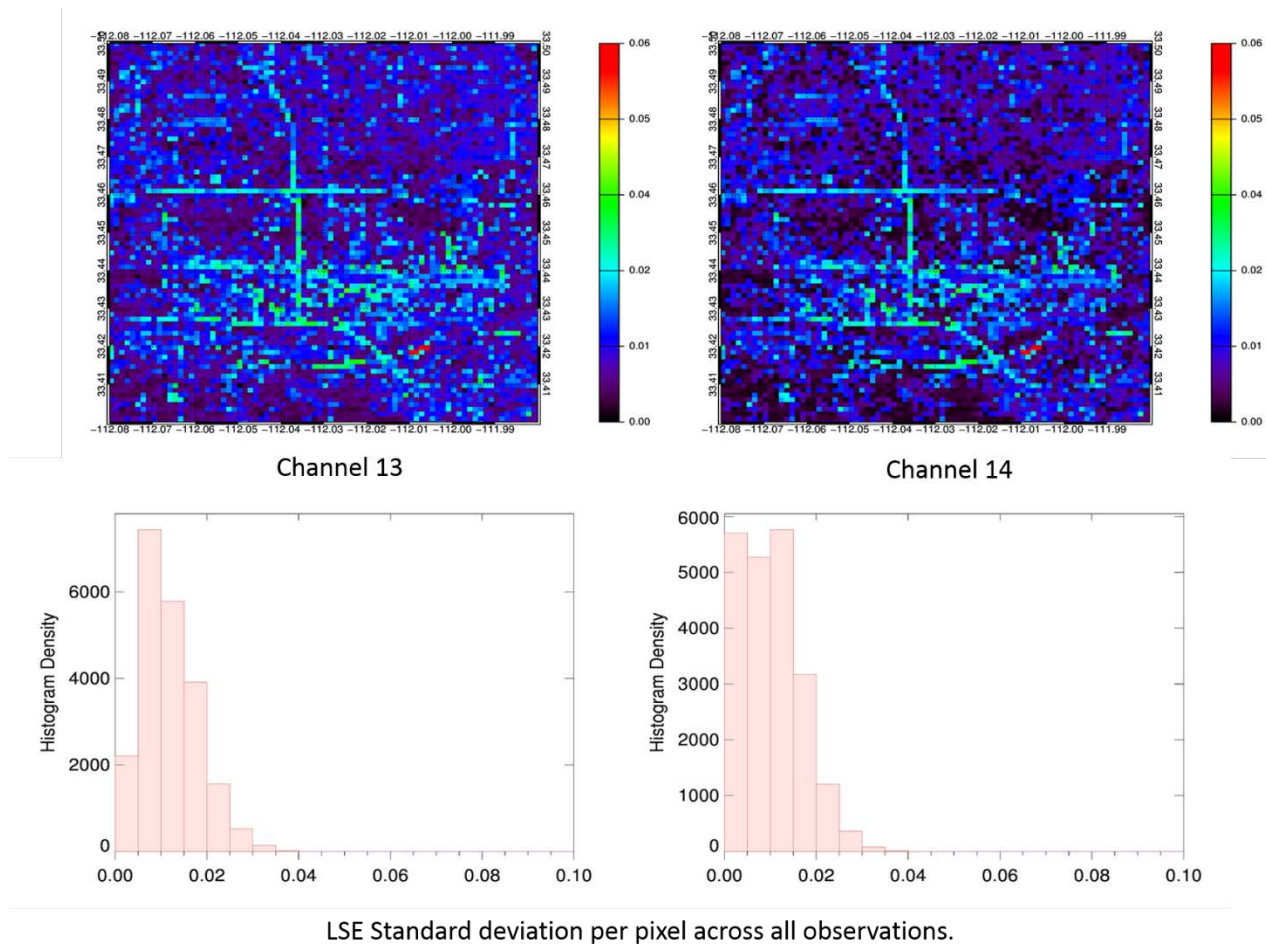


Figure 57 - The LSE standard deviations for all pixels in the subset. TOP: a map of the distribution of the standard deviation. BOTTOM: a histogram of all the pixels in the subset. LEFT to RIGHT: Channel 13 and 14.

	C10 LSE	C11 LSE	C12 LSE	C13 LSE	C14 LSE
Mean	0.988	0.991	0.977	0.992	0.996
Std Dev	0.001	0.003	0.004	0.007	0.008

Table 20 – Mean and Standard deviations for the LSE in all channels for the centre of the park between observations.

The principal source of LSE deviation from the mean in the retrieved pixels relates to the sub pixel variation. Taking an area with a consistently high variability this becomes clearer. The roadways intersecting at 33.46 N -112.35 W show a high standard deviation from the mean LSE for the subset, with deviations of 0.04 to 0.06. The road surface is covered in asphalt which has a distinctive LSE signal in the five TIR channels, see section 4.5. However the pixels here are larger than the roadway and therefore will only contain a fraction of the road surface. The rest of the pixel will contain road side vegetation, commercial and residential structures. These will all have differing quantities of materials with varied LSEs. This effect is amplified when looking at the same scene at different temporal intervals. Firstly changing vegetation will directly impact the real physical surface averaged within the pixel. Secondly the ASTER scenes are not perfect repeat overpasses and therefore small differences in the viewing geometry mean that the pixels have to be arranged on a common grid, especially so with the LIT data, see section 3.5. As the position of the constituent pixels shift the new grid pixel composition on a constant grid changes based upon where the underlying pixels lie in relation to the new grid. It seems clear overall that LSE deviation is able to highlight some road structures.

5.6.2 LST

In comparison to the LSE, the LST has significantly greater standard deviations across the scene. As seen in Figure 58 the spatial variation is significant across the subset. LST deviation ranges from 5 to 15 K with a mean standard deviation of 10.5 K across the time period observed.

The LST is expected to have greater variation than the LSE as the LSE will often represent a relatively static surface. Apart from the changes due to vegetation and gridding of observation the surface will experience changes at a much slower pace than that of the rapidly changing LST. The LST deviations seen here, with changes

of the order of 10 K or greater, show a variability far greater than the uncertainty in the a priori estimates, with a covariance of 5 K, and with a consistency that indicated real physical change in the temperatures present.

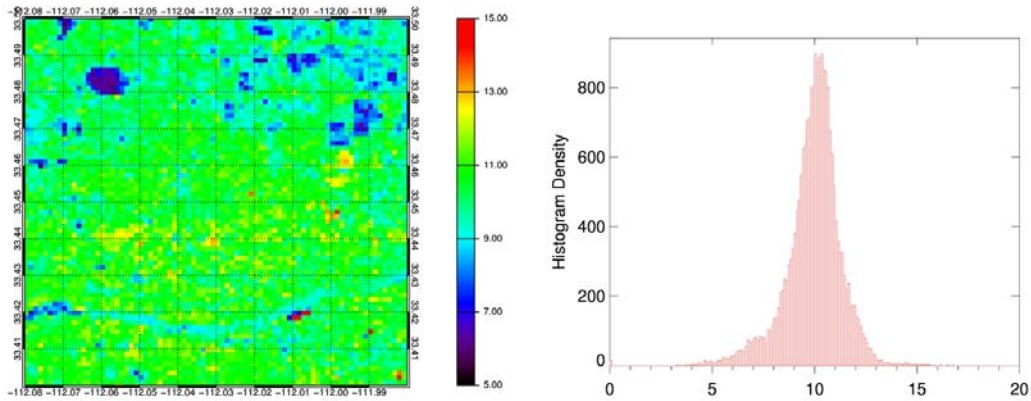


Figure 58 - The standard deviation for the LST from a mean calculated from a composite of all the scenes studies. The LEFT, panel shows the spatial distribution of the LST standard deviations (K). The RIGHT panel shows the histogram of the standard deviations across the subset (K).

Similarly to the LSE the most stable regions are those with distinct vegetation cover. However in the case of the LST retrieved this includes regions not purely dominated by vegetation such as the mixed urban and vegetation area in the north east of the subset. Even a small fraction of vegetation within an area is seen to stabilise the LST and reduce the fluctuation between snapshots. Vegetation providing a mean variation of 5 K, and mixed urban and vegetation with a mean variation of 7-9 K. The urban surfaces show a higher variation of 11-12 K.

The regions with the greatest LST variation are not found to follow the road ways and paved surface as they did for the LSE. The LST seems to vary most over two types of surface seen in the subset. Firstly exposed rock/bare soil areas such as the one located at 33.46 N and -111.995 W. This area is exposed and undeveloped land with little or no vegetation and it is often covered in sand. This area has very few cooling mechanisms and will vary greatly under daytime conditions, with variations of around 12-13.5 K.

The influence of the underlying land class was assessed and the subset LSTs broken down into the mean and standard deviation spatially for each land class type for each retrieved scene, see Table 21.

In all cases the urban and rock/bare soil surface show the highest LSTs. The urban class is consistently the dominate land cover type in all but the scene in January 2013. The vegetation unsurprisingly has the lowest LSTs and is typically approximately 10 K colder than the LSTs seen in the urban and bare soil types.

A difference in LST between the vegetation and the urban surfaces is common across all the retrievals, even the January retrieval, see Table 21. The difference is due to several factors, most notably cooling through evapotranspiration and shading (Weng & Lu, 2008). However in the environment of Phoenix it is possibly enhanced by the contrast between the water present in the vegetation and the dry materials surrounding it.

The mixed urban and vegetation land class has significant variation in percentage cover between the scenes, the reasoning behind this is the same as for the variation in the roadway LSEs. The vegetation fraction at the sub pixel level will vary as will the overall pixel composition due to re-gridding, especial in the suburban regions where the blending between the urban residences and the vegetative gardens results in extremely heterogeneous surfaces.

January in 2013 marks a significantly different thermal environment to the rest of the retrieved scenes. The other scenes range from March through to May and show temperatures ranging from 300 to 320 K between the scenes. Temperatures for January however peak at 295 K in the urban and rock/bare soil land classes. Interestingly at these temperatures not only is the mean LST lower but also the standard deviations and the differences between the classes mean LST are lower.

a priori class	Date	Mean LST	STDDEV	Cover (%)
Urban	<i>20/05/2011</i>	316.37	2.75	58.80
	<i>04/04/2012</i>	322.25	2.59	46.06
	<i>17/01/2013</i>	295.63	1.27	40.39
	<i>22/03/2013</i>	310.54	1.66	52.71
	<i>09/03/2014</i>	308.52	1.74	48.19
Mixed Urban and Vegetation	<i>20/05/2011</i>	313.39	2.43	14.00
	<i>04/04/2012</i>	318.43	2.53	18.57
	<i>17/01/2013</i>	294.54	1.03	46.23
	<i>22/03/2013</i>	307.81	2.11	19.41
	<i>09/03/2014</i>	306.27	1.90	29.51
Vegetation	<i>20/05/2011</i>	305.88	3.33	4.72
	<i>04/04/2012</i>	310.29	3.49	5.62
	<i>17/01/2013</i>	292.38	1.00	1.57
	<i>22/03/2013</i>	301.82	2.54	3.06
	<i>09/03/2014</i>	298.94	2.78	4.34
Rock/Soil	<i>20/05/2011</i>	317.66	3.17	22.49
	<i>04/04/2012</i>	322.50	4.26	29.75
	<i>17/01/2013</i>	294.56	3.07	11.82
	<i>22/03/2013</i>	310.78	3.10	24.81
	<i>09/03/2014</i>	306.87	2.94	17.96

Table 21 – The mean and standard deviation for all pixels with in the subset for all observations in (K). The data is divided into the a priori classifications used in the retrieval. For each class relevant percentage of the scene it covers is given in the right most column.

5.7 Scene Transects.

The behaviours of three key regions within the scene were highlighted for closer study. These regions were selected to explore the effect of vegetation and impervious surface on the LST and LSE seen.

5.7.1 Transect 1: Urban/Sand/Vegetation boundaries

Transect 1 is for a region of crop land located very close to the urban area. This region is the Salt river Pima-Maricopa Indian Community and as a reservation has restriction to urban development not seen elsewhere in the city. This area of crop land as seen in Figure 59, is unusually situated. It is enclosed on the north, west and southern sides by the city of Phoenix and is exposed to the desert on the eastern side. On the northern edge sub-scene there is a buffer zone between the city and the farm land of the desert. This scene was selected for two reasons, Firstly, it shows vegetation in a very different context to the park subset, there is no shelter, the land is cultivated and the composite vegetation will be representative of very different plant types, a significant proportion of the crop land in this area is dedicated to cotton growing with LSEs expected to be around 0.98 for channel 12 (Pandya et al., 2013). Also there is are clear regions of desert, vegetation and urban cover all in a small subset. This also represents an area where the retrieval was able to retrieve physically realistic LSE values despite miss-classification in the a priori.

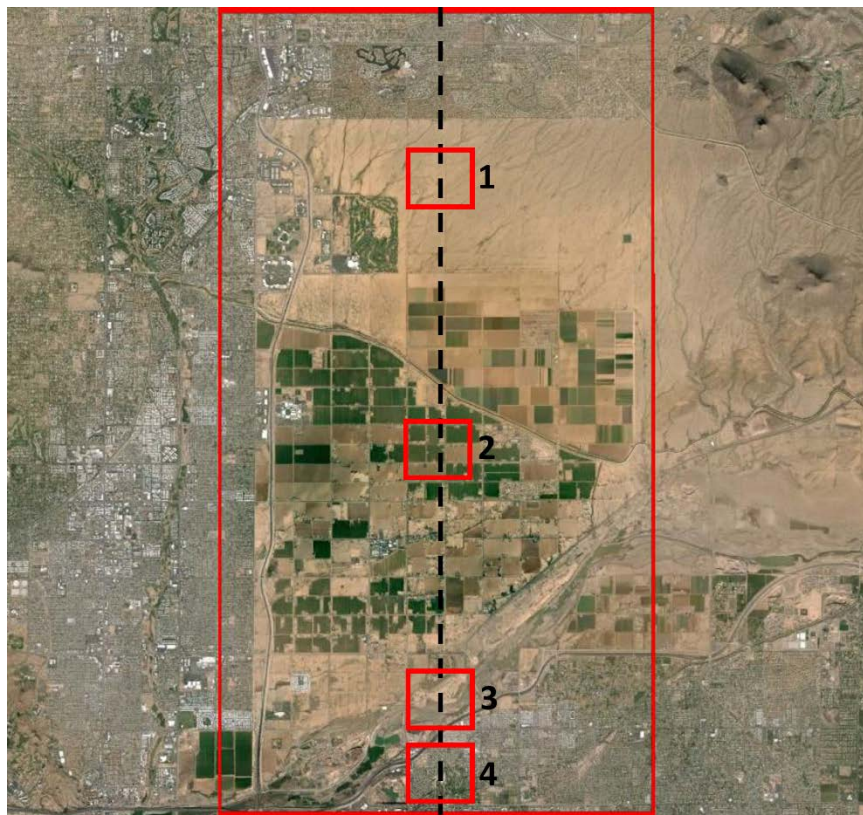


Figure 59 – Visible image from Google Earth for the site of Transect 1. Image taken from Google earth, 33.511 N, -111.860 E, image acquired 08/03/2014, image obtained 16/07/2016. The large red rectangle shows the area used in the LST and LSE maps. Each of the smaller boxes refers to a specific study site. 1: sand/soil, 2: cropland, 3: dry river basin and 4: urban.

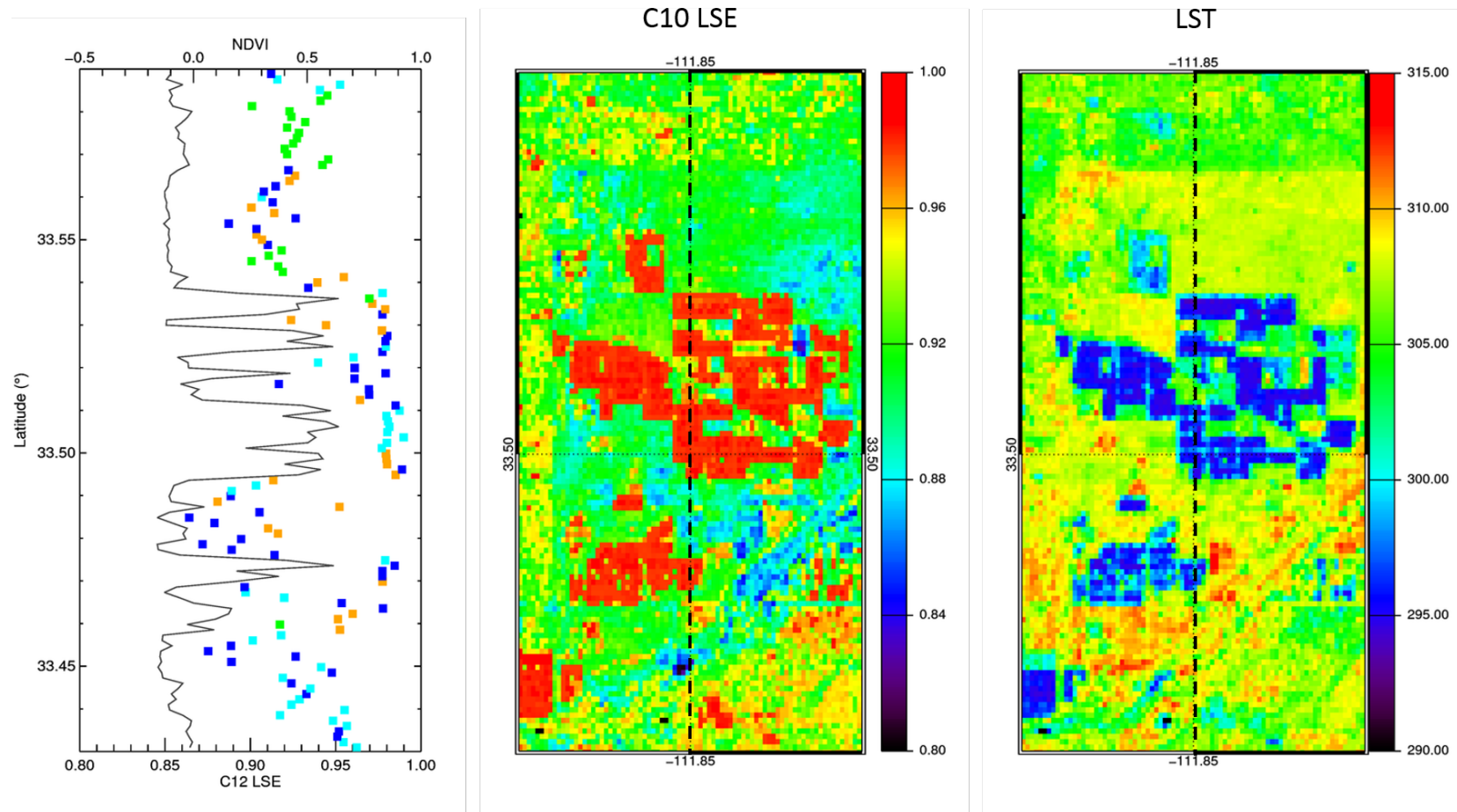


Figure 60 - Latitudinal transect for 09/03/2014. The LEFT panel shows the retrieved LSE in channel 12 for the whole range of latitudes. The colours correspond the a priori classification given to the pixel: dark blue = urban, cyan = mixed vegetation and urban, gold = rock/bare soil and green = vegetation. The MID panel shows a map of the retrieved LSE in the area surrounding the transect with the transect path denoted by a black dashed line. The RIGHT panel shows a map of the retrieved LST in the area surrounding the transect, path denoted by a black dashed line.

Transect 1 shows a region of high LSE that corresponds to the cropland seen in Figure 59. The increase in the LSE values is matched by a spike in the NDVI calculated over the transect. This in conjunction with the visible imagery, gives confidence that the retrieval has successfully identified the surface cover as crop land despite the fact that the a priori LSE shows a range of classifications, none of which being vegetation. The LSE values across all five channels are also consistent with vegetative LSEs, see Figure 61. The absolute values for the cropland are higher than the values for cotton as found by Pandya et al., (2013). However, this region is heavily irrigated due to the arid environment, resulting in an increased quantity of water present in these fields (Tennakoon & Milroy, 2003). The retrieval is able to identify this area and account for the increased LSE.

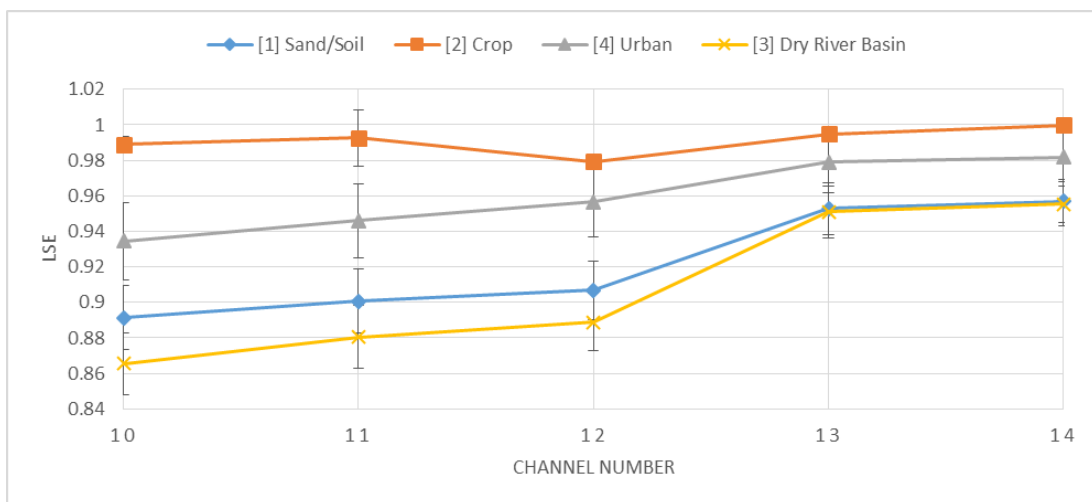


Figure 61 – LSEs with associated uncertainties for the specific sites with in Transect 1, for all channels.

Transect 1 also goes through a dry river basin, [3] in Figure 59. This area shows a much lower LSE in channel 12 than in the rest of the transect, this is also reflected in the LSE across all channels in Figure 61. The LSE here is representative of bare soil samples, see Chapter 4. Interestingly the open desert, region 1, shows a similar LSE but with a reduction in the LSE in channels 10, 11 and 12. Looking at high spatial resolution visible imagery it is apparent that there is small sparse shrubbery in the desert [1], which is not found in the dry river basin [3], this shows the possibility that the vegetation is reducing the pixel scale LSE for the observation, and may allow the retrieval to distinguish between sparsely covered and fully barren areas.

The urban region [3], shows LSEs of atypical or man-made materials, including masonry, concrete and roofing slate, see Chapter 4. This area, and the urban area to the north of Transect 1 shows LSTs lower than those seen in the desert. The desert is consistently warmer than these urban zones and demonstrates the possibility of a UCI effect.

In the visible imagery there is a sharp border between the vegetation and the desert at 33.54 N and the desert and the urban area at 33.57 N. However in the retrieved data there is a buffer of two pixels at each of these boundaries showing LSEs that are a mixture of both LSEs expected. Sub pixel boundary influence should only be one pixel at the boundary. The width of these features suggests a real physical surface difference. The sand in the desert could very well be contaminating the pixels around through deposition from wind causing these surfaces to have a marginal quantity of sand within them. This effect is seen in greater intensity in the boundary with the vegetation where there is no shelter to diminish the effect of transportation via the wind.

However the border is clearly defined in the LST data where the effect of the urban desert boundary denotes a LST contrast peaking at 4 K. This makes the possibility of sand deposition more likely as if this was a retrieval artefact, due to the mixing of surface types in the pixels, the effect should also be seen in the LST data, which it is not. In a clear boundary zone, this presents the possibility, for this retrieval, to identify the input of a free moving material (sand) into fixed surface type (urban).

5.7.2 Transect 2: LSE structures/Impervious surfaces

Transect 2 was taken through the Phoenix subset bisecting the suburbs, the airport and the dry river bed. The transect aimed to look at the LSE changes moving through these different areas to specifically identify the LSEs at key points relating to real physical feature along the transect.

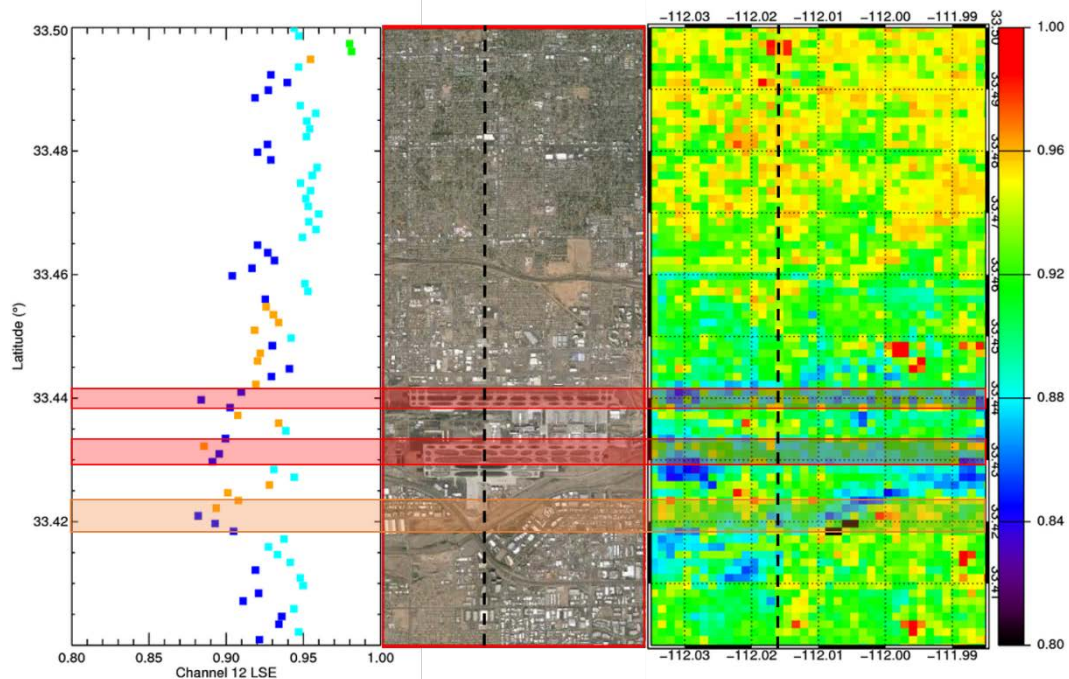


Figure 62 - Latitudinal transect for 09/03/2014. The LEFT panel shows the retrieved LSE in channel 12 for the whole range of latitudes. The colours correspond the a priori classification given to the pixel: dark blue = urban, cyan = mixed vegetation and urban, gold = rock/bare soil and green = vegetation. The MID panel shows a visible image of the area with the transect denoted by a black dashed line. The RIGHT panel shows a map of the retrieved LSE in the area surround the transect with the transect path denoted by a black dashed line. Across all three panels are three bounding boxes. The red boxes highlight the latitudes associated with the airport runways, and the brown box with the dry river basin.

The transect shown in Figure 62 shows the LSE for 09/03/2014. Several key features can be seen in this data. Firstly, there are three distinct primary dips in the LSE in the lower half, with one additional dip at higher latitudes.

The first three dips highlighted by the red and brown bounding boxes correspond to the locations of two different features. The red bounding boxes line up with the expected locations of the main runways for Sky Harbour Airport in Phoenix. The brown region coincides with the location of the dry river basin. Each of these features has a deviation from the mean LSE in the transect of over 0.05 showing a substantial change. This change can be linked back to the materials likely to be present within these different surface structures.

The runways are man-made impervious surface incorporating materials such as asphalt and concrete and as such have a distinctive dip in LSE at lower TIR wavelengths. The river basin is also impervious but the materials present are soil

based. In particular in Arizona there will be a high sand content in the soil which also has a distinctively low LSE at this wavelength, see Section 4.2. The absolute LSEs for these retrieved areas can be seen in Figure 63. [2] shows the LSE for a runway and has a very similar LSE to that of the feature identified as a road [1]. These two points are both man-made impervious surface, with long flat stretches of one material type, which makes the retrieved LSE more likely to be presentative of the true material than a pixel where the underlying sub-pixel surface is highly heterogeneous.

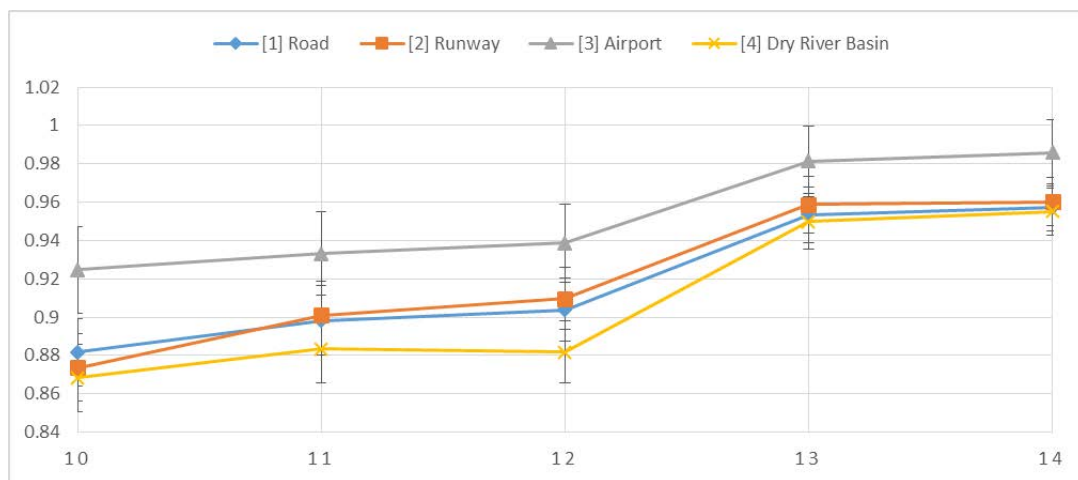


Figure 63 - LSEs with associated uncertainties for the specific sites with in Transect 2, for all channels.

The dry river bed shows small but important LSE differences from the man-made impervious surfaces. In this case, the river bed shares many of the LSE properties with the runways and road, but here is a difference in the shape for channels 11 and 12, distinguishing it. The river basin is at the point of intersection with the transect 350 m wide, 400 m including the sloped banks. Given that that river is identified by a depression in the transect LSEs five pixels wide this gives an idea of the scale of objects that can be resolved. The mixed middle pixels show the LSE matching the river bed expected LSE, indicating that three pixels at 90 m each correspond to the basin itself.

The retrieved LST also shows a difference between the man-made and natural impervious surfaces. Figure 64 shows the retrieved LST for the transect area. Both of the runways stand out with a higher LST than the surrounding by approximately 5-7 K. This region of heightened LST is not confined to the runways and is also seen

over the main airport structure, which had much higher absolute LSE, 0.92 or higher, than the runways due to a change in materials, see Figure 63.

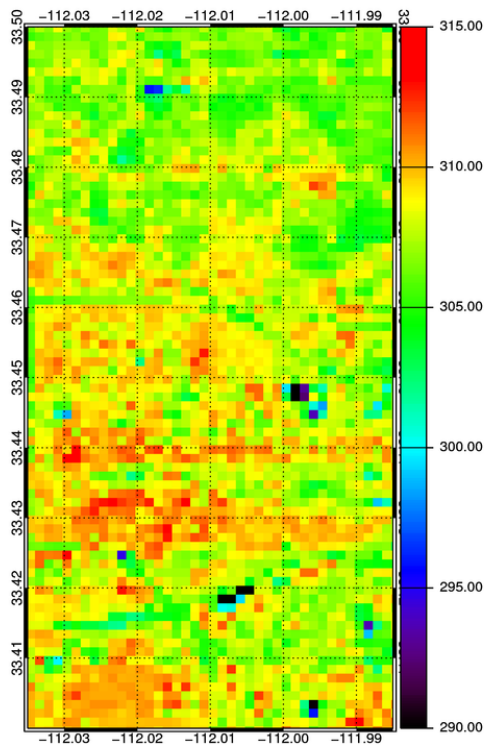


Figure 64 – Retrieved LST (K) for the area surrounding Transect 2.

The increase in temperature over both of these surfaces, whilst the river bed shows lower LST, demonstrates the effect of anthropogenic heating. The airport is a highly active industrial and commercial structure, with both the runways and the terminal in heavy use throughout the day and night for both commercial activity and regulatory measures such as air conditioning, this leads to an increase in the heat flux which the retrieval is able to identify in the LST.

The LSE towards the north of Transect 2 becomes higher as the pixels map out the suburban districts. The majority of these pixels are a blend of urban and vegetation but there are a few pure vegetation pixels. These correspond to a small green space called Los Olivos Park. This park has a length in the vector of the transect of approximately 180 meters, which just corresponds to less than the two pixel scale size seen in Figure 62. It is highly unlikely that the pixels and the park matched perfectly at this scale. This shows that a small quantity of vegetation within a pixel can dominate the BOA BT at the pixels scale. While this is a good way to identify

urban green space to analyse the effect of vegetation, it does imply the in heterogeneous areas with vegetation, the retrieved LSE may be biased towards vegetation and less useful in a diagnostic sense.

5.7.3 Transect 3: Urban Green Space

Transect 3 investigates the LST effect of urban green space. The park/golf course seen in the north west of the subset area is a stable zone of vegetation and is artificially irrigated to maintain this level of plant life. The effect of this region on the LST is important to gauge as the cost of providing this much water within the arid environment of Phoenix is high (Halper et al., 2012) amid the real possibility of droughts in Phoenix (Gober et al., 2009). The transect shown is for 2011 at 33.484 N between -112.08 and -111.98 W see Figure 65.

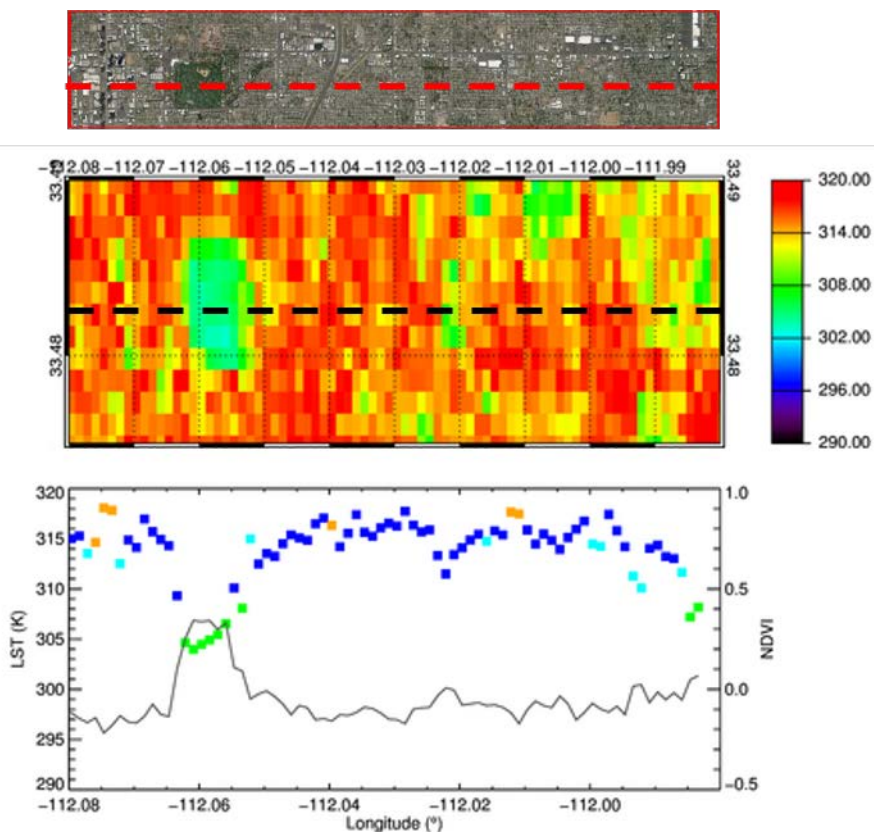


Figure 65 – Park transect for 20/05/2011. (TOP) Panel showing transect overlaid on visible imagery, red dashed line denotes the transect path. Image taken from Google earth, 33.460 N, -112.060 E, image acquired 04/03/2011, image obtained 16/07/2016. (MID) A subset showing the LST for the area surrounding transect. The transect path denoted by black dashed line. (BOTTOM) LST of the right axis for the transect, NDVI on the left. The colours correspond the a priori classification given to the pixel: dark blue = urban, cyan = mixed vegetation and urban, gold = rock/bare soil and green = vegetation.

The LST in the park is significantly lower than that of the urban surroundings, nearly 10 K lower than the urban average for the transect. The values seen here are representative of those observed in the mean LSTs for these classes shown in Table 21, with vegetation at 305.88 K and the urban mean LST at 316.37 K.

The correlation between the NDVI, the LST cooling and the a priori classification in the park shows a good agreement and suggests that for the case of pure vegetation the classification has correctly identified the relevant class to provide a priori LSEs for the retrieval.

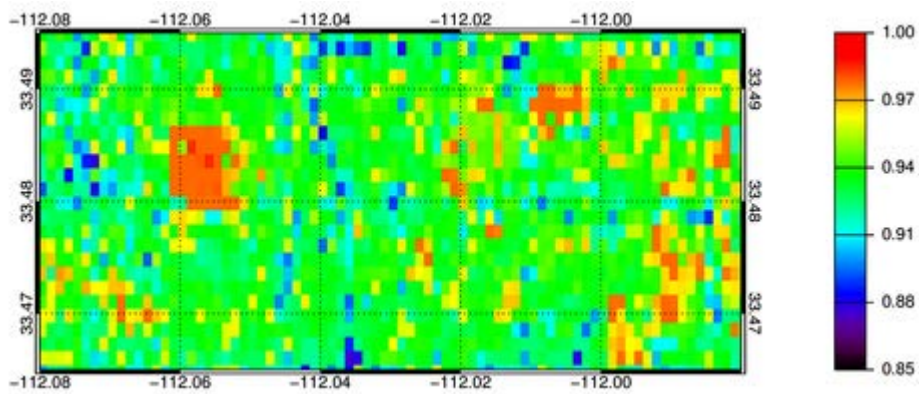


Figure 66 – Channel 12 LSE for the area of the park and Transect 3

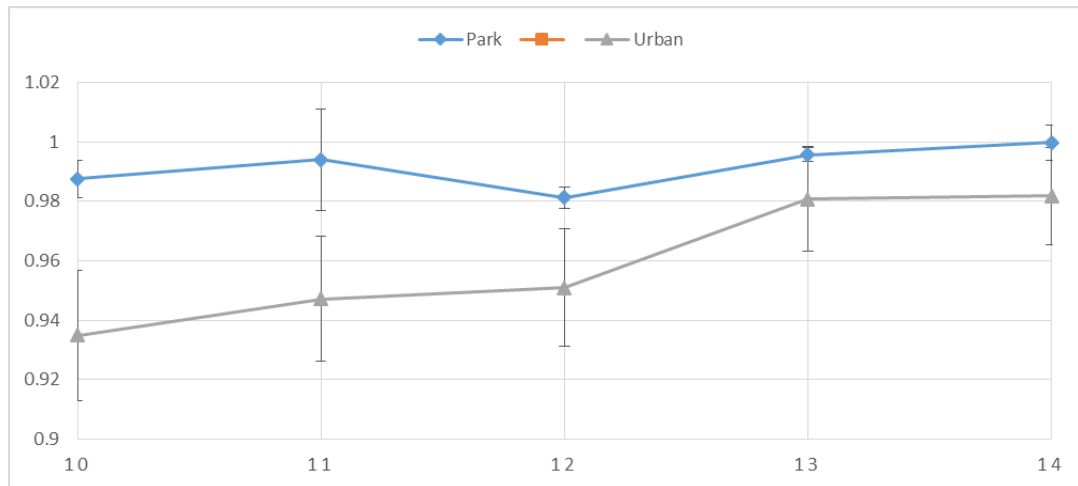


Figure 67 - LSEs with associated uncertainties for the specific sites within Transect 2, for all channels.

The park is clearly visible in the retrieved LSE data seen in Figure 66. All of the channel 12 LSEs in the boundary of the park are of 0.97 or higher matching the expected values for vegetation. The LSEs across all the channels also matches well

with the expected values for vegetation, are much higher than those retrieved for the urban surroundings, see Figure 67.

Figure 66, also shows a distinct pattern of low LSE that is mostly likely attributable to the road network. As well as the increase of LSE in the sub-urban areas identified in the east of the transect.

Interestingly the urban pixels on either side of the park show LSTs lower than the mean urban values. There is a noticeable temperature dip in the urban LSTs seen on the eastern side of the park. Upon closer inspection of the visual imagery it is apparent that there is a higher proportion of urban green space with in the suburban landscape near this boundary. This region trails off before greater levels of vegetation are seen to emerge at -112.025 W a trend which is also seen in the LST data in Figure 65, therefore the cooling of around 3 K surrounding the park is not attributable to the park itself.

To assess the stability of the park's cooling effect and the influence of the suburban vegetation, two scenes were inter compared with conditions as close to each other as possible. The scenes from 22/03/2013 and 09/03/2014 were selected as they were for the same month one year apart, therefore the vegetation present should be at the same stage with in the seasonal cycle. Also within this one year separation there were negligible real physical alteration to the transect area, such as building change or new constructions.

The two transects are shown in Figure 68. The observations have similar LSTs with the urban mean LST being 2 K higher in 2013 than that of 2014. The LST structure across the transect is also very similar between the observations. In both cases the prior classification identifies the vegetation and highlight mixed urban and vegetation towards the east of the transect. There are small differences between the distributions of urban to mixed pixels but across all pixels for all classes the classification is a match in over 84% of cases.

The effect of the park's vegetation is consistent between the observations with a reduction in LST over the park averaging approximately 10 K in both transects. The presence of two secondary dips in the LST is also a common feature showing the impact of urban greenery within the suburban region. The effect of the mixed urban vegetation pixels is weaker than that of the pure vegetation with an average reduction

of approximately 5 K between these regions and the urban background. This is a marginally stronger effect than the mean calculated for the whole subset, in Table 21. However given the potential for variation in this class a 1 K difference between the pixels in the transect and the subset mean is well within the standard deviation for the class.

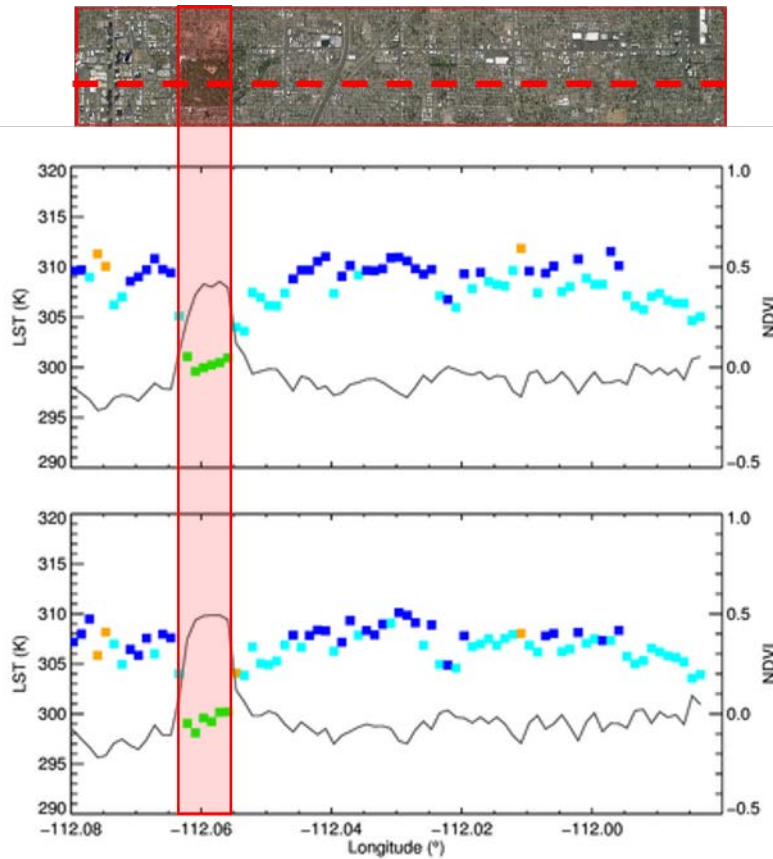


Figure 68 – Transects for 22/03/2013 and 09/03/2014. Left axis is retrieved LST, right axis NDVI. The colours correspond the a priori classification given to the pixel: dark blue = urban, cyan = mixed vegetation and urban, gold = rock/bare soil and green = vegetation. The red shaded region highlights the area bounded by the park for inter-comparison.. Image taken from Google earth, 33.480 N, -112.040 E, image acquired 08/03/2014, image obtained 16/07/2016.

Despite a variation in the surrounding urban area of 2 to 3 K the park LST remains within a maximum variation of 1 K between observations. This is in line with studies of the effect of urban parks on air temperature and shows the vegetation having a stabilising effect on the temperature of up to 1.3 K (Yu & Hien, 2006).

5.8 Summary

In this chapter the retrieval algorithm developed in Chapter 4 was deployed for multiple scenes over Phoenix Arizona spanning the time period 2011-2014. The scenes were analysed and used to isolate key features in both LST and LSE.

The algorithm was shown to retrieve LSE with a high degree of stability in all channels except channel 10, where a combination of effects from both the expected material cover and the atmospheric sensitivity made the LSE results more variable. From these results it is concluded that for use in land use and land classification studies channels 11 – 14 would be the most suited as they provide information on material variation, see Chapter 4, and are still stable between scenes in the majority of cases.

The variation of LST was analysed as a whole and by the prior classification. The classification was found to be stable in the majority of cases but that variation particularly in the separation of pure vegetation and mixed vegetation and urban can result in higher vegetative standard deviations. The urban green space was analysed in detail through transects was found to have an effect of up to 10 K of the LST. This shows huge difference and points to the effect of not only the effect of vegetation in evapotranspiration cooling but also the contrast in the water content of the vegetative and urban surfaces in the arid city.

Analysis of transects has demonstrated several important technical and scientific results of the retrieval. Firstly, the retrieval has demonstrated a robustness to the a priori classification. In instances where the a priori classification had misclassified the surface the retrieved LSE had correctly identified at true surface type. Also on the performance to the retrieval, the radiance residuals are very good, small mean and standard deviations show a good representation of the observations in the retrieved parameters.

The retrieved data was able to identify several key urban features; the park, featured in transect 3, was clearly identified and its impact of the LST quantified as depression of 10 K with high temporal and spatial consistency.

The crop land investigated in transect 1, was shown to have consistent LSEs with the expected irrigation and crop surface observed. Furthermore the analysis of the urban

desert boundary identified the visually-observed distinction in the LST but showed that there might be a mixing of sand in to the urban area through the LSE retrieved. The LST values themselves showed a desert warmer than the surrounding urban area, indicating a potential UCI effect of open desert.

Transect 2, assessed several types of impervious material visually identified as lying in the transect path. The retrieved LSE was able to distinguish between the man-made and natural surfaces, as well as giving a measure of the object scale resolution of the retrieval. Further to the this analysis of the LST showed the airport and runway have higher LST values than the surroundings and in particular and the impervious river basin, showing clear signs of warming from anthropogenic heating.

6 Case Studies II and III - Shanghai and New York

6.1 Introduction

Studies of the urban environment have to address different scientific questions specific to each city. The retrieval developed in Chapter 4 has been tested over the city of Phoenix, but this city is not representative of all urban environments as climate and materials will vary globally. The areas of urban investigation outlined in Chapter 1 cover a broad range of issues, and the OE retrieved LST and LSE can address them in a variety of ways. Two more case studies were chosen to investigate different urban parameters.

Firstly the rapidly expanding urban region of Shanghai was studied, with the aim of using the LSE and the LST to provide detection of the changes in the LULC between observations.

Secondly the city of New York was chosen for study, in this case study aimed to identify and explore the effects of LULC difference between different urban sub-classifications, and to also assess the temperature impact of urban green space spatially and temporally, in comparison to surrounding bodies of water.

6.2 Case Study II: Shanghai

Shanghai is, with the exception of Hong Kong, China's biggest economic centre. The urban environment of Shanghai has expanded at an incredible rate and is now considered a mega city with a population in excess of 20 million (Chang, Song, & Liu, 2009).

There have been numerous studies into the urban environment of Shanghai exploring many different parameters, LST and UHI being two significant highlights, (Cui &

Shi, 2012; Juan-juan Li, Wang, Wang, Ma, & Zhang, 2009; Junxiang Li et al., 2011). A primary driver behind research into the metropolis is the rate and effect of the rapid change of the urban environment (Y. Li, Zhang, & Kainz, 2012; Ren et al., 2003; H. Zhang et al., 2013). The underlying health concerns about the city are the key motivation behind the research being conducted, as even small effects geographically could have a large impact on human health given the high population density (Tan et al., 2010).

The rationale behind this case study was to take the retrieval developed in this thesis and apply it to the issues of urbanisation and rapid change due to human activity within Shanghai. In particular, to take observations with a large temporal separation and apply it to the large changes in land type and land use. Previous studies using remote sensing have primarily focused upon LANDSAT data which while excellent for object classification has a poorly calibrated LST retrieval and no way of determining the LSE. This study aims to be able to show the change in the city with the ASTER data, and also produce accurate and LST and LSE data from potential inclusion with urban energy balance models, to improve the accuracy of these techniques which are reliant on high quality LST and Surface LSE data (Zhang et al., 2013).

6.2.1 Study area

The area selected covers central Shanghai and as well as the islands in the delta of Changzing Dao and Chongming Dao. These areas whilst all urbanised are in different states of development and urban density, see Figure 69.

ASTER data was processed for two observations with similar viewing geometries. Both observations were taken in the winter months as Shanghai's subtropical climate means that the majority of the rainfall and cloud cover interference occurs in the period between May and September minimising the potential atmospheric influences and reducing the chance of cloud contamination, (Li et al., 2012).

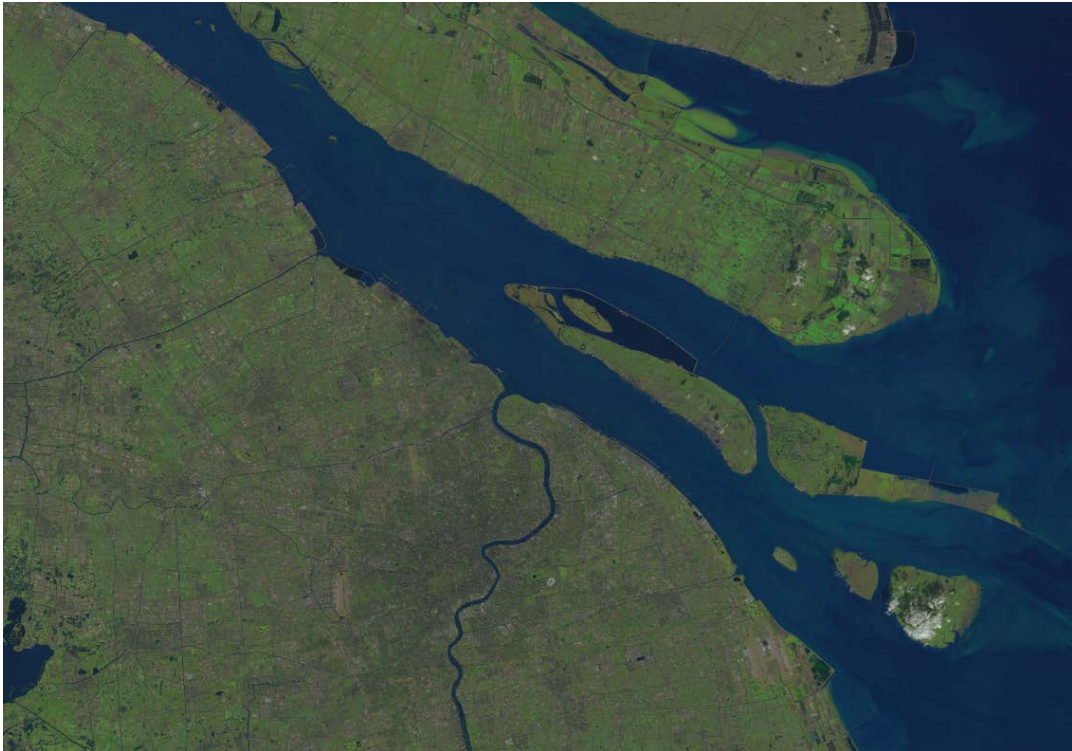


Figure 69 – RGB image from LANDSAT 8 data for Shanghai in 2014.

6.2.2 Urban change detection

The observations were taken on the 20th of October 2009 and the 3rd of November 2014 yielding a five year temporal gap. The urban environment would be expected to have undergone noticeable change in this period, especially in Shanghai where the rate of development is so high. The a priori classifications for both observations are shown in Figure 70.

There is an observed shift in the quantity of purely urban land cover between the two observations, there are also several alterations within the water covered areas that can be seen in the classification data. The differences between the observations based upon the a priori classification are summarised in Table 22. There is a net increase in the urban cover of 2.13 % between the observations, however this alone does not show the full picture and there is a large reduction in the urban pixels which are now classified as water covered of around 1%. Factoring this in the calculations the net urban change over land is around 3%.

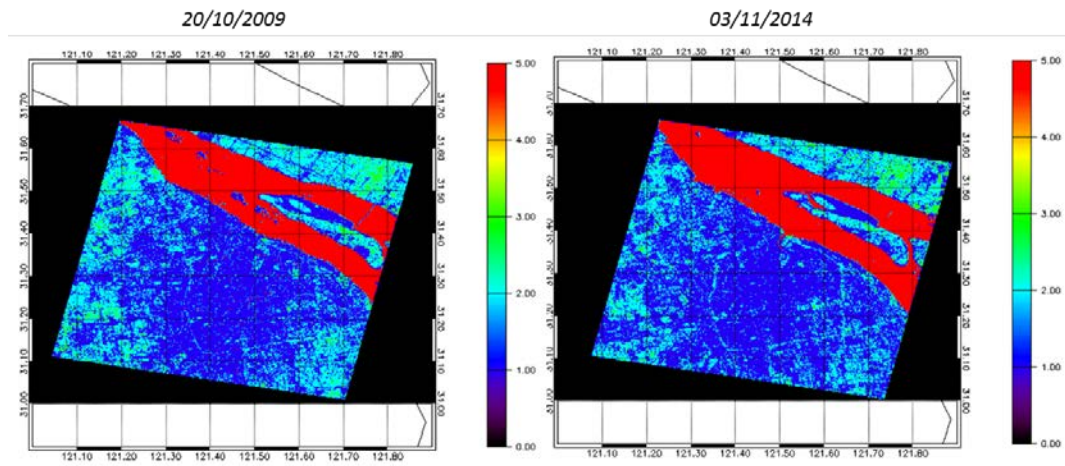


Figure 70 - K-means land classification map for the Shanghai observations. The five classifications returned here are: urban (blue), soil/dust (orange), vegetation (green), mixed urban/vegetation (cyan) and open water (red).

The temperatures seen follow an expected distribution with the urban LST presenting as the warmest, then the mixed urban and vegetation then the vegetation and finally the water with the lowest LSTs. Comparing the observations the biggest difference is seen not between the classes but, between the observations temporally.

The observation in 2009 is on average 3-4 K warmer than the observation in 2014. Whilst both retrievals have converged well and presented mean uncertainties of 0.958 K and 0.862 K respectively for the LST, additional data was consulted as a sanity check on the LST difference seen. The additional data is seen in Table 23.

The MODIS and in situ air temperature data sets collected for the same times as the observations show a large temperature disparity between the observations with MODIS LSTs showing an offset over 5 K and the air temperature record showing 2009 to be 5-6 K warmer than 2014. This corresponds to the bias between the LST in the two scenes.

Putting this together with the low retrieval uncertainty and the consistency of the offset between the LSTs in the observation this temperature differential is believed to be a real offset in the surface temperatures between these observations.

The confidence in the retrieved parameters is also due the retrieval radiance residuals, seen in Table 24. All channels for both retrievals report radiance residuals lower than 0.05 K and the residuals for channel 12 are extremely small in both observations, showing a good representation of the observations.

a priori class	Date	mean LST	STDDEV	Cover (%)
Urban	<i>20/10/2009</i>	303.90	2.46	49.45
	<i>03/11/2014</i>	296.42	1.86	51.62
Mixed Urban And Vegetation	<i>20/10/2009</i>	300.92	1.65	28.37
	<i>03/11/2014</i>	294.66	1.14	24.51
Veg	<i>20/10/2009</i>	297.64	1.11	3.17
	<i>03/11/2014</i>	292.06	1.00	2.80
Water	<i>20/10/2009</i>	295.77	0.75	19.01
	<i>03/11/2014</i>	292.77	0.49	21.08

Table 22 - The mean and standard deviation for all pixels with in the subset for the observations in (K). The data is divided into the a priori classifications used in the retrieval. For each class relevant percentage of the scene it covers is given in the right most column.

Date	MODIS		Station Data (Air Temp)			
	LST (K)	STD DEV (K)	Mean (K)	Min (K)	Max (K)	Wind Speed (km/h)
<i>20/10/2009</i>	299.07	2.47	290	285	294	5
<i>03/11/2014</i>	293.42	1.34	284	280	288	14

Table 23 – The mean and standard deviations from the MODIS LST data for the observations. Also the station data from Hongqiao Airport, in Shanghai.

Date		Radiance Residual (K)				
		C10	C11	C12	C13	C14
<i>20/10/2009</i>	Mean	0.040	-0.011	-0.006	-0.050	0.044
	Std Dev	0.079	0.096	0.050	0.082	0.111
<i>03/11/2014</i>	Mean	0.013	0.012	0.001	-0.025	0.009
	Std Dev	0.089	0.112	0.049	0.129	0.124

Table 24 – The mean and standard deviations for the radiance residuals for both retrievals.

The changes in classification were compared to the changes seen in the retrieved LSE, using channel 12, as this was the most reliable and precise retrieved LSE in the testing in Chapters 4 and 5. The spatial comparison between the class changes and the LSE changes can be seen in Figure 71.

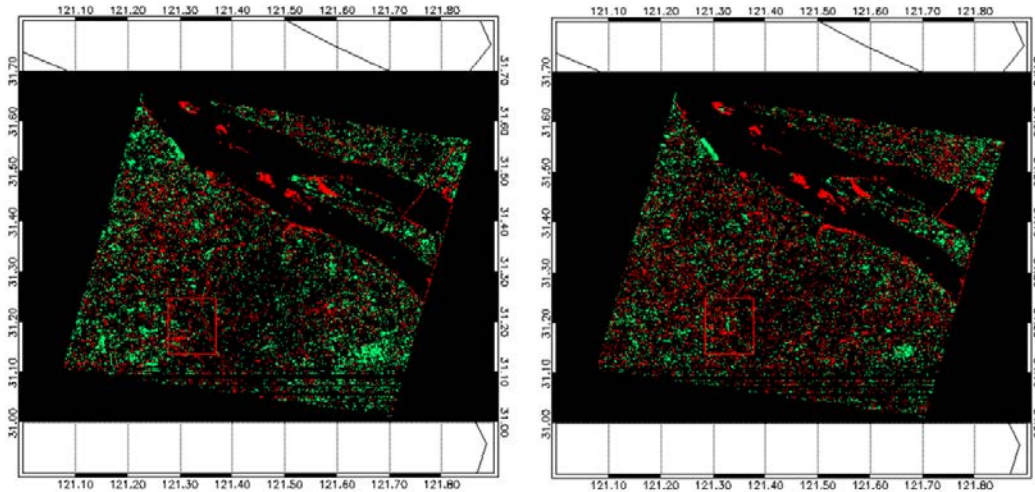


Figure 71 - Comparison of the a priori class changes to channel 12 LSE changes. LEFT: the change in class between observations, red indicates a change from urban in 2009 to non-urban in 2014, green indicates a change from non-urban in 2009 to urban in 2014. RIGHT: the change in channel 12 LSE between observations, red indicates an Increase in LSE from 2009 to 2014, green indicates a decrease in LSE from 2009 to 2014. In both cases black represent no significant change between the observations.

The LSE retrieved was filtered using the mean uncertainty retrieved to remove those LSE changes that were within the bounds of the potential uncertainty, leaving those changes most likely to represent real physical alteration of the surface. In the majority of cases the changes seen in the a priori classes were also seen in the LSE changes retrieved. However there are areas where the LSE reports changes not observed in the class changes. For verification four regions of interest were selected and compared visible data for the time period, to evaluate whether the detected change was representative of a true change in the surface state.

6.2.2.1 Regions 1 and 2: Land/Water change

The first two regions pertain to areas where there is a detected change between land and water. As mentioned previously there is a substantial change (approximately 1%) of land classes between the water and urban classes, which is greater than would be expected for the potential issues associated with any boundary issue with re-gridding. The LSE data for each band in 2009 was subtracted from that of the same band from 2014 and the difference assessed, and example of this in Channel 12 is seen in Figure 72.

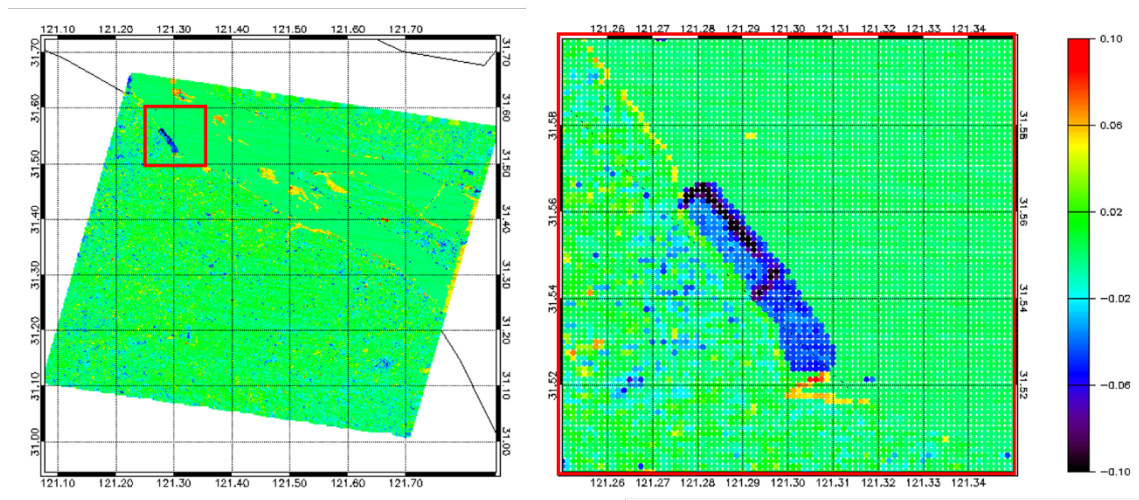


Figure 72 – The Channel 12 LSE difference between observations (2014 – 2009). LEFT for the whole scene. RIGHT for a subset where there was a noticeable shift.

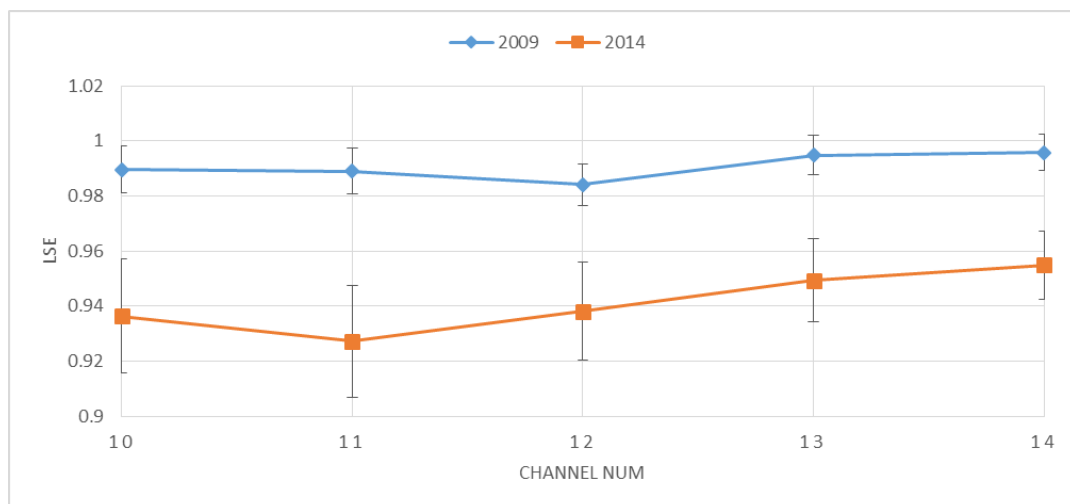


Figure 73 – Retrieved LSEs for change detected in region 1 with associated uncertainty.

Region 1 is highlighted in Figure 72 showing a substantial shift the retrieved LSE. A section where previously the LSEs were high and indicated the presence of water in 2009, shows much lower LSE in 2014. The change is of the order of -0.06 in Channels 12 LSE which would suggest a new surface matching with concrete or exposed rock/soil. This shift is large and ordered with defined boundaries and internal structures make it unlikely to be a natural phenomenon.



Figure 74 –RGB imagery from LANDSATs 5 and 8 for Shanghai region 1. TOP: LANDSAT 5 RGB for 21/10/2009, BOTTOM: LANDSAT 8 RGB for 04/11/2014.

To assess the realism of this change the visible LANDSAT imagery for the nearest matching time of each observation was assessed, see Figure 74. The substantial change in structure is also seen in the visible imagery as an extension of the urban environment into an area previously covered by water. Upon further investigation it was found the change was due to land reclamation which created a large area of exposed rock and soil bordered with large concrete boundaries, all of which matching the observed LSE change detected, seen in Figure 73. This gives us not only the visually identifiable change but also the ability to assess the surface properties for energy balance impacts.

The retrieved LSE in all five channels clearly demonstrate the surface change. In 2009 the LSEs are very high with values indicative of water. By 2014 the LSE has dropped in every channel and now show values associated more with man-made materials or exposed bare soil. The consistent change across the channels and the clear water signature identified shows that the retrieval was able to not only detect this change but also give an idea of the materials involved in the changes.

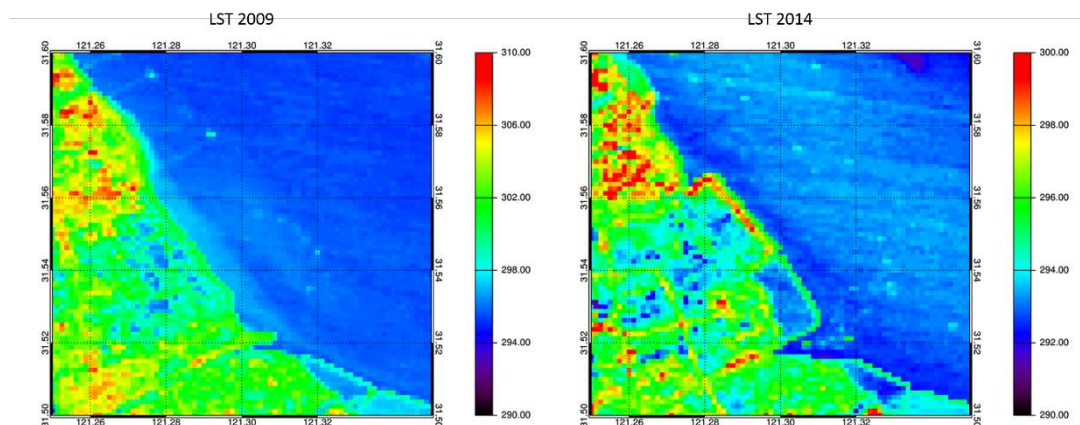


Figure 75 – The retrieved LST (K) for Region 1 in 2009 and 2014.

This change has important implications on the surrounding urban environment as large bodies of water have been shown to have a large cooling effect upon the day time summer air temperatures of the urban environment, but can also contribute towards thermal discomfort through increased humidity, especially at night or in the autumn (Theeuwes, Solcerová, & Steeneveld, 2013). The effect on the LST is seen in Figure 75, where the introduction of the impervious materials has increase the relative LST both immediately at the coastal barrier, but also further inland where

there is an increase in the LSTs retrieved approaching the area that were formerly river front.

Region 2 also identified a significant LSE change between the scenes and was located in the middle of the river itself in the Changjiang Estuary, see Figure 76. The LSE change here in Channel 12 is in the opposite direction to the previous subset. In this case the land changes from low LSE to high LSE with a net increase of nearly 0.1 in the LSE. The 2009 LSE is very low typically associated with sands and other low LSE rock/soil types. The new LSE in 2014 matches the surrounding water body. The effect is not isolated as there are within this subset several distinct regions where this change has occurred.

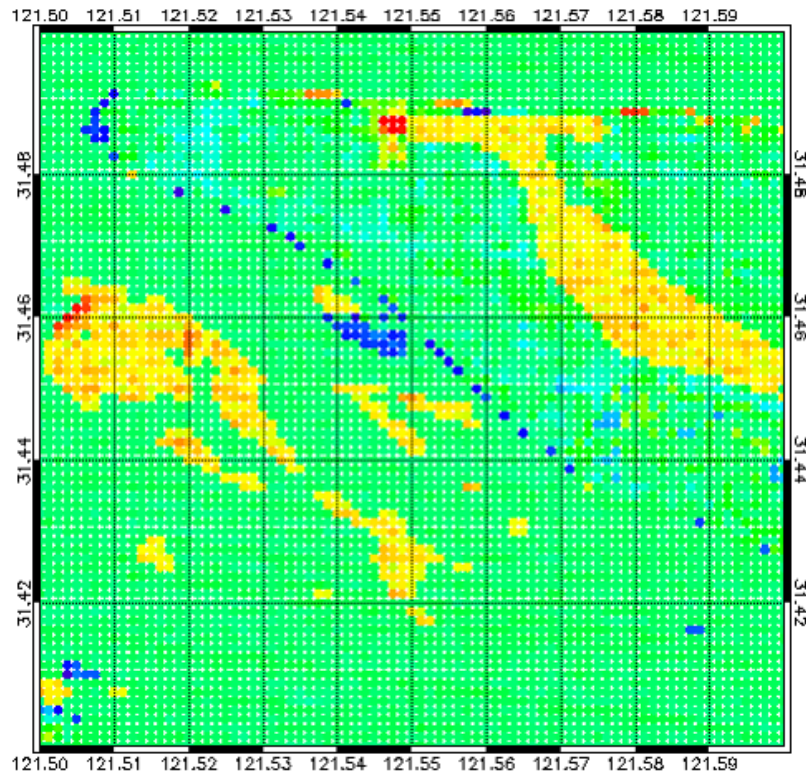


Figure 76 – The Channel 12 LSE difference between observations (2014 – 2009). Region 2, highlighting a substantial increase in LSE in 2014.

Consulting the visible imagery this change is also seen, see Figure 77. The visible image shows that in 2009 there are significant land masses in the estuary and in the water way passing through the Changning Dao land mass. The majority of these land

masses are not present in the 2014 imagery. The removal of these features is a secondary result of the “Deep waterway project on the Changjiang Estuary” which aimed to improve the navigational environment for shipping in Shanghai harbour, (Zhu, Ding, Zhang, Wu, & Cao, 2006). As a result the sedimentary land masses formed by flow down the river were destroyed.

The LSE retrieved here also show agreement with the visual data. Figure 78 shows the LSE in 2009 had much lower values in all channels than in 2014, but particularly in channel 10, 11 and 12. The shape of the LSE seen here is indicative of bare soils of man-made materials. This is in line with the expected materials for the sedimentary depositions.

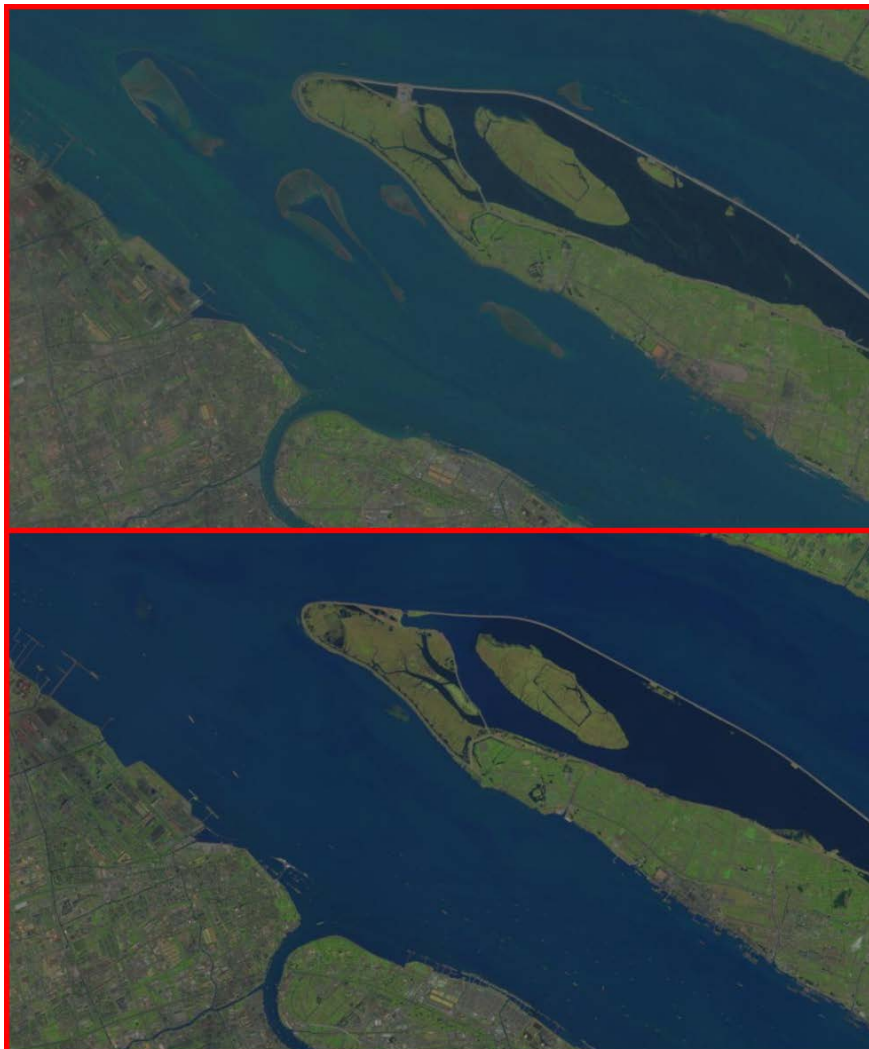


Figure 77 - RGB imagery from LANDSATs 5 and 8 for Shanghai region 2. TOP: LANDSAT 5 RGB for 21/10/2009, BOTTOM: LANDSAT 8 RGB for 04/11/2014.

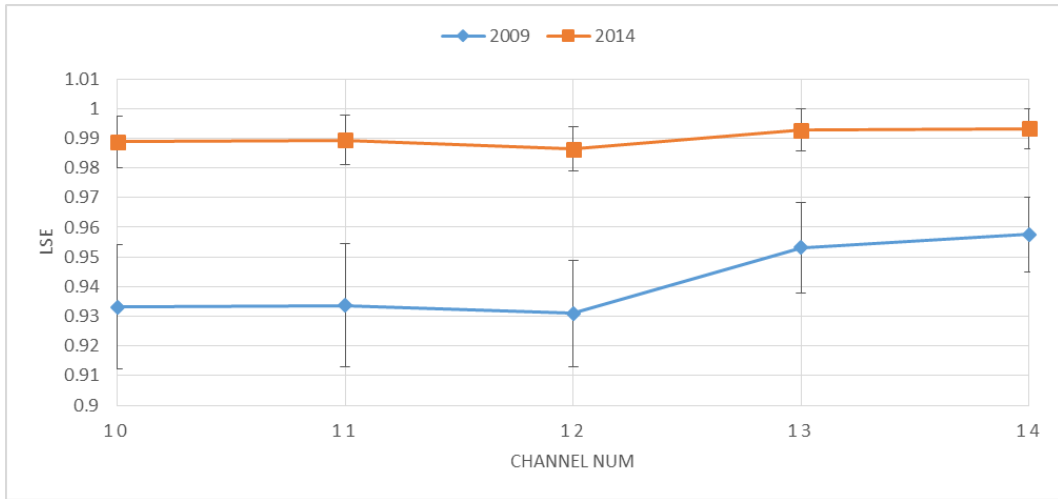


Figure 78 - Retrieved LSEs for change detected in region 2 with associated uncertainty.

The change seen here, whilst large, does not have a direct impact on the urban surface temperatures seen in the rest of the city. However increased shipping allowed by easier passage will result in greater anthropogenic flux in the urban energy balance as well as disrupting the latent and sensible heat fluxes due to the effect of the changing structure. The effect is not only in the LST but also in the SST as can be seen in Figure 79.

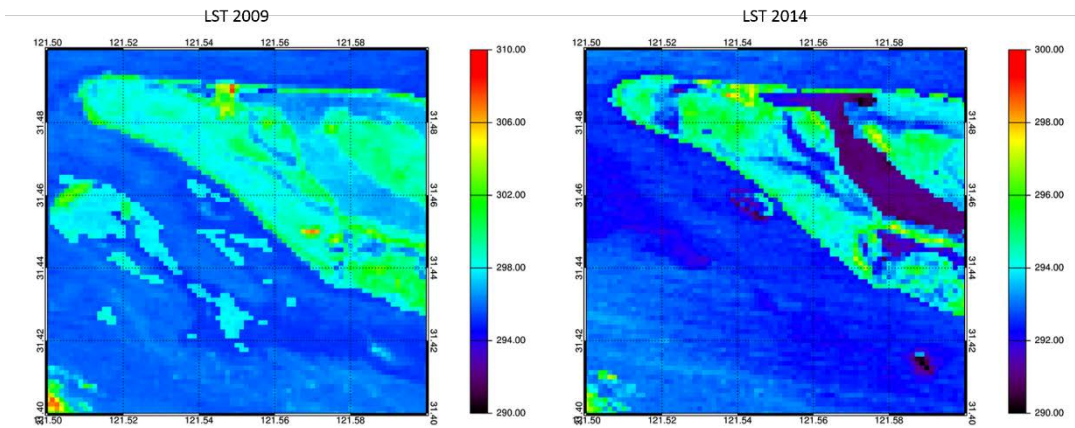


Figure 79 – Retrieved LST (K) for Region 2, for 2009 and 2014.

The relative surface temperature has decreased not only for the areas where the land masses have been removed but also for the water surrounding it, where the effect of the island’s removal seems to have been to lower the SST in a far larger region. The enclosed water in the island has also experienced a large relative SST reduction since the water way changes. These effect will all feed into the large energy balance with consequences for the urban environment.

6.2.2.2 Region 3: Vegetation to Urban

Region 3 was selected as it showed a substantial shift in the LSE indicative of a change from vegetation or mixed vegetation and urban to a region of urban domination. This change is not as extreme as the change seen in regions 1 and 2, but is still indicative of substantial land class/land use change.

Region 3 is in the south east of the case study site where there is an area of land that showed a change in LSE across all the channels, reducing in LSE between 2009 and 2014. The LSE in channel 12 for both observations is seen in Figure 80.

There are many stable features between the two observations of Region 3 such as the high LSE seen in the cluster at 31.13 N, 121.62 E and 31.16 N, 121.62 W which correspond to vegetation. Also the increase in lower LSE pixels in the north of the region from 31.18 to 31.20 N. This area shows more development than is seen in the rest of the region with a substantial increase in building density and reduction in the quantity of urban green space.

However the region denoted by the red box in Figure 80 shows a significant alteration in LSE over a large area. In 2009 this area shows LSE in channel 12 with an average of 0.95 up to highs of 0.98-0.99. The peak values correspond to the LSE associated with vegetation.

As the LSE in the surrounding area is high, it is likely the change is due to construction or redevelopment leading to higher urban density. The actual change seen in the visible data is indeed a reduction of vegetation and the input of urban materials into the region. The development seen here is the construction of the as yet still not completed Disneyland Theme Park.

This park includes large areas covering in paving and huge car parking areas which has contributed to the lower LSE retrieved in 2014. The development has had a substantial effect on the surrounding area with the large construction project dominating the area.

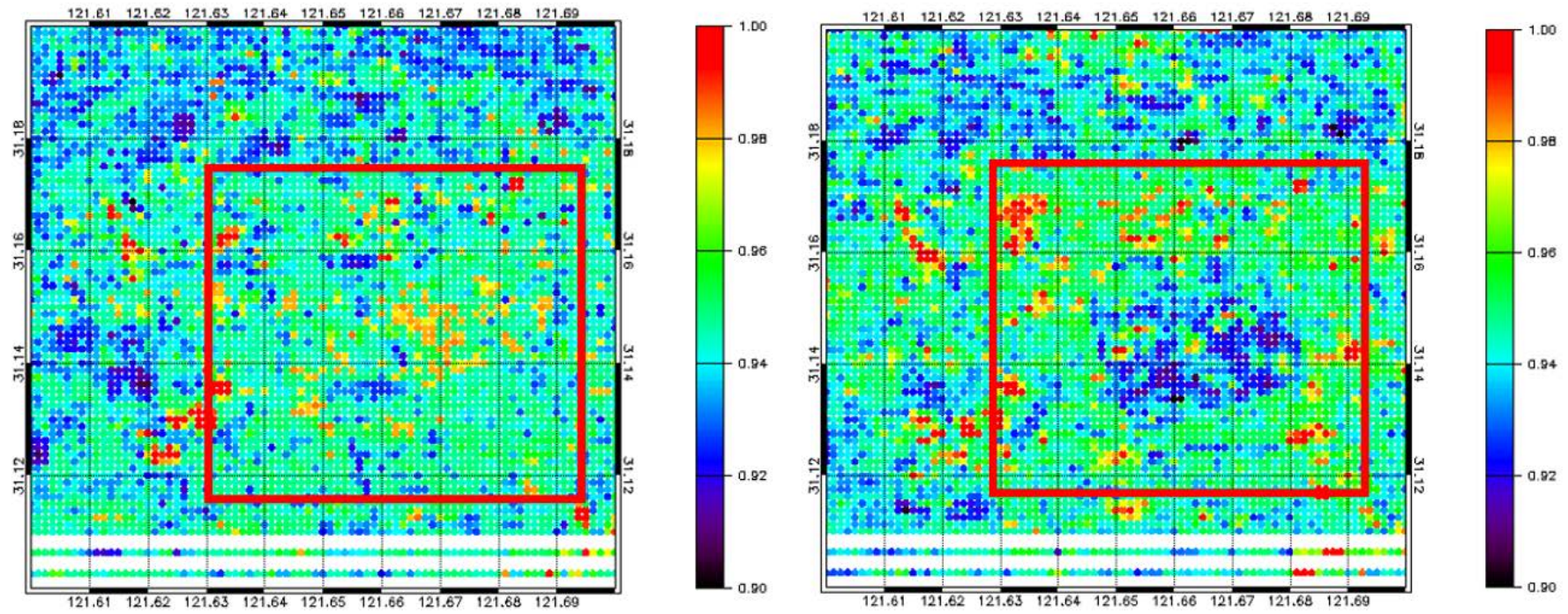


Figure 80 – The retrieved LSE for Region 3 in Shanghai in channel 12. LEFT: the retrieved LSE in 2009, RIGHT: the retrieved LSE in 2014.



Figure 81 - RGB imagery from LANDSATs 5 and 8 for Shanghai region 3. LEFT: LANDSAT 5 RGB for 21/10/2009, RIGHT: LANDSAT 8 RGB for 04/11/2014.

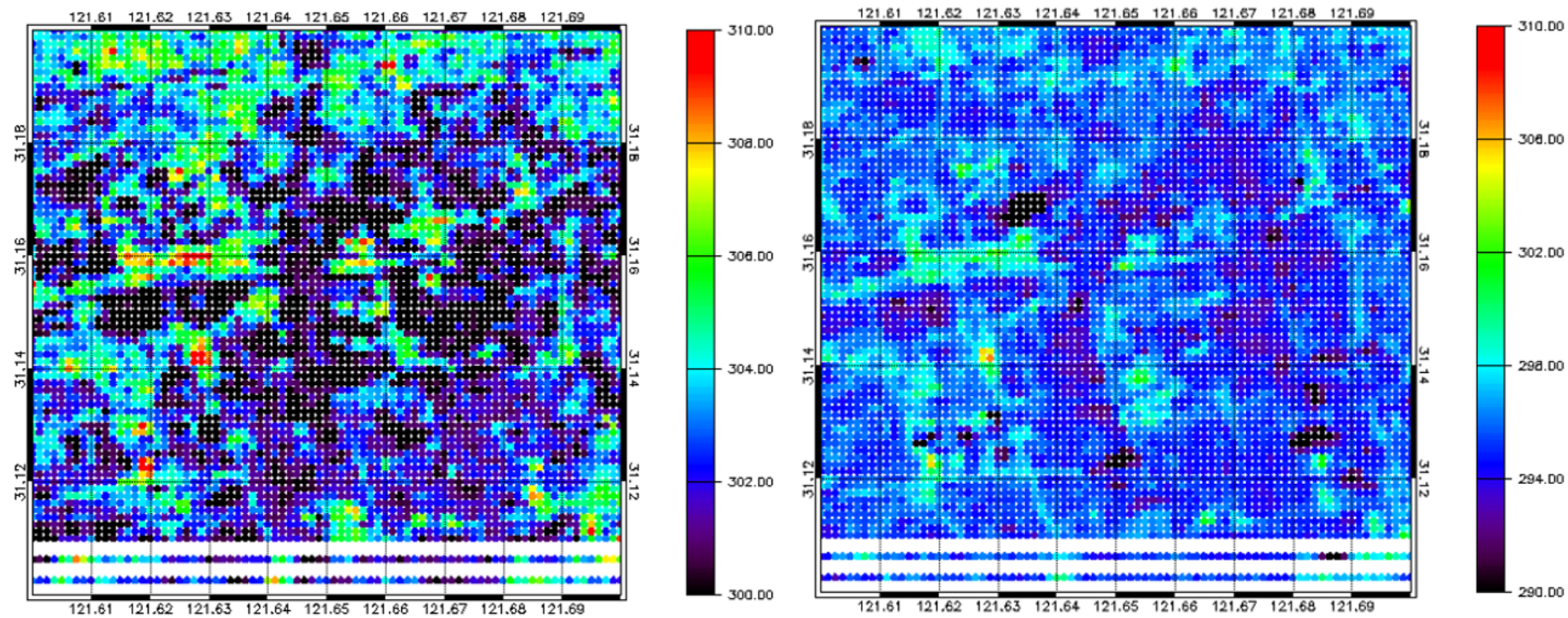


Figure 82 - The retrieved LST (K) for Region 3 in Shanghai. LEFT: the retrieved LST in 2009, RIGHT: the retrieved LST in 2014.

Analysing the LSE for the region identified as the car park the shift in material type is clear, see Figure 83. Channels 10 and 12 show a large reduction in LSE, with channels 11, 13 and 14 also showing a smaller decrease in LSE between observations. The change in LSE spectral shape is significant and shows a change in surface typically associated with the introduction of large impervious surface, such as concrete or asphalt.

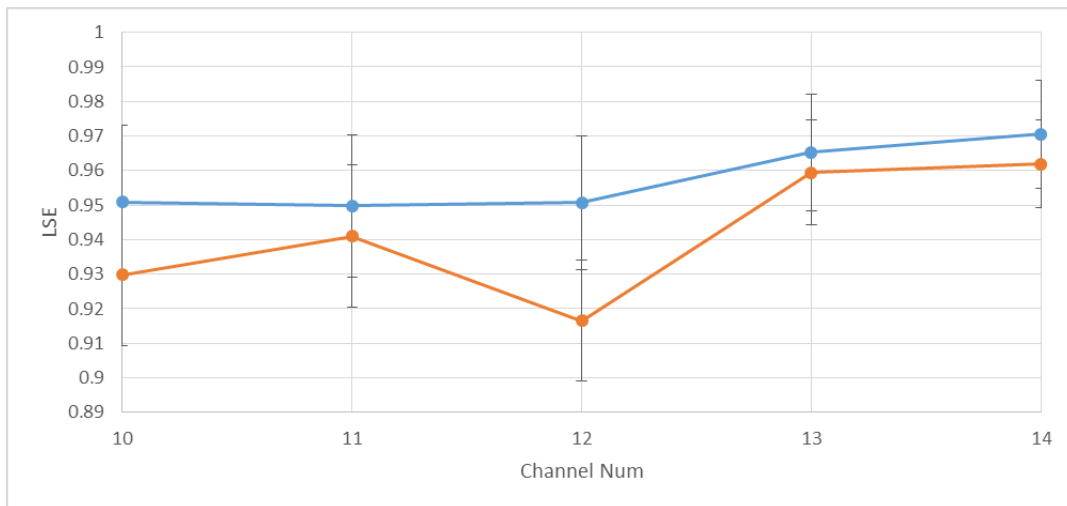


Figure 83- Retrieved LSEs for change region identified as the car park in region 3 with associated uncertainty.

However the road ways feeding into the site are not visible in the LSE data due to the small size of the road network compared to the pixel scale. The LST data is able to see the road network surrounding the site as lines of increased heating due to the anthropogenic heat generated here, see Figure 82.

The retrieved LST shows the paths of the roadways seen in the visible imager including the addition of/or increased use of new roadways running alongside the perimeter of the construction site.

The park itself is also apparent in the LST data but only along the edge connecting with the roadways. This area is the site car park and therefore is seeing considerable use, despite the parks lack of operation during the construction period. The LST in the south west of the new construction presents values approximately 5 K higher than in the rest of the region, despite the consistently lower LSE by 0.04. This demonstrates that the LSE and LST, while linked, are capable of determining

different surface properties in their own right. Identifying the material change in the park construction area shows the land class change, but the increase in the LST over the car park indicated the increase industrial use and the increase in temperature attributable to anthropogenic heating.

6.2.2.3 Region 4: Inter-urban change

Region 4 shows an area where the change in LSE is not seen in the a priori land classification data. The classification data shows the majority of this area as being consistently urban between the two scenes. The secondary class present is the mixed urban and vegetation class with a small quantity of vegetation. There are areas which show little or no LCLU shift, as seen in Figure 84. At 31.24 N 121.30 E for example there is a region with low LSE in both observations that show little change between the scenes. Additionally the majority of the scene east of 121.35 E shows very little change in either the LSE or the a priori data between observations, with the exception of a few pixels identified as water in 2009, not present in 2014.

However, at 121.33 E between 31.22 N and 31.18 N there is a region which is unchanged in the classification data between observations, but has substantially different LSE values.

In the centre of Region 4 there is a large structure that changes in LSE between the scenes. The change is not uniform and there is significant alteration in the structure as well as magnitude of the LSE. In 2009 the eastern terminal for Hongqiao International Airport, is visible as a long straight region of running from north to south with an average LSE of less than 0.90. This feature is also present in the 2014 LSE data. However, in 2009 to the west of this structure there is a large region from 121.34 to 112.31 E with lower than average LSEs and a diffuse distribution.

The 2014 LSE has a clearly defined western runway very similar in LSE to the eastern runway and clearly shows three passenger loading/aeroplane taxi zones halfway up the runway. Looking at high spatial resolution historical visible data the difference becomes clearer, see Figure 87.

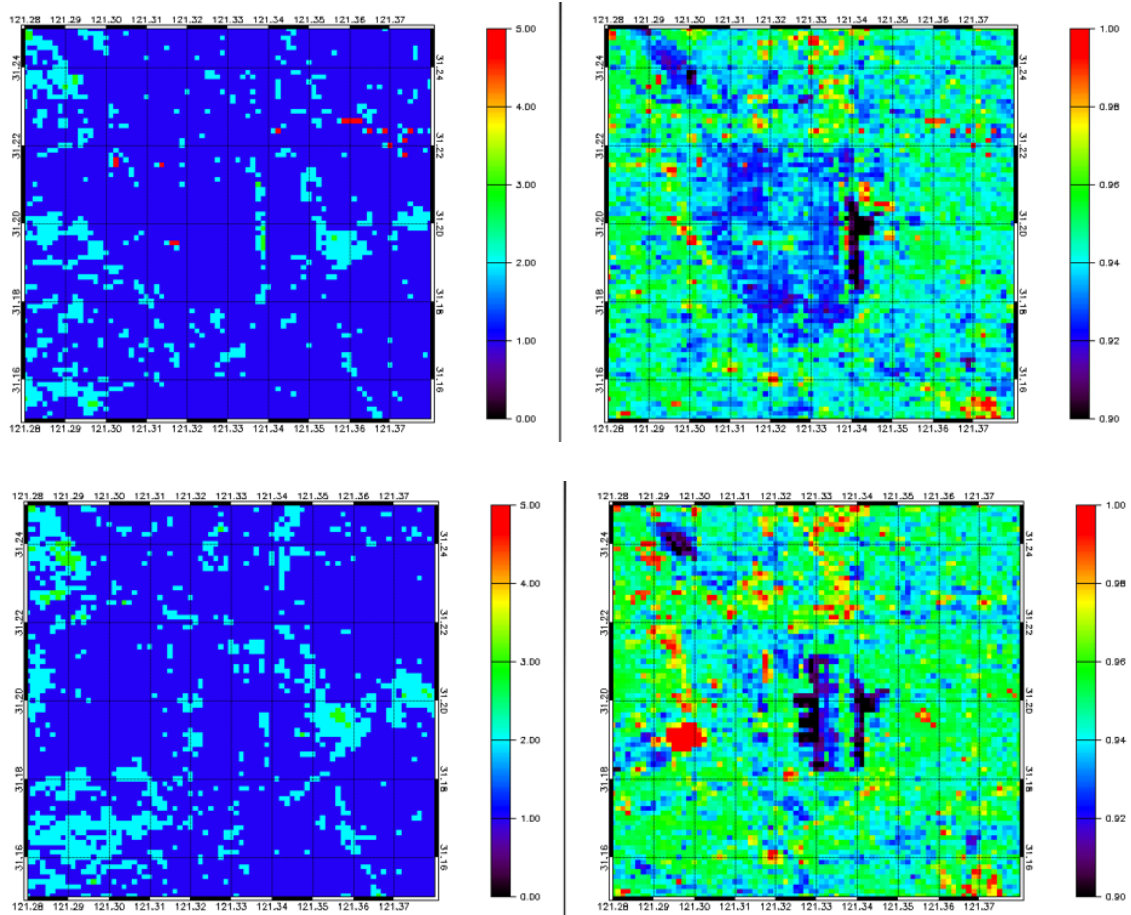


Figure 84 –LEFT the a priori classifications. Class numbers correspond to a particular cover type: 0 - no data, 1 - urban, 2 - mix: urban/vegetation, 3 - vegetation, 4 - rock/soil, and 5 - water. RIGHT the retrieved LSE data for channel 12. TOP panels show the data for 2009, BOTTOM panels for the data for 2014.

The visible imagery shows that the runway and taxi area are present in both observation time frames, but the materials and development of the structure are significantly different. The runway and passenger loading zones are still under construction in 2009, construction finished in 2010. The materials in the construction site are different to those in the finished runway as being a mixture of rock and bare soil as well as the man-made construction materials such as concrete. Importantly the finished runway layer, seen in the eastern runway in both observations, is not present and therefore the LSEs are significantly different, approximately 0.03.



Figure 85 - Visible imagery from DigitalGlobe and CNES ASTRUM obtained from Google Earth for a subset of Region 4. LEFT shows data from 2009, RIGHT for 2014. The top panels show the Airport runways, the bottom panels show a close up view of a loading and taxi way for the aeroplanes.

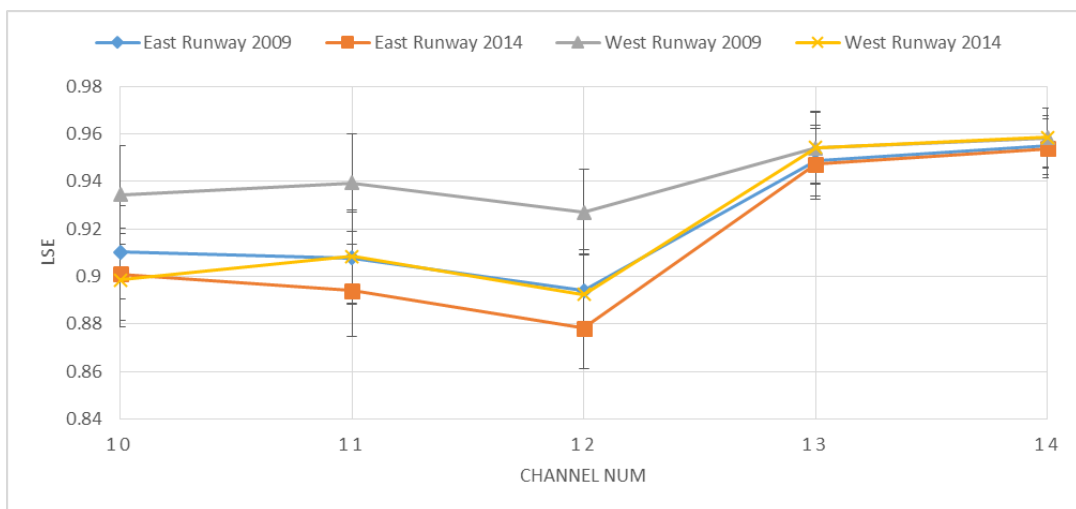


Figure 86 – Retrieved LSEs for all channel for two locations: The eastern runway and the site which became the western runway. The LSEs are shown for both 2009 and 2014.

This can be seen more clearly in Figure 86, where the LSEs are shown in all channels for two selected sites. The first site is at the centre of the western runway which is seen as a consistent feature between the two observations. The results from 2009 and 2014 show a high level of consistency and agree to within the retrieved uncertainty. The LSEs for the western runway show large difference between the observations. The spectral shape is similar, but the LSEs in channels 10, 11 and 12 are significantly lower in 2014. The 2014 LSEs are also a match to the LSE retrieved over the eastern runway, which was expected from the visible imagery as they appear to be made of the same material. In this case the retrieval is able to accurately identify a substantial material change and in doing so detect urbanisation in a transitional state. Given the rapid pace of urbanisation, particularly with in Shanghai this an important step forward.

Furthermore the surrounding area shows marked difference. In 2014, the area around the airport is urbanised with large highways and districts with industrial warehouses. In 2009 the entire area appears to be undergoing substantial redevelopment with evidence of bare soils, and construction throughout. The scale and spread of the construction process visually matches the region seen in the 2009 LSEs of LSE spread across a broad area.

There is a secondary feature identified during the analysis which exhibits large change between observations. In Figure 84 at 31.19 N and 121.298 E there is a region which shows a large change in LSE. In 2009, there is no definable structure to be seen and the LSE retrieved is close to that of the mean for the region. However, in 2014 this area has extremely high LSE in channel 12, with an increase of 0.04 in LSE.

Assessing the visible imagery shows a very clear change in the surface. In 2009 the area shows a mix of vegetation and industrial units with block of residential buildings in the south west. In 2014 the entire area has changed with only the canal running along the north east and the residential area remaining unchanged. The primary change and source of the increase LSE in 2014 is one extremely large structure.

This structure is the National Exhibition centre, the single largest exhibition complex in the world. The materials used here are not typical of those found in the rest of the urban environment and as such the LSE seen here is markedly different.



Figure 87 - Visible imagery from DigitalGlobe and CNES ASTRIUM obtained from Google Earth for the Subset. LEFT shows data from 2009, RIGHT for 2014.

In this case the LSE changes between the observations were able to identify urban change between different types of urban cover, and not just change from urban to non-urban or vis versa, this shows potential for in-depth study of the effect of urban redevelopment and density changes.

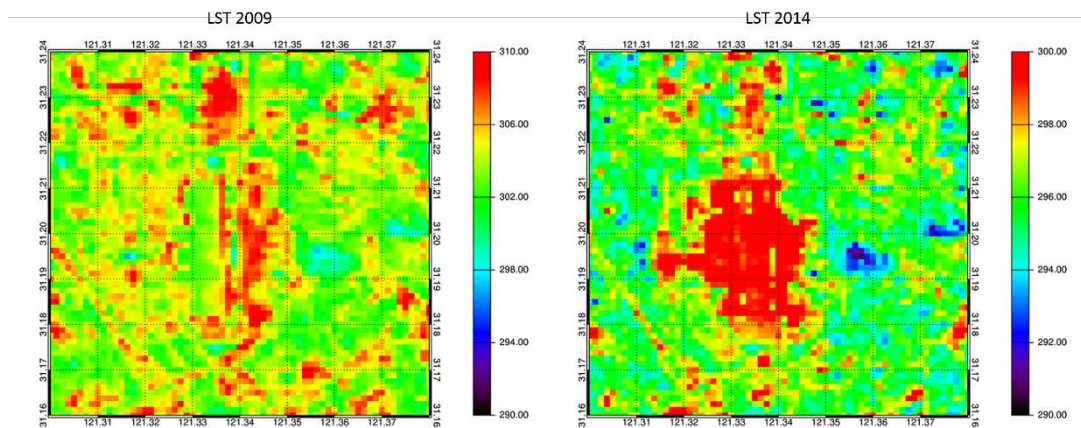


Figure 88 – Retrieved LST for Region 4, for 2009 and 2014.

The effect of these surface and land usage changes upon the relative LST is significant. As seen in Figure 88, the LST in 2009 was primarily focus on the eastern runway and airport structure, where the majority of the commercial activity would be located. After the construction of the second runway and terminal the region of heightened LST spread to not only incorporate the new runway and terminal but also the surround redevelopment. In relative terms the construction of the airport raised

the LST of the airport itself and the surrounding region by over 5 K, a clear demonstration of anthropogenic heating.

6.3 Case Study III: New York

New York is a major urban centre and has become the subject of significant scientific study, with research into the effect of urban heat mortality an area of increasing interest (Petkova et al. 2016)

New York city is an extremely large urban region, and the most populous city in the USA, with a population of 8,550,405 people as of the 2015 US Annual Estimate of Resident Population (Bureau, 2015). This population is also by no means stagnant with an increase of over 335,000 people between 2010 and 2015. The city is coastally situated and has several urban regions distributed between islands, peninsulas and the mainland. As such the city presents several unique challenges in understanding its UHI.

The UHI is highly dependent on the time of day with air temperature changes of 2 K between different urban sites in hourly measurements, (Gaffin et al., 2008). Gaffin et al. (2008) also showed that despite its high fraction of vegetation cover, that Central Park in Manhattan is a good representative indicator of the state of the cities UHI as a whole.

Furthermore New York's coastal location introduce a further variable affecting the UHI and LST in the form of sea breezes. A study by (Gedzelman et al., 2003) found that the sea breezes in the summer and spring seasons decrease the UHI and give it a spatial and temporal offset. The sea breeze effect can push back the spatial extent of the UHI up to 10 km west from the coast in strong breezes. Therefore analysing the SST and water conditions in addition to the LST and LSE is a requirement for assessing the New York UHI.

6.3.1 Study area

The site selected encompasses the primary urban zone with several key regions represented, see Figure 89. In addition to the urban land cover there is significant

vegetation to the west of the site and ocean to the south-east, with large water bodies feeding into this. Within the urban conurbation a full range of different land uses are present, including residential, commercial and industrial.

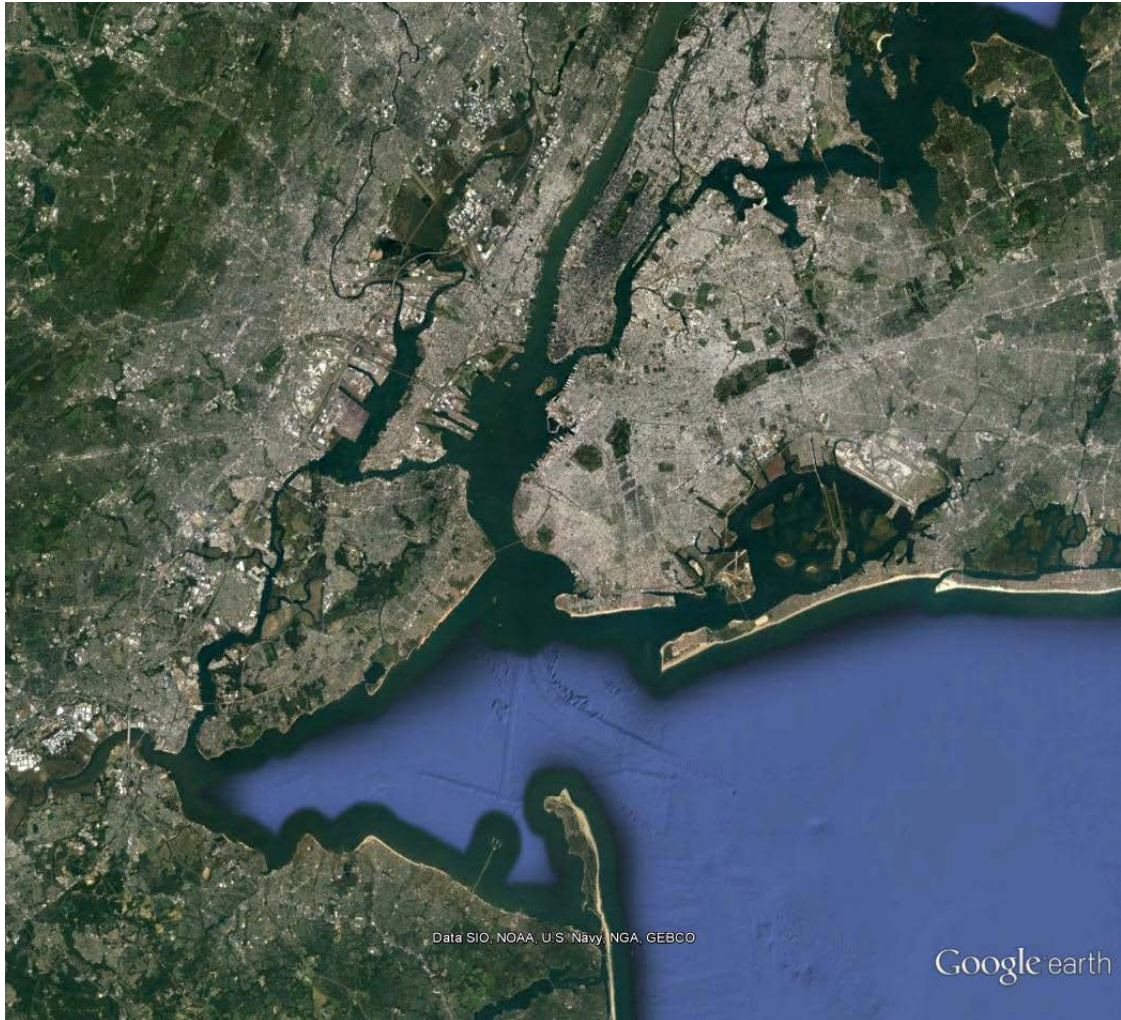


Figure 89 - Visible imagery of the selected New York City test site. Image taken from Google earth, 40.718 N, -74.012 E, image acquired 28/08/2016, image obtained 16/07/2016.

The scenes were selected to be as cloud free as possible, firstly using the ASTER and MODIS cloud flagging products and secondly using a manual assessment of the TOA BTS for anomalously low temperatures. However this the cloud filtering is not perfectly accurate. Due to cloud contamination in portions of the observations the study was limited to regions where there was no cloud detected in any of the observations. To this end the study area was reduced to a subset containing Manhattan and the surrounding coastline. Manhattan also possesses some of the most developed urban areas in the city and presents a level of urban density greater than any other region with in the observations, making it an ideal location to look at the

variability of the LST and LSE with the urban region as well providing the opportunity to investigate the effect of the vegetation and water on the temperatures observed.

6.3.2 Retrieval Performance

Due to the presence of water in large quantities there are two distinct distributions in the retrieved LST and LSE, as seen in Figure 90. There is a strong peak within the LST and each of the five LSE retrieved parameters that ties spatially to the water covered regions. This result is expected as due to the homogeneity of the sea water LSE, the a priori LSE is extremely close to the truth, therefore the retrieval has little movement from this, never exceeding the bounds of the a priori covariance. The LSE panels in Figure 90 show very sharp peaks at these water pixels, with LSEs as high as 0.998 in channel 14 observed.

The second distribution relates to the land pixels, here the range of LST and LSE values is much broader and across much of the scene with higher LSTs and lower LSEs than the water. Within the LST there is a broad spread with values trailing off at a shallower gradient towards the lower temperatures where there is a blending of vegetation and urban surfaces.

The retrieved uncertainty of the scene shows a similar dual distribution, with highly constrained values for the uncertainty of the water pixels with LST uncertainty of 0.5 K and LSE between 0.007 and 0.008 across all the channels, as seen in Figure 91. This uncertainty is in line with expectations given the size of the variability for the parameters, especially for the LSE retrieved over water. The land uncertainties follow a distribution which closely matches those of previous retrievals from Chapters 4 and 5, with the largest uncertainty seen in channel 10 peaking at 0.024 and channel 14 showing the lowest uncertainty with a maximum of 0.0129.

The LST uncertainty peaks at approximately 1.85 K, with a maximum retrieved uncertainty of 2.2 K. This uncertainty is significantly higher than expected from the simulated studies and the previous case studies. The radiance residuals for this scene are also significantly higher than those previously encountered, see Figure 92.

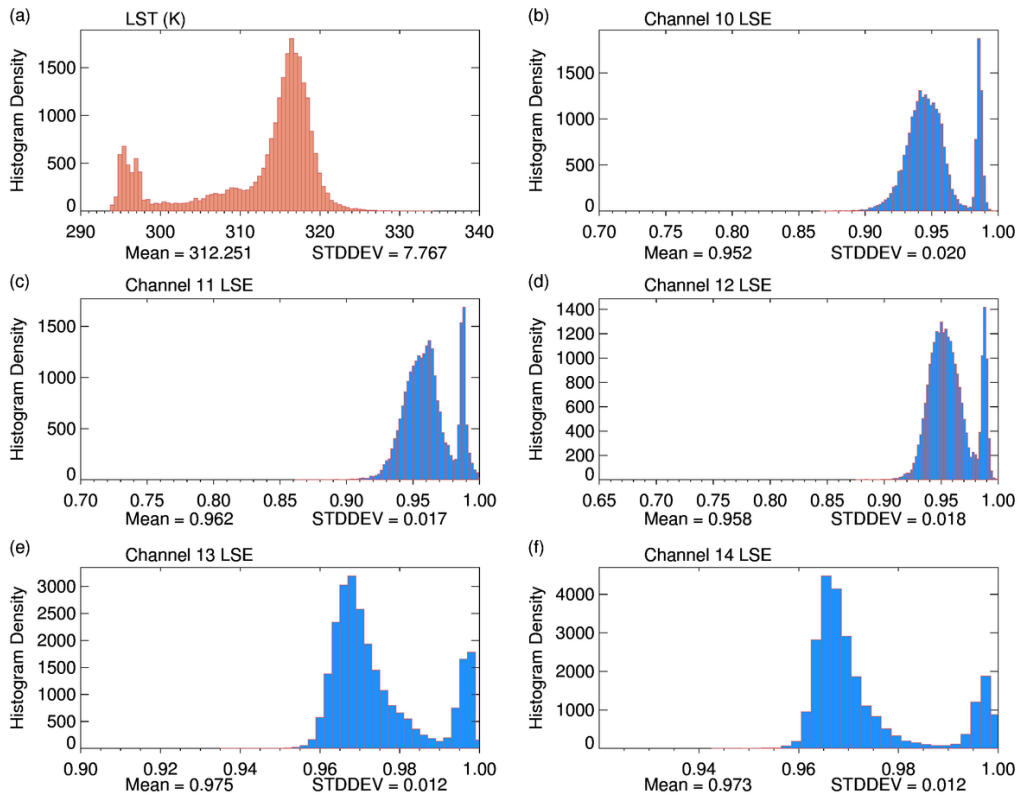


Figure 90 - Histograms of the Retrieved LST and LSEs for all TIR channels for the New York case study site. Means and standard deviations for each retrieved parameter are displayed below the main panel.

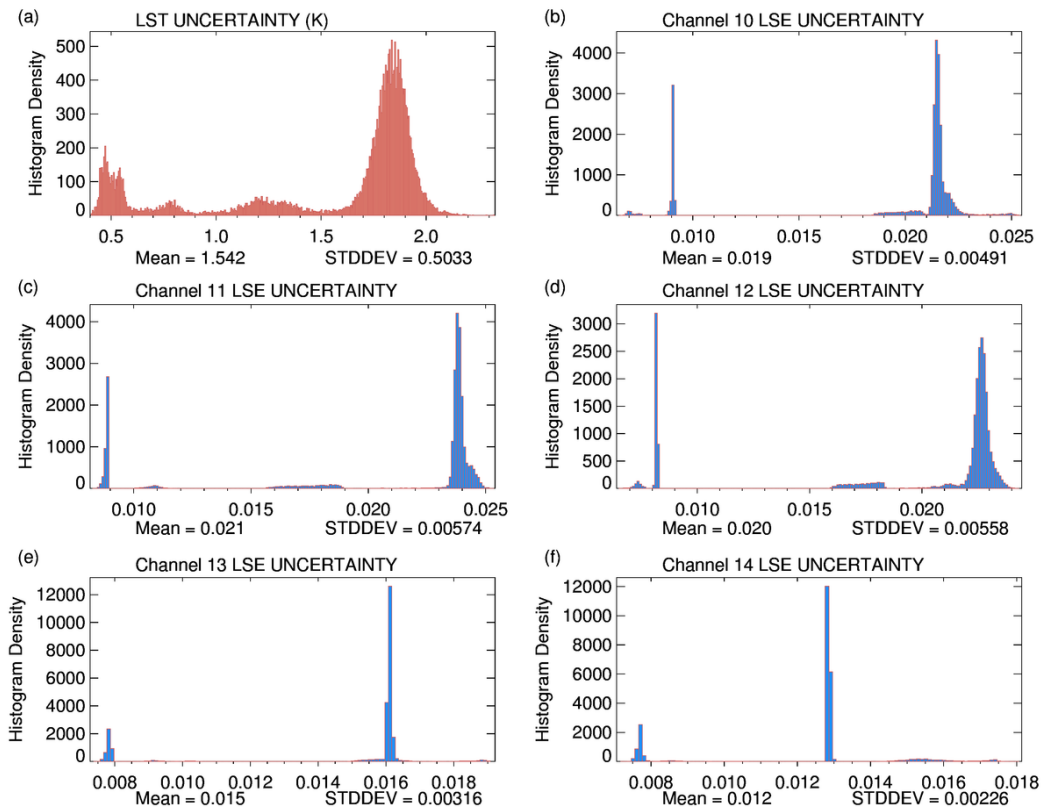


Figure 91 - Histogram of the retrieved LST and LSE uncertainty for all the TIR channels. Mean and standard deviation values for each retrieved parameter are displayed below the relevant panel.

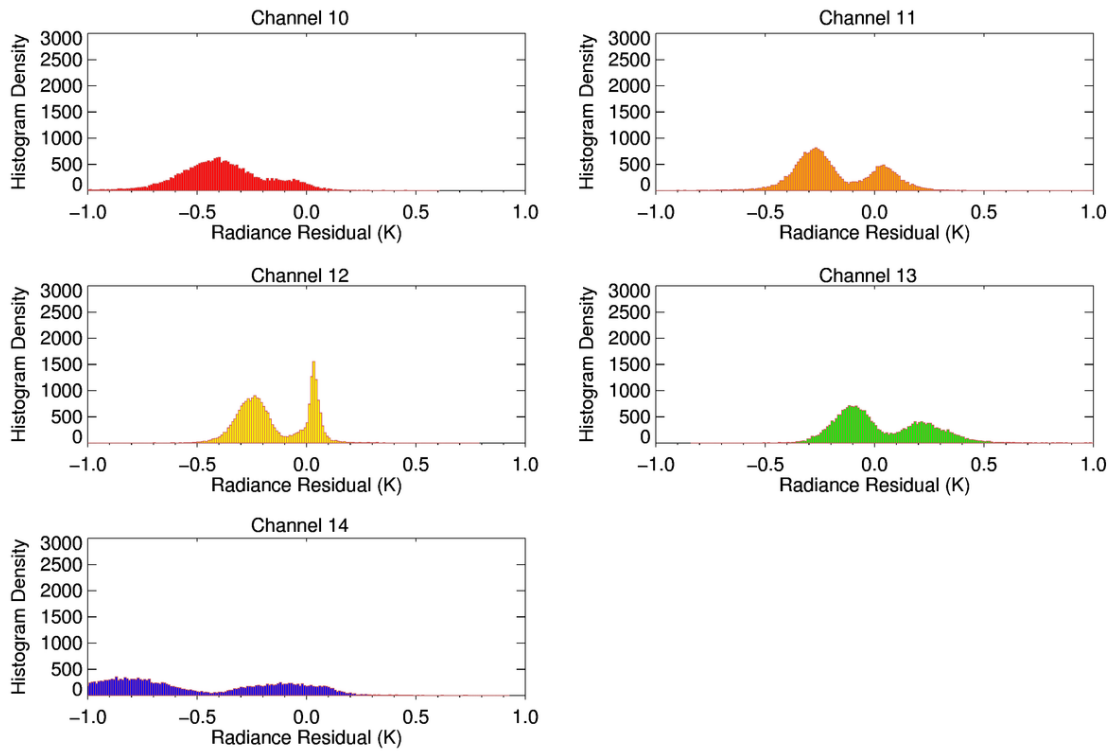


Figure 92 - Histogram of the Radiance residuals for the OE retrieval for all the TIR Channels.

There are two sets of retrievals shown in Figure 92. One set has very good radiance residuals and one has with poor performance. This is seen most clearly in channel 14 where one cluster of retrievals shows a mean radiance residual of 0.1 K and the other 0.75 K.

Tracing the cause of the increased uncertainty and increased radiance residuals led to the level of water vapour profiles. Previous studies had used profiles with 2 cm TCWV or less and an uncertainty of 2 mm, most commonly significantly less due to the arid environments studied. The water vapour in the ECMWF profiles for this scene ranged from 2.1 to 3.8 cm TCWV. Where the profiles showed the highest water vapour the retrieved uncertainty and radiance residuals were significantly higher. The retrieved uncertainty includes the effect of the water vapour, and while the a priori covariance is unchanged the effect of the water vapour on the simulated brightness temperature is not linear, therefore at higher TCWV values the TCWV Jacobian will have a greater impact on the retrieval and the retrieved uncertainty.

6.3.3 LST and LSE Spatial Structures

The retrieved LSE and LST results for the Manhattan subset show a range of spatial features, relating to the LULC. The LST results shown in Figure 93, show industrial regions in North Bergen, the region to the north-west of the subset, with higher LST than the urban background. In contrast the spatial distribution shows clear contrast between the land and water surface types as would be expected, with the SST values being 20 K lower than the LSTs.

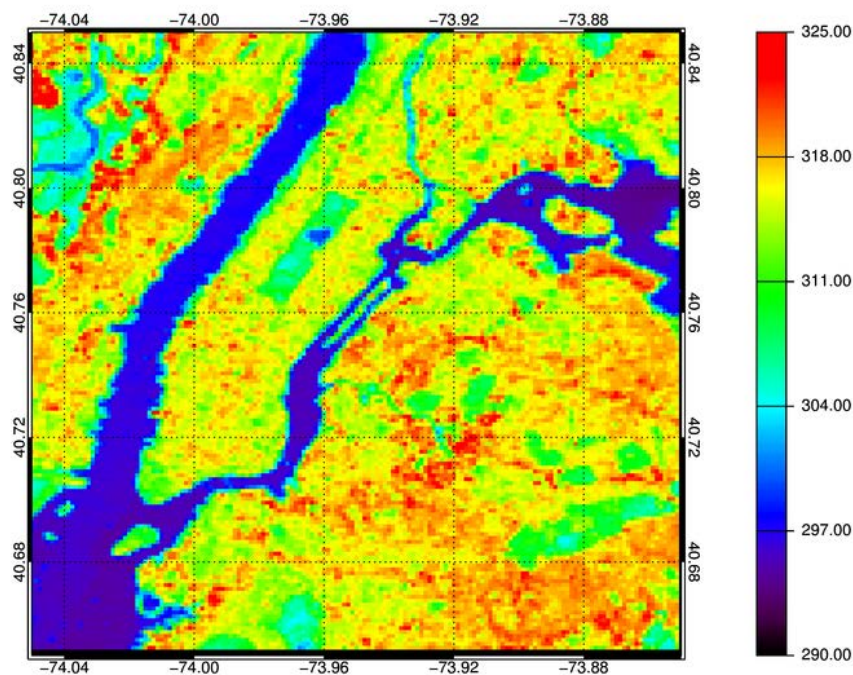


Figure 93 – LST map for the Manhattan study area for 01/07/2012.

Figure 93 also highlights the difference between the urban and vegetated regions with the higher LSTs seen only in the urban- industrial regions to the west of Manhattan Island. Additional large urban green space such as Central Park in Manhattan Island are clearly visible as regions of cooler LST, an effect consistent with the current understanding of temperature mitigation in urban regions by vegetation through evapotranspiration.

The vegetative areas also shows higher LSE seen in the parks and urban green spaces. There are also features with higher LST and LSE. Towards the south of Manhattan Island at 40.72 N -74.00 W, there is an area with LSEs around 0.97 but also with an

average temperature above that of the urban background. This area corresponds to a region of highly developed commercial and office land which is dominated by high rise builds.

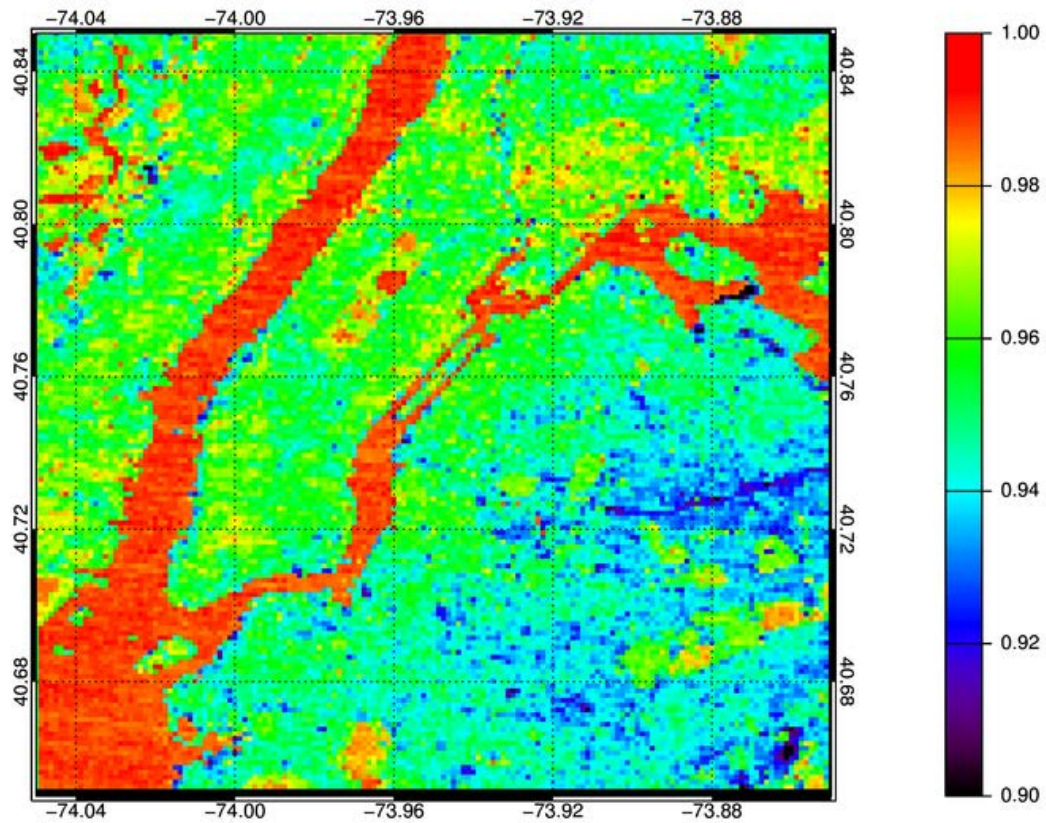


Figure 94 – LSE retrievals for the New York case study site in TIR channel 12.

6.3.3.1 Classification Analysis

Three observations were analysed for the Manhattan spatial subset, for the 1st of July 2012, the 25th of June 2012 and the 19th of July 2015. These scenes aimed to look at the apparent LST structure in terms of the classification. In each of the scenes the retrieved pixels were broken down into their a priori classifications and the mean and standard deviations found, see Table 25.

The classes showed the vegetation being the coolest surface, typically 7-8 K cooler than the urban region. This scene has extremely high proportion of urban materials as discussed in the k-means classification.

a priori class	Date	mean LST	STDDEV	Cover (%)
Urban	<i>01/07/2012</i>	316.23	2.94	86.33
	<i>25/06/2013</i>	312.72	4.17	88.19
	<i>19/07/2016</i>	315.39	2.71	84.23
Mixed Urban and Vegetation	<i>01/07/2012</i>	308.48	5.12	11.48
	<i>25/06/2013</i>	305.70	5.82	11.34
	<i>19/07/2016</i>	309.32	3.94	12.28
Vegetation	<i>01/07/2012</i>	306.54	2.13	2.20
	<i>25/06/2013</i>	303.85	1.43	0.47
	<i>19/07/2016</i>	305.02	1.90	3.50

Table 25 - The mean and standard deviation for all pixels with in the subset for all observations in (K). The data is divided into the a priori classifications used in the retrieval. For each class relevant percentage of the scene it covers is given in the right most column.

The high level of development in New York and the high proportion of urban pixels in the scene provides the opportunity to compare the responses of different urban sub classifications, as a means of assessing the anthropogenic heat.

6.3.3.2 Urban Sub-Classifications

Within New York, and particularly within this subset there are several types of urban cover, for this investigation three were identified: Industrial, Residential and Developed High rise, see Figure 95.

The three urban subsets were selected to explore the differences between the usage and construction within the urban classifications. Both the LST and LSE were assessed as shown in Table 26. In all three observations the Industrial sub-class was the warmest, with the residential sub-class showing the lowest LSTs. Given the level of anthropogenic heating commonly associated with industrial complexes this agrees with expectations. The scale of the differences was consistent between observations with the Industrial being an average 3-4 K warmer than the Residential areas, and 0.5–1 K warmer than the High rise sub-class, an indicator of differing land usage and increased anthropogenic heating.



Figure 95 Visible imagery for the subset identifying the locations of the three urban subsets analysed. Image taken from Google earth, 40.738 N, -73.934 E, image acquired 28/08/2016, image obtained 16/07/2016.

The LSE results show the observations on 10/07/2012 and 25/06/2013 to be very similar with agreement to be less than the standard deviation within each channels LSE. The LSEs seen in the industrial and residential areas are very similar which is also seen in the visible imagery as the building types are not hugely varied between the sites. However, despite the matching LSEs, the LST retrieval manages to distinguish the industrial land use from the similar land cover type. The two parameters in conjunction build a larger picture of the urban thermal environment. The high rise conversely has noticeably higher LSEs than either the Industrial or Residential subclasses showing a distinct change in the primary materials used in the construction. However, the LSE change could also be a product of the satellite view. The instrument views incoming light that comes from a range of angles even at such a small swath size. In flat homogeneous surface this effect is small on the LSE, however in this urban sub class there is significant vertical structure.

The pixel shows the surface that the light has come from, but it does not intrinsically determine whether that light has come from the ground level surface, the roof top, or potentially the face of a building. In this high rise district, it is highly probable that a

portion of the light captured by the instrument has originated from the building face and not just the ground.

Sub Class	Date		LST	C10 LSE	C11 LSE	C12 LSE	C13 LSE	C14 LSE
Industrial	01/07/2012	Mean	317.42	0.94	0.95	0.95	0.97	0.97
		Std Dev	3.854	0.016	0.015	0.012	0.006	0.005
	25/06/2013	Mean	314.86	0.95	0.96	0.96	0.97	0.97
		Std Dev	4.309	0.012	0.010	0.011	0.005	0.004
	19/07/2016	Mean	316.01	0.93	0.93	0.92	0.96	0.96
		Std Dev	3.253	0.019	0.016	0.015	0.007	0.006
Residential	01/07/2012	Mean	316.29	0.94	0.95	0.95	0.97	0.97
		Std Dev	1.754	0.010	0.010	0.008	0.004	0.003
	25/06/2013	Mean	312.55	0.96	0.97	0.96	0.97	0.97
		Std Dev	1.499	0.008	0.008	0.007	0.003	0.002
	19/07/2016	Mean	315.06	0.93	0.93	0.92	0.96	0.96
		Std Dev	1.722	0.012	0.010	0.008	0.003	0.002
High Rise	01/07/2012	Mean	316.01	0.95	0.96	0.96	0.97	0.97
		Std Dev	1.487	0.009	0.008	0.007	0.003	0.002
	25/06/2013	Mean	312.93	0.96	0.97	0.97	0.97	0.97
		Std Dev	1.248	0.006	0.006	0.006	0.002	0.002
	19/07/2016	Mean	315.83	0.94	0.94	0.92	0.96	0.96
		Std Dev	1.380	0.011	0.009	0.007	0.004	0.003

Table 26 - The mean and standard deviation for all pixels with in the subset for all observations the LST in (K). The data is divided into the urban sub-classes.

Additionally, in this environment shadows cast by the taller building will alter the amount of sunlight the surfaces are exposed to causing shifts in the temperature, (Lu & Weng, 2006).

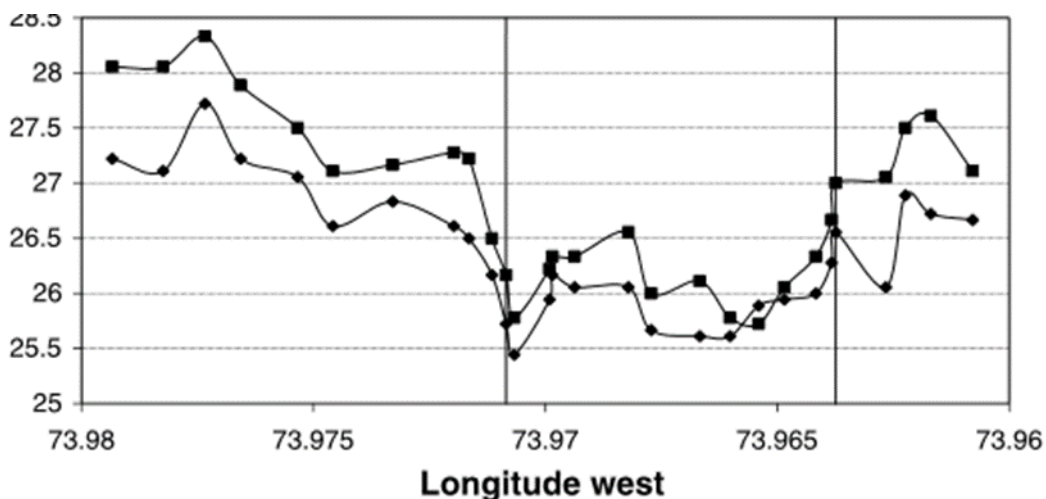
19/07/2016 however shows substantial deviation with LSEs in channels 10, 11 and 12 show lower LSEs than those seen in the other observations. The values seen in channel 12 make the LSE offset of 0.03 in 19/07/2016 highly unlikely. The exact cause of this offset is difficult to identify but the lowered Channel 12 LSE is indicative of a false minima being found within the retrieval due to channel 12 over weighting in the retrieval, as described in Chapter 5. Due to this this observation was flagged and is not used in subsequent analysis.

6.3.4 Transect Analysis

Given the high spatial density and development level of New York, any change in the LST could have important consequences for the surrounding heat and health of the city. A primary method of combating UHI and other urban health impacting phenomenon has been the management and introduction of vegetation into the city. Most famously the city focused upon this in the “MillionTreesNYC” campaign (Locke et al., 2011). To investigate the effect of vegetative and water cooling, and the effect of the land use on the anthropogenic heat, two transects were investigated.

6.3.4.1 Transect 1: Central Park Air Temperature comparison

In order to assess the potential impact of adding additional vegetation to city it is important to assess the effect of existing vegetation. Studies of urban green space in New York have focussed upon in situ air temperature data. (Gaffin et al., 2008) investigated the New York UHI in this manner looking at air temperature data across the urban area, and took a transect through central park and the surrounding urban regions to see the effect of the green space on the UHI, see Figure 96.



remotely sensed data is shown in Figure 97. The LST data shows a significant reduction over the vegetation in the park with an offset from the urban background of nearly 10 K. The spatial distribution of the dip in LST matches both the NDVI and the air temperature distribution from the literature. The literature air temperature data shows there is a reduction in temperature before entering the park, the authors commented that they suspected that this was due to the changes in the nocturnal cycle as the data was taken over the course of several hours. The satellite data does not have any temporal separation in the pixels and does not show this structure. The satellite data therefore can confirm that this structure is not likely to be a real effect of the vegetative area.

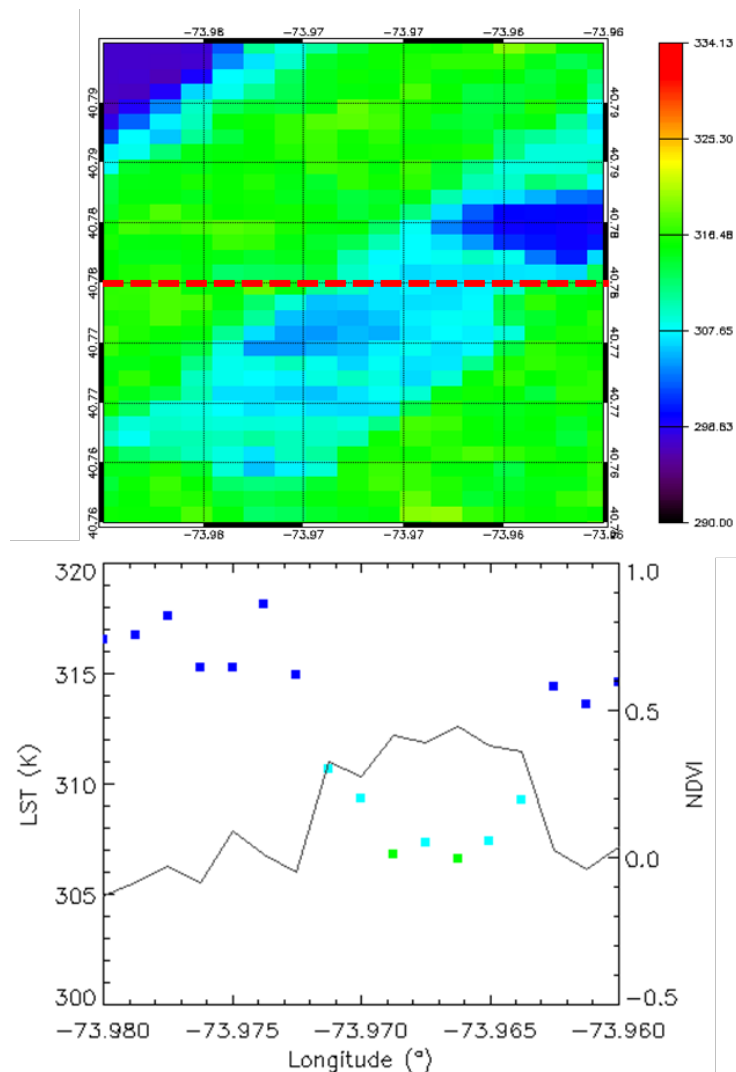


Figure 97 – TOP The LST for the region surrounding the park transect, the red dashed line denote the transect path. BOTTOM the transect LST and NDVI. The colours correspond the LST for different a priori classifications given to the pixel: dark blue = urban, cyan = mixed vegetation and urban, gold = rock/bare soil and green = vegetation. The solid line shows the NDVI

6.3.4.2 Transect 2: Comparison of Vegetation and water cooling

Having tested the initial area around the park the study was expanded. The ability to take readings over a large area simultaneously is one of the primary advantages of remotely sensed data and in this case it allow the building upon previous knowledge to look at the broader LST effects. The bounds of the transect were expanded such that Transect 2, covered the whole of Manhattan island as well as the industrial region to the west in Hudson and LaGuardia airport in the east, see Figure 98.

The extended transect shows a number of key features. Firstly and most notably the water surrounding Manhattan Island and LaGuardia are immediately visible are regions of significantly lower LST, far lower than the reduction seen in the park which is still apparent in this path. The water is also easily isolated in the LSE data, seen in Figure 99, as very high LSE values.

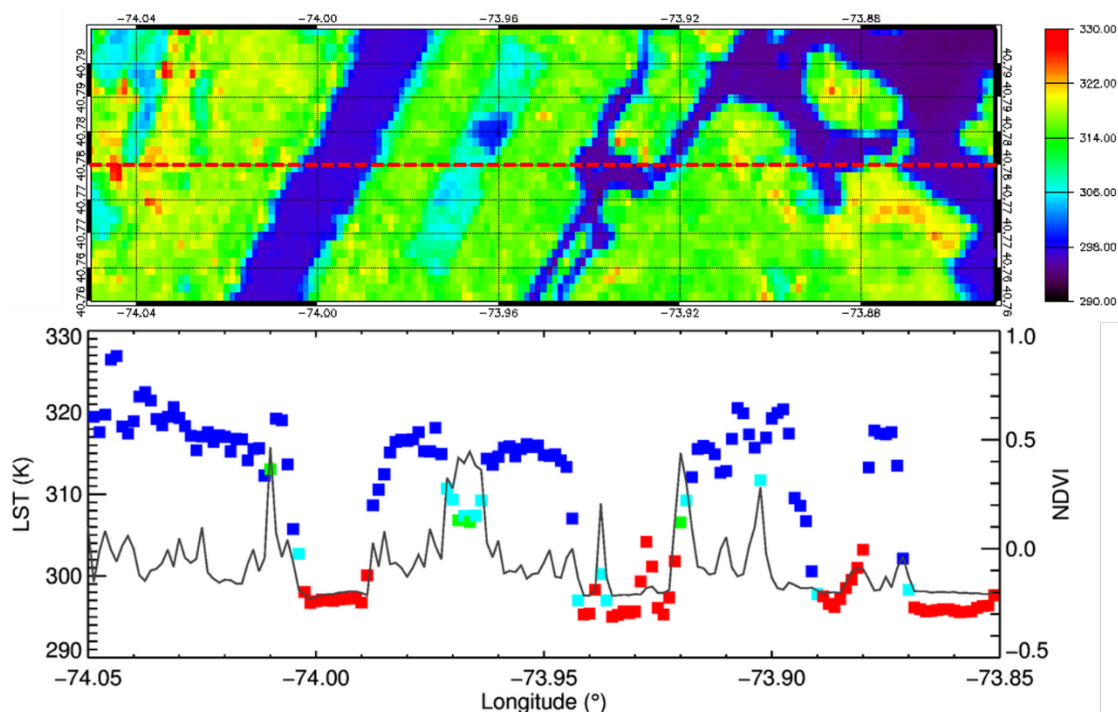


Figure 98 – TOP The LST for the region surrounding the extended transect, the red dashed line denote the transect path. BOTTOM the extended transect LST and NDVI. The colours correspond the a priori classification given to the pixel: dark blue = urban, cyan = mixed vegetation and urban, gold = rock/bare soil and green = vegetation.

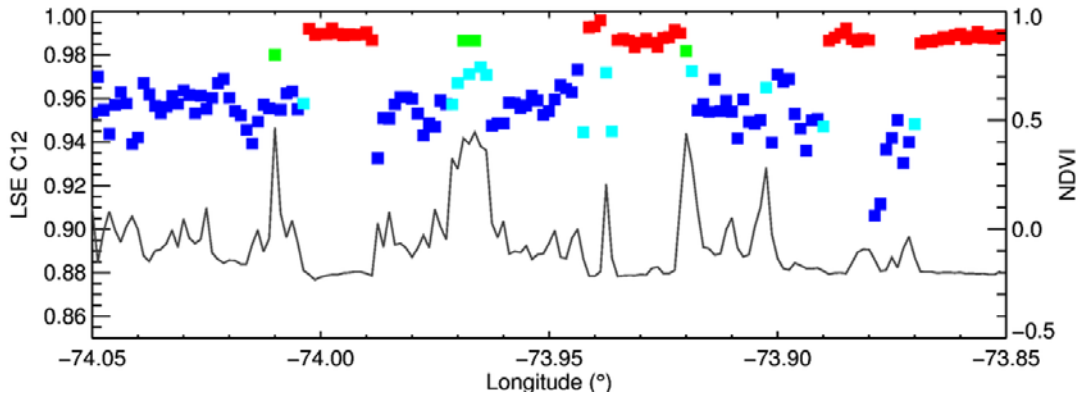


Figure 99 - The extended transect LSE and NDVI. The colours correspond the a priori classification given to the pixel: dark blue = urban, cyan = mixed vegetation and urban, gold = rock/bare soil and green = vegetation.

The LSE values for the water and the park are very high, and in line with expectations, see Figure 100. The airport is not visible as a region of higher temperature in the intercept (which is cutting through the runway) but instead the LSE at -78.88 W is the lowest in the transect showing values typically associated with large asphalt like materials. Also the industrial area, despite the high LST, does not show a lower LSE typically associated with large amounts of impervious materials, see Figure 100.

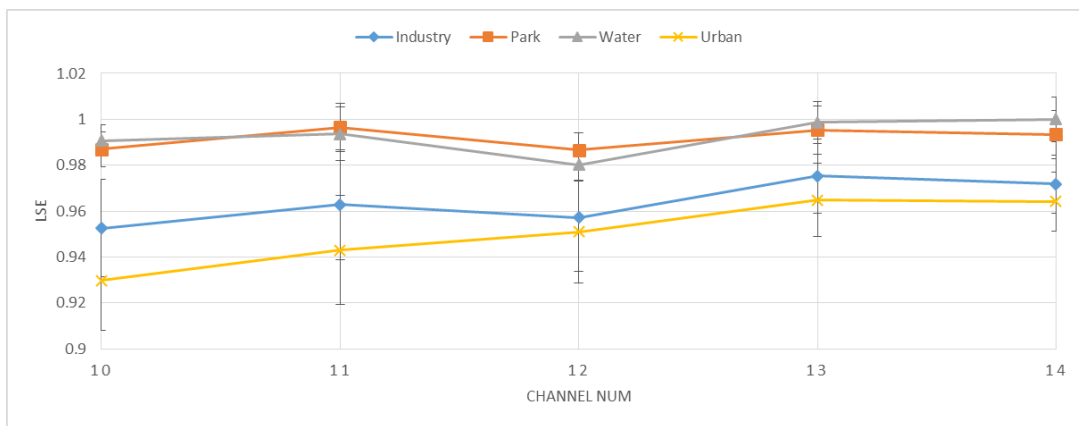


Figure 100 – Retrieved LSE in all channels for four samples from Transect 2. The four samples are for industrial, parkland, water and urban background areas.

The industrial area to the extreme west of the transect shows a similar LSE retrieved to that of the surround in urban areas. However, the area is denoted in the LST with much higher temperatures than the surroundings; nearly 5 K hotter than the urban background, a clear indication of anthropogenic heating. The heightened LST in the

industrial district as well as the depression in temperature due to the water and vegetation are seen across the observations, see Figure 101.

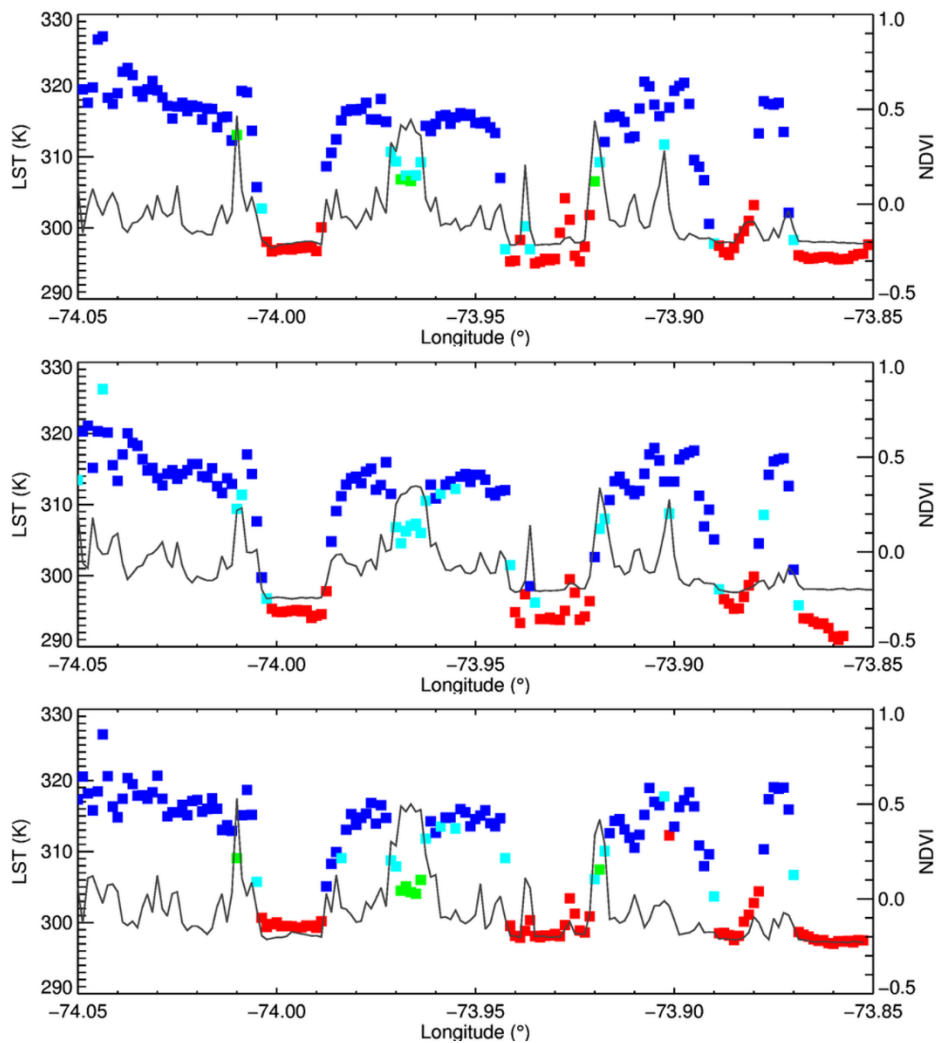


Figure 101 - LST transects for all observations. The colours correspond the a priori classification given to the pixel: dark blue = urban, cyan = mixed vegetation and urban, gold = rock/bare soil and green = vegetation.

There is a strong correlation shown between the observation transects, with the same distribution seen between the different temporal snapshots. The water appears to be on average 20 K cooler than the urban, with warmer water seen on the western side of Manhattan Island, approximately 2 K hotter than the water to the east of Manhattan and around LaGuardia.

Additionally there is a slope in the LST surrounding the water which is, on average, larger than two pixels in width, with reduced LST. The size of the slope makes it unlikely that this is due to sub-pixel mixing of cover types and show a cooling effect

of the water of 3 to 6 K. The vegetation cools for a more moderate 10 K. Manhattan Island has typically lower LSTs than those seen on the land either side possibly showing the combined effect of green space and the water bodies surrounding it, as cooling influence on the urban heat island.

6.4 Summary

In this chapter two different cities with specific urban challenges were taken as case studies to assess the retrieval's ability to meet these requirements and further knowledge in these studies.

Shanghai is at a rapid stage of urban expansion and development and as such the primary focus of many investigations is in detecting these changes and looking at their effect upon the urban landscape. In this manner the retrieval was used to focus on changes observed between two scenes with significant temporal separation. The resulting analysis found that the retrieval was able to identify a number of changes, ranging from the dramatic LSE shifts due to land reclamation or from the removal of land masses from water ways. The received LSEs were a match to the expected surface changes identified the water, rock/bare soil and several different types of urban surface cover.

The retrieval identified the construction of an amusement park causing a loss in vegetation and an increase of impervious surfaces. With a corresponding increase in the LST due to the increase in anthropogenic heating associated with the construction project. Secondly, a large scale re-development and construction project at Hongqiao Airport was identified through the change in surface materials present in the incomplete and finished runways. Comparisons between the retrieved LSEs were able to confirm the change using the pre-existing runway as a LSE baseline. The increase in the anthropogenic heating was observed in the LST data informing both the effect of the change in materials, and in areas where there was less extreme surface change, the effect of the increase commercial and industrial use.

Throughout the process of the identification it was found the best outcomes in terms of successful detection and interpretation of urban changes came from the use of LST

and LSE data in conjunction. Typically LSE data is assimilated in LST retrievals as merely a parameter to optimise to improve the LST, but in this study it was found the use of both was a key tool in making the important jump from land class to land use detection.

In the case of the New York case study the retrieval was able to investigate the LST and LSE changes between different types of urban sub-class. In particular it was able to use the LSE and LST in conjunction as there were surface that were similar in LST but not in LSE and vis versa. This allowing the identification of three distinct groups with in New York: industrial, residential and high rise. These three had different behaviour in the LSE and LST and their separation allows insight into the primary challenges of each type. The industrial areas had relatively standard LSE values in comparison to the rest of the scene but the anthropogenic usage resulted in LSTs much higher than the mean. Conversely the high rise sub-class showed average an LST distribution but the materials present were significantly different to those found elsewhere in the scene and had a significant impact on the LSE.

Additionally in assessing the literature on UHI studies in New York the retrieval was able to recreate the analysis of air temperature transects through central park and go on to extend the range of the transect to assess no only the vegetation effect on the LST but also the water surrounding Manhattan. The vegetation and the water both had a depressing effect upon the LST, but whereas Central parks cooling effect seemed limited, at least in LST terms, to the park its self, the land surrounding the waterways was on average 5 K cooler than the areas further inland. This effect would seem to be in line with the literature where this effect is seen with greater intensity in the air temperature data due to the sea breeze effect.

7 Conclusions and Future Work

7.1 Summary

This thesis has produced the first optimal estimation retrieval of LST and LSE from ASTER data, and indeed any other high spatial resolution thermal infrared instrument. In Chapter 4, a novel methodology was constructed that utilised the inter-channel correlations between the LSEs in the ASTER spectral library to generate a priori covariance. This approach was rigorously tested against two other methodologies. The approach utilising the ASTER spectral library a priori LSE and off-diagonal covariance was found to consistently perform with the highest accuracy and precision. This methodology gave the retrieval the adaptability to converge to the true LSEs across the entire range of materials tested including simulations where the a priori knowledge given to the retrieval was a poor descriptor of the true LSE, maintaining an accuracy of within 1 K.

The OE retrieval has been extensively evaluated over a large range of material drawn upon from two independent spectral libraries. The accurate and precise simulated retrievals with the SLUM spectral library materials were especially important as the materials in this library are representative of the urban material types that this retrieval algorithm was designed to primarily work with. The retrieval produces LST with per pixel retrieval uncertainties of 1.1 to 1.7 K in LST and 0.017 to 0.025 for emissivity.

The retrieval was adapted to retrieve a proxy for water vapour through an adaptation referred to as INC_WV. The retrieval was able incorporate water vapour into the state vector with a reduction in the radiance residuals across the channels and with comparable performance on the retrieved LST and LSE. The inclusion of water vapour also incorporated the uncertainty associated with atmospheric water vapour

into the a postori covariance matrix eliminating the potentially large forward model parameter error, (Comyn-Platt, 2014). The OE including INC_WV has the most generic applicability whilst maintaining the accuracy and precision. As such this version of the retrieval method is considered the most practical retrieval and was used subsequently moving forward.

Inter-comparison and verification of the OE retrieval was conducted for a scene over Algodones, USA. This was the first test of an OE scheme with real ASTER data and was compared to the pre-existing TES methodology. The LST retrieved was comparable between the two methods, but there was a distinct difference in the retrieved LSEs. The OE method retrieved higher LSEs in vegetative regions and lowers LSE across the rock and bare soil surfaces. Comparisons between the two methods and the verification site showed the OE method to perform comparably to the TES algorithm, with a marginal improvement in the retrieved LSE primarily driven by a reduction in the error in channel 12. The OE also produced a robust uncertainty estimate for each pixel, which is not information provided in the standard TES product, it must be independently requested. Channel 12 agrees well with TES but it is expected that TES would struggle over urban scenes. Hence the Algodones scene shows robustness of channel 12 and to some extent channels 13 and 14, with some increasing bias from channel 11 to channel 12. Therefore, the algorithm can be taken forward to apply OE to urban scenes as the OE is not particularly scene dependant.

Several case studies were made using the retrieval. Firstly, in Phoenix Arizona spanning the time period 2011-2014. The retrieved LSE cross all of the scenes had a high degree of stability in in all the channels except channel 10, which is subject to the greatest atmospheric influences. In particular, for LSEs over sites of continuous vegetation through the time period studied showed the variation between retrieved LSEs in all channels was less than 0.005. Such a low level of variation demonstrates a very high level of consistency in the retrieved result. From these results it is concluded that for use in land use and land classification studies channels 11 – 14 would be the most suited as they provide information on material variation. The most stable channel was that of channel 12 which, also possessed the consistently lowest radiance residuals. Due to this it was recommended that channel 12 be used as the default channel in change detection studies.

The retrieval for a transect was able to correctly identify, in the retrieved LSE, a region of cropland that was misclassified in the a priori data. Whilst showing the a priori to be a potentially significant source of error, it also demonstrated the adaptability of the OE retrieval to correctly converge to the true surface type, for cotton.

Latitudinal transects across diverse surface materials demonstrated the retrievals ability to isolated physical contrast associated with vegetation, normal urban surfaces and areas of high imperviousness. However it became apparent for large impervious areas distinguishing between man-made and natural material types was difficult due to the spectral similarities.

The urban green space was assessed in detail through longitudinal transects. The vegetation was found to have a cooling effect of up to 10 K on the LST. This was in line with expected levels within the literature and is particularly important in an arid environment where the water used to irrigate the vegetation has an increased cost associated with it.

In the second cases study, Shanghai was investigated. The urban challenges facing Shanghai revolve around the rapid expansion and development of the urban environment. The focus of this study was on the identification of change in the urban environment, as it is a vital parameter in the assessment of health risks and urban planning. The resulting analysis identified four regions of substantial land use changes relating to the land reclamation, and landscaping around the city's waterways and urban construction and redevelopment.

Region 4 in particular showed differing spatial structures in the LST and LSE parameters, highlighting the difference between changes in the materials of the surface and the impact of anthropogenic heating. With regions showing a homogenous LSE change between scenes of 0.04 but with heterogeneous distribution of LST showing a LST range of 5 K dependant on location with in the area identified as having undergone change.

The third case study assessed the LST and LSE structure of New York. The analysis focused on three distinct sub classes within the subset of New York: industrial, residential and high rise. The industrial and residential areas had similar LSE values sharing common building and construction materials. LSTs in the industrial regions

we much higher than those in the residential areas, showing the effect of anthropogenic activity due to different land usage between the two areas. The high rise sub-class showed LSTs consistent to the mean in the urban area but with higher LSEs in all channels. This indicate a substantial change in the materials present which is in line with change differences expected between the materials used in high rise builds and the rest of the scene.

A study of transects was made across Manhattan island. The study first compared the retrieved LST data to that of previous investigations into the urban heat island made using air temperature data gathered in situ. The transects were able to show a similar spatial distribution of temperatures and demonstrate the park's effect on depressing the urban heat effect. This transect was expanded to include a larger area including areas of industry and the water surrounding Manhattan Island. The water showed a consistent decrease in LST of 20 K whilst the vegetation showed a smaller offset of 10 K, and the water showed a cooling influence of approximately 5 K on the adjacent land.

Overall absolute LSE, and LSE variance, proved a surprisingly good marker of urban change, detecting the reclamation of land from the river, the removal of sedimentation, the construction of large commercial and industrial sites, as well as the differentiation between urban surfaces in different states of development/construction.

7.2 Future work

The work presented in this thesis shows potential for expansion and further work into a number of areas. Work continuing from this thesis spans improvements to the retrieval itself, the use of the algorithm and production of LST/LSE data in a large range of studies to enhance our knowledge of many aspects of the urban environment.

7.2.1 Improvements to the retrieval

The OE algorithm developed in this thesis demonstrates a proof of concept for simultaneous retrieval of LST and LSE from ASTER, and further work in critical

areas could improve the quality of the retrieved parameters. The key enhancements are as follows.

7.2.1.1 Inclusion of atmospheric temperature in the state vector

The introduction of mean atmospheric temperature could allow the retrieval even more flexibility and versatility to adapt to the observation with minimal reliance on ancillary data from modelling. The effect of atmospheric temperature is relatively small when compared to the dominate effects of LSE and atmospheric water vapour. However the perturbations are an additional source of forward model error that could be mitigated through the inclusion in the state vector. Initial studies on the inclusion of this parameter have already been conducted and tested with ASTER data with a marginal increase in uncertainty, less than 0.1 K, but requires more rigorous examination for implementation.

7.2.1.2 Atmospheric profile dependence

The atmospheric profiles contain many major gases which control the radiance obtained by the simulated forward model. The number of layers and gases included in the profile govern the resemblance to the real physical system. There are differences between different simulated forward models and in particular the treatment of the atmosphere can be markedly different between two models. The RTTOV model used in the large scale application of the algorithm, i.e. over a full scene has only the major gases utilised in its retrievals warranting the need to quantify the effect the absence of the these gases has on the retrieval.

The default RTTOV atmospheric gases include ozone and water vapour but do not include several other gases including CFCs. To assess the impact which the different atmospheric profiles have on the retrieval a simulation was performed with RFM; the RFM was described in section 2.41. RFM is a line-by-line model which takes considerable time and computing power, making it unsuitable for large data volumes; it can include a large number of gases and is able to simulate radiative transfer to a higher accuracy (Dudhia 2014). This study, shown in Figure 102, simulates the atmospheric profile differences in the forward models by recreating the atmospheric profiles used by RTTOV and running them on RFM for comparison with the native profile gases.

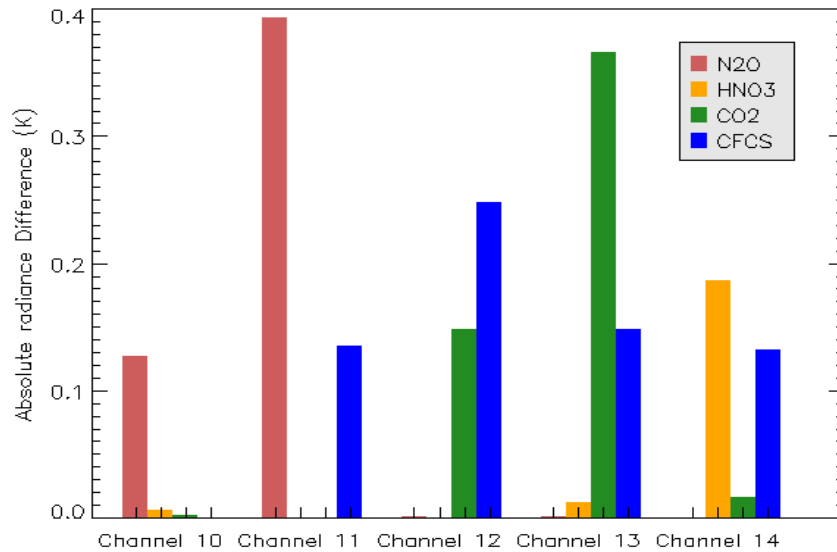


Figure 102 - Radiance differences between the gases used in the RFM and RTTOV simulations. Gases include N₂O, NHO₃, CO₂, and a collection of CFCs.

The radiance difference caused by the addition of these gases into the RTTOV simulation would have a measurable impact on the band radiance as the contributions of N₂O and CO₂ in channels 11 and 13 respectively make a significant reduction on the TOA brightness temperatures. The combined impact of these gases in channel 13 could account for a reduction of approximately 0.55 K. It is an additional source of error, and the follow on errors in the LSE retrieval can be significant. Further analysis of these terms is important as the scale of the offsets are not insignificant. Future studies should conduct larger scale simulation of these parameters with the retrieval in a linin-by-line model such as RFM and determine the variability and biases associated with them. The aim of such a study would be to introduce correction factors to improve the accuracy of the retrieval.

7.2.1.3 Classification

The a priori classification used in this thesis is based upon the VNIR channels of ASTER. A combination of the limited number of channels and the inter-scene variability of the unsupervised k-means cluster analysis make the returned classification subject to potential errors and inconsistencies between retrievals.

A full assessment of the accuracy of the land classification scheme is an important process and may inform updates to the a priori LSE based on the variability in performance of the classification.

A limited assessment of the classification has been conducted in the scenes studied in Phoenix, using the US National Land Cover Database (NCLD) from 2011 (Walker, 2015). However differences between classification groups used in the k-means cluster analysis and the classes used in the NCLD classifications meant that a direct inter-comparison was not appropriate. However a full study would allow the investigation and harmonisation of the different classifications to a common format where the accuracy of the retrieved classifications from ASTER VNIR could be rigorously assessed.

7.2.1.4 Backtracking the LSE to spectral library materials

Initial attempts to use the five retrieved LSEs to backtrack these LSEs to the nearest material match within the various available spectral libraries have been made. The aim was to utilise the retrieval to identify the most common or most spectrally dominate material type present within the pixel. An example is shown in Figure 103.

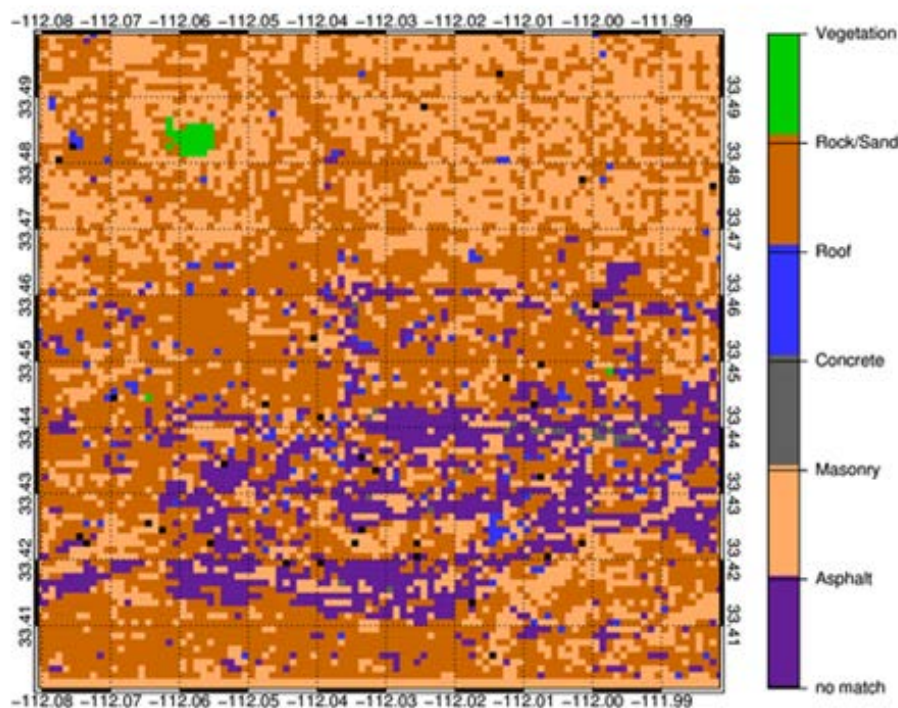


Figure 103 – Backtracked materials identified within the Phoenix subset for the 26/05/2011. The labels correspond to sub groups of materials from within the MODIS and SLUM spectral libraries.

There has been success in the identification of vegetation, water and several types of paving or brick work. However, the current results suffer from an inability to separate certain material groups. Most notable from Figure 103 is the un-realistic abundance of rock and sand within a predominately urban scene. Also the identification of asphalt in a region known to be a dry river bed. These issues arise as a result of the similarity between the spectra in a number of the materials within these sub groups, making a robust method of separation a body of work outside the scope of this thesis, but one with the potential to greatly enhance our knowledge of the urban environment.

7.2.2 Future Instrumentation and datasets

ASTER is an excellent system for use with the retrieval developed and used within this thesis, but it is neither optimal nor the only instrumentation system that could benefit from this methodology.

7.2.2.1 3-Band retrievals

Preliminary work has been conducted into a 3-band ASTER retrieval. The existing OE retrieval was modified to work with ASTER bands 12, 13 and 14.

A simulated study was conducted to assess the viability of a three channel simultaneous retrieval of the LST and the LSE. In order to analyse this the ASTER instrument was used as a testing platform. The testing was conducted using a range of several hundred atmospheres and over a hundred different material types taken from the MODIS spectral library.

This scenario was idealised in that the a priori data was not far removed from the truth but, the results shown in Figure 104 are promising in the potential for the retrieval accuracy. Clearly there is much work that could be done in fully optimising the retrieval approach.

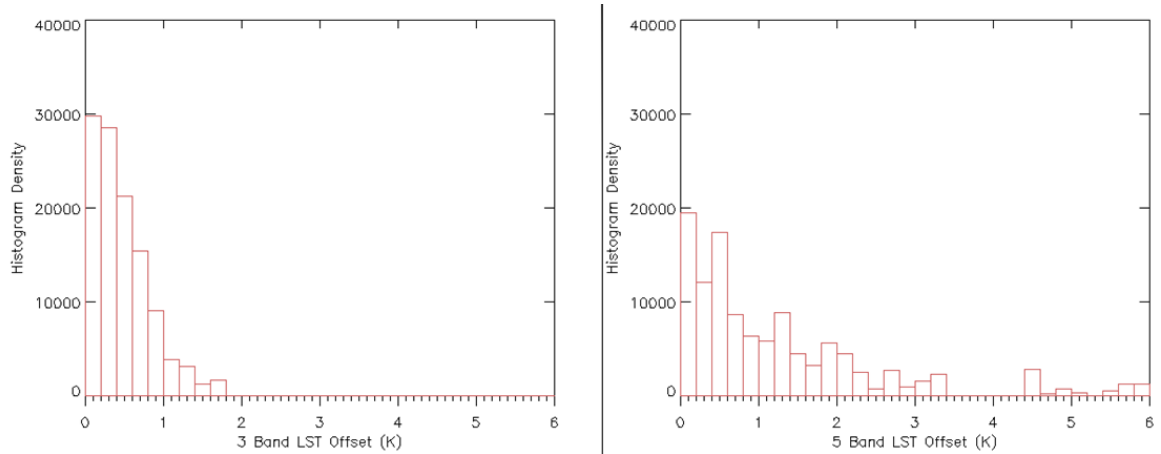


Figure 104 LEFT: the retrieved LST offset from truth values for the 3 band retrieval RIGHT: the 5 band retrieval

The retrieved uncertainty is larger in the three band retrieval by approximately 0.2 K on average. However the LST bias is very comparable to the five band retrieval. The structuring seen in Figure 105 is as a result of the three different land types input as the a priori land classification.

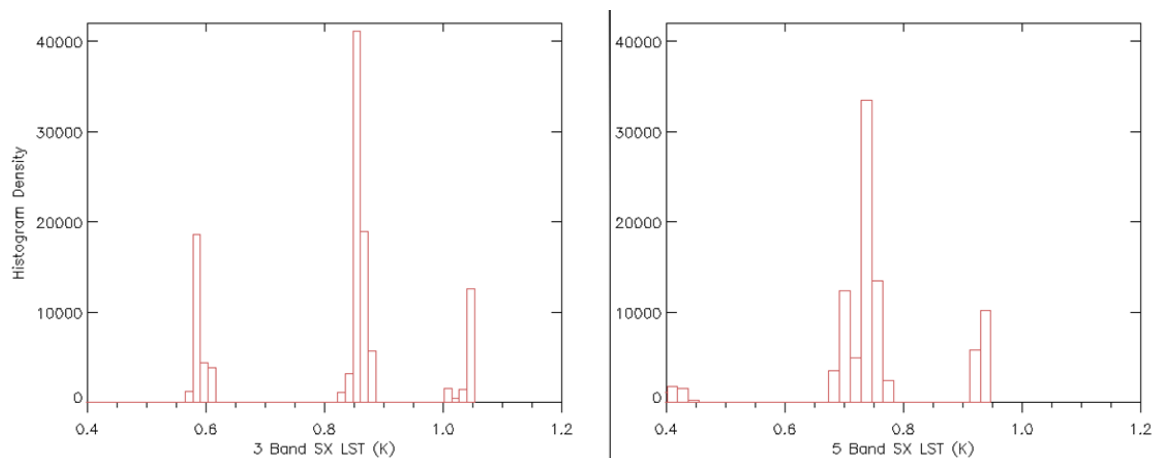


Figure 105 – LEFT: the retrieved LST uncertainty values for the 3 band retrieval RIGHT: and the 5 band retrieval

Given the premise of a three-band retrieval, a further possibility is to apply this methodology to MODIS bands 29, 31 and 32. This retrieval adaptation would require significantly more work, but has the potential for medium resolution studies including those pertaining to the diurnal cycle using MODIS.

The development of a three band retrieval also increases the options moving forward for the algorithm's application to future instrumentation.

7.2.2.2 Future instrumentation

Moving forward with studies of LST and LSE, particularly within the urban environment, a new high spatial resolution instrumentation is a logical step to meet increasing user and science requirement needs. ASTER has been the only high spatial resolution instrument in orbit capable of multi-channel retrieval of LST and or LSE. The LANDSAT satellites whilst possessing thermal instrumentation do not have the capabilities for split-window or OE methodologies resulting in a highly reliance on ancillary data for atmospheric and surface knowledge. LANDSAT 9 may alter this in future since LANDSAT 8 suffered from stray light problems which will hopefully be corrected.

To meet expanding and scientific requirements, whilst maintaining accuracy, new missions will need multiple channels (minimum of two for LST, three for LST/LSE) to improve upon the current state.

To this end a study was conducted to assess the optimal placement of similarly size bands to ASTER in the thermal infra-red. The aim was to identify band locations which provided the maximum sensitivity to change in the surface LST whilst being as independent from the influence of atmospheric water vapour as possible. In order to assess this, calculations of RFM spectra with spectral filters of 50 cm^{-1} were combined with Jacobians calculated for each.

Results are shown in Figure 106, a simple study based upon these criteria was conducted. It found that the ASTER TIR bands whilst well, placed for use in the retrieval of LSE were not necessarily optimally placed. In this study five new band locations were proposed. Future work building upon this could outline a framework of band requirements from which instrumentation could be derived for use in LST and or LSE retrieval.

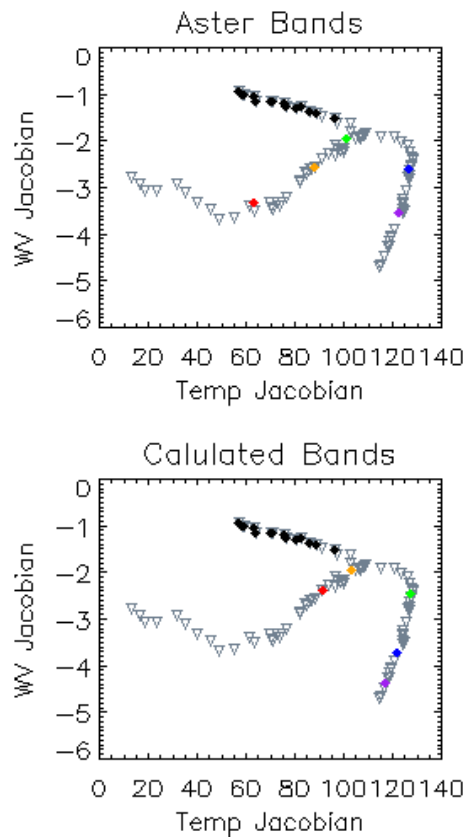


Figure 106 - Analysis of the effect of the location of the band centroid on the water vapour and surface temperature Jacobians, the y and x axes respectively. The TOP panel shows the location of potential bands with a band width of 50 cm^{-1} (the grey triangles). The black triangles correspond to those areas within the ozone absorption spectrum. And the coloured markers correspond to the locations the ASTER bands: channel 10 – red, channel 11 – gold, channel 12 – green, channel 13 – blue and channel 14 – purple. The BOTTOM panels show the same but for new proposed channels, where the coloured markers denote the new channels.

7.2.3 Applications of data

In this thesis the retrieval is applied to three case studies assessing the scientific questions relevant within the respective urban environment. Moving forward there are numerous areas in which this work can be applied to enhance our knowledge of key factors in urban studies.

7.2.3.1 Energy balance studies

A primary driver behind the retrieval of LST and LSE in the urban environment is the assessment of the urban energy balance. Knowledge and understanding of this aid in areas of health risk, pollution, thermal comfort and the long term adaptation of the urban environment to climate change. To do this, information regarding the

radiation budget is required. The LST informs the longwave outgoing radiation and the LSE can inform the material and hence the emissivity across a broad spectrum. This enables the estimation of longwave fluxes and could be used to estimate the night-time energy balance.

7.2.3.2 Holistic temporal and spatial LST and LSE

Observations from satellite instrumentation cover a range of spatial and temporal scales. Utilising a combination of these different spatial and temporal observations allows far more complex and in-depth analysis of the urban environment. In order to compare both LSE and LST there are several requirements. To obtain these parameters separately, the observing system must either have multiple bands (greater than two) for retrieval from a single observation. In the case of geostationary system, must have temporal resolution such that LSE can be derived using multiple observations over a short time interval during which the LSE is considered to be invariant. Ideally hyperspectral data can be used to such as observations from HyTES to obtain the LSE.

Acquisition of both high spatial resolution data and coarser spatial resolution but high temporal resolution data allows the monitoring of both long and short term changes in the urban thermal environment, features such as the diurnal cycle of season change as well as keeping the capability to understand the structure of the urban environment at a level where details pertaining to building planning and green space are relevant. The combination gives a robust and flexible platform from which investigate, and provide a logical step forward in urban studies.

To investigate the urban environment and in particular the UHI and health impacts, a key factor is the air temperature. In an ideal case high spatial resolution air temperature data retrieved consistently throughout the urban environment would mark a huge step forward in understanding and planning around some of the most important environmental influences which govern the urban landscape. However this is not currently possible. Air temperature networks such as BUCL (Azevedo, Chapman, & Muller, 2016) are excellent steps forward but are not wide spread nor do they have the required spatial resolution. But the use of LST data could help supplement this and bridge this gap.

7.3 Conclusions

Presently the best way to meet the requirements temporally and spatially for temperature data in the urban landscape is to retrieve LST from remote sensing. However, most current methods require prior knowledge of the LSE to retrieve accurate LST. The work shown in this thesis demonstrates that it is possible to retrieve accurate and precise values for not only LST but also of LSE in the urban environment. This presents a step forward in the capabilities of urban climate studies around temperature and enables the real possibility that with the refinements and further work suggested in this chapter, this work can be integrated into the large range of urban studies utilising both the LST and the LSE.

This work marks the first OE retrieval from ASTER data, and produces a great deal more new data from ASTER. Overall the retrieval gives better knowledge of LSE if compared to TES retrievals, with potentially significant improvement in urban areas.

8 Bibliography

- Abrams, M. (2000). The Advanced Spaceborne Thermal Emission and Reflection Radiometer (ASTER): Data products for the high spatial resolution imager on NASA's Terra platform. *International Journal of Remote Sensing*, 21(5), 847–859. <http://doi.org/10.1080/014311600210326>
- Abrams, M., Hook, S. J., & Ramachandran, B. (2014). *aster user guide v2*. Pasadena: JPL. Retrieved from http://asterweb.jpl.nasa.gov/content/03_data/04_Documents/aster_user_guide_v2.pdf
- Akbari, H., & Konopacki, S. (2005). Calculating energy-saving potentials of heat-island reduction strategies. *Energy Policy*, 33(6), 721–756. <http://doi.org/10.1016/j.enpol.2003.10.001>
- Allen, R. G., Tasumi, M., Morse, A., & Trezza, R. (2005). A Landsat-based energy balance and evapotranspiration model in Western US water rights regulation and planning. *Irrigation and Drainage Systems*, 19(3–4), 251–268.
- Anandakumar, K. (1999). A study on the partition of net radiation into heat fluxes on a dry asphalt surface. *Atmospheric Environment*, 33, 3911–3918.
- Arai, K., & Tonooka, H. (2005). Radiometric performance evaluation of ASTER VNIR, SWIR, and TIR. *IEEE Transactions on Geoscience and Remote Sensing*, 43(12), 2725–2732. <http://doi.org/10.1109/TGRS.2005.850392>
- Azevedo, J., Chapman, L., & Muller, C. (2016). Quantifying the Daytime and Night-Time Urban Heat Island in Birmingham, UK: A Comparison of Satellite Derived Land Surface Temperature and High Resolution Air

- Temperature Observations. *Remote Sensing*, 8(2), 153.
<http://doi.org/10.3390/rs8020153>
- Bäckström, E. (2005). *The surface energy balance and climate in an urban park and its surroundings*. Uppsala University. Retrieved from <http://uu.diva-portal.org/smash/record.jsf?pid=diva2:159145>
- Badarinath, K. V. S., Chand, T. R. K., Madhaviatha, K., & Raghavaswamy, V. (2005). Studies on urban heat islands using ENVISAT AATSR data. *Journal of the Indian Society of Remote Sensing*, 33(4), 495–501.
- Balling Jr, R. C., & Brazel, S. W. (1987). Time and space characteristics of the Phoenix urban heat island. *Journal of the Arizona-Nevada Academy of Science*, 75–81.
- Barnes, W. L., Pagano, T. S., & Salomonson, V. V. (1998). Prelaunch characteristics of the moderate resolution imaging spectroradiometer (MODIS) on EOS-AM1. *IEEE Transactions on Geoscience and Remote Sensing*, 36(4), 1088–1100.
- Bastiaanssen, W. G. M. (2000). SEBAL-based sensible and latent heat fluxes in the irrigated Gediz Basin, Turkey. *Journal of Hydrology*, 229(1), 87–100.
- Beltrami, H. (2001). Surface heat flux histories from inversion of geothermal data: Energy balance at the Earth's surface. *Journal of Geophysical Research*, 106(1), 21979–21993.
- Boreman, G. D. (2001). *Modulation Transfer Function in Optical and Electro-Optical Systems*. Bellingham WA: SPIE Press.
- Brazel, A., Gober, P., Lee, S., Grossman-Clarke, S., Zehnder, J., Hedquist, B., & Comparri, E. (2007). Determinants of changes in the regional urban heat

- island in metropolitan Phoenix (Arizona, USA) between 1990 and 2004. *Climate Research*, 33(2), 171–182.
- Bureau, U. S. C. (2015). American FactFinder - Results. Retrieved 1 September 2016, from <http://factfinder.census.gov/faces/tableservices/jsf/pages/productview.xhtml?src=bkmk>
- Burrough, P. A., van Gaans, P. F. ., & MacMillan, R. A. (2000). High-resolution land form classification using fuzzy k-means. *Fuzzy Sets and Systems*, 113, 37–52.
- Campbell, G. S., & Norman, J. M. (1998). *An Introduction to Environmental Biophysics* (2nd ed.). Springer Science+Business Media, Inc.
- Chang, D., Song, Y., & Liu, B. (2009). Visibility trends in six megacities in China 1973–2007. *Atmospheric Research*, 94(2), 161–167. <http://doi.org/10.1016/j.atmosres.2009.05.006>
- Chen, F., Yang, S., Su, Z., & Wang, K. (2016). Effect of emissivity uncertainty on surface temperature retrieval over urban areas: Investigations based on spectral libraries. *ISPRS Journal of Photogrammetry and Remote Sensing*, 114, 53–65. <http://doi.org/10.1016/j.isprsjprs.2016.01.007>
- Chen, G., Hay, G. J., Carvalho, L. M. T., & Wulder, M. A. (2012). Object-based change detection. *International Journal of Remote Sensing*, 33(14), 4434–4457. <http://doi.org/10.1080/01431161.2011.648285>
- Choudhury, B. J., Reginato, R. J., & Idso, S. B. (1986). An analysis of infrared temperature observations over wheat and calculation of latent heat flux. *Agricultural and Forest Meteorology*, 37(1), 75–88.

- Clinton, N., & Gong, P. (2013). MODIS detected surface urban heat islands and sinks: Global locations and controls. *Remote Sensing of Environment*, 134, 294–304.
- Cohen, B. (2006). Urbanization in developing countries: Current trends, future projections, and key challenges for sustainability. *Technology in Society*, 28(1–2), 63–80. <http://doi.org/10.1016/j.techsoc.2005.10.005>
- Comyn-Platt, E. M. (2014). *Land surface temperature: a comparison of products from polar orbiting and geostationary satellites*. Department of Physics and Astronomy. Retrieved from <https://ira.le.ac.uk/handle/2381/28815>
- Connors, J. P., Galletti, C. S., & Chow, W. T. L. (2013). Landscape configuration and urban heat island effects: assessing the relationship between landscape characteristics and land surface temperature in Phoenix, Arizona. *Landscape Ecology*, 28(2), 271–283. <http://doi.org/10.1007/s10980-012-9833-1>
- Corburn, J. (2009). Cities, Climate Change and Urban Heat Island Mitigation: Localising Global Environmental Science. *Urban Studies*, 46(2), 413–427. <http://doi.org/10.1177/0042098008099361>
- Cui, L., & Shi, J. (2012). Urbanization and its environmental effects in Shanghai, China. *Urban Climate*, 2, 1–15. <http://doi.org/10.1016/j.uclim.2012.10.008>
- Dash, P., Göttsche, F.-M., Olesen, F.-S., & Fischer, H. (2002). Land surface temperature and emissivity estimation from passive sensor data: Theory and practice-current trends. *International Journal of Remote Sensing*, 23(13), 2563–2594. <http://doi.org/10.1080/01431160110115041>
- Dee, D. P., Uppala, S. M., Simmons, A. J., Berrisford, P., Poli, P., Kobayashi, S., ... Vitart, F. (2011). The ERA-Interim reanalysis: configuration and

- performance of the data assimilation system. *Quarterly Journal of the Royal Meteorological Society*, 137(656), 553–597. <http://doi.org/10.1002/qj.828>
- Dudhia, A. (2014). REFERENCE FORWARD MODEL (RFM). Retrieved 18 October 2014, from <http://www.atm.ox.ac.uk/RFM/index.html>
- Fan, H., & Sailor, D. (2005). Modeling the impacts of anthropogenic heating on the urban climate of Philadelphia: a comparison of implementations in two PBL schemes. *Atmospheric Environment*, 39(1), 73–84. <http://doi.org/10.1016/j.atmosenv.2004.09.031>
- Fast, J. D., Torcolini, J. C., & Redman, R. (2005). Pseudovertical temperature profiles and the urban heat island measured by a temperature datalogger network in Phoenix, Arizona. *Journal of Applied Meteorology*, 44(1), 3–13.
- Feng, X., Foody, G., Aplin, P., & Gosling, S. N. (2015). Enhancing the spatial resolution of satellite-derived land surface temperature mapping for urban areas. *Sustainable Cities and Society*, 19, 341–348. <http://doi.org/10.1016/j.scs.2015.04.007>
- French, A., Schmugge, T., Ritchie, J., Hsu, A., Jacob, F., & Ogawa, K. (2008). Detecting land cover change at the Jornada Experimental Range, New Mexico with ASTER emissivities. *Remote Sensing of Environment*, 112(4), 1730–1748. <http://doi.org/10.1016/j.rse.2007.08.020>
- Friedl, M. A. (2002). Forward and inverse modeling of land surface energy balance using surface temperature measurements. *Remote Sensing of Environment*, 79(2), 344–354.
- Fujisada, H., Sakuma, F., Ono, A., & Kudoh, M. (1998). Design and preflight performance of ASTER instrument protoflight model. *IEEE Transactions on Geoscience and Remote Sensing*, 36(4), 1152–1160.

- Gabriel, K. M. A., & Endlicher, W. R. (2011). Urban and rural mortality rates during heat waves in Berlin and Brandenburg, Germany. *Environmental Pollution*, *159*(8–9), 2044–2050.
<http://doi.org/10.1016/j.envpol.2011.01.016>
- Gaffin, S. R., Rosenzweig, C., Khanbilvardi, R., Parshall, L., Mahani, S., Glickman, H., ... Hillel, D. (2008). Variations in New York city's urban heat island strength over time and space. *Theoretical and Applied Climatology*, *94*(1–2), 1–11. <http://doi.org/10.1007/s00704-007-0368-3>
- Gedzelman, S. D., Austin, S., Cermak, R., Stefano, N., Partridge, S., Quesenberry, S., & Robinson, D. A. (2003). Mesoscale aspects of the urban heat island around New York City. *Theoretical and Applied Climatology*, *75*(1–2), 29–42.
- Gillespie, A. R., Rokugawa, S., Hook, S. J., Matsunaga, T., & Kahle, A. B. (1999). Temperature/emissivity separation algorithm theoretical basis document, version 2.4. *ATBD Contract NAS5-31372, NASA*. Retrieved from http://crs.itb.ac.id/media/jurnal/refs/critical_review/Download/12Jun/atbd-ast-05-08.pdf
- Gober, P., Brazel, A., Quay, R., Myint, S., Grossman-Clarke, S., Miller, A., & Rossi, S. (2009). Using Watered Landscapes to Manipulate Urban Heat Island Effects: How Much Water Will It Take to Cool Phoenix? *Journal of the American Planning Association*, *76*(1), 109–121.
<http://doi.org/10.1080/01944360903433113>
- Gong, P., Liang, S., Carlton, E. J., Jiang, Q., Wu, J., Wang, L., & Remais, J. V. (2012). Urbanisation and health in China. *The Lancet*, *379*(9818), 843–852.

- Grigsby, S. P., Hulley, G. C., Roberts, D. A., Scheele, C., Ustin, S. L., & Alsina, M. M. (2015). Improved surface temperature estimates with MASTER/AVIRIS sensor fusion. *Remote Sensing of Environment*, *167*, 53–63.
<http://doi.org/10.1016/j.rse.2015.05.019>
- Grimm, N. B., Faeth, S. H., Golubiewski, N. E., Redman, C. L., Wu, J., Bai, X., & Briggs, J. M. (2008). Global change and the ecology of cities. *Science*, *319*(5864), 756–760.
- Grimm, N. B., & Redman, C. L. (2004). Approaches to the study of urban ecosystems: the case of Central Arizona—Phoenix. *Urban Ecosystems*, *7*(3), 199–213.
- Grimmond, C. S. B., & Oke, T. R. (2002). Turbulent heat fluxes in urban areas: observations and a local-scale urban meteorological parameterization scheme (LUMPS). *Journal of Applied Meteorology*, *41*(7), 792–810.
- Guhathakurta, S., & Gober, P. (2007). The Impact of the Phoenix Urban Heat Island on Residential Water Use. *Journal of the American Planning Association*, *73*(3), 317–329. <http://doi.org/10.1080/01944360708977980>
- Halper, E. B., Scott, C. A., & Yool, S. R. (2012). Correlating Vegetation, Water Use, and Surface Temperature in a Semiarid City: A Multiscale Analysis of the Impacts of Irrigation by Single-Family Residences: Correlating Vegetation, Water Use, and Surface Temperature in a Semiarid City. *Geographical Analysis*, *44*(3), 235–257. <http://doi.org/10.1111/j.1538-4632.2012.00846.x>
- Harlan, S. L., & Ruddell, D. (2011). Climate change and health in cities: impacts of heat and air pollution and potential co-benefits from mitigation and adaptation. *Current Opinion in Environmental Sustainability*, *3*, 126–134.

- Harman, I. (2003). *The energy balance of urban areas*. University of Reading, Reading. Retrieved from <http://www.met.rdg.ac.uk/phdtheses/The%20energy%20balance%20of%20urban%20areas.pdf>
- Hawkins, T. W., Brazel, A. J., Stefanov, W. L., Bigler, W., & Saffell, E. M. (2004). The role of rural variability in urban heat island determination for Phoenix, Arizona. *Journal of Applied Meteorology*, 43(3), 476–486.
- Herold, M., Gardner, M. E., & Roberts, D. A. (2003). Spectral resolution requirements for mapping urban areas. *IEEE Transactions on Geoscience and Remote Sensing*, 41(9), 1907–1919. <http://doi.org/10.1109/TGRS.2003.815238>
- Hocking, J., Rayer, P., Rundle, D., Saunders, R., Matricardi, M., Geer, A., ... Vidot, J. (2014). *RTTOV v11 Users Guide (User Guide)*. Exeter: MET Office. Retrieved from http://nwpsaf.eu/deliverables/rtm/docs_rttov11/users_guide_11_v1.3.pdf
- Hook, S. J., Johnson, W. R., & Abrams, M. J. (2013). NASA's Hyperspectral Thermal Emission Spectrometer (HyTES). In C. Kuenzer & S. Dech (Eds.), *Thermal Infrared Remote Sensing: Sensors, Methods, Applications* (pp. 93–115). Dordrecht: Springer Netherlands. Retrieved from http://dx.doi.org/10.1007/978-94-007-6639-6_5
- Hook, S. J., Vaughan, R. G., Tonooka, H., & Schladow, S. G. (2007). Absolute Radiometric In-Flight Validation of Mid Infrared and Thermal Infrared Data From ASTER and MODIS on the Terra Spacecraft Using the Lake Tahoe, CA/NV, USA, Automated Validation Site. *IEEE Transactions on*

Geoscience and Remote Sensing, 45(6), 1798–1807.

<http://doi.org/10.1109/TGRS.2007.894564>

Hulley, G. C., & Hook, S. J. (2011). Generating Consistent Land Surface Temperature and Emissivity Products Between ASTER and MODIS Data for Earth Science Research. *IEEE Transactions on Geoscience and Remote Sensing*, 49(4), 1304–1315. <http://doi.org/10.1109/TGRS.2010.2063034>

Hulley, G. C., Hughes, C. G., & Hook, S. J. (2012). Quantifying uncertainties in land surface temperature and emissivity retrievals from ASTER and MODIS thermal infrared data. *Journal of Geophysical Research*, 117(D23). <http://doi.org/10.1029/2012JD018506>

Hussain, M., Chen, D., Cheng, A., Wei, H., & Stanley, D. (2013). Change detection from remotely sensed images: From pixel-based to object-based approaches. *ISPRS Journal of Photogrammetry and Remote Sensing*, 80, 91–106. <http://doi.org/10.1016/j.isprsjprs.2013.03.006>

Jenerette, G. D., Harlan, S. L., Buyantuev, A., Stefanov, W. L., Deplet-Barreto, J., Ruddell, B. L., ... Li, X. (2016). Micro-scale urban surface temperatures are related to land-cover features and residential heat related health impacts in Phoenix, AZ USA. *Landscape Ecology*, 31(4), 745–760. <http://doi.org/10.1007/s10980-015-0284-3>

Jiménez-Muñoz, J., & Sobrino, J. A. (2003). A Generalised Single-Channel Method for Retrieving Land Surface Temperature from Remote Sensing Data. *Journal of Geophysical Research*, 108. Retrieved from http://www.uv.es/~ucg/articulos/2005/Publications_2003_13.pdf

Justice, C. O., Vermote, E., Townshend, J. R., Defries, R., Roy, D. P., Hall, D. K., ... others. (1998). The Moderate Resolution Imaging Spectroradiometer

- (MODIS): Land remote sensing for global change research. *IEEE Transactions on Geoscience and Remote Sensing*, 36(4), 1228–1249.
- Kotthaus, S., Smith, T. E. L., Wooster, M. J., & Grimmond, C. S. B. (2014). Derivation of an urban materials spectral library through emittance and reflectance spectroscopy. *ISPRS Journal of Photogrammetry and Remote Sensing*, 94, 194–212. <http://doi.org/10.1016/j.isprsjprs.2014.05.005>
- Li, J., Song, C., Cao, L., Zhu, F., Meng, X., & Wu, J. (2011). Impacts of landscape structure on surface urban heat islands: A case study of Shanghai, China. *Remote Sensing of Environment*, 115(12), 3249–3263. <http://doi.org/10.1016/j.rse.2011.07.008>
- Li, J., Wang, X., Wang, X., Ma, W., & Zhang, H. (2009). Remote sensing evaluation of urban heat island and its spatial pattern of the Shanghai metropolitan area, China. *Ecological Complexity*, 6(4), 413–420. <http://doi.org/10.1016/j.ecocom.2009.02.002>
- Li, Y., Zhang, H., & Kainz, W. (2012). Monitoring patterns of urban heat islands of the fast-growing Shanghai metropolis, China: Using time-series of Landsat TM/ETM+ data. *International Journal of Applied Earth Observation and Geoinformation*, 19, 127–138. <http://doi.org/10.1016/j.jag.2012.05.001>
- Liang, S. (2001). An optimization algorithm for separating land surface temperature and emissivity from multispectral thermal infrared imagery. *Geoscience and Remote Sensing, IEEE Transactions on*, 39(2), 264–274.
- Liang, S., Goward, S., Ranson, J., Dubayah, R., & Kalluri, S. (1995). Retrieval of atmospheric water vapor and land surface temperature from AVHRR thermal imagery. In *Geoscience and Remote Sensing Symposium, 1995. IGARSS'95. 'Quantitative Remote Sensing for Science and Applications'*,

- International* (Vol. 3, pp. 1959–1961). IEEE. Retrieved from http://ieeexplore.ieee.org/xpls/abs_all.jsp?arnumber=524078
- Liang, X., & Ignatov, A. (2013). AVHRR, MODIS, and VIIRS radiometric stability and consistency in SST bands: AVHRR-MODIS-VIIRS Consistency. *Journal of Geophysical Research: Oceans*, *118*(6), 3161–3171. <http://doi.org/10.1002/jgrc.20205>
- Liang, X., Wood, E., & Lettenmaier, D. (1999). Modeling ground heat flux in land surface parameterization schemes. *Journal of Geophysical Research*, *104*, 9581–9600.
- Locke, D. H., Grove, J. M., Lu, J. W., Troy, A., O’Neil-Dunne, J. P., & Beck, B. D. (2011). Prioritizing preferable locations for increasing urban tree canopy in New York City. *Cities and the Environment (CATE)*, *3*(1), 4.
- Lu, D., & Weng, Q. (2006). Use of impervious surface in urban land-use classification. *Remote Sensing of Environment*, *102*(1–2), 146–160. <http://doi.org/10.1016/j.rse.2006.02.010>
- MacCallum, S. N., & Merchant, C. J. (2012). Surface water temperature observations of large lakes by optimal estimation. *Canadian Journal of Remote Sensing*, *38*(1), 25–45. <http://doi.org/10.5589/m12-010>
- Martilli, A., Clappier, A., & Rotach, M. W. (2002). An urban surface exchange parameterisation for mesoscale models. *Boundary-Layer Meteorology*, *104*(2), 261–304.
- Masson, V. (2000). A physically-based scheme for the urban energy budget in atmospheric models. *Boundary-Layer Meteorology*, *94*, 357–397.
- Matricardi, M. (2009). Technical Note: An assessment of the accuracy of the RTTOV fast radiative transfer model using IASI data. *Atmos. Chem. Phys.*

- 9(2). Retrieved from
<http://citeseerx.ist.psu.edu/viewdoc/download?doi=10.1.1.453.685&rep=rep1&type=pdf>
- Monteith, J. L., & Unsworth, M. H. (2013). *Principles of environmental physics: plants, animals, and the atmosphere* (4th ed). Amsterdam ; Boston: Elsevier/Academic Press.
- NASA. (2004a, September 7). ASTER SWIR. Retrieved 11 January 2016, from <http://asterweb.jpl.nasa.gov/swir.asp>
- NASA. (2004b, September 7). ASTER VNIR. Retrieved 11 January 2016, from <http://asterweb.jpl.nasa.gov/vnir.asp>
- NASA. (2015). *AST_LIT Product User's Guide*. Retrieved from https://lpdaac.usgs.gov/sites/default/files/public/product_documentation/aster_11t_users_guide.pdf
- Neteler, M. (2004). MODIS time series remote sensing for epidemiological modelling. *International Symposium on Geoinformatics for Spatial Infrastructure Development in Earth and Allied Sciences*. Retrieved from http://www.academia.edu/853387/MODIS_time_series_remote_sensing_for_epidemiological_modelling
- Noyes, E. J. (2005). *An investigation into the accuracy of surface temperature retrievals from the AATSR*. Physics and Astronomy. Retrieved from <https://ira.le.ac.uk/handle/2381/30690>
- Oke, T. R. (1988). The urban energy balance. *Progress in Physical Geography*, 12(4), 471–508. <http://doi.org/10.1177/030913338801200401>
- Oltra-Carrio, R., Cubero-Castan, M., Briottet, X., & Sobrino, J. A. (2014). Analysis of the Performance of the TES Algorithm Over Urban Areas. *IEEE*

Transactions on Geoscience and Remote Sensing, 52(11), 6989–6998.

<http://doi.org/10.1109/TGRS.2014.2306441>

- Pandya, M. R., Shah, D. B., Trivedi, H. J., Lunagaria, M. M., Pandey, V., Panigrahy, S., & Parihar, J. S. (2013). Field Measurements of Plant Emissivity Spectra: An Experimental Study on Remote Sensing of Vegetation in the Thermal Infrared Region. *Journal of the Indian Society of Remote Sensing*, 41(4), 787–796. <http://doi.org/10.1007/s12524-013-0283-2>
- Petkova, E. P., Vink, J. K., Horton, R. M., Gasparri, A., Bader, D. A., Francis, J. D., & Kinney, P. L. (2016). Towards More Comprehensive Projections of Urban Heat-Related Mortality: Estimates for New York City under Multiple Population, Adaptation, and Climate Scenarios. *Environmental Health Perspectives*. <http://doi.org/10.1289/EHP166>
- Piringer, M., Grimmond, C. S. B., Joffre, S. M., Mestayer, P., Middleton, D. R., Rotach, M. W., ... Guilloteau, E. (2002). Investigating the surface energy balance in urban areas—recent advances and future needs. *Water, Air and Soil Pollution: Focus*, 2(5–6), 1–16.
- Prata, A. J. (2002). Land surface temperature measurement from space: AATSR algorithm theoretical basis document. *Contract Report to ESA, CSIRO Atmospheric Research, Aspendale, Victoria, Australia*. Retrieved from http://earth.esa.int/pub/ESA_DOC/LST-ATBD.pdf
- Qin, Z., & Karnieli, A. (1999). Progress in the remote sensing of land surface temperature and ground emissivity using NOAA-AVHRR data. *International Journal of Remote Sensing*, 20(12), 2367–2393. <http://doi.org/10.1080/014311699212074>

- Ren, W., Zhong, Y., Meligrana, J., Anderson, B., Watt, W. E., Chen, J., & Leung, H.-L. (2003). Urbanization, land use, and water quality in Shanghai. *Environment International*, 29(5), 649–659. [http://doi.org/10.1016/S0160-4120\(03\)00051-5](http://doi.org/10.1016/S0160-4120(03)00051-5)
- Ridd, M. K., & Liu, J. (1998). A comparison of four algorithms for change detection in an urban environment. *Remote Sensing of Environment*, 63(2), 95–100.
- Roberts, R. E., Selby, J. E., & Biberman, L. M. (1976). Infrared continuum absorption by atmospheric water vapor in the 8–12- μm window. *Applied Optics*, 15(9), 2085–2090.
- Rodgers, C. D. (2000). *Inverse methods for atmospheric sounding - Theory and Practise*. (Vol. 2). World Scientific Publishing Co. Pte. Ltd.
- Roth, M., Oke, T. R., & Emery, W. J. (1989). Satellite-derived urban heat islands from three coastal cities and the utilization of such data in urban climatology. *International Journal of Remote Sensing*, 10(11).
- Sakuma, F., & Ono, A. (1993). Radiometric calibration of the EOS ASTER instrument. *Metrologia*, 30(4), 231.
- Sakuma, F., Ono, A., Tsuchida, S., Ohgi, N., Inada, H., Akagi, S., & Ono, H. (2005). Onboard calibration of the ASTER instrument. *IEEE Transactions on Geoscience and Remote Sensing*, 43(12), 2715–2724. <http://doi.org/10.1109/TGRS.2005.857887>
- Stefanov, W. L., & Netzband, M. (2005). Assessment of ASTER land cover and MODIS NDVI data at multiple scales for ecological characterization of an arid urban center. *Remote Sensing of Environment*, 99(1–2), 31–43. <http://doi.org/10.1016/j.rse.2005.04.024>

- Stone, B., Hess, J. J., & Frumkin, H. (2010). Urban Form and Extreme Heat Events: Are Sprawling Cities More Vulnerable to Climate Change Than Compact Cities? *Environmental Health Perspectives*, *118*(10), 1425–1428.
<http://doi.org/10.1289/ehp.0901879>
- SWIR - ASTER User Advisory. (2016). Retrieved 23 March 2016, from
<https://asterweb.jpl.nasa.gov/swir-alert.asp>
- Tachikawa, T., Hato, M., Kaku, M., & Iwasaki, A. (2011). Characteristics of ASTER GDEM version 2. In *Geoscience and Remote Sensing Symposium (IGARSS), 2011 IEEE International* (pp. 3657–3660). IEEE. Retrieved from
http://ieeexplore.ieee.org/xpls/abs_all.jsp?arnumber=6050017
- Taha, H. (1997). Urban climates and heat islands: albedo, evapotranspiration, and anthropogenic heat. *Energy and Buildings*, *25*(2), 99–103.
- Tan, J., Zheng, Y., Tang, X., Guo, C., Li, L., Song, G., ... Chen, H. (2010). The urban heat island and its impact on heat waves and human health in Shanghai. *International Journal of Biometeorology*, *54*(1), 75–84.
<http://doi.org/10.1007/s00484-009-0256-x>
- Tennakoon, S. B., & Milroy, S. P. (2003). Crop water use and water use efficiency on irrigated cotton farms in Australia. *Agricultural Water Management*, *61*(3), 179–194. [http://doi.org/10.1016/S0378-3774\(03\)00023-4](http://doi.org/10.1016/S0378-3774(03)00023-4)
- Theeuwes, N. E., Solcerová, A., & Steeneveld, G. J. (2013). Modeling the influence of open water surfaces on the summertime temperature and thermal comfort in the city: SURFACE WATER AND URBAN TEMPERATURES. *Journal of Geophysical Research: Atmospheres*, *118*(16), 8881–8896.
<http://doi.org/10.1002/jgrd.50704>

- Tomlinson, C. J., Chapman, L., Thornes, J. E., & Baker, C. J. (2011). Including the urban heat island in spatial heat health risk assessment strategies: a case study for Birmingham, UK. *International Journal of Health Geographics*, *10*(1), 1.
- United Nations. (2015). *World Population Prospects: The 2015 Revision, Key Findings and Advance Tables*. (No. ESA/P/WP.241). Retrieved from https://esa.un.org/unpd/wpp/publications/files/key_findings_wpp_2015.pdf
- van den Hurk, B. J., Jia, L., & Menenti, M. (2002). Assimilation of land surface temperature data from ATSR in an NWP environment-case studies with ATSR data in Spain and The Netherlands. In *Geoscience and Remote Sensing Symposium, 2002. IGARSS'02. 2002 IEEE International* (Vol. 1, pp. 36–38). Retrieved from http://ieeexplore.ieee.org/xpls/abs_all.jsp?arnumber=1024933
- van der Meer, F. D., van der Werff, H. M. A., van Ruitenbeek, F. J. A., Hecker, C. A., Bakker, W. H., Noomen, M. F., ... Woldai, T. (2012). Multi- and hyperspectral geologic remote sensing: A review. *International Journal of Applied Earth Observation and Geoinformation*, *14*(1), 112–128. <http://doi.org/10.1016/j.jag.2011.08.002>
- Voogt, J. ., & Oke, T. . (2003). Thermal remote sensing of urban climates. *Remote Sensing of Environment*, *86*(3), 370–384. [http://doi.org/10.1016/S0034-4257\(03\)00079-8](http://doi.org/10.1016/S0034-4257(03)00079-8)
- Walker, S. (2015). Close-Range Photogrammetry and 3D Imaging. *Photogrammetric Engineering & Remote Sensing*, *81*(4), 273–274.
- Wan, Z. (2006). *MODIS LST products Users guide C5* (p. 30). Santa Barbara: Universtiy of California. Retrieved from

http://www.icesb.ucsb.edu/modis/LstUsrGuide/MODIS_LST_products_Usage_guide_C5.pdf

- Wan, Z. (2008). New refinements and validation of the MODIS Land-Surface Temperature/Emissivity products. *Remote Sensing of Environment*, 112(1), 59–74. <http://doi.org/10.1016/j.rse.2006.06.026>
- Wan, Z., & Li, Z. -L. (2008). Radiance-based validation of the V5 MODIS land-surface temperature product. *International Journal of Remote Sensing*, 29(17–18), 5373–5395. <http://doi.org/10.1080/01431160802036565>
- Wan, Z., Zhang, Y., Zhang, Q., & Li, Z. (2002). Validation of the land-surface temperature products retrieved from Terra Moderate Resolution Imaging Spectroradiometer data. *Remote Sensing of Environment*, 83(1), 163–180.
- Wan, Z., Zhang, Y., Zhang, Q., & Li, Z.-L. (2004). Quality assessment and validation of the MODIS global land surface temperature. *International Journal of Remote Sensing*, 25(1), 261–274. <http://doi.org/10.1080/0143116031000116417>
- Wang, C., Myint, S., Wang, Z., & Song, J. (2016). Spatio-Temporal Modeling of the Urban Heat Island in the Phoenix Metropolitan Area: Land Use Change Implications. *Remote Sensing*, 8(3), 185. <http://doi.org/10.3390/rs8030185>
- Wang, J., & Bras, R. (1999). Ground heat flux estimated from surface soil temperature. *Journal of Hydrology*, 216, 214–226.
- Ward, D., Phinn, S. R., & Murray, A. T. (2000). Monitoring Growth in Rapidly Urbanizing Areas Using Remotely Sensed Data. *The Professional Geographer*, 52(3), 371–386. <http://doi.org/10.1111/0033-0124.00232>
- Weng, Q., & Lu, D. (2008). A sub-pixel analysis of urbanization effect on land surface temperature and its interplay with impervious surface and vegetation

- coverage in Indianapolis, United States. *International Journal of Applied Earth Observation and Geoinformation*, 10(1), 68–83.
<http://doi.org/10.1016/j.jag.2007.05.002>
- Weng, Q., Lu, D., & Schubring, J. (2004). Estimation of land surface temperature - vegetation abundance relationship for urban heat island studies. *Remote Sensing of Environment*, 89, 467–483.
- Xiong, X., & Barnes, W. L. (2006). An Overview of MODIS Radiometric Calibration and Characterisation. *Advances in Atmospheric Sciences*, 23(1), 67–79.
- Xiong, X., Chiang, K., Esposito, J., Guenther, B., & Barnes, W. (2003). MODIS on-orbit calibration and characterization. *Metrologia*, 40(1), S89.
- Xiong, X., Salomonson, V. V., Chiang, K., Wu, A., Guenther, B., & Barnes, W. L. (2004). On-orbit characterization of RVS for MODIS thermal emissive bands. *Passive Optical Remote Sensing of the Atmosphere and Clouds IV*.
<http://doi.org/10.1117/12.578344>
- Xiong, X., Sun, J., Barnes, W., Salomonson, V., Esposito, J., Erives, H., & Guenther, B. (2007). Multiyear On-Orbit Calibration and Performance of Terra MODIS Reflective Solar Bands. *IEEE Transactions on Geoscience and Remote Sensing*, 45(4), 879–889.
<http://doi.org/10.1109/TGRS.2006.890567>
- Xu, L.-Y., Yin, H., & Xie, X.-D. (2014). Health Risk Assessment of Inhalable Particulate Matter in Beijing Based on the Thermal Environment. *International Journal of Environmental Research and Public Health*, 11(12), 12368–12388. <http://doi.org/10.3390/ijerph111212368>

- Yamaguchi, Y., Kahle, A. B., Tsu, H., Kawakami, T., & Pniel, M. (1998). Overview of advanced spaceborne thermal emission and reflection radiometer (ASTER). *Geoscience and Remote Sensing, IEEE Transactions on*, 36(4), 1062–1071.
- Yu, C., & Hien, W. N. (2006). Thermal benefits of city parks. *Energy and Buildings*, 38(2), 105–120. <http://doi.org/10.1016/j.enbuild.2005.04.003>
- Zarr, R. R., Chavez, J. A., Lee, A. Y., Dalton, G., & Young, S. L. (2015). *NIST Heat Transmission Properties of Insulating and Building Materials, NIST Standard Reference Database Number 81*. National Institute of Standards and Technology. Retrieved from <http://srdata.nist.gov/Insulation/>
- Zhang, H., Qi, Z., Ye, X., Cai, Y., Ma, W., & Chen, M. (2013). Analysis of land use/land cover change, population shift, and their effects on spatiotemporal patterns of urban heat islands in metropolitan Shanghai, China. *Applied Geography*, 44, 121–133. <http://doi.org/10.1016/j.apgeog.2013.07.021>
- Zhang, X., Zhong, T., Feng, X., & Wang, K. (2009). Estimation of the relationship between vegetation patches and urban land surface temperature with remote sensing. *International Journal of Remote Sensing*, 30(8), 2105–2118. <http://doi.org/10.1080/01431160802549252>
- Zhang, Y., Balzter, H., & Wu, X. (2013). Spatial–temporal patterns of urban anthropogenic heat discharge in Fuzhou, China, observed from sensible heat flux using Landsat TM/ETM+ data. *International Journal of Remote Sensing*, 34(4), 1459–1477. <http://doi.org/10.1080/01431161.2012.718465>
- Zhu, J., Ding, P., Zhang, L., Wu, H., & Cao, H. (2006). Influence of the deep waterway project on the Changjiang Estuary. In *The environment in Asia*

Pacific harbours (pp. 79–92). Springer. Retrieved from
http://link.springer.com/chapter/10.1007/1-4020-3655-8_6